GSI

Diss. 2005 -16
December

A NEW DEVELOPED CALORIMETER TELESCOPE FOR IDENTIFICATION OF RELATIVISTIC HEAVY-ION REACTION CHANNELS

R. Lozeva

(Dissertation St. Kliment Ohridski University of Sofia)

Gesellschaft für Schwerionenforschung mbH
Planckstraße 1 · D-64291 Darmstadt · Germany
Postfach 11 05 52 · D-64220 Darmstadt · Germany

University of Sofia "St. Kliment Ohridski"
Faculty of Physics, Sofia, Bulgaria

Gesellschaft für Schwerionenforschung, GSI
Darmstadt, Germany

Radomira Lozeva

A NEW DEVELOPED CALORIMETER TELESCOPE FOR IDENTIFICATION OF RELATIVISTIC HEAVY-ION REACTION CHANNELS

A thesis submitted for the PhD degree

Scientific code: 01.03.04. (Nuclear Physics)

Scientific supervisors

Dr. Dimiter Balabanski
University of Sofia
Bulgaria

Dr. Jürgen Gerl
GSI-Darmstadt
Germany

Sofia, April 2005

This thesis presents results from scientific work done at the GSI, Darmstadt, Germany and at the Faculty of Physics at the University of Sofia "St. Kl. Ohridski", Bulgaria. These results have not been used for the award of any other degree or diploma in any university. To the best of the author's knowledge and belief, it contains no material previously published or written by another person, except where due reference is made in the text.

April, 2005 Radomira Lozeva

Contents

Chapter 1

Introduction and Motivation

Due to the possibilities, which are provided by the **SIS/FRS** (Synchrotron/FRagment Separator) [Geis92] facility at GSI, fragmentation or fission of relativistic heavy ions is performed with primary targets, located at the entrance of the FRS. In this way hundred unstable rare isotopes are generated and separated by the FRS (using the Bρ-ToF-Bρ technique [Geis87]), identified by a system of tracking detectors and with sufficient intensity, transported to a detector setup for in-beam γ-ray spectroscopy.

At that place the recent **RISING** (Rare Isotope Spectroscopic Investigations at GSI) [Woll04] spectrometer is build, dealing with the use of fifteen of the ex-EUROBALL Cluster Ge-detectors for γ-ray spectroscopy. In its first "fast beams" stage, the heavy particles are used at relatively high energies of $\sim$ 90 - 410 A·MeV for ***relativistic Coulomb excitation*** and ***fragmentation*** reactions with a secondary target, yielding nuclear structure information.

To identify the outgoing reaction products and to get an information about their scattering angle, a new ΔE-E CAlorimeter TElescope (**CATE** [Loze03]) has been designed, consisting of a *Si* and a *CsI(Tl)* detector arrays. The position sensitive *Si* detector array measures the particle (x, y) **position** for scattering angle (impact parameter) determination. The energy loss **(ΔE)** of the ions in the *Si* detectors gives their **charge Z**. In the following *CsI(Tl)* detector array, the impinging ions are stopped, and the residual energy **(E_{res})** is detected. This is a measure of the particle **mass A** under the assumption that all particles with the same mass have the same velocity.

Thus, the CATE detector system, which is the subject of the present work, has been used for the detection of primary and secondary heavy ions from ^{54}Cr up to ^{132}Xe in the energy range between 90 and 400 A·MeV (at the detectors) with instantaneous rates between $1 \cdot 10^2$ and $5 \cdot 10^4$ p/s.

Chapter 2

Interaction of heavy ions with matter and its detection

2.1 Energy loss of the ions in matter

2.1.1 The interaction of the ions with matter

Heavy charged particles, such as the α-particles, interact with matter primarily through Coulomb forces between their positive charge and the negative charge of the orbital *electron* within the absorber atoms. Upon entering any absorbing medium, the charged particle immediately interacts simultaneously with many *electrons*. The *electron* feels an impulse from the attractive Coulomb force as the particle passes the encounter vicinity. Depending on the proximity of the encounter, this impulse may be sufficient either to raise the *electron* to a higher-lying shell within the absorber atom (*excitation*) or to remove completely the *electron* from the atom (*ionization*). The energy that is transferred to the *electron* comes at the expense of the charged particle, and its velocity is therefore decreased as a result of the encounter. The maximum energy that can be transferred from a charged particle of mass m with kinetic energy E to an *electron* of mass m_0 in a single collision is $4Em_0/m$, or about 1/500 of the particle energy per nucleon [Knol00]. Because this is a small fraction of the total energy (E_{tot}), the primary particle loses its energy in many such interactions during its passage through an absorber and decreases its velocity continuously until is stopped. Except at their very end, the tracks tend to be straight, because the particle is not greatly deflected by any one encounter, and interactions occur in all directions simultaneously. Charged particles are therefore characterized by a definite range in a given absorber material. The *range*, represents a distance beyond which no particles will penetrate. The products of these encounters in the absorber are either excited atoms or ion pairs. Each ion pair is made up of a free *electron* and the corresponding positive ion of an absorber atom from which an *electron* has been totally removed. The ion pairs have a natural tendency to recombine to form neutral atoms, but in some types of detector media, this recombination is suppressed so that the ion pairs may be used as the basis of the detector response. In close encounters, an *electron* may undergo a large enough impulse so that after having left its parent atom, it still may have sufficient kinetic energy to create further ions, but having range smaller compared with the range of the incident charged particle. These energetic *electron* are called δ-electrons and represent an indirect means by which the charged particle energy is transferred to the absorbing medium. Under typical conditions, the majority of the *energy loss* (ΔE) of the charged particle occurs via these δ-*electron*s.

2.1.2 Stopping power - Bethe-Bloch formula

The theoretical work about the differential stopping power [Beth78] of charged particles in matter has been started by Bohr [Bohr13, Bohr15, Bohr48] as a classical formula at non-relativistic velocities. Further on, quantum-mechanical derivations have been made by Bethe and Bloch [Beth30, Bloc33], where the interaction between particle and target have been averaged over all target shells. Individual atomic shell structures have been considered later, using of numerical computer calculations [ChuP69]. The linear *stopping power* (S) for charged particles in a given absorber is defined as the differential energy loss for that particle within the material divided by the corresponding differential path length:

$$S = -\left(\frac{dE}{dx}\right) \tag{2.1}$$

The value of $-(dE/dx)$ along a particle track is called its *specific energy loss*. For particles with a given charge state, S increases as the particle velocity is decreased. The classical expression that describes the specific energy loss is known as the *Bethe-Bloch formula* and is written:

$$-\left(\frac{dE}{dx}\right) = \frac{4\pi e^4 z^2}{m_0 v^2} \cdot N \cdot B, \tag{2.2}$$

where

$$B = Z \cdot \left[\ln \frac{2m_0 v^2}{I} - \ln\left(1 - \frac{v^2}{c^2}\right) - \frac{v^2}{c^2}\right]. \tag{2.3}$$

In these expressions, v and z are the velocity and charge of the primary particle, N and Z are the number density and atomic number of the absorber atoms, m_0 is the *electron* rest mass, and *electron* is the electronic charge. The parameter I represents the average excitation and ionization potential of the absorber, it is an experimentally determined parameter for each element. For non-relativistic charged particles ($v << c$), only the first term in B is significant. Equation 2.2 is valid for different types of charged particles, providing that their velocity remains large compared with the velocities of the orbital *electrons* in the absorbing atoms. The expression for B varies slowly with particle energy. For a given non-relativistic particle, dE/dx therefore varies as $1/v^2$, or inversely with particle energy. This behavior is explained by nothing that because the charged particle spends a greater time in the vicinity of any given *electron* when its velocity is low, the impulse felt by the *electron*, and hence the energy transfer, is largest. When comparing different charged particles of the same velocity, the only factor that may change outside the logarithmic term in eq. 2.2 is z^2. Therefore, particles with the greatest charge will have the largest specific energy loss. α-particles, *i.e.*, will lose energy at a rate that is greater than protons of the same velocity, but less than that of more highly charged ions. In comparing different materials as absorbers, dE/dx depends primarily on the product $N \cdot Z$, which is outside the logarithmic term. High-density materials, with a high atomic number, will consequently result in the largest linear stopping power.

The Bethe-Bloch formula begins to fail at low particle energies, where charge exchange between the particle and the absorber medium becomes important [Sigm98, Knol00]. The positively charged particle will then tend to pick up *electron* from the absorber, which effectively reduce its charge and consequently linear energy loss. At the end of its track, the particle accumulates *z-electron* and becomes a neutral atom. The leading parameter in

the stopping process is the projectile velocity. It determines what interaction will give the decisive contribution to the stopping of the projectile. When the projectile velocity $v_p \gg v_e$, the velocity of the outer target *electron*, the projectile will dissipate its kinetic energy by excitation or ionization of the target atomic shells. When $v_p \ll v_e$, this inelastic process, called "*electronic stopping*", vanishes with decreasing v_p and the *elastic scattering* of the projectile from the screened Coulomb potential [Beth78] of the target increases. This later process is called "$nuclear-stopping$". In fig. 2.1 the $electronic-stopping\ power$ (dashed line), the $nuclear-stopping\ power$ (dashed-dotted line), and the resulting $total-stopping\ power$ are qualitatively presented as a function of the projectile energy, E/amu. As can be seen, the electronic-stopping range has two parts: the so-called *"Lindhard-Scharff-Schitt"* (LSS) [Lind63] and the *"Bethe-Bloch"* (BB) [Beth78] region. According to this separation the LSS-range could be denoted as the "$slow$" and the BB-range as the "$fast$" velocity region (excluding the relativistic velocities).

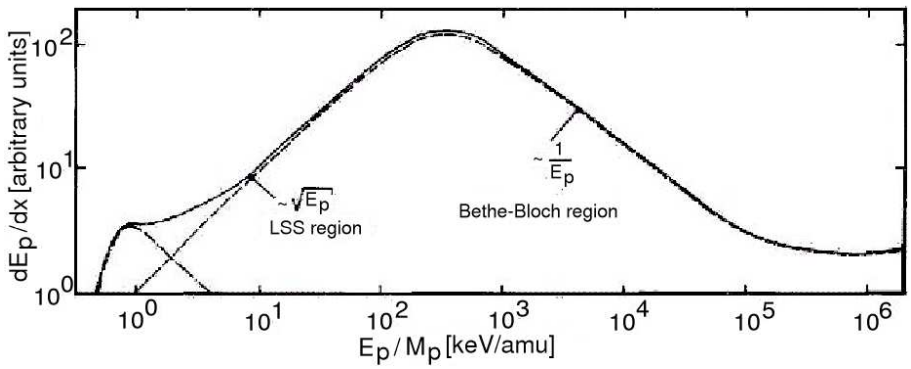

Figure 2.1: Schematic presentation of the mean stopping power dE_p/dx of ions in matter as a function of their kinetic energy E_p per mass (amu, ^{12}C scale). M_p is the projectile mass (solid line: total mean stopping power; dashed line: electronic-stopping contribution; dashed-dotted line: nuclear-stopping contribution) [Beth78].

Experimental detection instruments have been improved to the extend that the accuracy of the determination of *i.e.* the energy of an ion is limited by the statistical fluctuations in the stopping process. This can be very disturbing in the separation of close lying reaction channels in heavy-ion collisions, *i.e.* in the separation of adjoining masses or nuclear charges with Time-of-Flight (ToF) spectrometers or $(\Delta E - E_{res})$ detection systems [Goul75]. For light particles with a fixed charge theoretical calculations of energy-loss distributions are in good agreement with experimental data. For fast heavy ions substantially wider distributions are found than expected from the Bohr formula [Bohr48]. When heavy ions penetrate matter, their continual charge change is a statistical process as well and together with its statistical fluctuation results in an additional widening of the energy-loss distribution. As shown empirically [Voll74], the fluctuation in the charge change of heavy ions can be so dominant in determining energy-loss straggling, that the collision straggling first calculated by Bohr [Bohr15] may be completely ignored. For slow heavy ions, the influence of charge change on energy-loss straggling decreases. In the velocity region, where the nuclear-stopping process dominates, the theoretical estimates of energy-loss straggling are in reasonable agreement with the experimental data.

2.1.3 Born approximation and corrections to the Bethe-Bloch formula

At relativistic energies above 100 A·MeV, the projectiles are fully stripped or carry only very few *electron* during their passage trough matter. The *energy loss* of these heavy charged particles results in an inelastic collisions with target *electron*, leading to the *excitation* or *ionization* of target atoms [Sche98]. Extending the work of Bohr and Bethe, that in a first order quantum-mechanical perturbation treatment [Beth30, Beth33], the *Born approximation* is created, where the velocities: $v_p >> v_e$, and have approach even in case: $v_p < v_e$ for calculation the ionization probability for the inner shells. The energy loss per unit path-length dE/dx depends then on the momentum transfer to the target *electron* [Inok71]:

$$\frac{dE}{dx} = N \sum_n (E_n - E_0) \int d\sigma_n(\vec{q}), \tag{2.4}$$

where N is the number of target *electron* per unit volume, E_0 the target-*electron* ground-state energy, and $d\sigma_n(\vec{q})$ is the differential cross-section to excite a target *electron* to the energy level E_n by the transferred momentum $\vec{q}$. The summation over n means a summation over all discrete excitation states of the target *electron* and as an integration over all possible continuum states. In a relativistic treatment [Sche98] the stopping power for fully stripped ions reads:

$$\frac{dE}{dx} = \frac{4\pi e^4 Z_1^2 N}{mc^2\beta^2} \left(\ln \frac{2mc^2\beta^2}{I} + \ln \gamma^2 - \beta^2 \right) = \frac{4\pi e^4 Z_1^2 N}{mc^2\beta^2} L_{Bethe} \tag{2.5}$$

Here, I is the mean ionization potential of the target atoms, and L the so-called *stopping number*. The strict Z_1^2-dependence is a characteristic feature of first order perturbation theory [Sche98]. Corrections to the Bethe formula (eq. 2.4) are necessary [Bloc33, Ferm40] to describe precisely the experimental values. Some of these corrections and their origin are qualitatively discussed in the following:

- *Shell corrections:* Shell corrections account for the fact that at projectile velocities comparable or smaller than the orbital velocities of the bound target *electron*, the energy transfer is less effective. They decrease with $1/\beta^2$ and thus for relativistic ions the contribution to the stopping power from the interaction with target K-shell *electron* is affected very little and shell corrections can safely be ignored [Sche98].

- *Density effect:* With increasing projectile energy, larger and larger impact parameters contribute to excitation and ionization processes because of the Lienard-Wiechert potential [Sche98] leading to a term proportional to $\ln \gamma^2$. If in the target medium the density of atoms is high, the projectile charge is screened by dielectric polarisation of the medium [Ferm40] and the energy transfer in large-impact parameter collisions is less effective. That is why the density-effect correction is negative and the factor 1/2 effects only the distant collisions [Fano63]. Thus the relativistic rise of the stopping power is reduced depending on the density of the absorbing medium.

- *Bloch correction:* Bloch showed that independent of the magnitude of the projectile charge a first-order perturbation treatment is sufficient for the distant collisions since terms odd in Z_1 cancel and higher-order contributions of even terms are negligible [Bloc33]. However, he noticed that for small-impact-parameter collisions the exact scattering amplitudes for a Coulomb field [Gord28] must be used rather than those of the Born approximation. This leads to the so-called Bloch correction, which is valid at non-relativistic and relativistic

velocities. The main contributions to the Bloch correction arise from small momentum transfers, *i.e.*, from small scattering angles [Bloc33, Sore97].

- *Mott correction:* Like Bethe, Bloch used for the case of large scattering angles the first-order Born differential scattering cross section. In this case of large energy transfers to the target *electrons* their initial binding energy can be neglected and the scattering cross-section of free *electron* off nuclei can be used. However, for large nuclear charges the scattering cross section in Born approximation differs significantly from the exact cross section. An exact solution of the Dirac equation for the scattering of a relativistic *electron* in the central field off a point nucleus without any restriction with respect to its atomic number was first given by Mott [Mott29, Mott32]. The sum of Mott and Bloch corrections coincides with the close-collision correction, derived by Lindhard and Sorensen for point nuclei [Lind96].

- *Lindhard - Sorensen correction:* A theoretical description of stopping power and energy loss straggling beyond the first order Born approximation has been developed by Lindhard and Sorensen and called LS theory [Lind96]. The rigorous treatment of close collisions in this theory shows, that the slowing down of highly relativistic heavy ions is affected by the nuclear charge distribution of the projectiles. The nuclear charge distribution had been originally explored in extensive studies of high-energy *electron* scattering after deviations from pure Coulomb scattering had been observed [Hofs48, Hofs64]; when the de Broglie wave-length of the *electron* becomes comparable to the diameter of the target nuclei or even smaller, the differential scattering cross section deviates from the Mott cross section for point charges and exhibits a characteristic diffraction pattern with maxima and minima.

The three latter correction terms can be obtained in closed form from a rigorous calculation starting with the Dirac equation [Lind96]. The origin of the various correction terms is detailed a first-order Born-approximation calculation. Including them more precisely the theoretically and experimentally energy stopping power values are confirmed ([ATIM04]).

2.1.4 Energy loss characteristics

The Bragg curve

A plot of the specific energy loss along the track of a charged particle such as that shown in fig. 2.2.a. is known as a *Bragg curve*. The example is shown for α-particles of several MeV initial energy. For most of the track, the charge on the α particle is two electric charges ($2e$), and the *specific energy loss* increases roughly as l/E as predicted by eq. 2.2. Near the end of the track, the charge is reduced through *electron* pick-up and the curve falls off. Plots are shown both for a single α-particle track and for the average behavior of a parallel beam of α-particles of the same initial energy. The two curves differ somewhat due to the effects of straggling, discussed below. Important is to mention here that charged particles with bigger number of nuclear charges begin to pick-up *electron* early in their slowing down process and their specific energy loss functions dE/dx are maximized at different particle energy [WiFr76].

Energy straggling and multiple scattering

Because the details of the microscopic interactions undergone by any specific particle vary randomly, its energy loss is a statistical or stochastic process. Therefore, a spread in energy always results after a beam of mono-energetic charged particles has passed through a

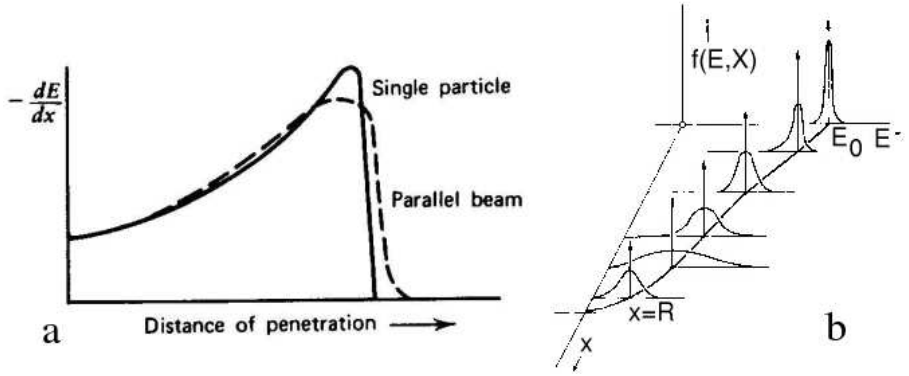

Figure 2.2: **a** - The specific energy loss along an α-track; **b** - plots of energy distributions of a beam of initially mono-energetic charged particles at various penetration distances. E is the particle energy and X is the distance along the track [WiFr76].

given thickness of absorber. The width of this energy distribution is a measure of *energy straggling*, which varies with the distance along the particle track. The range of this path length or depth of penetration is shorter because of numerous small deflections, called *multiple scattering*. Furthermore, the range distribution or distributions of penetration depths, arising from the statistical nature of the *energy-loss* process is called *range straggling*. Fig. 2.2.b. shows a schematic presentation of the energy distribution of a beam of initially mono-energetic particles at various points along its range. Note that, over the first portion, the distribution becomes wider (and more skewed) with penetration distance, showing the increasing importance of energy straggling. Near the end of the range, the distribution narrows again because the mean particle energy has greatly been reduced.

Energy range

When the charged particles lose their energy in matter, they penetrate a distance which is a well defined and the same for all identical particles with the same initial energy. This quantity, is called *the range of the particle*, and depends on the type of absorber material, the particle type and its energy. Experimentally, the range can be determined by passing a beam of particles at the desired energy through different thicknesses of the material in question and measuring the ratio of transmitted to incident particles. A typical curve of this ratio versus absorber thickness, known as a *range number-distance curve*, is shown in fig. 2.3. As can be seen, for small thicknesses, all the particles manage to pass through. As the *range* is approached this ratio drops. The ratio does not drop immediately to the zero level, instead the curve slopes down over a certain spread of thicknesses. This result is due to the fact that the energy loss is not in fact continuous, but statistical in nature. Indeed, two identical particles with the same initial energy will not in general suffer the same number of collisions and hence the same energy loss. It is experimentally proven that for an ensemble of identical particles [LeoW94], the statistical distribution of ranges is centered about some mean value. This phenomenon is known as *range straggling*. In a first approximation, this distribution is Gaussian, with mean value, known as the *mean range*, corresponds to the midpoint on the descending slope of fig. 2.3. This is the thickness at which half the particles are absorbed. For the thickness at which all the particles are absorbed, the point at which the curve drops to the background level is taken. This point

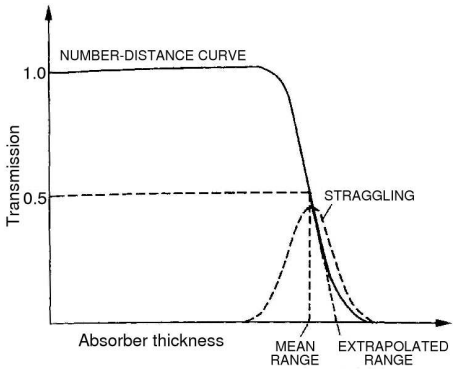

Figure 2.3: Typical range number-distance curve. The distribution of range is approximately Gaussian in form [LeoW94].

is found by taking the tangent to the curve at the midpoint and extrapolating to the zero-level and known as the *extrapolated or practical range* (see fig. 2.3). Since various charged particles and heavy ions have different ranges in the different detector materials, range-energy relations are necessary for calculating deciding the sizes of detectors for measuring the full incident energy of a charged particle or ion. Therefore, the active thickness of a detector must be that greater than the range of the passing particle in this detector material.

The origin of energy loss in thin absorbers

For thin absorbers (or detectors) that are penetrated by a given charged particle, the energy deposited within the absorber is calculated from:

$$\Delta E = -(\frac{dE}{dx})_{avg} \cdot d, \tag{2.6}$$

where d is the absorber thickness and $-(dE/dx)_{avg}$ is the *linear stopping power* averaged over the energy of the particle while in the absorber. If the energy loss is small, the stopping power does not change much and it can be approximated by its value at the incident particle energy. For absorber thicknesses through which the energy loss (ΔE) is not small, it is not easy to obtain a properly weighted $(-dE/dx)_{avg}$ value directly from specific energy data tables as [Nort70], but rather from the deposited energy in a way that makes use of range energy data. The basis of the method is as follows: let R_1 represent the full range of the incident particle with energy E_0 in the absorber material (see fig. 2.4). By subtracting the physical thickness of the absorber: d from R_1, a value R_2 is obtained which represents the range of those alpha particles that emerge from the opposite surface of the absorber. By finding the energy corresponding to R_2, the energy of the transmitted charged particles E, is obtained. The deposited energy ΔE is then given by $E_0 - E_d$. The procedure is based on the assumption that the charged particle tracks are perfectly linear in the absorber, and the method does not apply in situations where the particle can be significantly deflected [Knol00]. The effects of particle range and the decrease in dE/dx with increasing energy are typical for a combination of two detectors with different thicknesses, such that first has thickness that is smaller than the range of the penetrating particle and second, whose thickness is bigger than the particle range. Therefore, the energy deposited in the first thinner detector increases linearly and if the range is exactly equal to the detector thickness, the energy loss function is peaking with

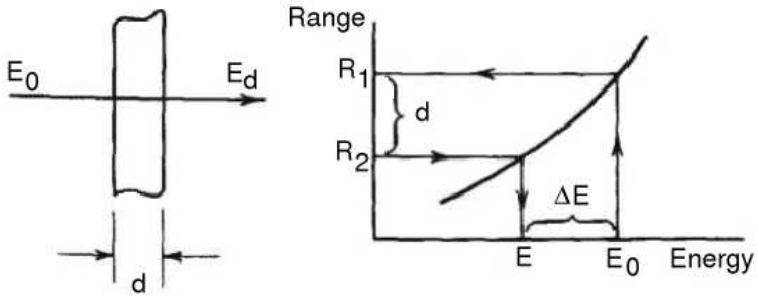

Figure 2.4: Deposition of energy range [Knol00].

respect to the incoming enery. In case the incident energy is higher, in the first detector only a portion is deposited, and the transmitted particle carries off the remainder. Under these conditions, the energy deposited in the second thicker detector is given by eq. 2.6, or the product of the detector thickness and the average linear stopping power. Because the stopping power continuously decreases with increasing energy in this region the deposited energy therefore decreases with further increases in the incident particle energy.

Energy loss for mixtures and compounds

The dE/dx formula in eq. 2.6 applies to pure elements. For the stopping: dE/dx of ions in mixtures and compounds, resort to direct measurements are required [LeoW94]. However, a good approximate value can be found in most cases by averaging dE/dx over each element in the compound weighted by the fraction of *electron* belonging to each element *(Bragg's Rule)*. Thus:

$$\frac{1}{\rho}\frac{dE}{dx} = \frac{w_1}{\rho_1}\left(\frac{dE}{dx}\right)_1 + \frac{w_2}{\rho_2}\left(\frac{dE}{dx}\right)_2 + \cdots, \tag{2.7}$$

where w_1, w_2, *etc.* are the fractions by weight of elements 1, 2, $\cdots$ in the compound. More explicitly, if a_i is the number of atoms and A_i is the atomic weight of the *i-th* element in the molecule M, then:

$$w_1 = \frac{a_i A_i}{A_m}, \quad A_m = \sum_m a_i A_i. \tag{2.8}$$

By expanding eq. 2.7 and regrouping terms, could be defined the effective values for Z, A, I, *etc.* which may be used directly in the *Bethe-Bloch formula* (eq. 2.2.),

$$Z_{eff} = \sum_i a_i Z_i,\ A_{eff} = \sum_i a_i A_i,\ \ln I_{eff} = \sum_i \frac{a_i Z_i \ln I_i}{Z_{eff}},\ \delta_{eff} = \sum_i \frac{a_i Z_i \delta_i}{Z_{eff}}, \tag{2.9}$$

where the *mass stopping power* is used, rather than the *linear stopping power dE/dx.*

2.1.5 Energy loss measurements and particle identification

The particle spectroscopy can be done via energy loss measurement or by total energy deposition measurement. If the object of interest is the specific energy loss (dE/dx) of the incident particle, rather than the total energy (E_{tot}), a measurement of where the particle passes a detector, retaining most but not all of its initial energy is required.

The number of incident particles, for a detector with thickness Δd, is $(dE/dx)(\Delta d/\epsilon)$ and a signal proportional to (dE/dx) is observed. In such applications the device for this measurement is called *energy loss detector*. The ΔE can have completely different type, depending on the purpose of the measurement (see section 2.3.2). These can be *Si* (or Si(Li)) semiconductors (see sections 2.2.1), or thin plastic (or film) scintillators (see section 2.2.2), or gas-filled ionization chambers (or parallel plate counters). A transmission detector of that type is commonly combined with a thick detector, where the particles stop, depositing their residual energy (E_{res}). Thus forming a *particle identifier telescope* arrangement, as shown on fig. 2.5, for the energy detection. By accepting only those

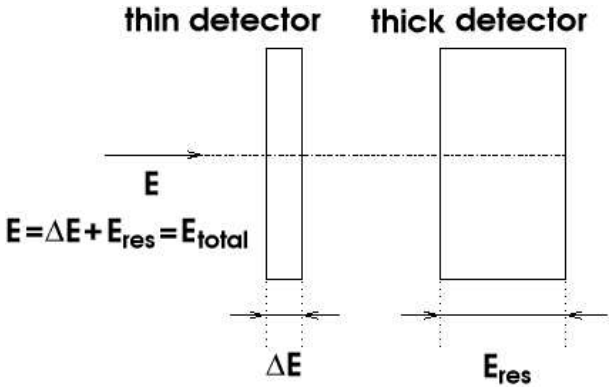

Figure 2.5: A sketch of a telescope consisting of two detectors for energy loss (ΔE) and residual energy (E_{res}) measurements.

events that occur in coincidence between the two detectors a simultaneous measurement of dE/dx and E_{res} is carried out for each incident particle. For non-relativistic charged particles of mass m and charge ze, Bethe's formula (eq. 2.2) predicts that:

$$\frac{dE}{dx} = C_1 \frac{mz^2}{E_{res}} \ln C_2 \frac{E_{res}}{m} \tag{2.10}$$

where C_1 and C_2 are constants. If $E_{res}(dE/dx)$ are formed out the result is mildly dependent on the particle energy but a sensitive indicator that characterizes the particles involved remains to be mz^2. If the incident radiation consist of a mixture of different particles whose energy do not differ by large factors, the product of the pulse amplitudes from both detectors is nearly unique parameter for each transmission detector of thickness Δd, and the remainder of its energy E_{res} in the thick detector. Then

$$\frac{\Delta d}{a} = (E_{res} + \Delta E)^a - (E_{res})^b \tag{2.11}$$

The value of a is a constant for a given particle type and is roughly proportional to $1/mz^2$. The value of b does not change greatly if ions of similar mass are involved (b=1.73 for protons and b=1.65 for carbon ions). Therefore, choosing a reasonable value for b to carry out the operations with ΔE and E_{res} may lead to introducing a parameter that is characteristic of its type but independent of its energy.

This is one of the widely used methods for determining the identify of particles from the information provided by the $\Delta E - E_{res}$ detector (see section 2.3.2). Another method involves storing of a range-energy table for an isotope of interest in database and then comparing the obtained from the experiment with the stored one. More appropriate

method is involving in addition of the fragment *Time-of-Flight* technique to the $\Delta E - E_{res}$ technique in order to provide an independent determination of the fragment masses ([Posk68, Thom68]). From its introduction this method has been very successful for the identification of neutron reach light nuclei, produced via interaction of high energy protons with heavy nuclei. Magnetic analysis together with an energy loss measurement (ΔE) in the focal plane of a spectrometer has been used for heavy-ion identification since 1969 ([Jacm69]). The ambiguity of this method is the fact that the different isobars can have the same effective charge (Z_{eff}) and also different nuclides can have similar value of Z_{eff}^2/A. That difficulty have been eliminated by combining an additional *Time-of-Flight* measurement with the magnetic identification. Another method of particle identification (started by [Artu69, Artu70]), is the coupling of a whole ΔE system to magnetic analysis (*i.e.* in heavy-ion transfer reactions). In this way directly the nuclear charge not just the atomic charge can be measured.

2.1.6 The power low velocity dependence

The *power law*, based on the above methods and their subsequent modifications are developed in the past by Goulding and Landis [Goul64, Goul66]. The later applicability [Butl70, Goul75] is limited by the approximations made to the actual energy loss or range behavior of the particles involved.

A recent treatment of the response from a $\Delta E - E_{res}$ telescopes for charge (Z) and mass (A) identification based on the Bethe formula with a *power law velocity dependence* has been developed by Tassan-Got [Tass02] for the INDRA detector array [Parl02]. With a help of energy functionals, interpolation or extrapolation in regions with low statistics is allowed, when is applied to telescopes involving detectors delivering a linear response. It has been tested with silicon detectors and ionization chambers as ΔE detectors and with $CsI(Tl)$ as a thick stop (E_{res}) detectors. The algorithm had shown a good accuracy [Tass02] for mass and charge identification up to Z=50, except at low residual energy region in comparison to used in the past identification functionals [Goul64, Butl70, Shim79]. For the identification of each event, two methods can be implemented: interactive drawing of lines on top of ridges corresponding to a given charge or mass, or contours around events clustered around these ridges. Any event is being identified from its distance to ridge lines or its inclusion in one contour, or fit of the ridge lines with a functional in which Z and A enter as parameters. The identification is being obtained by inversion of the functional for given ΔE and E_{res} in order to extract Z and A. In the following prescription a more complex method is described, applicable for multi-detector systems [Tass02]. It is assumed that the stopping power of a fragment of energy E, mass A and nuclear charge Z in a detecting medium takes the simple form:

$$\frac{dE}{dX} = \frac{Z^2}{f(E/A)} \tag{2.12}$$

The derivation of this expression is straight forward from Bethe's formula [Beth37] when the charge state inside the stopping medium is strictly equal to the nuclear charge Z. Its range of validity is restricted to light ions with energy sufficient to fulfill the condition that they are fully stripped. In particular the stopping zone of the Bragg curve (fig. 2.2.a), where the mean charge state is no more constant, is not addressed by this expression. A functional F is defined as a integral of $f(E/A)$, representing the range-energy relation

$F(E/A)$:

$$F(x) = \int_0^x f(t)dt \;\Rightarrow\; F(E/A) = \frac{Z^2}{A}X \tag{2.13}$$

This relation is applicable for $\Delta E - E_{res}$ telescopes. In the first detector, with a thickness ΔX the incoming fragment releases a part ΔE of its energy. The residual energy E_{res} is deposited in the rear detector for a residual range X. When applied to the total energy ($E_{tot} = \Delta E + E_{res}$) and to the residual energy (E_{res}), relation 2.13 reads:

$$\frac{Z^2}{A}(X + \Delta X) = F\left(\frac{\Delta E + E_{res}}{A}\right), \quad \frac{Z^2}{A}X = F\left(\frac{E_{res}}{A}\right) \tag{2.14}$$

which, by elimination of X, delivers the $E_{res} - \Delta E$ relation:

$$\Delta E = A\left\{F^{-1}\left[F(E/A) + \frac{Z^2}{A}\Delta X\right] - \frac{E_{res}}{A}\right\} \tag{2.15}$$

This formula is valid as long as the stopping power takes the form from eq. 2.13 [Tass02]. However, to reach a practical use a specification of the function f is required. A form close to Bethe's behavior is chosen in order of obtain an analytical form of the integral inverse F^{-1}. A specialization of the function f in the non-relativistic domain, $f(E/A)$ is almost proportional to E/A, therefore a *power law dependence* is chosen:

$$f(E/A) = (E/A)^{\mu} \tag{2.16}$$

with $\mu \approx 1$. This particular form is advantageous because it leads to an analytical form of eq. 2.17, which reduces to:

$$\Delta E = \left[E^{\mu+1} + (\mu+1)Z^2A^{\mu}\Delta X\right]^{\frac{1}{\mu+1}} - E_{res} \tag{2.17}$$

This relation is equivalent to the functional used in eq. 2.13, because they are based on the same hypotheses. For getting the slope at the starting point of the above expressed identification lines, in order to fit experimental data Tassan-Got proposes to take a derivative of the expression 2.17 over E at $E = 0$. In this way series of crossing points of identification lines with the energy loss axis can be set:

$$\Delta E_0 = [(\mu+1)\Delta X]^{\frac{1}{\mu+1}}\, Z^{\frac{2}{\mu+1}} A^{\frac{\mu}{\mu+1}} \tag{2.18}$$

In particular for $\mu = 1$, which is more close to reality, these energy loses are proportional to $Z\sqrt{A}$. At high energies the second term in eq. 2.17 becomes small, compared to the first one, and an expansion to first order can be performed:

$$\Delta E_{\infty} = \Delta X \frac{Z^2}{(E/A)^{\mu}} \tag{2.19}$$

The power law functional, which assumes linear response from the detector and which is used to fit experimental data, is defined than as the following function:

$$\Delta E = \left[(gE)^{\mu+1} + (\lambda Z^{\frac{2}{\mu+2}} A^{\frac{\mu}{\mu+1}})^{\mu+1}\right]^{\frac{1}{\mu+1}} - gE_{res} \tag{2.20}$$

where the parameters are g (the ratio of electronic gains), λ (includes the thickness of the first detector) and the μ parameter. The last is close to 0.7 (can take values between 0.5 and 1 [Shim79]). Furthermore, E_{res} and ΔE are the net signals from which pedestals have been subtracted (see section 3.2.3). In this case the formula 2.20 is a 3-parameter one or a 5-parameter formula if the pedestals fits are included. To guarantee a convergence of the fit in all situations a reasonable starting values and constrain on the constants have to be provided. The starting value *i.e.* $\mu_0 = 1$, the initial value λ_0 of λ should be determined from the starting point of an identification line, and g_0 should be obtained from the slope at the same point [Tass02] . In this way the functional 2.20 can be used to extract Z and eventually A associated to any $\Delta E - E_{res}$ pair. This is achieved by an analytical inversion of eq. 2.20, which delivers the quantity $Z^2 \cdot A$. If the interest is only in the charge identification A is set dependent on Z. Thus $A = 2Z$, eq. 2.20 is solved for Z, and the solution is projected onto the nearest integer number Z_i. The mass information can be obtained when the value Z_i is taken for Z and the equation is solved for A. This supposition is used for the experimental data presented in sections 3.4 and 9.4.1. However, for these cases several modifications on the parameters of eq. 2.20 are needed, in order to make use of the power low functional and obtain a good mass information.

Direct illustration of power low functional in the explained case is given on fig. 2.6.a, where the $\Delta E - E_{res}$ map is obtained with a calibration module of INDRA [Bord89, Pour95, Taba99]. It is made of a silicon detector (of thickness 70 μm) and a (2 mm thick) lithium diffused silicon detector, placed in front of a $CsI(Tl)$ crystal, used as a veto removing all particles punched through the silicon-lithium detector. The result of the

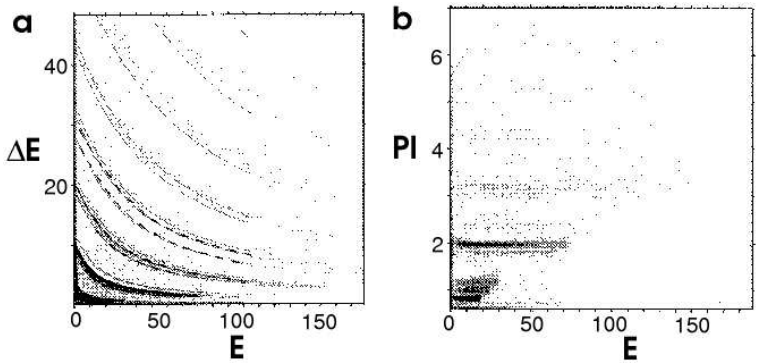

Figure 2.6: **a**: $\Delta E - E$ map and **b**: particle identification example from the Indra detector array [Tass02].

5-parameter fit [Tass02] is shown on fig. 2.6.b, which displays the particle identification, PI:

$$PI = Z_i + 0.2(A - 2Z_i) \tag{2.21}$$

vs the energy released in the silicon-lithium detector. It is verified [Tass02], that distortions are very small and that the extrapolation toward boron an carbon elements is correct. Thus it indicates, that the power law formula models correctly the data in this range.

In older articles of a similar method for particle identification with a wide dynamic range, the PI has been derived to a slightly different expression [Butl70, Shim79] and

parameters:

$$PI \simeq \frac{\alpha \Delta E}{300} \left(\frac{E_{res} + c\Delta E}{300} \right)^{\alpha - 1} \tag{2.22}$$

That approximation has been made to speed up computational time without making a sacrifice of the quality of PI [Butl70]. It originates from same power law but only with a constant α, which has deviations when is applied to heavy-nuclei detection [Shim79]. Accordingly, a ΔE dependence in α has been introduced:

$$\alpha = a - b\frac{\Delta E}{T}, \tag{2.23}$$

where a and b are fixed parameters, and T represents the thickness of the ΔE detector, for which deferent thicknesses of ΔE detectors do not directly influence the value of α. In practice even a more simplified form with logarithm has been used when calculating the PI:

$$PI \equiv \ln(\alpha \Delta E) + (\alpha - 1)\ln(E_{res} + c\Delta E) - \alpha \ln(300) \tag{2.24}$$

This convention distorts the display of the PI spectrum such that the spacings between different particles do not follow the $M \cdot Z^2$ scaling. However, it provides a wide range of coverage for PI, especially for heavy particle region. The parameters a, b and c, used in eq. 2.23 and 2.24 are determined experimentally. For light particle detection the parameter α is 1.73 and thus the parameter a of 1.85 is used. Since the correction term with parameter b is small and positive, and depends from the thickness T of the Si-ΔE detector (in mg/cm^2), a value of 0.046 is proposed and a value of 0.19 when the thicknesses are from 30 to 150 μm [Shim79]. The parameter c is obtained with fixed value

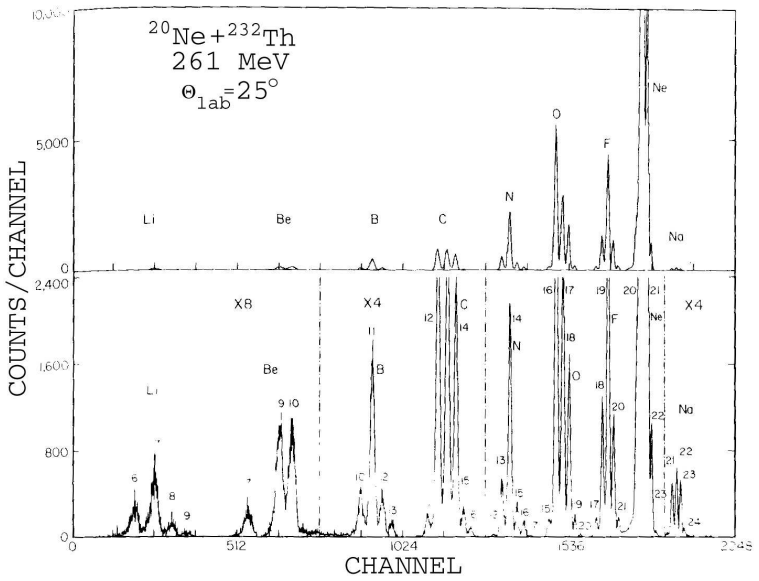

Figure 2.7: Particle identification example: the upper part shows the overall spectrum, the bottom part is in expanded scale [Shim79].

of 0.5. As shown in the example on fig. 2.7 by Shimoda [Shim79], all products from the reaction induced by ^{20}Ne on ^{232}Te target with energy of 261 MeV (namely more than 40

isotopes from lithium to sodium nuclei) are identified. For the construction of PI spectra a $\Delta E - E_{res}$ system of Si (96 μm thick) and Si (1512 μm thick) has been used.

This method has been successfully applied for the detection of light ions with the CHIMERA $\Delta E - E_{res}$ system [Aiel95, Paga96, Aiel00, Paga01, Nein02] (see section 2.3.2). A parameter improvement using a minimization procedure helped for an unique charge (up to $Z = 50$) and mass (up to $Z \leq 10$) identification [Nein02]. In comparison, the mass identification achieved following the Tassan-Got algorithm [Tass02] directly has been limited to light isotopes with $Z \leq 4$ (see more examples in section 2.3.2).

To summarize, the capability of the power law method has been tested for light and medium range nuclei. However, no data exist for heavier propagators. In this way, it became a challenge for the work described in the following chapters.

2.2 Detectors for heavy ions

The *detectors for heavy ions* have played an important role in nuclear physics experiments since many decades. With the advent of high energy heavy-ion accelerators, there has been a growing need to develop different types of them to meet various experimental requirements. Several kinds of detectors, in particular **Si semiconductors** and **CsI(Tl) scintillators** for such necessities will be described in the following chapter with their advantages and comparison to the other types of nuclear radiation detectors.

2.2.1 Silicon semiconductor detectors

A silicon semiconductor detector [PeBr55, Brau74] is a large Si diode, following the planar technology [Kemm80] of the *p-n* or *p-i-n* type. By applying an *electric field* and operated in the reverse *bias* mode (see below) it collects the charge carriers liberated by an ionizing radiation [Scho31, Mott31].

Structure

Because of the crystalline nature of the semiconductor materials their outer shells atomic levels exhibit an energy **band structure**, forming discrete levels. The atomic arrangement (lattice spacings) and the Pauli principle cause their degeneracy. The highest band created is the *conduction band*, where the *electrons* are moved after becoming some thermal energy. Thus leaving *holes* at their original locations, which move (slower) in the opposite direction. The formed (non-equilibrium) state of *electron*-*hole* **generation** is characterized with a *valence band*. The kinetic energy of an *electron* is measured from the lower edge of the conduction band upwards, that of the *hole* is downward from the upper edge of the valence band (see fig 2.8.a). Thus a conductivity is created, corresponding to an *energy gap* E_g, which is very small and does not exist in case of the conductor or insulator materials. An *electron* recombines with a *hole* by dropping from the conduction band into an open level in the valence band by emission of a photon, in process of *electron-hole* **recombination**. That can be caused by intrinsic **impurities** (trap centers) and lattice dislocations, or by extrinsic impurities from other **doped** atoms. The controlled doping of the semiconductor, with minority of *hole*-carriers (**n-type**) and with minority of *electron*-carriers (**p-type**), defines its functioning. It depends on the formation of the *np* **junction**.

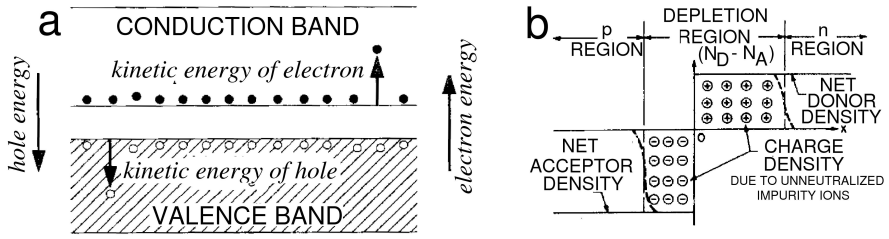

Figure 2.8: **a** - The kinetic energy of a semiconductor in band representation [Lutz99]; **b** - Schematic diagram of *np* junction - diffusion of *holes* into *n*-region [SzeS81].

Principle of operation

The thermal diffusion drives *electrons* and *holes* across the *np* junction and leads to a (**depletion region**) of free carriers, bounded by conductive regions, which are *n*- or *p*-doped (see fig 2.8.b). The formation of the two adjacent space charge regions builds up a potential barrier between the *n* and *p* regions, which impedes the further flow of charge - *thermal equilibrium*. By application of an *external potential*, two distinctly different *non-equilibrium* modes can be established: (1) - externally applied voltage V (+V to the *p* region and -V to the *n* region) reduces the *potential barrier* and allows increased charge transfer across the junction (**forward bias**); (2) - externally applied voltage V (-V to the *p* region and +V to the *n* region) increases the *potential barrier* across the junction, impeding the flow of current (**reverse bias**). The *np* junction is asymmetric with respect to this *small current flow*, becoming a *diode* [SzeS81, LeoW94, Lutz99]. Since the *depletion region* is a volume with an electric field, it is particularly attractive to radiation and is used as a radiation detector. The width of the *depletion region* is increased by *reverse bias*.

If an **ionizing particle** penetrates the detector it produces *electron-hole* pairs along its track, the number being proportional to the energy loss (ΔE). The externally applied electric field separates the pairs before they recombine. If electrical contacts are placed on either end of the junction device a current signal proportional to the ionization is detected. The **charge is collected** by the electrodes and produces there a current pulse, whose integral equals the total charge generated by the incident particle, which is a *measure of the deposited energy*. The *read-out* goes through a charge-sensitive preamplifier, followed by a shaping amplifier. At full depletion, the electric field is at maximum in the junction and decreases to zero at the ohmic contact, which is a metal deposited on the *n* side. In order to avoid losses in charge collection, the *Si* detectors are over-biased.

Characteristics and effects

The main *characteristics* of such detectors and the caused by them *effects* are:

• The intrinsic **energy resolution** for heavy charged particle, is related to the low energy threshold of only 3.6 eV to produce an *electron-hole* pair, which is low ionization energy compared to a gas detector or a plastic scintillator. The good **spatial resolution** comes from the high density of *Si*, which reduces the range of the secondary *electrons*. On the other hand, the average energy loss in *Si* is high (about 390 eV/μm corresponds to about 110 *electron-hole* pairs [Barn96]).

• To limit the multiple Coulomb scattering (see section 2.1.4), the detector thickness is kept thin, to an optimum **thickness** of $\approx$ 300 μm. The thickness of the detector also determines the **amplitude of the signal**. As there is no charge multiplication in *Si*, the *signal-to-noise*

ratio is, therefore, a critical issue (see below). For 300 μm, one can get on average $3.2x10^4$ electron-hole pairs, what is a signal requiring low-noise electronics [Lint87].

• Since the electric field in the detector is not constant but decreases linearly from the contact at which the *np* junction is made to the end of the depletion region, for a given bias, the **depletion depth** increases (with increasing resistivity), and correspondingly, the electric field decreases (with increasing material resistivity). If this happens in the overall thickness of the silicon slice, the detector is totally depleted.

• As the *Si* detectors are *diodes* with parallel (planar) electrodes they have therefore a **capacitance** of the corresponding parallel-plate capacitor.

• The effective **electronic noise** of preamplifiers, used with *Si* detectors, increases with increasing the capacitance [Lutz99]. The electronic noise increase per unit capacitance increase is called the *preamplifier's "slope"* [Blan60, SzeS81].

• **Radiation damage** is a major effect of irradiation is to create defects in the crystalline lattice which behave like donor or acceptor levels whitin the *Si* band structure. As a result, this is a decrease in the charge carriers lifetime which leads to an increase of the leakage current (see below) and to an incomplete charge collection. Resolution gets worse and a trail can be observed towards the low energies [Canb04].

Radiation	Critical doses $[p/cm^2]$
fast electrons	10^{14}
protons	10^{12}
alpha particles	10^{11}
neutrons	10^{11}
fission fragments	10^{8}

Table 2.2.1 Radiation doses for a *Si* detector [Euri01].

Table 2.2.1 presents some critical doses for which the detector deterioration is sure [Euri01], which are taken into account in the experimental studies with *Si* detectors (see section 3.1). For a strong **radiation doses** the donor level of *n* type *Si* are compensated by vacancies which introduce acceptor levels in the band gap. *n* type *Si* shifts to a *p* type like material (*type inversion*).

• **Leakage current** is the unwanted current leaking between two electrodes under voltage. In these detectors, the leakage currents can be observed even without ionization caused by the passage of a charged particle. **Radiation damage** can increase the leakage current, which translates into a decrease of the signal-to-noise ratio. Leakage currents are also relevant in the operation of semiconductor circuits, particularly at high *temperatures*. At high temperature the leakage current increase but it increases also if a radiation damage in present. That may occur at *high particle flux* in the interaction regions of the semiconductor. As a result the operation and the detector performance is affected (increased leakage current, increased noise compared to the signal or signal double peaking) [Fret96]. The temperature and flux effects are very important especially for the surface barrier semiconductor types (*i.e.* with Au deposition on the *Si*) or the doped types Ge(Li), *Si*(Li), while not that important *i.e.* in other techniques like ultra ion implantation or silicon dioxide passivation [Orte04].

• Because of the *electron-hole collection time*, the location of these charges with respect to the electrodes the **pulse shapes** of these semiconductors vary in form and rise time [LeoW94]. The detector **rise time** is a combination of charge *transit time*, corresponding to the charge migration time from its point of formation to the opposite extremes of the depletion region and a *plasma time*, corresponding to the time for dispersing formations as *plasma-like clouds* of charge and proceeding with normal charge collection. The last formations are caused by the density the of *electron-hole* pairs along the particle track and acts as shield to the interior from the influence

of the electric field [Knol00]. The *actual rise time* observed from a *detector-preamplifier* (see section 2.2.4) combination is also influenced by the preamplifier properties. The *time constant* of the equivalent input cirquit must be short if the rise time is to be held to that determined by the detector charge collection.

• In these crystalline materials the rate of energy loss of a charged particle can depend on the **orientation** of its **path** with respect **to the crystal axes**. Particles that travel parallel to the crystalline planes can on the average show a rate of energy loss that is lower that for particles directed in some arbitrary direction. Therefore these can penetrate significantly further trough the crystal, causing an effect of **channeling**. They are particularly significant for totally depleted detectors because of the amount of energy deposited, dependent on the orientation of the crystal planes to the particle direction. To minimize this tendency the Si detectors *i.e.* are cut so that crystal orientation in perpendicular to the wafer surface [Orte04, Canb04]. Consequence of this effect is the pulse hight corresponding to a fully stripped particle in the active volume. The pulse high defect for heavy ions *i.e.* is less probable in comparison to that for α-particles [Knol00].

There are other effects to the detector performance as: the detector *area* and hence capacitance, the *electric field* strength and hence the *breakdown voltage*, all consequencing in detector noise and increased energy resolution. A common compromise exist *i.e.* for the area and the detector's sensitive depth (volume), which increase the detector capacitance and result as noise and/or leakage current. Minimum total system noise is obtained by matching the capacitance of the detector to the appropriate preamplifier. In applications involving spectrometry of heavy charged particles, rather large electric fields are required to ensure complete charge collection, energy *linearity* and optimum resolution.

Position measurement

A very important application of the semiconductor detectors is the **position sensing**. Two types of detectors using different methods of obtaining spatial information have been developed [Spie99]: the discrete arrays of readout elements and the continues readout method with a resistive charge division (the second type is sometimes replaced by using a delay line technique [Stel91]). The first (*direct*) type is common for the two dimensional arrays of small pixels, where each of them is separately read out. The second (*interpolating*) type with charge carriers is used for one or two dimensional position determination from the Si detectors. This method is used further in this work and is explained for the concrete Si detectors in section 3.1).

Other applications

The semiconductor detectors are widely used in high-energy physics applications in the form of pixel detectors [Heij89], micro-chip detectors pads [Hall96]. They are popular due to their unmatched energy and spatial resolution, having an excellent response time. Their properties have been pushed to: *position localization accuracy of 5 μm in one coordinate, two-track separation down to 10 μm, bias voltages less than* $100V$*, time response less than* $5ns$ *and relatively simple installation.* For charged particle measurement *i.e.* the *surface barrier type* is popularly used [Orte04, Canb04]. These detectors rely on junction created in between the semiconductor and metal (n-type Si with Au and p-type material with Al). The *ion-implanted junction* is another type, formed by bombarding the semiconductor crystal with a beam of impurity ions, which are shot into the crystal and whose doping is controlled by an incoming energy control [Micr04, Advp04]. An oxide *passivation* and *ion implantation* methods are typically used for the reduce of the noise and the leakage

current [Euri01, Canb04]. Additional famous type is the *Li drifted Si type* (Si(Li)), where the Li is used as a compensator for forming the p-i-n junction with no space charge in the compensated zone, implying a constant electric filed. Such detectors are employed for *i.e.* β- or low energy x-ray detection [Orte04, Canb04, Micr04, Advp04]. A particularly important application for the further investigations in this work is their use in the identification of charged particles as front elements in telescope-detector systems, *i.e* in the ΔE-E technique (see section 2.3.2). The feasibility of the ΔE-E identification depends primarily on the characteristics of the ΔE detector, such as thickness, uniformity, microscopic homogeneity and energy loss distribution function (see section 2.1.4). These criteria are needed in order to select the optimal ΔE detector for particle charge and mass resolution [Mart78].

2.2.2 Scintillation detectors

As already mentioned, any *ionizing particle* passing through *matter* undergoes *energy loss* in *excitation* and *ionization* processes. The same is true of γ-rays and neutrons, which interact in an indirect way via (n, γ)- or (n, p)- reactions. With a certain probability the subsequent *de-excitation* process in the medium lead to the *emission of light*. This phenomenon is called *scintillation*, and the *scintillation light* is used to detect the primary particle or photon and to measure its *range, absorption and straggling* [Geig13, Kreb41, Curr48] or *energy deposit* in the medium [Kara23, Birk64]. The *scintillation* is a special case of *fluorescence*, which denotes the stimulation of light emission (*i.e.* by light of shorter wavelength). A material with sufficient *scintillation efficiency*, coupled to an *amplifying device* - *photomultiplier* or *photodiode* (see below) which convert these *scintillations* into *electrical pulses* for analysis and electronic counting, is called **scintillation detector**, giving an information concerning the incident radiation. The modern electronic scintillator still undergoes new developments and improvements as *i.e.* will be shown in section 3.2.2 of this work.

Organic scintillators

The two basic types of scintillators, classified by the nature of their structure [Birk62], are the organic and inorganic. Since in the current work only one member of the organics is used, namely the plastic scintillator, their description will be limited to the following.

The *principal scintillation light*, the prompt *fluorescence* process in *organics* arises from transitions in the *energy level* structure of a *single molecule* (*excitation of individual molecule*) and therefore can be observed from a given molecular species independent of its physical state. This implies the features [Hild97] of *good transparency* for the light to be transmitted, *decay time or the scintillation efficiency* depending on the *temperature*. The scintillation light in the *organic compounds* comes by the free valence *electron* of the molecules movement. The delocalized *electron* are not associated with any particular atom in the molecule and occupy the high-lying *vibrational states* in the organics structures [Zmer59], known as the π-molecular orbitals [Birk64]. The higher π-state is given by the long wavelength edge of the corresponding absorption band in the molecule [Plat49], which represent the absorption of kinetic energy from a charged particle passing nearby. Additional emissions of de-excitations from higher-lying states correspond to *delayed light emission*, characterized as *phosphorescence*, with longer wavelength than for the *fluorescence* and re-excitations and de-excitations through normal *fluorescence* representing the *delayed fluorescence* for organics [Jabl35]. Additionally, all organic scintillators contain

a *wave-length shifting agent*, which absorbs the primary *UV* light and emits it again in the visible light region [Hild97]. Their *effective attenuation length* determined by the dimensions and the quality of the surfaces is for practical importance, since the light undergoes many *reflections* with unavoidable losses before reaching the photo-sensitive device. Apart from the *organic crystal compounds* as *anthracene and stilbene*, and *loaded organic scintillators* where the interaction occurs by Compton scattering rather than by photo-electron emission as the *liquid scintillators* [Alar87], the *plastic scintillators* are the most important class of organic scintillators used in radiation monitoring [Bicr04]. Together with the wave-length shifter, the primary organic scintillating agent is dissolved in a solvent which can be polymerized (*i.e.* aromatic solvents such as *vinyltoluene and styrene*).

In terms of achievable *energy resolution* such scintillators are inferior to inorganic crystals, but they offer many *advantages*, namely a *fast time response* and *position sensing*, *large or small volume* in variety of forms, easily cut, tooled and (*i.e.* diamond) matched for high-quality surfaces. After heating the material can also be bent or pressed to any thickness with many practical applications in nuclear and in high-energy physics.

Inorganic Scintillators

The other basic scintillation detector's class, used more widely in this work presents the *inorganic materials*. Scintillation processes in these materials are closely related to their *crystal structure* [Kara23, Birk64, Ishi92].

In semiconductors *i.e.* with a *band diagram* (see section 2.2.1), the primary radiation ionizes the constituent atoms by promoting some of the *electrons* into the *valence band*, the *decay* of the formed *electron-hole* pairs, leads to the *emission of photons*. This situation, (when simplifying the importance of the lattice interactions) is found only in *intrinsic (pure) crystals* (2.9.a). *Extrinsic materials* (doped crystals), in which the pure host is doped with a small amount of a metallic impurity (2.9.b) have much higher practical importance. The *ground state* and the *excited state* of these *"activators"* are located within the *forbidden energy gap* of the host crystal. The *de-excitation* of primary

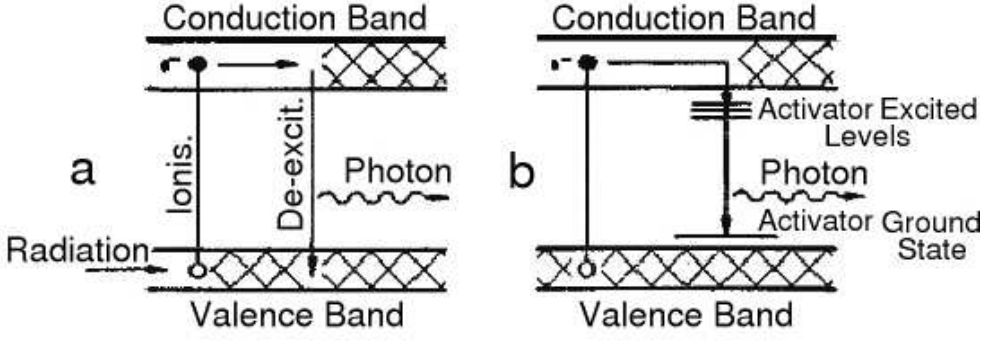

Figure 2.9: Scintillation process in inorganic materials are connected with the band structure in the crystals: **a** - intrinsic (pure) crystal, **b** - extrinsic (doped) crystal [Hild97].

electron-hole pars proceeds via the upper *activator states* into the *activator ground states*. The *half-lives* of these transitions are much longer than the *migration times* of the free *electrons* in the crystal. What is the *decay time* of the activator, which determines the *decay characteristics* of the *scintillation light*. Since the final transition energy is smaller than the *gap energy*, the *emitted light* is shifted to longer wavelengths (compared to the

pure crystal's scintillation light) [Kara23, Badw67, Alar87, Hild97, Scio04]. The crystal becomes *transparent* for this light, since *self-absorption* is reduced. The crystal properties are decisive for practically all features of *inorganic scintillators*. This leads to the characteristic points as *the concentration and distribution of the activator atoms*, *light output, decay times, energy resolution*, *impurities* and *activator concentration*, *radiation damage temperature dependence* and *scintillation efficiency*. All of them are important for the scintillator properties and differ among the various crystals.

Some of the most common *inorganic scintillators*, that are used in the experimental studies further in this work are specified below:

NaI(Tl)

The *Tl-doped NaI* has the highest *light output* (see table 2.2.2), what is used as reference material for all other inorganics. It combines a rather linear *energy response* with a modest temperature dependence. A certain disadvantage is the long *decay time* of 230 ns [Bicr04], which is unfavorable to high count rates. The *time resolution* of a few ns, is connected to its slow pulses. It can be grown in crystals of big volume, but the material is fragile and hygroscopic, therefore the crystals are encapsulated hermetically. Since its discovery [Hofs48] $NaI(Tl)$ has been the most prominent material for photon detection with application in scintillation monitoring and counting, but not used for particle detection. Recently it has been reported [Suda02, Tama02], that the $NaI(Tl)$ is suitable for heavy-ion calorimetry, if it acts as a residual energy detector and is combined with a Si transmission detector in front (in $\Delta E - E$ configuration). The good energy resolution for charged particles (≈1.5%) at intermediate energies (≈35 A·MeV) is found to depend mainly on the position of the crystal. The variations from center to corner observed are in the order of 2-3% for (31x31) mm square NaI(Tl) crystal. The same effect has been found in case of the $CsI(Tl)$ scintillation crystal and will be described in details in the experimental part of this work.

CsI(Tl) and CsI

The *light output* of $CsI(Tl)$ is about a factor of two lower than the one of $NaI(Tl)$, with much longer *decay times* (see table 2.2.2). Due to its higher *density* it has a larger γ-ray *absorption coefficient* and a shorter *radiation length*. In these respects it is surpassed only by $Bi_4Ge_3O_{12}$, which has a much lower *light output*. The biggest advantage in comparison with $NaI(Tl)$ is that $CsI(Tl)$ is much less *hygroscopic*. *CsI(Tl)* emits a small UV component at 330 nm with a shorter *decay time* of about 0.5 μs [Bicr04]. The main intensity is found in a broad distribution in the visible range, peaking at 550 nm, which is connected to the emission from the Tl activation centers, which increases the visible component (and the total intensity). The UV component is due to the pure intrinsic de-excitation of the crystal, hence ultra-pure CsI emits preferentially in the 260 nm region, with maximum 315 nm [Bicr04]. It is a rather *fast* scintillator, since the long decay time (see table 2.2.2) is caused by the long-wavelength component. For a given Tl content the relative intensity of the UV component increases with the ionization of the exciting radiation [Gwin63].

The effect of the light output in different wave length regions depending on the ionization density [Birk64] in these materials can be used for the discrimination of γ-rays and charged particles [Bigg61, Winy71]. One of the first investigations of this crystal coupled to photomultiplier is obtained by Halbert [Halb57, Quin59] for 10 A·MeV ^{12}C, ^{14}N and ^{16}O ions and demonstrated on fig.2.10.a. Later investigations on the intrinsic particle identification have reported that the scintillator light components are able to distinguish between p, d, t and He isotopes [Alar86, Guin89, Mosz93] (fig.2.10.b.), Li isotopes [Gras85, Kreu87], and C isotopes [Horn92]. Therefore a separation of the isotopes from light and heavy elements can be made by pulse-shape discrimination [Kreu87]. The identification achieved with the $CsI(Tl)$ scintillators, caused by its good *energy resolution* and is of particular interest for the following experimental studies in this work. The lower limit of the energy resolution itself has been studied by Wagner [Wagn01],

who has reported a value of 0.5%. Inspite of using very stable photodiodes (see section 2.2.4), he has observed variations of the light output from the crystal, caused by the Tl doping gradients in the CsI material. Additionally, charge and mass dependences in the energy or light output relationship for very light ions have been determined by calibrating with energetic projectile fragmentation beams. The mass identification ability for heavier isotopes will be demonstrated in section 9.4.2. Another application of the $CsI(Tl)$ scintillators, coupled to an appropriate photomultiplier, is found in a space astrophysical mission [Kroe97]. Such detectors are used for position imaging with reported resolution of 1-8 mm for γ-ray detection. These features of the $CsI(Tl)$ have made it very popular as a detector material for high-energetic photons [Kilg90], in heavy-ion discrimination [Alar87, Aiel95] and in high-energy physics, when used for shower detectors and electromagnetic calorimeters [Bock98].

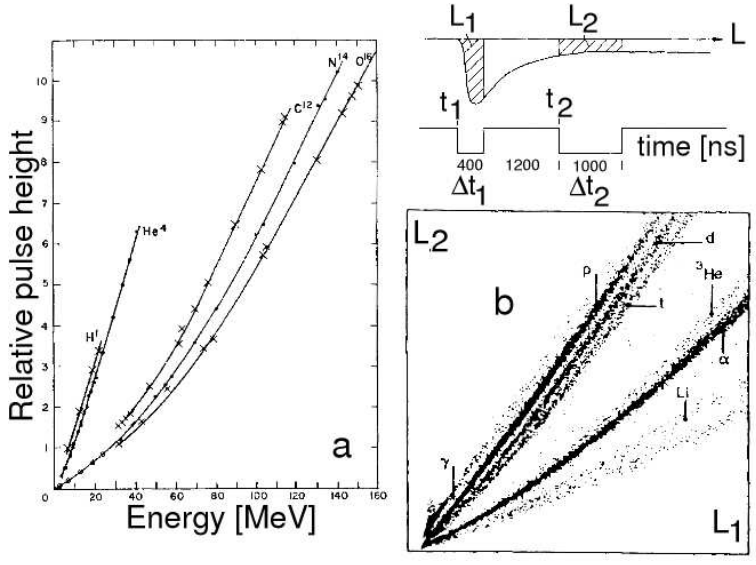

Figure 2.10: **a** - The relative pulse hight response of CsI versus particle energy [Halb57], **b** - discrimination of light particles in $CsI(Tl)$ by their light components [Alar86].

$Bi_4Ge_3O_{12}$

Bismuth germanate (BGO) (see table 2.2.2), has the highest *density* among all inorganic scintillators, what is of practical importance [Bicr04]. Due to its high effective element number it has a sizable *photo-peak efficiency* and γ-ray absorption. These features, however, go along with a very modest *light output* of less than 10% of that of $NaI(Tl)$, which leads to an only moderate *energy resolution* and the material is mainly used for the γ-ray detection efficiency as Compton-suppression shields for high-resolution Germanium γ-detectors. In high-energy physics, BGO is being used in electromagnetic calorimeters [Groo84]. For p or α-particles it has been reported that the BGO has better performance in spite of the poorer energy resolution [Saml86]. In calorimeter studies, is reported that BGO have also poorer linearity to higher energy depositions, compared to the $CsI(Tl)$, but is still able to distinguish their difference (caused by the different impinging particles) [Valt90]. Other inorganics type as BaF_2 with very fast *rise time* and *decay time* of $\sim$0.6 ns [Lava83], is used for *timing* discrimination of γ-rays from neutrons. Its characteristics are also compared with the above described scintillators on table 2.2.2), together with a $CsI(Na)$ inorganic member, that has the same application as the BGO and also poor energy resolution.

Scintillator material / Property	NaI(Tl)	CsI (Tl)	CsI (Na)	CsI	BaF_2	BGO
Density [g/cm³]	3.67	4.51	4.51	4.51	4.88	7.13
Melting point [K]	924	894	894	894	1627	1323
Hygroscopic	Yes	slightly	yes	slightly	No	No
Wavelenght of emission max [nm]	415	550	420	315	310 (220)	480
Lower wavelenght cutoff [nm]	-	320	300	260	135	320
Refractive index at max emission	1.85	1.79	1.84	1.95	1.50 1.54	2.15
Primary decay constant	0.25 μs	1 μs	0.63μs	0.016μs	s630 ns f0.7 ns	300 ns
Photoelectron yield [% of NaI(Tl)]	100	45	85	4 - 6	s16 f5	15 - 20

Table 2.2.2. Scintillation materials properties [Bicr04].

2.2.3 General properties of the scintillators

Energy resolution

One important property of a detector is its *energy resolution* (R), determined *i.e.* for a mono-energetic source. Different pulse heights may produce different energy distributions, called *response function* of the detector [MoMi48]. The last shows effects due to the finite energy resolution of the detector. R is defined as:

$$R = \frac{FWHM}{MEAN},$$

where $FWHM$ is the *full width at half maximum* of the full energy peak and $MEAN$ is the *mean pulse height* channel, corresponding to the same peak. It has a relation to the standard deviation (σ_G) of the Gauss distribution ($FWHM = 2.35\sigma_G$), that is the statistical contribution to the energy resolution. If single contributions to the overall $FWHM$ is measured, the total $FWHM$ is the quadratic sum of the individual values of fluctuation sources, assuming that they are not correlated:

$$FWHM^2_{overall} = FWHM^2_{statistical} + FWHM^2_{noise} + FWHM^2_{drifts} + ...$$

The total *energy resolution* of any detector may contain *contributions* due to the separate effects of charge collection statistics, electronic noise, variations in the detector response over its active volume and drifts in operating parameters of the measurement [LeoW94]. Fluctuations in the PMT's gain (*i.e.* contribute to the electronic noise), variations in the light collected in the scintillation crystal, high counting rate or temperature deteriorate the energy resolution. Other sources of *resolution loss* in scintillation spectrometers are characteristics of the crystal itself (the intrinsic crystal resolution). It includes any variation caused by local fluctuations in the scintillation efficiency of the crystal or due to reflection conditions that exist at the surface of the crystal. The consequent nonuniform light collection efficiency introduces significant line broadening (*i.e.* in crystals of a large size). Almost all of these effects on the energy resolution have been observed in the experimental studies described further. For γ-rays it is conventional to quote the energy resolution from the ^{137}Cs (0.662 MeV) energy [Kell56], such a conversion for charged particles or heavy ions is still under investigation.

Detection efficiency

All radiation detectors give *rise* to an output pulse for each quantum of radiation that interacts within its active volume, which survives with a certain probability (*detection efficiency*). The efficiency that depends on the intrinsic properties of the detector material is *intrinsic efficiency*, defined as the number of pulses which are recorded, divided to the number of quanta incident. An efficiency specified as the recorded pulses from the detector, divided to the emitted radiation from the source (including geometry) is known as *absolute efficiency*. The *total efficiency* (related to the peak-to-total ratio in a γ-spectrum) is mainly used for the γ-ray counting. Efficiency is property used for all other types detectors. For a position measurement *i.e.* with semiconductors, the size and the interaction probability to incoming radiation defines their detection efficiency. Efficiency of multiple detector systems is dependent on the single properties of the constituents and by their coincidence work together. In this way the geometrical efficiency (calculated from distances and sizes) of such systems might be different than the measured efficiency due to above consequences.

Linearity of the system

A very important characteristic of the coupled scintillator-read-out system is the *linearity* which arises *i.e.* from multiplication factor of the PMT or from the electron propagation of the PIN *diode*. The amount of light generated per unit energy loss (dL/dE) is the scintillator, depends both on the particle type and its kinetic energy E. For an ideal spectrometer, dL/dE is a constant independent of particle energy. Then the *total light yield* is directly proportional to the incident particle energy E, and the response of the scintillator is perfectly linear [Birk64]. *Non-linearities* can arise for very large pulses due to space charge effects between *i.e.* the last dynode and anode of the PMT, where the number of *electrons* is greatest. The build-up of a space charge affects the trajectories of *electrons* in this region and causes their loss instead of a collection. Another factor that causes *non-linearities* at high pulse amplitudes is any deviation of dynode voltages from their equilibrium value during the pulse. In practice, a calibration is usually carried out in which peak positions are plotted versus known energies. In case of a diode read-out, the detector response is usually linear but *i.e.* very high fluxes or radiation damages can also cause non-linearities.

Effects connected to the detection

∘ Quenching

Nevertheless, the total light output in all scintillations is very low, some effects may decrease it even further. They are globally summarized by the expression *"quenching"* [Birk51]. During *i.e.* the *concentration quenching*, the light output is at a maximum for a certain concentration of *emitting centers*, the activators in inorganic crystals or the primary scintillating molecules in organic scintillators. At any given concentration the output strongly depends on the energy amount deposited over a certain distance (on dE/dx) [Birk64]. When this quantity becomes too high, the number of scintillating centers becomes too small and an increasing fraction of the energy is not converted into light. This leads to a *non-linear response* (the curve of light output vs. deposited energy is not a straight line). The dependence on dE/dx explains why this *quenching* is stronger the slower and the heavier the particles are [Hild97]. When the *electrons*, which are not affected show a linear response, the p deviate from this ideal behavior. For a quantitative

comparison of different scintillators the ratio of the light output of particles to that of *electrons* is quoted [PrRu61]. For heavier nuclei the effect is stronger [Badw67, Becc76]. The quenching effect is mostly pronounced when heavy ions interact with the scintillator media, due to their high ionization power. Therefore strong nonlinearities in the obtained light response can be found [LeoW94].

◦ Nuclear reactions

Additional effect caused by *nuclear reactions* in the scintillators media are possible. It consist of different reactions with the scinttillator's atoms, which can produce light, heavy charged or neutral particles and ions. Besides this the *fragmentation reactions* in the media can be significant. They depend on the (A, Z) of the scintillator material, but also on the incoming particle or ion's energy. Beam *fragmentation reactions* has been very successful in producing nuclei far from stability. However, due to the high velocity of the fragments, the energy resolution is limited due to different effects. When a scintillator is used *i.e.* as a ΔE instead of E detector at high beam current, two other effects can be monitored the: *punch trough* and the *pile-up effect*. Both of them are observed as saturation already at preamplifier level and as a deterioration of the energy resolution (see section 7.2.3).

2.2.4 Read-out systems

The achievable *energy* and *time* resolution in scintillation detectors depend also on the properties of the devices which are used to record the very weak scintillation light. There is a choice between two technical possibilities:

- photomultiplier tubes (PMT) [MoSu58]
- semiconductor photodiodes (*PIN diodes*)

The coupling to the crystal scheme is demonstrated on fig.2.11. The light flow from the

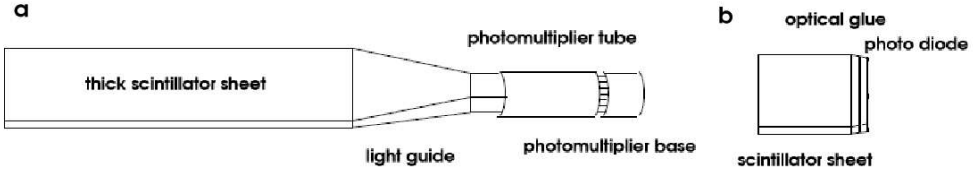

Figure 2.11: Coupling of **a** - a photomultiplier tube and **b** - a photodiode to a scintillator.

scintillation material is guided by the use of total reflection. Via a transparent material, called *light guide* [Timm50] usually made of plexiglas, plastic or glas this light arrives the photocathode of the PMT. Light guides are not applicable for the case of photodiodes, instead a thin layer of an optical glue, with very high reflection coefficient is used between the scintillator and the readout. In both devices the incident *photons* (γ) release *electrons* from a photosensitive layer (photo-electric effect). In the PMT this is the thin photo-cathode at the inner surface of the glass bulb (characterized by a conversion efficiency), in a diode it is the silicon layer between the electrodes. In the case of the *diode* the corresponding charge is read out directly, while in the PMT the *electrons* are *accelerated* through a system of electrodes (*dynodes*), creating entire electric fields [Hama04]. On their surface each *electron* releases a certain number of secondary *electrons*, what defines the amplification factor (*gain*), until the final charge pulse is collected at the anode [Tiss00].

Some of the most important considerations for the scintillator coupling to the *PMT or photodiode* read-out are described with the following:

• *PMTs* offer high *gain factors* (up to 10^7) and fast *pulse rise times* (down to and below 1 *ns*). They do suffer significantly from *magnetic fields* [Engs52] and have to be shielded (typically using μ-metal [Hama04]). One disadvantage common to all *PMTs* is the exponential dependence of their gain factor on the *applied high voltage*. Therefore they need highly stable supplies, but even then the gain may drift for various reasons. Besides this the *PMTs* suffer from *pulse-height and pulse-form variations* at high *count rates* and/or high-intensity *pulses*, caused in both cases by the high *space charge* (high current) in the dynode system. The effect can be reduced by a design of the tube base, which supplies the high voltage to the dynodes [EleT01, Hama04].

• *photodiodes* have a *gain factor* of one [Canb04]. Consequently, they need a *preamplifier* (*PA*) for readout, followed (if necessary) by a shaping *main amplifier* (*MA*). As *semiconductor* devices they have the intrinsically caused noise, which limits their *size* to a few cm^2 of active area [Hama04]. On the other hand, they require much less *space* than a *PMT* and can be run in *magnetic fields*. Their *rise time* cannot compete (worse) with that of PMTs. That is why they are mainly used in set-ups, where the timing properties are not decisive (in connection with inorganic scintillators, the slow *rise time* of which do not allow for fast tuning).

• An important condition for *effective light conversion* is the matching between the *emission wavelength* of the respective scintillator and the sensitive range of the *PMT cathode* or the *diode*. The spectral *sensitivity curve* of the *PMT*s, typically does not vary too much between different types [EleT01] and matches well with the emission *wavelength* of certain scintillator crystals. It can be chosen to fully cover *i.e.* $CsI(Tl)$ or plastic organic wavelengths. The last can be covered together by *photodiodes* in different types [Hama04] and for low-wavelengths emitting crystals the diodes are preferable because *PMTs* require in these case entrance windows of quartz glass and wavelength-shifters, that absorb and re-emit the light in the sensitive region.

Preamplifiers

When a semiconductor or an inorganic scintillator, coupled to photodiode are used for a measurement their output signals are usually very week.

As the detector itself is a capacitive device its impedance is very high. Therefore, at the readout output a preamplifier is connected, developed to detect the total amount of charge flowing from the detector, which has high input impedance and providing a low impedance output (*charge sensitive preamplifiers*) [Hama04, Fast04, Scio04]. As a result of the *pulse* event an output that is proportional to this ionizing particle (or γ-ray) is produced. The main characteristic (the *gain*) is equal to the reciprocal of the *feedback capacitance*, and independent of the *input capacitance*. Additionally, a large value resistor in parallel to the feedback capacitor slowly discharges the capacitor, restoring the preamplifier output to its original state. Unlike voltage sensitive preamplifiers [Fast04], charge sensitive preamplifiers have low input impedance so that the preamplifier can easily supply charge from the detector [Hama04].

In general, the characteristics required for a charge preamplifier are high gain, low noise, excellent integration linearity, high speed rise time, high temperature stability *etc.* but they differ depending on the detector capacitance. Series of noises influence the detection systems using charge sensitive preamplifiers [Rade82, GoLa82] in the preamplifica-

tion stage [BePu93]. They are important for the *rise and decay times* of the preamplifier, when the feedback capacitance is charged and discharged through the feedback resistance [Hama04].

The shaping amplifier

Important point is the effect of pulse *pile-up* after the preamplifier, what are pulses coming at the same time. The *output pulse* usually is filtered through a *shaping (main) amplifier*. This amplifier dramatically changes the shapes of the pulses, generally giving them a longer *rise time* and a much quicker *fall time*, and restores the baseline to prevent pile-up as much as possible. Events that appear to pile-up before the shaping amplifier often become very clearly separated after the shaping amplifier (see section 5.3). The important feature of that amplifier is the *shaping time*, defined as the time-equivalent of the "standard deviation" of the Gaussian output pulse. Sometimes an *integration* and/or *differentiation* of this signal is added together with the shaping before providing the information to a digital electronic converter (ADC). Shaping amplifiers that are used in the experimental studies described in the next sections typically have different electronics design and pulse performance [CAEN02, Sile04, Orte04, ElMo02].

2.3 Calorimetry and $\Delta E - E$ telescopes

Stacks of detectors, called *telescopes*, measuring the *energy loss* (ΔE) and *residual energy* (E_{res}, or just E, as often will be used further in the text) of charged particles have been used for a long time to get charge (Z) and mass identification (A). Several combinations of detectors have been used for this purpose: ionization chambers, Si detectors, plastic scintillators, CsI(Tl) scintillators read by PMTs or photodiodes. The identification is obtained by plotting the energy loss (ΔE) in one or several components of the detector stack versus the residual energy (E_{res}) released in the detector in which the particle has stopped or when plotting the energy loss (ΔE) versus the total deposited energy in all detectors of the stack ($E_{tot} = \Delta E + E_{res}$). In such a plot events of a given charge and mass cluster together what might be drawn with identification lines.

2.3.1 Calorimeters

A composite detector using total absorption of particles to measure the energy and position of incident particle jets have been used in the high energy physics branches at CERN [Bock98]. In the process of absorption showers of particles are created by cascades of interactions and detected by a shower counter for a **calorimeter**. In the course of showering, most of the incident particles are converted into *"heat"*, which explains the name calorimeter *(calor = Latin from heat)* for this kind of detector. With this detector no temperature is measured but characteristic interactions with matter (*i.e.* atomic excitation, ionization) are used to generate the detectable effect via particle charges. Calorimetry is also the only practicable way to measure neutral particles among the secondaries produced in high energy collisions. Calorimeters are usually composed of different parts, custom-build for optimal performance on different incident particles. Each calorimeter is made of multiple individual cells, over whose volume the absorbed energy is integrated. The cells are aligned to form towers typically along the direction of the incident particle. The analysis of cells and towers allows to measure lateral and longitudinal shower profiles.

Typically, the incident electromagnetic particles (*i.e.* e or γ) are fully absorbed in the electromagnetic calorimeter, which is made of the first for the particles layers of a composite calorimeter. Electromagnetic showers have a shape that fluctuates within narrow limits, its overall size scales with radiation length. The incident hadrons, on the other hand will start their showering in the electromagnetic calorimeter, but will be nearly absorbed fully only in the later layers *i.e.* in the hadronic calorimeter. When heavier and more energetic particles are concerned *i.e.* heavier ions they will pass all other layer and totally be deposited in a last layer depending on their range (see chapter 2.1.4). Two main types of calorimeter are used in the practice from constructional point of view [Bock98]:

• *homogeneous counter calorimeters*, where the functions if passive particle absorption and active signal generation and readout are combined in a single material. Such materials are used for electromagnetic calorimeters *i.e.* crystal calorimeters like glass PbO, SiO_2, plastic scintillators or inorganic scintillators as BGO, CsI.

• *heterogeneous counter (sampling) calorimeters*, where the functions of particle absorption and active signal readout are separated. This allows optimal choice of absorber materials and a certain freedom in signal treatment. Heterogeneous calorimeters are mostly build as sandwich counters, sheets of heavy-material absorber (*i.e.* of Pb, Fe or U) alternating with layers of active material (*i.e.* liquid or solid scintillators, or proportional counters). Only the fraction of the shower energy is absorbed in the active material measured. Hadron calorimeter, which need certain depth and width are typical sampling calorimeters.

Calorimetry is the art of compromising between conflicting requirements. The principal requirements are usually formulated in terms of resolution in energy, spatial coordinates, and time, in triggering capabilities, in radiation hardness of the materials used, and in electronics parameters like dynamic range, and signal extraction. In nearly all cases, cost is the most critical limiting parameter. Depending on the physics goals, the energy range that has to be considered, the beam particle characteristics and experimental set-up, some goals are favored over others. The span of possible solutions for calorimeters is much wider than tracking devices, in the last two decades the calorimeters became the key components of the particle detectors.

2.3.2 $\Delta E - E$ telescopes

The first reported $\Delta E - E$ system have been arranged by Aschebrenner (1955) [Asch55] of a thin *plastic* and a thick $NaI(Tl)$ scintillator. In the same year Wolfe [Wolf55] have described a two $NaI(Tl)$ system for identifying charged particles with 100 MeV energy. Following that method for particle identification but using a *proportional* counter and a $CsI(Tl)$ detector several other systems have been constructed [Marc58, KuoL61]. Goodmann and Ball [GoBa62] first have employed a $surface-barrier$ detector as a ΔE counter, coupling it to a $NaI(Tl)$ as E counter for the detection low energy protons. On an international symposium (Harwell 1962) Birks [Birk62], Hubbard [Hubb62] and Bryant [Brya62] first have described the design of $\Delta E - E$ spectrometers for studies of cosmic radiation and charged particles. In the telescope designed by Bryant a thin *plastic* scintillator combined with a thick $CsI(Tl)$ crystal have been used for the particle discrimination.

Another earlier investigations in this aspect, for identification with $\Delta E - E$ telescopes have been started by NASA program in 1975. A IMP Goddard Medium Energy (GME) [IMPG91] instrumentations has been designed to measure fluxes as a function of energy and make elemental identification for protons, α-particles and heavier ions (HI) with energies from $\geq$1 to $\leq$400 A·MeV. This instrument, consisting if three particle telescopes

covering different energy ranges using the $\Delta E - E$ technique (combining Si, *plastic* and CsI scintillation detectors), has been employed from 1978 to 1991 for ions from He up to Fe. Designed and tested similar instrumentation became functional in the telescopes of the Ulysses spacecraft [Simp92], launched in October 1990, undertaking measurements in the heliosphere far from the ecliptic plane over the polar regions of the Sun. The instrumentation carried by the spacecraft included six charged particle telescopes to measure the energy, composition, intensity and anisotropy of nucleons with energy range from 0.5 to 600 A·MeV for elements in the HI range from H to Ni with flux 10^7. The care for the Ulysses mission has been gone to the design of the GOSPIN ("Cosmic Ray and Solar Particle Investigation") detector, used recently.

In heavy-ion reactions at relativistic energies (20-100 A·MeV) the emission of complex fragments is an interesting problem, widely investigated both from theoretical and the experimental point of view, being relied to the behavior of nuclei at high temperature and density. From experimental side, it is necessary to detect and identify complex fragments in a large range of Z values and energy ranges with an energy threshold as low as possible. Furthermore, it is necessary to cover as close as possible to the complete 4π solid angle with a detector of suitable granularity, to obtain the correct fragment multiplicity value, depending on the reaction kinematics. Since the late 80's the construction of different detector arrays satisfying these requirements more or less has been started [Sara88, Poul88, Mura89, Fowl89, Drai89, Bord89, Shap91, Keho92, Iori93].

Some examples of different detector systems used for heavy-ion selection and identification are listed below:

• Using the $\Delta E - E$ method a $resistive - wire$ position-sensitive *proportional* transmission counter has been built for the detection of heavy ions in the focal plane of a magnetic spectrometer [Harv72]. The 45x6 cm^2 counter has been employed for measuring position and energy loss with a resolution of 0.7 mm and 8-10%, respectively. Additionally, Time-of-Flight has been detected with a plastic scintillator behind the proportional counter. The position, time and energy loss signals have been used to identify heavy ions with unit mass and atomic number resolution up to about $A = 20$, $Z = 10$.

• Another such example is the MINIT array used as well for detection of intermediate mass fragments at Catania [Aiel97]. Its modular structure of *multiplayer ionization* chamber with proportional avalanche multiplication allowed the detection of heavy ions with a very low energy threshold. The mechanical structure, based on a glass microstrip plate allowed the realization of cheap large area arrays of similar detectors in view of experiments with radioactive ion beams.

• Nuclear fragments of Z=5-10 that have resulted from an interaction of 5.5 GeV protons with ^{238}U, have been identified by a combined method of ToF and $\Delta E - E$ by Butler et al [Butl70]. Isotope identification for neutron reach nuclei as ^{18}C and ^{20}Ne have been obtained using the power law method from type: $[(\Delta E + E)/k]^b - [E/k]^b$, where b and k are parameters, as described in section 2.1.6. The detector system consisted of three Si detectors with different thickness from μm to cm, attached to an adjusted for that case electronic circuit. Reported is a mass resolution of 4.0% for A$\sim$11 isotopes and 4.1% for A$\sim$18 isotopes with time resolution of the particles $\approx$ 250 ps, calculated from the mass with a correction for the contribution from the energy resolution [Butl70]. A two-parameter particle-mass plot obtained is shown on fig.2.12. The element lines increase with mass because of the particle signal which is a function of the mass of the isotope as well as of its charge. Acording to Butler, a difficulty would appear if this method is used for absolute mass cross section measurements because of the multiple scattering effect (see section 2.1.4).

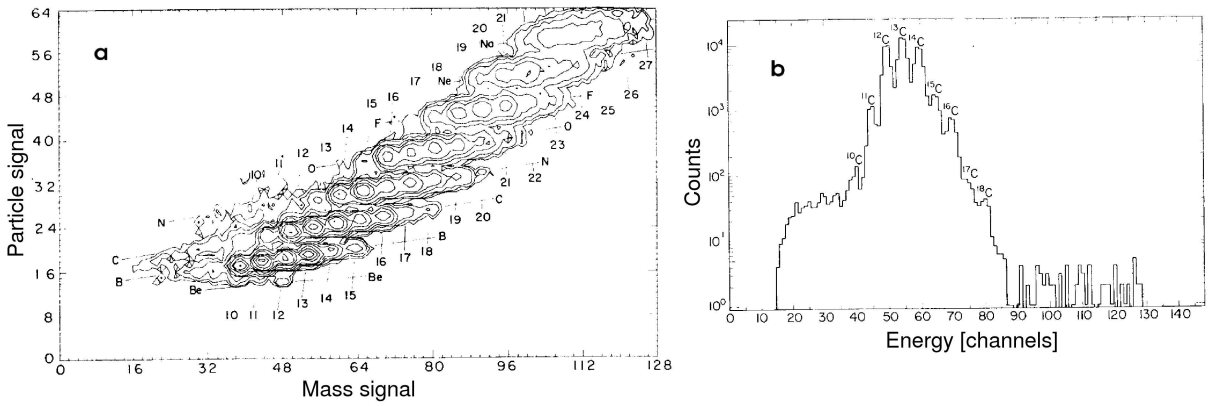

Figure 2.12: An example for **a** - two dimensional and **b** - one dimensional projection for the C isotopes mass identification spectra from a $\Delta E - E$ telescope [Butl70].

• Another example of using the modified (with additional parameters for the specific case) power law algorithm for a $\Delta E - E$ system is given by Shimoda et al [Shim79], using two Si surface barrier detectors (see section 2.2.1). A particle separation for all nuclei up to the Na isotopes has been obtained in this case in the energy range from 10 MeV to 260 MeV. A thickness of the ΔE detector of 92 μm and 1.5 cm of the E detector has been chosen for the detection of 261 MeV ^{20}Ne beam after reaction with a ^{232}Te target. The nuclei which remained after cut of or stop in the ΔE detector have been identified as shown on fig.2.13.a. The capability of this method continued exploring in building large systems of ΔE detectors.

• A large position sensitive $\Delta E - E$ array is used at LBL/s SuperHILAC [Wilc81], for energetic light charged particles detection. The detector has a total area of 43 cm^2 and consists of a *gas* proportional counter used as ΔE detector and stop E detector of three 19 mm thick *plastic* scintillators coupled to PMTs. A two dimensional position readout is obtained from the proportional counter by a combination of division and electron drift time measurements. The detector is suitable for α-particles with energies between 6.5 and 180 MeV. Position resolution of 1 mm in both directions, ΔE resolution of 10% and energy resolution of the scintillators of 3% is obtained from the system. The application of this detector is made in studies of charged particle emission in heavy-ion induced reactions. The identification from the scintillators is done following the fact [Birk64] that the light output L of the plastics is a nonlinear function of the particle energy E, and its charge Z and mass A (see section 2.2.2). A comprehensive study by Becchetti [Becc76] showed that the relative light output as a function of E, Z and A is fitted quite well by an expression of the power law form: $L(Z, A, E) = f(A, Z)E^{1.62}$ The light output of scintillators irradiated with e depends linearly on the e kinetic energy.

• A compact array for charged particle detection covering 89% of 4π [Souz90], consisting of 188 fast *plastics* and $CsI(Tl)$ phoswich detectors arranged in 11 rings coaxial to the beam axis is employed at the MSU Minibal. Each of them is comprised of a 40 μm thick *plastic* scintillator and 2 cm thick $CsI(Tl)$, read out by PMT. Elemental identification up to $Z = 18$ and isotopic identification of H and He like ions is achieved by exploiting pulse shape discrimination techniques.

• A multi-element detector array has been used at GANIL for light particle detection. Improvement of that system (Nautilus) is installed at LNS in Catania [Iori93] for identification of heavy fragments, emitted in intermediate energy nuclear reactions together with

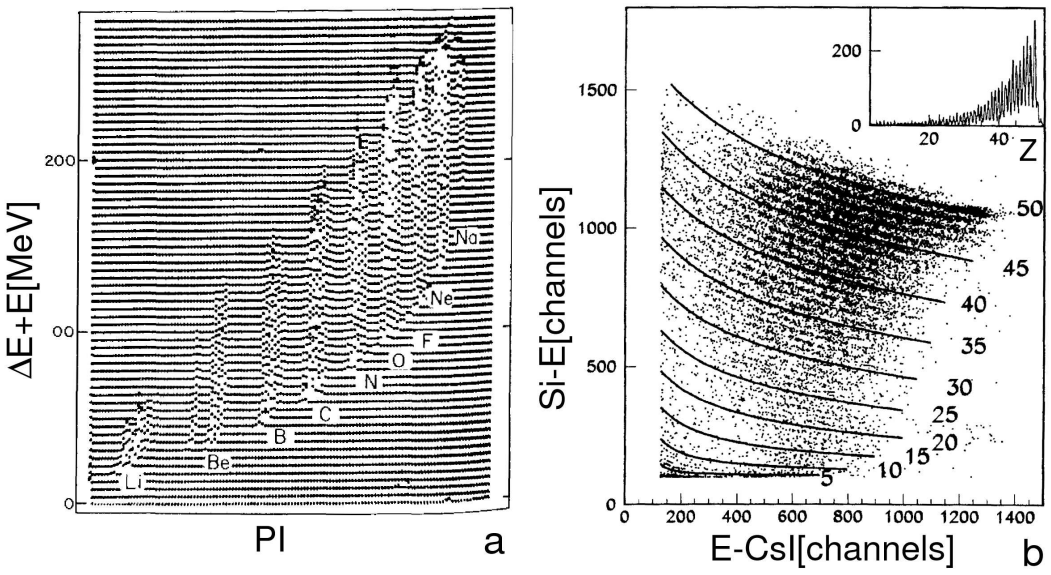

Figure 2.13: **a** - Particle identification spectra for for light isotopes at low energies [Shim79]; **b** - experimental $\Delta E - E$ scatter plot from the Chimera telescope [Nein02].

a γ-rays array. The tree element telescopes have been constructed to measure energy, charge and emission angles of fragments with Z values from 2 up to projectile atomic number ($\approx$ 54) when studying reaction in inverse kinematics. The detector is made of 48 modules consisting of *ionization* chamber, filled with CF_4 gas at high pressure up to 300 mbar, a Si detector (500 μm thick) and a $CsI(Tl)$ detector (41 mm thick) readout by photodiode has a good efficiency for high multiplicity events from fragmentation. The reported energy range for the detection of intermediate mass fragments is 20-100 A·MeV.

• The INDRA array [Pour95, Taba99, Parl02], installed at GANIL, is a highly segmented detector array for charged particle detection, operational since 1992. It covers geometrically 90% of the 4π solid angle, consist of 336 independent cells placed in 17 rings. Those cells have a "sandwich" structure of tree layers: *gas ionization* chamber, 300 μm thick Si detector and a $CsI(Tl)$ scintillator of 5 to 14 cm length, readout by PMT. Charge resolution up to $Z = 50$ and isotopic separation up to $Z = 3$ is achieved. The system is used for ions from ^{40}Ar to ^{181}Ta ions with energies from 95 A·MeV for ^{40}Ar to 24 A·MeV for ^{238}U.

• Chimera (Charged Heavy Ions Mass and Energy Resolving Array) is second generation 4π [Aiel95, Paga96] detector for high resolution particle and fragment measurements in intermediate energy nuclear reactions, accomplished in 1997. At 2000 the CHIMERA array (consisting of 32 telescopes) was coupled with the INDRA multi detector array (see above) and became operational at LNS in Catania within the REVERSE experiment [Aiel00, Paga01]. 1192 $Si-CsI$ telescopes in 35 rings are used for ToF, velocity and mass measurements at energies 20-100 A·MeV and beam rates $5x10^7$ pps with maximum counting rate of 1 KHz. The Si detectors used, have a thickness of 300 μm and the $CsI(Tl)$ scintillators have a ranging thickness from 3 to 12 cm depending on the detection range. Tree different identification techniques are simultaneously used. Firstly, the $\Delta E - E$ technique is employed for charge identification of heavy ions. The ΔE signal is used in connection with ToF for velocity measurements. Finally, the light charged particles stopped in the scintillator are identified by a pulse shaping method. The dimensions of the CHIMERA modules are commensurate to a reasonable mass ($A \leq$30 amu) identification

obtained by ToF. An example of the CHIMERA response [Nein02] is shown on fig.2.13.b for the identification for ^{112}Sn beam at 35 A·MeV. The lines shown are calculated values from the particle identification method explained in section 2.1.6.

• A logarithmic detector system has been designed and investigated at Lanzhou for the HIRFL beam line and RIB studies [Jinc96]. The system consists of four parts: an axial *ionization* chamber (IC), a position sensitive Si detector (PSSD), a large area Si pin diode (SPD) and 16 element $CsI(Tl)$ scintillator array read out by photodiodes. The reported energy resolution for the IC and PSSD with ^{241}Am (5.5 MeV) sources 3 and 2.6% (FWHM), respectively, with a PSSD position resolution of ≤ 1 mm (FWHM). Fragment identification up to $Z = 21$ is achieved *i.e.* with resolving power $Z/\Delta Z \approx 44$ (FWHM) for $Z = 18$ reactions of primary ^{40}Ar beams with heavy targets.

• A very similar system has been created for the GARFIELD apparatus for use at the ALPI linear accelerator at Padova [Gram97]. The $\Delta E - E$ calorimeter has been designed to identify at very low energy threshold both light charged particles and heavy ions in the energy range from 10^{-1} up to 10^3 MeV. That is based on the use of a *gas drift* chamber which convenes primary ionization e on gas microstrip devices where multiplication occurs and the energy loss signals are generated. With the help of Si diodes and $CsI(Tl)$ scintillators an identification *i.e.* of $Z/\Delta Z \approx 34$ (FWHM) for $Z = 16$ is obtained as a constant value in the whole range of the detected ions. Reported is that light charged particles can be distinguished in particular, protons of kinetic energy ranging from 1 MeV up to 70 MeV together with 1 degree angular resolution.

• Ancillary detector in combination with a spectrometer is *i.e.* the CHICO array consisting of 20 *parallel plate* counters, combined with the Gammaspere at Rochester [Simo00]. It is a 4π position sensitive heavy-ion system with an angular coverage 12 to 168 degrees in θ and 280 degrees in ϕ. The segmented detector measures the angular distribution and combined with a ToF measurement (with 500 ps resolution) allows the identification of masses with resolution of $\Delta m/m \approx 5\%$ at energies 780 MeV and heavy ions up to ^{238}U in Coulomb excitation experiments.

• Recently, a large area two-dimensional position sensitive detector telescope (LAPSDT) has been designed and fabricated at NSC, New Delhi [Nage03] for performing ERDA based material characterization experiments, without using a semiconductor detectors. Used are *ionization* chambers with tree different intersections for ΔE and E measurements. Reported is position resolution of better than 2 mm and good Z resolution in both high and low mass regions. It covers a large solid angle and has large two dimensional position sensitivity. The $\Delta E - E$ system has been employed with 15-200 A·MeV (Ag) heavy-ion beams for the identification of secondaries with help of different material and kinematic corrections.

Another new system for **Z** and **A** identification as well as for position information, called CATE [Loze03], has been recently developed at GSI for the use of the fast beams RISING project [Woll04]. The experimental selections of the best candidates for the ΔE and E detectors, the implementation of that system at relativistic energies, what is not covered by any of the systems briefly presented above, the methods for charge and mass identification of middle and heavy ions will be described in the following chapters.

Chapter 3

Basic detector investigations

The following experimental chapter describes the experimental laboratory and in-beam tests of Si semiconductors and various scintillators for position sensitivity and energy resolution. Among the scintillators the CsI(Tl) reveales the best performance and it is tested with different readouts in several in-beam measurements for position sensitivity of its energy, response in a $\Delta E - E$ system, mass resolution and $ToF - E$ response. The properties achieved during all these investigations of different detectors are used for the selection of the best candidates for the construction of a new $\Delta E - E$ system.

3.1 The Silicon ΔE detectors

The *Si* ΔE-detectors, as described in section 2.2.1 are often used because of their good position and energy resolution [Euri01, Orte04, Canb04, Micr04, Hama04]. Two types of *Si* detectors (IPP-2D [Euri01] and PIPS [Canb04] - see below) are tested to find their position resolution and energy resolution with α particles and with heavy ions. The results of these investigations are presented below and both types have been employed in the RISING experiments.

The IPP-2D *Si* semiconductor detector *(model: IPP 2D 50x50-300-SPE)* follows the passivated ion implanted junction planar technology [Euri01]. The basic material is a high resisting *n*-type *Si* of high purity and the thickness of the *Si* wafer is 300 μm processed in the several different steps to become a detector. Its schematic electrode configuration corresponds to fig.3.1.a. used for position and energy determination. When a particle

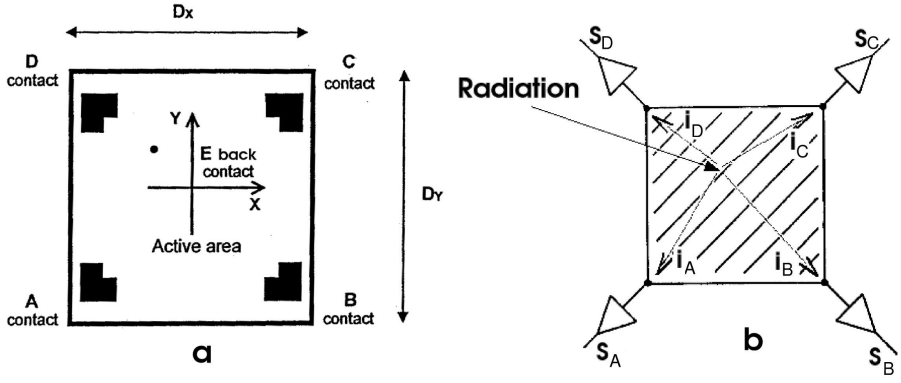

Figure 3.1: *Si* detector **a** - contacts [Euri01]; **b** - charge division [Spie99].

impinge the detector it creates a charge carrier (see section 2.2.1) in the carbon resistive layer (the sheet resistance is 2 kΩ/cm^2, that serves as a charge divider (see fig.3.1.b)). The **position** of the interaction is obtained from a relative comparison of the signals coming form the collected charges q_a, q_b, q_c and q_d in the four corners **A**, **B**, **C** and **D**, respectively, placed on the front side of the detector (see eq.3.1). Each corner contact has in addition a resistor of 1 kΩ to reduce nonlinearities in the position determination as described *i.e.* in [Doke87, Yagi89, Brun92, Cowi97].

$$x = \frac{D_x}{2}\frac{(q_a + q_d) - (q_a + q_b)}{q_a + q_b + q_c + q_d},\ y = \frac{D_y}{2}\frac{(q_a + q_c) - (q_b + q_d)}{q_a + q_b + q_c + q_d}, \tag{3.1}$$

The used geometrical algorithm assumes that the center of the co-ordinate system is in the center of the active area. D_x and D_y are the dimensions of the detector active area, which in this case are same and equal to 50 mm.

The **energy** of the incident particle is given by the back contact (output) **E** (see fig.3.1.b.), which is connected to the rear side of the detector and the signal is proportional to the total charge created. From the energy loss in the detector (ΔE), the impinging particle number Z can be deduced following the dependence $\Delta E \approx Z^2$. The particle energy, is independent from the impinging position in general [Euri01].

The other type *Si* position sensitive PIPS[1] *(model: PF50x50-300 EB-L)* detectors used [Canb04], have a thickness of 321 μm and an ion implanted entrance window of about 500 $\mathring{A}$ thickness. They have the same corner read-out as the IPP type but the sheet resistance is twice higher (4-5 $k\Omega/cm^2$) and the additional resistor is 1.6 $k\Omega$. The position and energy information is obtained in the same way as explained above.

The nominal leakage current for both IPP and PIPS types is 60-80 nA and 30-40 nA, respectively (for biasing at +30 V to the +40 V), with an electronic resolution of 40-60 keV (FWHM) [Euri01, Canb04].

Since *maintenance* of these detectors requires an installation chamber under minimum vacuum of 10^{-2} torr. For the next tests either vacuum at the order of 10^{-5} torr (clean and free of oil vapour) was used or dry N_2 with constant pressure. Since the entrance window of these detectors is very sensitive to all kind of pollution, chemical contamination or physical damage they are examined after irradiation under microscope in laboratory conditions and usually stored in dry plastic containers. Pollution has the same effect as the radiation damage (see section 2.2.1) in increasing the leakage current. In such cases the background-noise increases during the operation and the detector is replaced. In order to detect any operating or irradiation failure the detector's noise is being monitored on an oscilloscope and the reverse leakage current is monitored on a HV module always when the detector is in use.

3.1.1 The preamplifier

The five readout wires from a *Si* detector are soldered to a single detector frame, positioned in a motherboard and placed in the test chamber. Outside the chamber each of these detector signals is connected to a **charge-sensitive preamplifier** *(model: CSTA2)* constructed in SMD technique and designed, and built by the electronic laboratory of the Institute of Nuclear Physics, Technical University of Darmstadt [Bone01]. The preamplifier (see section 2.2.4), connected to an output from the detector, provides an energy and time outputs (see fig.3.2). The detector biasing goes trough the preamplifier connected

[1]PIPS is a Trademark of Canberra

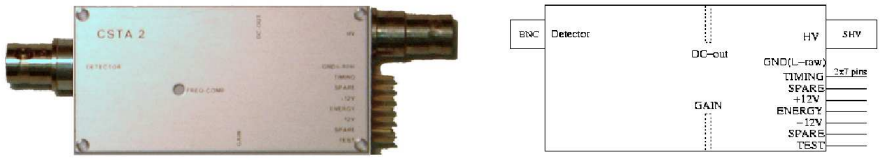

Figure 3.2: The charge sensitive preamplifier CSTA2 - side view [Bone01].

to the energy (back) contact of the Si, while all other preamplifiers are terminated with 50 Ω resistors. The preamplifier **gain** is adjusted internally for α-particles or heavy ions. Fine **gain** and **DC level** adjustments are provided via screw controls as shown on fig.3.2. To check the preamplifier linearity, its response on different pulses from a pulse generator are examined and calibrated.

3.1.2 α-source tests

The α-source measurements aim at testing the position resolution and energy resolution of the Si detectors. Any α-source do not emit monoenergetic α-particles but have an intrinsic line width (due to scatter) that contributes to the detector resolution and may lead to a detector contamination [Canb04]. Therefore, in the α-resolution measurements the ^{241}Am (energy 5.5 MeV) α-source is enclosed in Cu foil acting as a collimator with 1 mm diameter of the hole. It is placed at about 80 mm in front of a Si detector in a test chamber filled with dry N_2 with pressure of around 10^{-5} torr.

Pulses

After biasing of +40 V acting with leakage current of 60 nA, the raw preamplifier pulses from the Si IPP detector are demonstrated using a digital oscilloscope DPO Tektronix (model: TDS 7104 - 1GHz, 10Gs/s) with 20 MHz frequency filter on fig.3.3. The back energy contact ($E3$) has a negative **pulse** with an amplitude proportional to the energy of the registered particles. It is characterized with a 500-600 ns **rise time** (fig.3.3.a) and 60-80 μs **fall time** (fig.3.3.b). The position signals $E1$, $E2$, $E4$, $E5$ corresponding to corners D, C, A, B (as sketched on fig. 3.1.b) have positive pulses with **rise times** of approximately 1-2 μs (fig.3.3.c) and **fall times** of 80-100 μs (fig.3.3.d). For their detection a trigger with the back ($E3$) contact is used. The amplitudes of the shown position pulses are small and nosy (1-5 mV) because of the distance detector-source, and of the unavoidable noise of the test preamplifiers and grounding of the chamber. Similar pulse characteristics with an α-source revealed the Si PIPS detectors, therefore such example is omitted.

Electronics

The electronics set-up used during the α-test measurements is schematically shown on fig.3.4. The preamplifier signals from the four position and the back energy channels are connected to five single channel main amplifiers (MA), for shaping and amplification. For the tests different MA were used: Silena (with shaping time of 2 μs) or Tennelec (241) (with shaping time of of 1.5 μs) for the position channels, and ORTEC (572A) for the energy channel (with shaping time of 2 μs). A 8 V Silena amplitude digital converter (ADC) was used for a readout. The time output of the preamplifier, corresponding to the

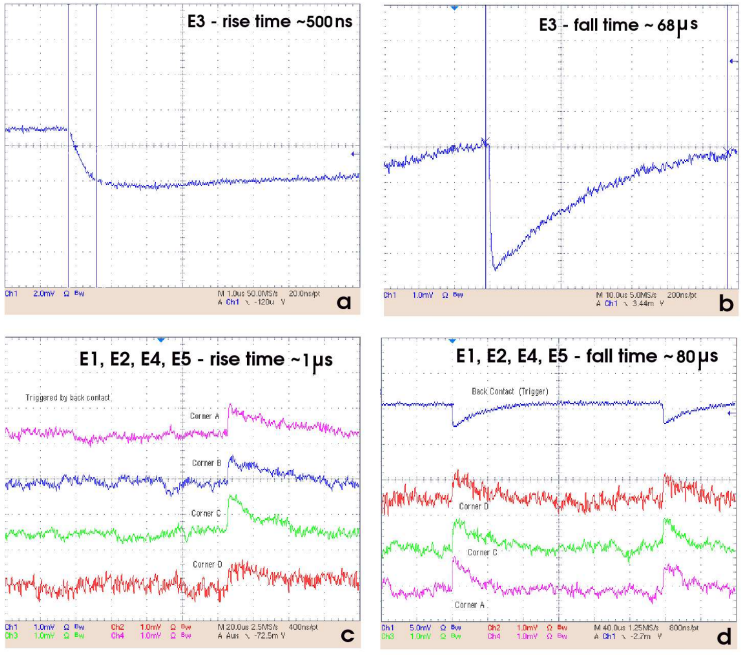

Figure 3.3: *Si*-IPP pulses with α-particles: **a** - rise time and **b** - fall time of the energy channel; **c** - rise times and **d**- fall times of the position channels.

back energy signal is inverted (since positive) and amplified in a timing filter amplifier (TFA ORTEC 474). It is fed into a constant fraction discriminator (CFD) with about 30 mV noise cut off, with fraction and delay of 0.2 and 32 ns, respectively. A time signal from the CFD is fed into a time digital converter (TDC) for readout, after certain delay (with delay module or gate generator *i.e.* in the *Si* PIPS case about 200 ns) if required. Since in this case the detector is used alone in the set-up the triggering signal is sent from the CFD to a trigger module which after certain processing time returns an accepted trigger for the acquisition. If the detector is used in combination with other detectors (as *i.e.* in case of the *Si*-IPP test) certain delay might be introduced for creating a coincidence signal between them before sending it to the trigger module. From the accepted trigger, using gate generators (GG) the gates for the ADC of about 9 μs (to 10 μs) and for the TDC of about 8 μs are created. The energy signals are examined with the ADC gate as sketched on the figure. The TDC stop signal from the CFD is examined with respect to the TDC start coming from the accepted trigger [ElMo02].

Measurements and results

To test the position and energy resolution of both *Si* types on α-particles, measurements with an aperture (mask), placed between the source and the detector are performed. Their configuration and the experimental set-up are depicted on fig.3.5.

• Position resolution

The aperture used for the *Si* IPP detectors is made of plastic and wrapped with thin alluminized Mylar[1] foil (as can be seen on the top-right corner of fig.3.5) and the aperture used for the *Si* PIPS detectors is made of Kapton[1] (as can be seen on fig.3.6.a). Both apertures are sufficiently thick to stop the α-particles with energy of 5.5 MeV.

[1]Mylar is a Trademark of DuPont [DuPo04]

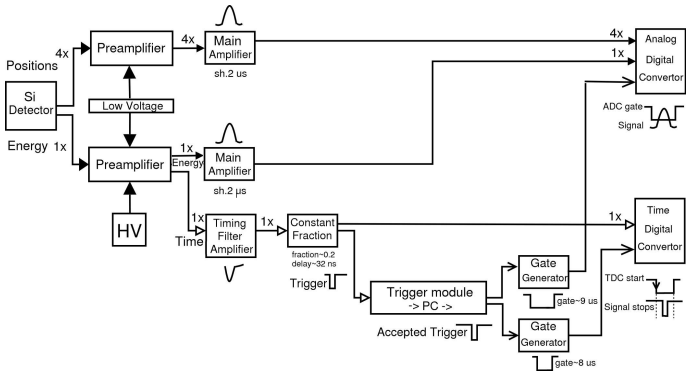

Figure 3.4: Electronic scheme for a test measurement of Si detector with α-particles.

If the diameter of the holes, which are drilled on the mask, is as big as the position resolution of the detector, a position image, representing the holes can be expected. Therefore, several configurations with differently distributed holes, sizing from a mm up to 7 mm are performed, until optimum aperture is found. Thus the diameter of the holes of 5 mm was the best for the test of the Si IPP detectors and correspondingly 3 mm for the test of the Si PIPS detectors. Since the detectors revealed similar performance, an example from one of them is given below. Five calibrated (for α-particles) preamplifiers

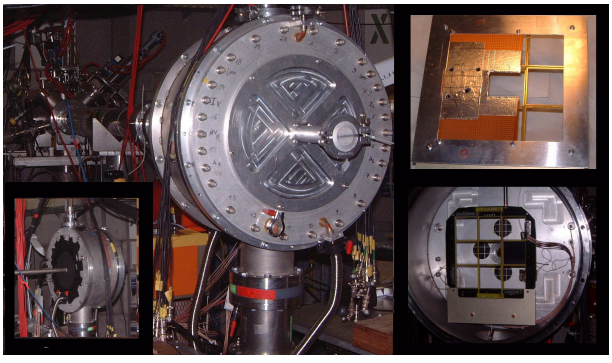

Figure 3.5: Setup for a test measurement of Si IPP detector with α-particles and with low energetic ^{58}Ni ions.

are used for the test of each detector in a separate measurement. In the user analysis the four **position** spectra of a Si detector have a peak structure to low channel positions as can typically be seen on fig.3.6.b. It appears because of the preamplifier noise seen already on pulse level. Another reason for that is the incomplete charge collection, caused by every missing interaction with an opposite (diagonal) corner when the charge carriers reach mainly one corner (see section 6.1). The position obtained on the detector is constructed from its four position signals using the geometrical algorithm from eq.3.1, under the condition that all of them are present simultaneously (multiplicity four selection).

Without mask, a typical **position** spectrum of *i.e.* a Si PIPS detector is presented on fig. 3.6.c. As can be seen the (x,y) distribution is centered (at the "0" position) but has limits of its x:(x_{min},x_{max}) and y:(y_{min},y_{max}) projections of x=y=(-15.9,15.4) mm instead of the real size (-25.0,25.0) mm (or "shrinks"). Thus, a normalization ("blowing") factor is needed (here equal to 1.595), to expand to the geometrical size of the detector and it is different for the different detectors. Often this factor vary also in the x and y

directions and do not conserve when irradiating the detectors with heavy ions (see section 6.1). Therefore, it must be always determined and applied separately for each detector and measurement. As also can be seen the position shape is not always symmetrical for both *Si* PIPS and IPP types, which is due to the different amplifications of the position channels, including preamplifier and amplifier gains. It is also nonlinear in case of the *Si* IPP types but this effect can be better observed with heavy ions than with α-particles and therefore is discussed in section 6.1. The typical detector response in the measurement

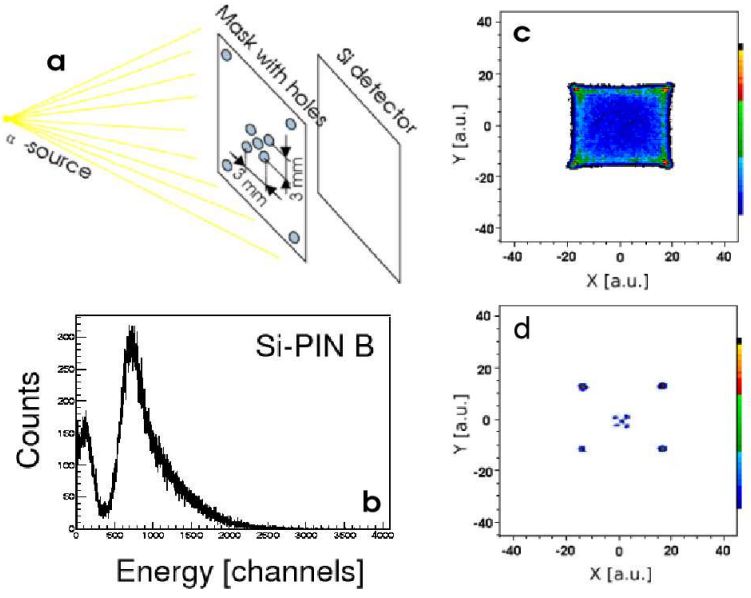

Figure 3.6: **a** - Source-detector configuration in *Si* (IPP and PIPS) α-test measurements; **b** - typical signal from a single corner. Position (x, y) spectrum with *Si*-PIPS detector **c** - without mask and **d** - with mask.

with mask is depicted in fig.3.6.d. It is visible that the image represents the holes with size of 3 mm, thus informing that the position resolution in x and y directions is at the order of 3 mm for the *Si* PIPS detectors. The same is present for the *Si* IPP detectors but for the holes with size of 5 mm, which represents its position sensitivity of 5 mm. Around the holes small scatterings of the particles are visible, which correspond to energy losses in the hole edges of the mask at different angles. These losses widen the total energy spectrum from the back contact and also may appear at low channels. A condition at this spectrum, set around the main energy peak, eliminates the scatterings in the measured position picture.

• **Energy resolution**

The **energy** deposition in a *Si* detector, detected from the back contact, is demonstrated on fig.3.7. The α-particles that impinged the detector stopped at a range of 278 μm of its thickness, according to a calculation with the code ATIMA ([ATIM04]). One of the best values of the **energy resolution** revealed from IPP detector is in the order of 7 % (FWHM), which corresponds to about 300 keV, although the intrinsic energy resolution of this detector is of 80 keV [Euri01]. The **energy resolution** of PIPS detector is also determined with accuracy of 7.4 % (FWHM), which is about 400 keV, in comparison to the manufacturer value of 60 keV [Canb04]. For all other IPP and PIPS detectors tested, the measured energy resolution ranges between 6.7 and 8.2 % (FWHM).

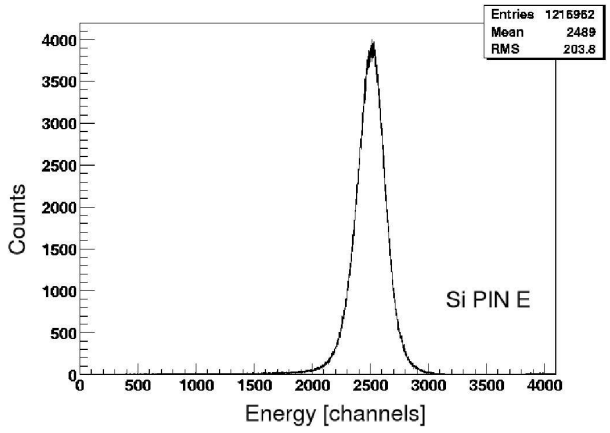

Figure 3.7: Energy deposition spectrum from Si-IPP detector for stopped α-particles.

3.1.3 In-beam tests

To test the Si detector response on heavy ions, a test measurement with ^{58}Ni heavy ions accelerated to the Coulomb barrier energy (3.6 A·MeV) is performed at one of the exits (X7) from the linear accelerator (LINAC) at GSI with particle rates of about 2-3 kHz. The test is a combination measurement of the Coulomb excitation of ^{58}Ni (or ^{197}W with energy of 3.7 A·MeV) on ^{197}Au target [Door03] with help of a Si IPP detector and a parallel plate chamber (PIPAC) for scattering angle reconstruction, and Ge detector for γ-ray detection. In this geometry the Si detector covers an opening angle, θ, between 27.8 to 47 degrees and also acts as a stop detector for the low energetic ions.

• **Position resolution**

The aperture used for in front of the detector with 5 mm diameter of the holes (3.8.a) projected the position image on the Si detectors shown in fig.3.8.b. As for the α-particles, also in this case the **position resolution** is in the order of 5 mm in both directions but the size of the projected spot from a hole due to scatterings is about 7 mm. The detector

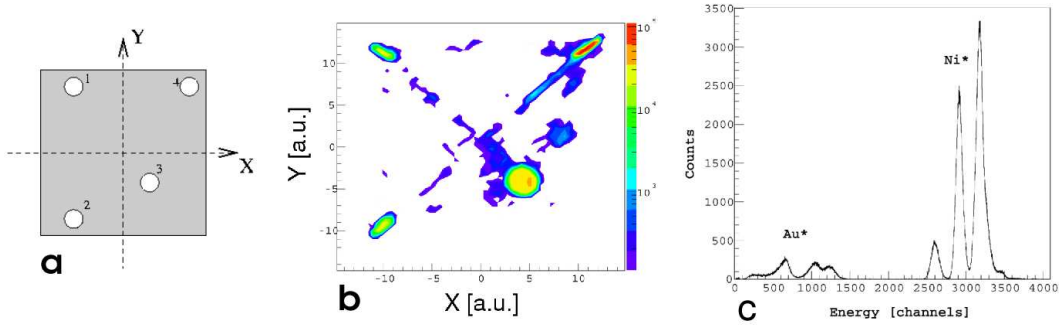

Figure 3.8: **a** - Aperture, **b** - position response and **c** - energy deposition from Coulomb excited Au particles (left) and Ni particles (right) inside a Si-IPP detector [Door03].

response, as in the previous test does not reproduce its real size, and the squeezing is quantitatively different. Additionally, a position offset of 1-2 mm is detected in x and y directions and nonlinear reconstruction very close to the corners. As mentioned, its registration with α-particles is not that severe, because of their low atomic charge (Z), and is even highly pronounced for heavier ions (see section 6.1).

• **Energy resolution**
Since the ^{58}Ni particles impinge on a ^{197}Au target, a Coulomb excitation of the projectiles and of the target nuclei appear. It is detected, apart from the other detectors in the set-up, also with the Si detector. Both particle types deposit fully their energy with a range *i.e.* for ^{58}Ni ions of 29.8 μm, according to a SRIM calculation [IBMS00]. The corresponding energy spectrum from of the Si IPP detector is shown in fig.3.8.c, where the events are separated on two parts: excitation of the Ni particles (projectile Coulomb excitation) (left) and excitation of the Au particles (target excitation) (right). The obtained energy width of the Ni peaks is approximately 3-4 % and 10-12 % of the Au peaks, which is quantitatively different than with α-particles.

3.1.4 Z resolution with heavy ions

To determine the particle charge Z resolution, a consequence from the energy resolution of the Si IPP detectors [Euri01], another in-beam test has been performed at the LAND setup [LAND02] (at CAVE B at GSI). Note that the particle charge is approximated to the atomic number Z of the particles at relativistic energies [Geis92]. ^{124}Sn ions with energies around 250-300 A·MeV and rate about 10^{5-6} pps are transported to an experimental set-up, where the Si detector has been placed and triggered by another plastic detector in front. In this case the Si detector acts as a transmission detector for the particles, which are stopped in another detector behind. The Si detector signals are read-out in the same way as during the α-test measurements with gain of the preamplifiers appropriate for heavier particles [Bone01]. From the energy deposition in the Si detector, **the** Z

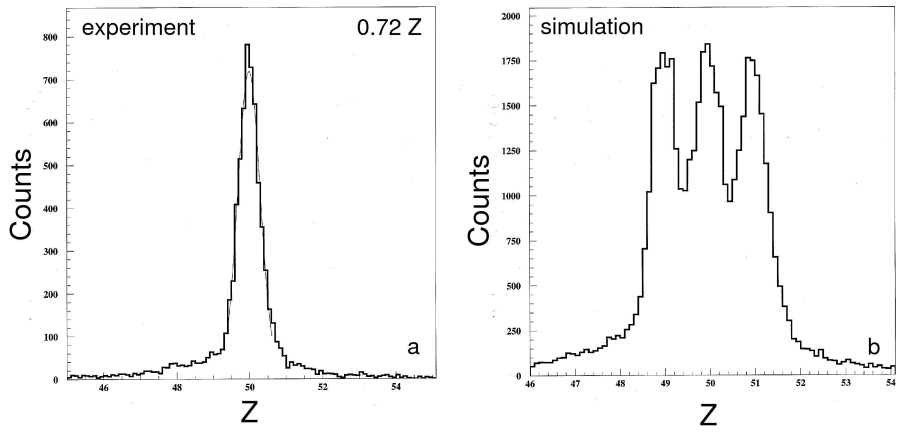

Figure 3.9: **a** - Charge (Z) resolution from a Si-IPP detector with heavy ions. **b** - Simulation for the possible separation of the neighboring ($Z-1$ and $Z+1$) charges, assuming the experimental Z resolution.

resolution on ^{124}Sn particles could be determined after calibration to the incoming particle charge (Z=50). This response is demonstrated on fig.3.9.a and the obtained resolution is 0.72 (FWHM). Assuming that this resolution is kept for the neighboring charges ($Z-1$ and $Z+1$), an experimental spectrum from the detector could be simulated to have the charge separation depicted on fig.3.9.b. By including more matter in the set-up, the experimental charge resolution changed between 0.68 Z (FWHM) and 1.14 Z (FWHM). These results are consistent with previous measurements of Si detectors done with the same experimental set-up by H. Emling et al [EmAu02]. They have reported a Z resolution of 0.5 Z (FWHM) for the 500 A·MeV fission products of ^{238}U.

3.1.5 The dose

During the α and the heavy-ion test measurements with the Si IPP detector a **dose** estimate is performed as a consequence of the particle irradiation. The effects [Eise72,

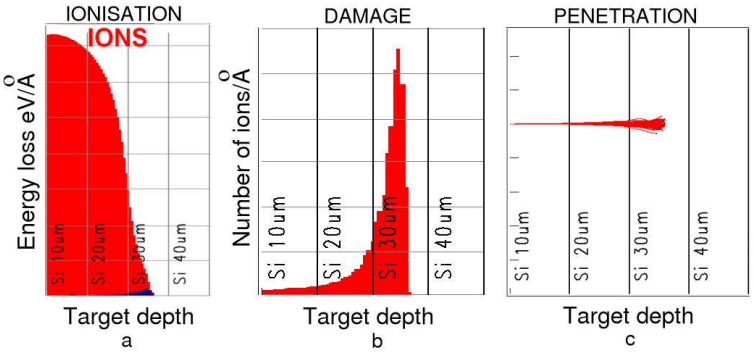

Figure 3.10: **a** - Ionization, **b** - damage and **c** - penetration of the 3.6 A·MeV ^{58}Ni ions in the Si-IPP detector, according to a SRIM simulation [IBMS00].

Feld82] from deposition of different particles, clusters or atoms in the Si lattice have been studied [Bree93, King95] with various energies at various conditions. Several techniques [Dauv99, Wang02] are used to estimate the radiation dose and damage in the Si detectors. Typical atomic dosage ranges of 8x10^{12} to 1x10^{15} atoms/cm^2 are given in [XieZ00, Sele02].

During the penetration of *i.e.* the ^{58}Ni ions in the Si detector an ionization is expected as simulated with SRIM on fig.3.10.a. The damage in the crystal lattice appears than in the region where these particles are stopped (see fig.3.10.b). In this way the penetration particles (see fig.3.10.c) with typical particle rate of 2 kHz for several days cause radiation damages in the detector. After further increase of their rate to 10 kHz (even for several hours), the stopping layer which has already many dislocations due to the channeling effects is destroyed. That causes drastic increase of the reverse leakage current of the detector. The **dose** is related to the number of particles coming to the detector for the irradiation time. It is measured dependent on the increase of the leakage current of the Si. In this example after irradiation with approximately 10^{19} particles, the leakage current raised from 60 nA to 2,1 μA (as shown on fig.3.11). The effect is observed also as an increased detector noise and double peaking in the measured energy spectra. After such dose the Si detector reach its lifetime and should be replaced.

Outcome from the Si detector tests

From the Si PIPS and IPP detector tests is clear that these detectors have good position resolution $(\Delta x, \Delta y)$ of (3,3) mm^2 and (5,5) mm^2, respectively. Their good energy resolution with heavy ions caused good particle charge resolution of about 0.7 Z (FWHM). These results helped the selection of the Si detectors as ΔE detectors of a new system.

3.2 The $CsI(Tl)$ E detectors

Many investigations are performed to select a stopping detector with sufficient energy resolution to resolve masses in the region A≥100 and more importantly to work in the relativistic energy region ≥100 A·MeV. A first in-beam test for selecting such detector have been made at the FRS [Loze01]. These results, which are briefly described below, and those from other in-beam tests with heavy ions revealed the best detector type, namely the

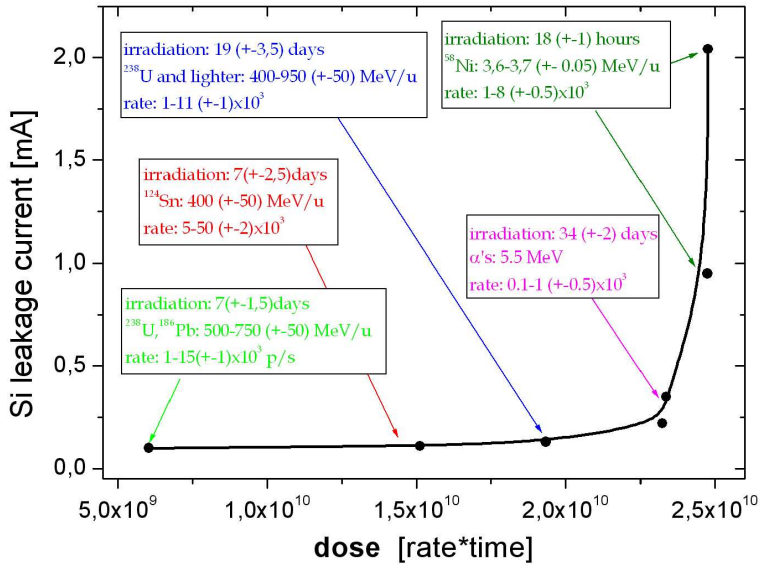

Figure 3.11: Estimation of the dose for Si-IPP detector after irradiation with particles.

$CsI(Tl)$. Later on, tests were performed for optimizing the readout and the electronics combinations under different experimental conditions. As a result, a new detector system consisting of ΔE and E detectors was developed.

Theoretical calculations, the selection of the detectors, their preparation and performance, together with the readout combinations studies under different experimental conditions as well as the analysis and outcoming results will be the main points hereafter.

3.2.1 Stopping-power calculations

Since the energy-range relation differs for every ion and material medium, the energy-range curves required to find adequate detector thickness, have to be determined theoretically or experimentally on an individual basis. Apart from the data derived for different materials and relative stopping powers with light ions and extrapolated for heavy ions [Nort70, Zieg80, Zieg85], program (Monte Carlo) codes are available for the calculation for more massive ions as ATIMA [ATIM04] and SRIM [IBMS00]. Due to the different sets of data it turns out that ATIMA yields more accurate results for high energy ions, whereas SRIM is superior at low energies. Additionally, in some cases (Monte Carlo) codes as MOCADI [MOCA04] and LISE++ [LISE04] are used to compare the experimental values to theory under certain set-up and ion optical conditions.

The stopping range, energy straggling and energy loss are calculated for ions [ATIM04] in the relevant mass range between A=10 and A=238 and energy range from 50 A·MeV to 400 A·MeV. CsI, NaI, BGO ($Bi_4Ge_3O_{12}$), BaF_2 and some type of plastic (Polystyrene - H_8C_8) are included as media detecting *i.e.* ^{197}Au ions [Loze01]. Such results are depicted on fig.3.12 and used for an in-beam test for a scintillator selection. It is clear that, due to the material density, the inorganic scintillator thickness of $\leq$ 15 mm is sufficient to fully stop the Au ions, whereas for the plastic scintillator a thickness of about 3 cm is required.

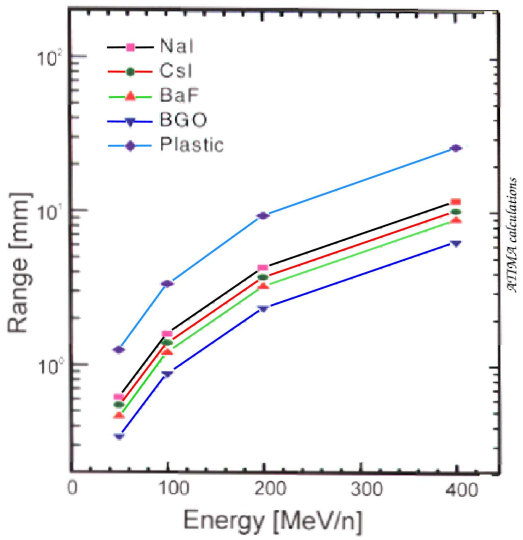

Figure 3.12: Range of ^{197}Au in different scintillator materials for energies up to 400 A·MeV.

3.2.2 Selecting the scintillator

To find out the best candidate for a calorimeter, various scintillators have been tested for energy resolution with high energetic heavy ions. Many of them, potentially suitable for high resolution relatvistic-ion calorimetry are chosen, collecting information from sources as experiments, investigations or data tables as NaI(Tl), BGO, Plastic, CsI(Na), CsI, $CsI(Tl)$, read out by photomultipliers (PMT) or photodiodes (PIN).

Description and preparation

The selected scintillators have different shapes, sizes, housings and manufacturers, therefore several of them did not provide good light collection and showed strong dependence on the interaction position (as *i.e.* case of the CsI(Na) and BGO [Loze00]). These detectors are shown on fig.3.13.a. Two scintillation detectors are laboratory prepared for the current case [Loze01] from CsI(Tl) crystals. First of them is with cubic shape (dimensions (41 x 30 x 30) mm) and covered by 100 μm thick Teflon[1] tape, 5-10 μm thick metalized Mylar[1] [DuPo04] foil and 0.3 mm black tape. It is coupled for read-out to a photomultiplier (type 9903KB / 6367 [Hama04]). The second scintillator is manufactured using a technology described in [Norb95] from crystal with rectangular shape (dimensions of (10 x 30 x 52) mm), covered by 4-8 μm silver by sputtering [Dobr01] and sprayed by black paint approximately 0.1 mm thick. The scintillation light is read-out by a PIN diode with ceramic package, (type S2744-08) with (10 x 20) mm^2 active area. The PIN diode has a slow light response compared to photomultipliers what may be advantageous for heavy-ion calorimetry, since saturation problems due to intense light production would be avoided. A preamplifier (PSC 823C [Euri01]) is used (with AC coupling) to the diode.

Other tested scintillators are photographed on fig.3.13.b. These are CsI(undoped) and $CsI(Tl)$ coupled to PMTs or to photodiodes. Note that the main differences of these two crystals are the maximum wavelengths, which are at 315 nm for the CsI undoped and 550 nm for the CsI doped with Tl and the number of light (decay) components (only one but very fast decay component of 16 ns for the CsI undoped and one fast of 0.6 ms and

[1]Teflon and Mylar are Trademarks of DuPont [DuPo04]

one slow 3.4 ms for the doped with Tl CsI). Correspondingly, because of the absence of doping centers the conversion efficiency (light produced in the crystal) for the undoped CsI is ten times less (≈4-5) than the one in $CsI(Tl)$ (≈45).

The CsI(undoped) crystal, delivered by Scionix (type R35*30C35-CSIU) [Scio04] has a rectangular shape with dimensions of (3 x 35 x 29) mm [ScNo04], covered by 2 μm thick Mylar[1] and is coupled in laboratory conditions to a PMT or photodiode. The used PMTs are type R1828-01 (diameter of 46 mm) [Hama04] and R2924-05 (with diameter of 25 mm) [Hama04] with spectral sensitivity between 300 and 650 nm, with maximum at 420 nm. The used photodiodes are type S3590-01 (active area size (10 x 10) mm^2) [Hama04] and S3204-08 (active area size (18 x 18) mm^2) with spectral sensitivity from 320 up to 1100 nm, with maximum around 960 nm. To assure that no external light can arrive to the crystal or/and the readout and no internally generated light can be lost, wrapping is done using Kapton[1] foil of 50 μm thickness and Teflon[1] of 100 μm thickness around the attachment zone.

The Tl doped CsI crystals are also delivered from Scionix. One of them (type V52PM25/18-E2-Cs-X) [ScNo04] has a truncated trapezoidal shape with bases of 52 and 18 mm and hight, used as thickness of 20-35 mm. Its sides are covered by 2 μm Mylar, except the rare side, which is polished and non-coupled to a readout. The second crystal (type V52P25/18M-E2-Cs-X (SSX848)) has the same shape and sizes except the thickness, which is 10-25 mm (see section 5.1.2). It is coupled [ScNo04] to a photodiode directly from Scionix and has attached preamplifier board including a Scionix preamplifier.

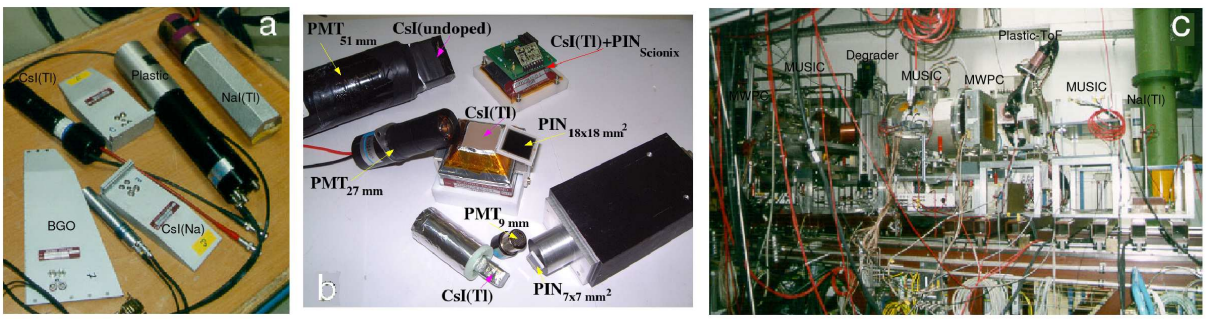

Figure 3.13: The tested scintillator-readout combinations in the **a** - first test at the FRS and in the **b** - in-beam tests at CAVE C. **c** - The experimental set-up used for the FRS test.

All detectors, read out by photomultipliers, are precisely laboratory tested before the in-beam experiment using γ-sources. Since the deposited energy of the γ-rays is 3 to 4 orders of magnitude less then the ion energy and the interaction in the light producing zone is different, such test can only give some indication of the behavior of a particular detector with beam particles.

The $CsI(Tl)$+PIN diode detector is tested with the two preamplifiers available: a Scionix preamplifier [Scio04] and a Milano preamplifier (PA3.2A-7, Q 444763 Milano [Puli02]. They act with similar pulse performance, but the electronics resolution of the Milano preamp turned to be better. It is found to be 3%, 2%, 1% for the amplifier shaping times 1, 2, 4 μs, respectively, and it is selected for the next studies.

Heavy-ion test experiments

Three in-beam tests have been performed with primary ^{197}Au heavy ions with energies in front of the scintillators from 50 A·MeV up to 364 A·MeV at the FRagment Separator,

FRS, at GSI (see fig.3.13.c and section 4.1), with ^{48}Ca with energies between 115 A·MeV and 210 A·MeV and with ^{40}Ar with energies from 51 A·MeV up to 200 A·MeV at CAVE C at GSI (see fig.3.14). During the first test the ion energy is slowed down with a help of a degrader (potential source of an atomic charge exchange) with different thicknesses, while during the rest two the energy is changed by the GSI accelerator.

The tests of the detectors in all cases are performed with standard electronics (similar to that with the Si tests from fig.3.4) with different shaping amplifiers (ORTEC 572 [Orte04], Eurisys 227 [Canb04], Tennelec 244 [ElMo02] and Caen N568B [CAEN02]) with shaping times between 1 and 10 μs.

The analysis are performed in an event by event basis with the FRS data acquisition (see section 4.3) and user developed programs using the APE PAW and PAW packages [CERN95, PAWC04] in the first analysis, and user developed programs of the ROOT and Go4 [ROOT04, Go4G04] packages in the rest cases.

The results from the first test of the scintillators with ^{197}Au ions are listed in table 3.2.3, where R is the energy resolution.

Detector	$E_{@detector}$ [A·MeV]	R_{raw}	$R_{pos.corr}$	$R_{\Delta Ecorr}$
CsI(Tl)+PIN	125	10.54%	5.15%	10.18%
CsI(Tl)+PIN	200	6.11%	4.76%	10.18%
CsI(Tl)+PIN	350	2.62%	1.17%	2.58%
CsI(Tl)+PMT	100	2.25%	1.97%	2.16%
CsI(Tl)+PMT	156	2.12%	1.90%	1.97%
CsI(Tl)+PMT	200	0.77%	0.71%	0.74%
CsI(Tl)+PMT	306	0.70%	0.46%	0.63%
Plastic+PMT	200	24.19%	23.28%	23.27%
BGO+PMT	364	1.82%	1.52%	1.79%
BGO+PMT	200	3.83%	2.98%	3.77%

Table 3.2.3. Energy resolution results using the selected scintillators on ^{197}Au heavy ions with different energies.

It is important to note here that lowering the energy from 364 A·MeV to 100 A·MeV the beam spot at the tested detectors increase *i.e.* from (x,y)≈(7.8,20.1) to (14.3,13.6) mm^2, thus widening the energy distribution of the incoming ions and increasing the beam dependence.

An intrinsic **position dependence**, is found for the scintillator crystals due to inhomogeneity and also the capability of the CsI atoms for light conversion (see section 7.1.3). It is studied with software gates on the beam spot distribution at the detectors. Avoiding its contribution the improvement of the energy resolution manifested the intrinsic value of 0.46% (FWHM) for the $CsI(Tl)$+PMT scintillator [Loze01]. This result is in complete agreement with the prediction of 0.5% (FWHM) for the minimum energy resolution of the $CsI(Tl)$ crystals, which has appeared almost at the same time by Wagner [Wagn01].

Selecting the scintillator-readout combination

In comparison to the good response of the $CsI(Tl)$+PMT, the spectra of $CsI(Tl)$+PIN diode scintillator show an energy resolution value of 2.5% (FWHM) for an energy of 364 A·MeV and without using slowing down matter. This diode gives not such a good resolution as the PMT, but for the small active area to crystal surface and the standard

preamplifier the result was quite encouraging and provoked further studies of $CsI(Tl)$ detectors with different readouts.

Another comparison between the CsI and $CsI(Tl)$ detectors tested in the CAVE C setup (fig.3.14) is performed using different readouts and electronics in order to optimize the best combination. The intensity of the beam particles during these investigations is also varied between 10^3-10^9 p/spill, distributed in a spill length of 5 s (see section 4.1). Two plastic scintillators of (3 mm and 1.5 mm thickness) are placed 3.3 m apart from each other, measuring the ToF. The thinner plastic is also used as a ΔE detector (≈12 cm) in front of the tested stopping scintillator prototype.

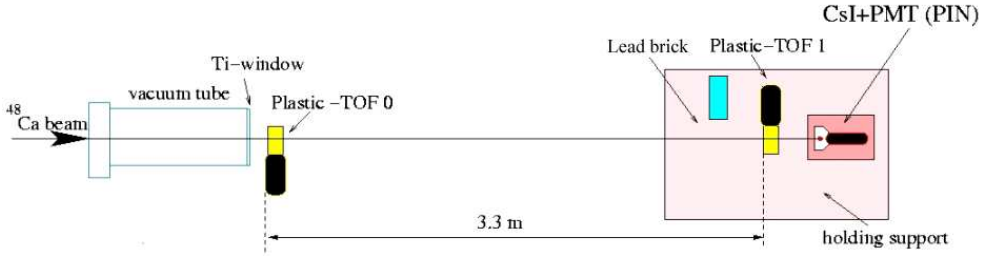

Figure 3.14: The experimental setup at Cave C.

Electronically, as depicted on fig.3.15.a., certain shaping times are optimal for minimum energy resolution. This tendency follows a local minima functional behavior, despite of the bigger shaping times which seem to be best suited to any variations in the detector pulse with long decay time of several μs. During the amplifier study is found that the best

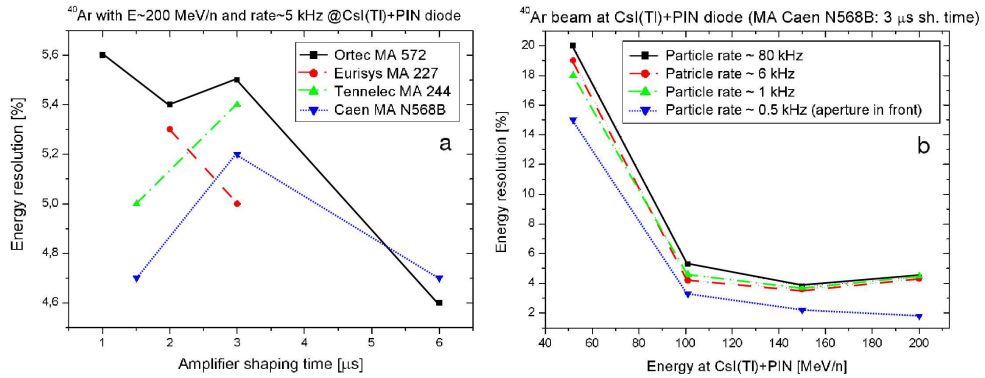

Figure 3.15: **a** - Shaping times scan of the $CsI(Tl)$ signal with different amplifiers and **b** - rate dependence of the $CsI(Tl)$ signal.

performance has the Caen (16ch N568B) [CAEN02] amplifier and the module is chosen for the following investigations of the energy resolution. Although, during the measurements, the bigger shaping times show better resolution, it is expected (following the literature [Horn92, Mosz93]) that the appropriate shaping constant for the $CsI(Tl)$ pulse is about 3 μs.

Additional investigations are performed in order to study how the **particle rate** influence the energy resolution. Such example using the selected detector-readout combination is demonstrated on fig.3.15.b. As can be seen, qualitatively, the particle rate deteriorate the energy resolution. However, it influences differently the different readouts of the scintillator.

To find the optimum solution a test is performed using ^{48}Ca ions with energy of 115 A·MeV and 165 A·MeV. The results for the energy resolution of $CsI(Tl)$ detectors readout by PMT or PIN diode are compared together with the results from CsI+PMT combination in table 3.2.4.

Particle rate [kHz]	Detector	MA / HV [V]	MA sh.time [ms]	Energy resolution [%]
2	CsI(undoped)+PMT(27mm)	Tennelec/700	6	4.0
2		Tennelec/400	1	2.3
2		Ortec/700	6	3.8
2		Ortec/350	1	1.9
4-5	CsI(Tl)+PMT(51mm)	Ortec / -734	2	2.4
4		Ortec / -734	10	1.6
0.5	CsI(Tl)+PMT(27mm)	Ortec / 700	10	0.5
0.5		Ortec / 700	8	0.94
0.5		Tennelec / 700	6	0.98
0.5		Ortec / 800	10	1.0
2		Ortec / 750	10	2.6
3	CsI(Tl)+PIN diode	Ortec / 30	1	3.8
3		Ortec / 30	2	3.9
3		Ortec / 30	4	4.0
1		Ortec / 30	4	2.5
50		Ortec / 30	4	3.0

Table 3.2.4. Energy resolution results from CsI+PMT, $CsI(Tl)$+PMT and $CsI(Tl)$+PIN diode scintillators on ^{48}Ca ions with different particle rates.

As can be seen the energy resolution of the $CsI(Tl)$+PMT is better than the obtained with the PIN diode. However, the amount of light from the E-scintillators is so large that the PMT goes into saturation, despite lowering the voltage and reducing the number of dynodes. Therefore, the PMT readout has instability with increasing the particle rate, thus being not suitable for the high currents which it is aimed to detect. The PIN diode readout is selected for further investigations.

Measurement with an aperture

An Al block with thickness of 113 mm is used during a measurement with ^{48}Ca ions as a collimator with size of its hole of 10 mm, located in front of the second ToF (ΔE) detector. Inspite of the low Z of the Al, the piece is acting as a target for the passing particles (which do not stop inside). Since the collimator is centered, the particle which survive after the collimator target are mainly the primary beam like. Few nucleon removal is possible, according to crossection calculations using KAROL [Karo02].

At 100 A·MeV the energy resolution of the $CsI(Tl)$+PIN is 8.5% with and 2.5% without collimator. In the higher energy case of 210 A·MeV the resolution is 8.7% with collimator and 2.9% without it. This is stable performance, compared to the measurement with CsI+PMT at 164 A·MeV, where the obtained resolution is 9.1% with and 2.8% without a collimator.

The same aperture measurement using ^{40}Ar ions showed that the wide beam distribution results in wide energy spread which is at the same time combined with a position dependence effect of the scintillation crystal itself. Assuming that this hole position is in the exact center of the crystal (with front size of (52 x 52) mm^2) the aperture is moved to hole positions apart from the center at distances of 10 mm, 14.1 mm and 22.4 mm. As a result the energy resolution deteriorated as a function of these distances as demonstrated on fig.3.16.a. The existence of this effect comes from particles impinging at various positions, which create many scattering centers in the scintillator media and widen the energy due to the internal losses. A control of this effect would than be extremely difficult and

it must be corrected by the software in order to obtain the net energy resolution from the scintillator (see section 7.1.3).

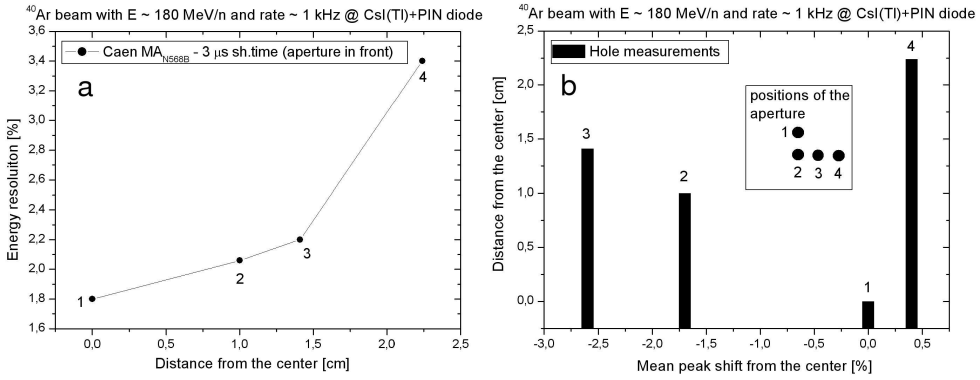

Figure 3.16: **a** - The energy resolution depends on the position of the particles; **b** - the energy centroid shifts depending on the irradiation position.

3.2.3 In-beam $\Delta E - E$ test with plastic and $CsI(Tl)$ detectors

The best candidate, the $CsI(Tl)$ readout by PIN diode, acting as E detector, is tested in a combination with another detector using the same set-up (see fig.3.14) with primary ^{40}Ar particles. For this purpose the second plastic ToF detector is selected, acting as a ΔE detector.

Energy calibration

From a measurement with four different incoming energies, an energy calibration for the used detectors is performed. For the theoretical calculation of the energy loss in all materials (including tiny foils and air spacings) ATIMA [ATIM04] and LISE++[LISE04] are used. By plotting the calculated energies versus the channel number from the detector's spectrum, rather quadratic than linear (function) behavior is observed. To avoid that (gain linear behavior) the pedestals from the spectra of the plastic ΔE and the $CsI(Tl)$ E detectors are subtracted. Those low energy peaks in the experimental spectra come due to the sum of low energies registered (as a decreasing function) and an electronic noise (as a rising function). The linear dependence is examined in additional target measurement when 1 mm thick peace of Al is placed in front of the ΔE detector. The reaction of the ^{40}Ar beam with the target contributes to the linear behavior of the calibration plot as demonstrated on fig.3.17.a,b for the ΔE and E detectors, respectively. Since in the higher energy case (E_{SIS}=244 A·MeV) the Al aperture does not stop the ^{40}Ar particles a corresponding energy peak is observed in the $CsI(Tl)$ spectrum. To add more experimental points the calculated energy and peak channel values are also taken into account for the energy calibration depicted in fig.3.17.b.

$\Delta E - E$ response and reaction probabilities

The energy resolution obtained with the plastic scintillator during these measurements is found to be at the order of 5-6% when acting as a ΔE detector. In the $\Delta E - E$ correlation plot, shown of fig.3.18.a, is clearly visible that the plastic detector reveal good

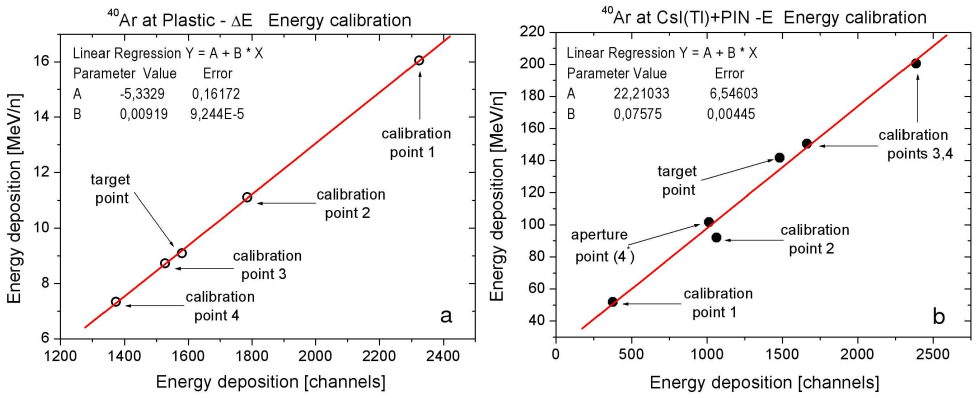

Figure 3.17: Energy calibration of the **a** - ΔE and **b** - E detectors.

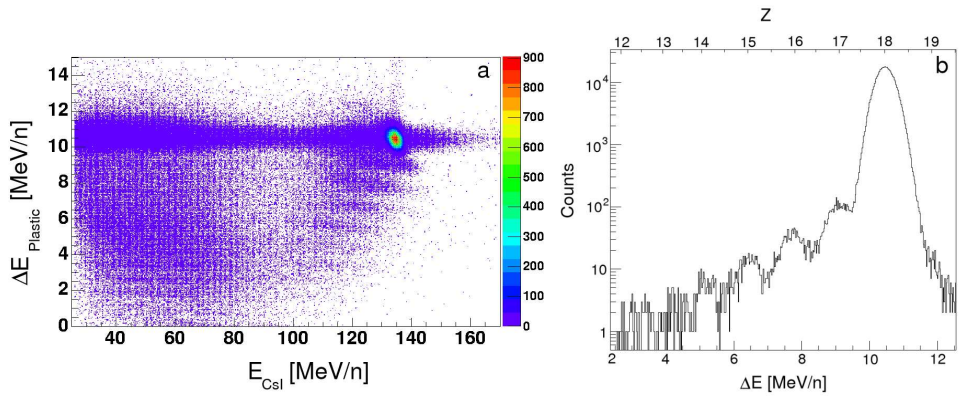

Figure 3.18: **a** - Energy calibrated $\Delta E - E$ spectrum; **b** - ΔE (Z) projection after linearization.

Z resolution of ($\leq$1 Z) for the reaction products of the ^{40}Ar with the Al target. Such response from a plastic detector was reported also in the past for heavy ions from $Z = 1$ to $Z = 35$ [Becc76]. After a linearization (described below) the Z projection ($\sim \sqrt{\Delta E}$) is plotted in logarithmic scale as seen on fig.3.18.b.

Because of the high energy the dominant process here is the **fragmentation reaction**. Therefore, using the EPAX 2 [EPAX04, SuBl00] parameterization a calculation is performed to find the expected fragment products ater the reaction with the target. The different ions and their crossections are visualized on the graphs 3.19.a-d. The fragmentation crossections on the first graph decrease with decreasing Z and A, or with the abrasion of nucleons. In this example are depicted the $(Z - k, A - n)$ nuclei, produced from the primary beam (Z, A) for $k = 1 - 4$ and $n = 1 - 8$. Since another potential targets for reactions are the first and the second ToF detectors, the crossections, the ΔE's and the residual energies E are calculated simultaneously (using LISE++ [LISE04]). Obviously, the reactions with them are not negligible. An interesting point reveals due to the slopes of the energy loss lines, depicted on the rest two (fig.3.19.b,c) and as summed up energy (E_{tot}) on the right bottom (3.19.d) graphs. As observed, these slopes depend on the target Z (Al or C) and the difference in the calculated energies is very small. Because of these slopes the resulting ΔE spectrum is a combination of overlapping energies simultaneously coming from different reaction targets. Consequently, the energy definition of these ions, becomes much worse than the intrinsic detector resolution, and the separation of the differently produced reaction channels would be hard. This means that same particles can

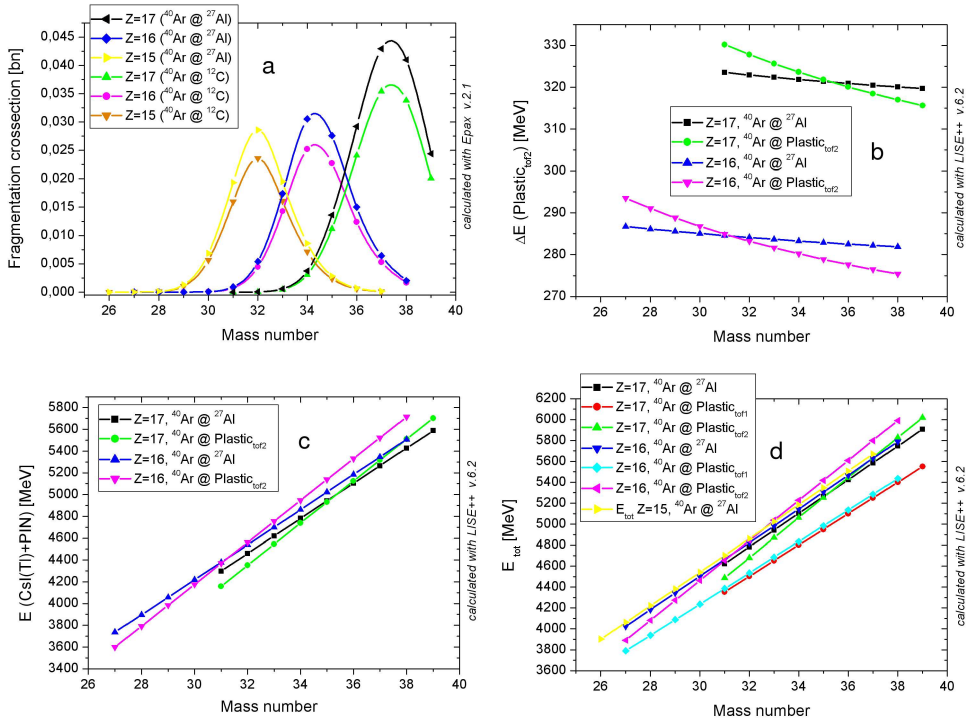

Figure 3.19: **a** - Fragmentation crossections for Z=15-17 products of the reaction ^{40}Ar on Al target; **b** - calculated ΔE in the plastic detector for Z=16,17; **c** - calculated E in the scintillation detector for Z=16,17; **d** - calculated E_{tot} in both $\Delta E - E$ detectors for Z=15-17.

be produced in the first and/or in the second ToF detector and/or in the target. Some of them will not survive to be detected in the ΔE detector because of the aperture in front, which will either stop them or will deflect them and decrease their energy drastically. Hence, they will be observed at another part of the $\Delta E - E$ spectrum, towards the lower channels, as represented on the experimental spectrum shown on fig.3.18.a. Nevertheless, the produced ions in the second ToF detector and in the target will not 'suffer' from stopping in the aperture, but will overlap in energies. Thus reducing drastically the chance to be separated in the stop detector. As can be seen on the correlation plot the different $\Delta E - E$ channels (isotopes with the same Z) are tilted. This is a consequence not only from the different reaction targets but also because of the different gain (amplifications) of both detectors registering the energy losses. In order to perform a projection on the E axis (and get an information about the particle mass) a linearization has to be performed as explained in section 3.3.

Comparison of the $\Delta E - E$ experimental data (after calibration and linearization) and the calculations is plotted in the fig.3.20. The experimental data are depicted as scatter points and the top black circles represent the calculated energies (using LISE [LISE04]) of the produced isotopes. The graph is separated on two parts, depicted with red and blue regions, which correspond to the reaction channels with the Al and with the plastic targets, respectively. As can be seen big amount of the produced isotopes overlap in energies.

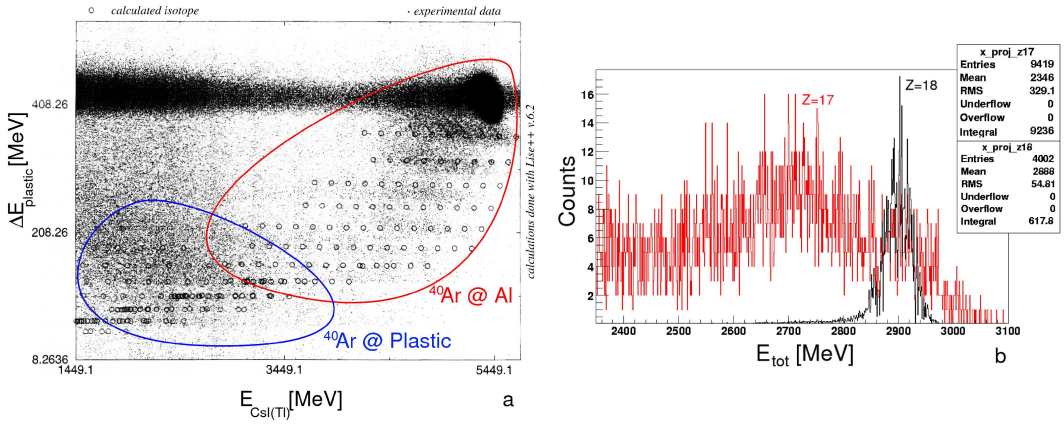

Figure 3.20: **a** - Comparison of the experimental $\Delta E - E$ plot with a calculation for Al and plastic targets. **b** - E_{tot} projection after linearization for the Ar and Cl isotopes.

Mass resolution

To find out the **mass resolution**, A, a projection on the E axis is done for every Z. The mass of the particles within a single Z distribution is proportional to the total energy E_{tot}. It is a sum of the energy losses in both $\Delta E - E$ detectors: E_{tot}=$\Delta E + E$, where E is the residual energy deposited in the $CsI(Tl)$ scintillator. Usually, the energy loss in the ΔE detector is much smaller ($\ll 1\%$) than the residual energy E and can be excluded from the sum. The E_{tot} approximates than to the energy in the second detector E. In this case, the ΔE accounts to 3.6% of E for the highest energy and to 30.8% of E for the lowest energy. Consequently, ΔE can not be ignored in the sum and it is added to the E after the linearization. The total energy projection for *i.e.* the Cl (Z=17) isotopes is plotted on fig.3.20 (in red). The total energy projection of the primary Ar particles (Z=18) is scaled to the hight of the Z=17 and plotted in black. It is visible that the width of the primary particles can be entered several times within the Z=17 projection. The structure of this Z=17 projection corresponds to the different masses of Cl, which can be identified in correspondence to the abandoned mass, calculated with EPAX.

To purify the projection spectrum in order to completely separate the different masses the following procedure was implemented in the software. Between every three single Z distributions are located two spacing regions with very few data points (see fig.3.22.b). These data points come from scatterings events and they contribute to the tails of the mass distributions. Therefore, a two dimensional subtraction is performed in order to 'clean' the corresponding single Z distributions. The intermediate sections are subtracted with different weights. If the distribution for Z=17 is *i.e.* denoted as A, the intermediate section towards the distribution Z=18 is called B and the intermediate section towards the distribution Z=16 is called C. The part to be subtracted from the distributions is like $A - kB - lC$, where k and l are coefficients between 0 and 2. Several such subtractions were performed for Z=17,16...13 distributions with coefficients k and l of 0.7 and 0.5, 1.1 and 1.3, 1.5 and 2 etc. However, the resulting mass spectra were lowered by statistics without significant purification or better separation. That gives a proof of the fact that the different masses are placed (in energy) also in between two Z distributions and probably have a different angle than the Z distribution angle.

To obtain better mass information the distribution is linearized using the algorithm described in section 3.4. The spectrum shown on the fig.3.21.a. is the result of such

linearization procedure which represents the different masses as labeled on the figure. However, because of the limitation of the data set obtaining of their shapes and slopes (if they exist) is not possible. The E_{tot} projection for the Cl isotopes is depicted on

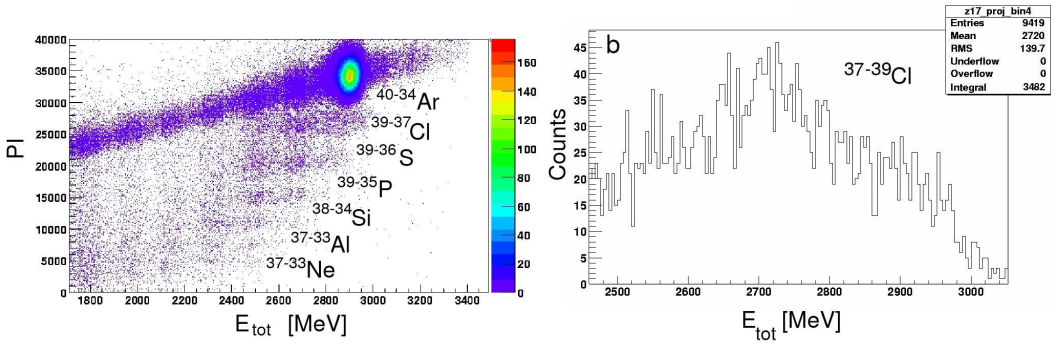

Figure 3.21: **a** - PI(E_{tot}) spectrum after the physical linearization of the data and **b** - E_{tot} projection for the Cl isotopes.

fig.3.21.b. The structure represents the different masses from 37 to 39. It is not possible to fully separate them because of the overlap of their energies when they are produced in the plastic detectors or/and in the Al target (see fig.3.20. The other reason for the overlapping energies is the effect of Goldhaber [Gold74], which is discussed in section 9.4.2. This result is very important because it shows that the $CsI(Tl)$ has mass resolution even in the relativistic energy range. Prior to any corrections of the experimental data is achieved information about masses heavier than those measured by other authors at other facilities. At the same time many effects as the position of the impinging particles and their beam distribution and rate show that the experimental setup and conditions should be optimized in order to get the good mass resolution of these detectors.

3.3 Geometrical linearization procedure

The linearization described below for the $\Delta E - E$ distribution from section 3.2.3 is general and is applied also for other distributions *i.e.* for the correction methods in sections 7.1.3 and 7.2.3. Essentially, it is done by fitting every two-dimensional Z distribution separately with linear function $y = ax + b$ (using XMGR or ROOT-Go4 routine) as depicted with the line on fig.3.22.a. The tilting angle can be determined from the parameters $a = -0.04345158$ and $b = 14.9086$ (*i.e.* for Z=17). It is calculated as:

$$\alpha = arctg(-a/b) \tag{3.2}$$

and equals to 0.071 rad (4.07 deg). In order to linearize, the rotation should be performed on angle $\alpha/2$. The same parameters are found also for lower Zs, but due to statistics they are less acurate. Therefore, the angle for Z=17 is taken for a rotational procedure and shows to be rather good approximation.

Another way to determined this angle easily is a calculation from the coordinates of the 'beginning' (x_1,y_1) and the 'end' (x_2,y_2) of the distribution (see fig.3.23.). The angle α is than:

$$\alpha = arctg(\frac{y_2 - y_1}{x_2 - x_1}) \tag{3.3}$$

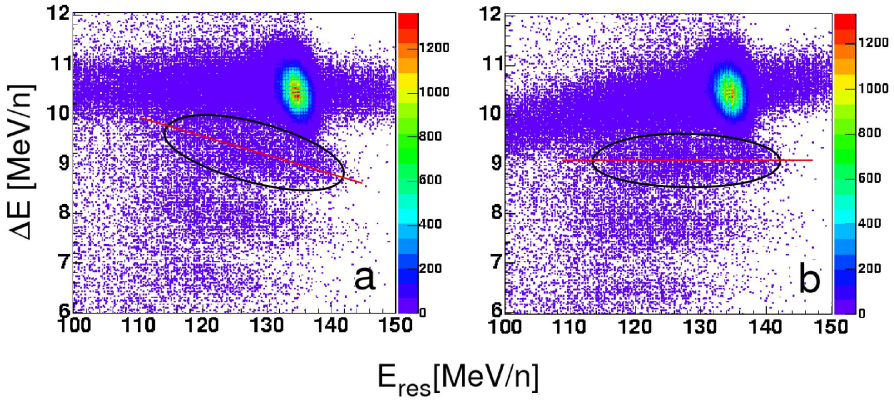

Figure 3.22: **a** - Two dimensional fit of $\Delta E - E$ plot for Z=17 (encircled); **b** - linearization of the $\Delta E - E$ distribution.

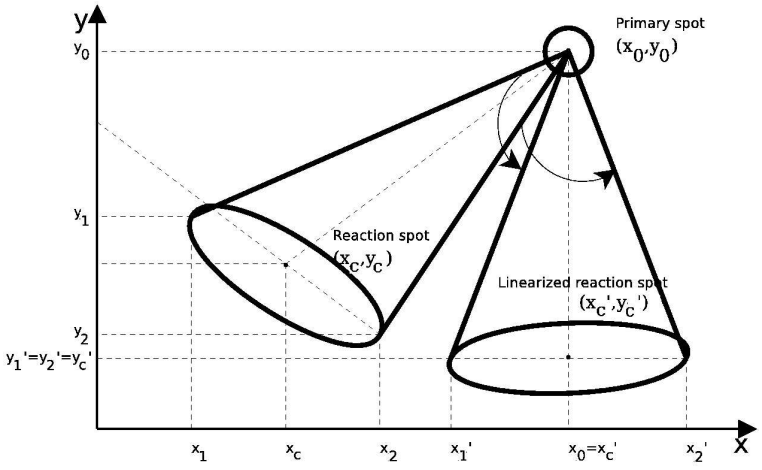

Figure 3.23: The linearization procedure which includes translation, rotation and translation of the two dimensional distribution.

and equals to 0.043831 rad (2.51 deg), but is not so accurate as the angle above.

A new **linearization procedure** is applied to linearize this data in correspondence to the primary beam spot (observed on the pictures with highest intensity and at the highest energies). As shown on the fig.3.23, the center of the coordinate system is the same as in the $\Delta E - E$ spectrum $(0, 0)$ but here for (x_0, y_0) are taken the coordinates of the primary beam spot. In order to linearize this distribution the following **translation-rotation-translation** (-$\hat{T}$ $\hat{R}$ $\hat{T}$) operations are used; the example for Z=17 is described. The known parameters are the two dimensional coordinates (x_0, y_0), which equal to (134.8,10.4) in this case and the angle of rotation α, found by one of the methods described above. The *first translation step* -$\hat{T}$ (the minus sign comes from the directions of the (x, y) coordinate system with center $(0, 0)$) is the movement of the coordinate system from $(0, 0)$ to (x_0, y_0), than the result (x_t, y_t) is:

$$(x_t, y_t) = (x_i - x_0, y_i - y_0) \tag{3.4}$$

Here, with (x_i, y_i) is denoted any point in the distribution. A *second step* is the rotation $(\hat{R}_\alpha)$ around the new center (x_0, y_0). To linearize in this case means to make the distribution parallel to the x axis. Hence the rotation will be in direction against the clockwise

and the angle of rotation will be negative ($R_{-\alpha}$). Since the rotation in two dimensions is described by a matrix with diagonal elements of $\cos(\alpha)$ and anti-diagonal of $\sin(\alpha)$, the result of the rotation (x_{tr}, y_{tr}) is:

$$(x_{tr}, y_{tr}) = (x_t, y_t) * (R_{-\alpha}) = (x_t * cos(\alpha) + y_t * sin(\alpha), -x_t * sin(\alpha) + y_t * cos(\alpha)) \quad (3.5)$$

After the rotation the distribution is 'returned' to its original coordinate system. Therefore, another translation $+\hat{T}$ is needed as a *third step*. The result of it (x_{trt}, y_{trt}) is than:

$$(x_{trt}, y_{trt}) = (x_{tr}, y_{tr}) + (x_0, y_0) \quad (3.6)$$

The operations in total to every point (x_i, y_i), knowing in advance only the coordinates (x_0, y_0) of the primary beam and the angle of the tilted distribution α in order to obtain the linearized distribution $(x_i\prime, y_i\prime)$ are:

$$x'_i = ((x_i - x_0) * cos(\alpha) + (y_i - y_0) * sin(\alpha)) + x_0 \quad (3.7)$$
$$y'_i = -(y_i - y_0) * sin(\alpha) + (x_i - x_0) * sin(\alpha)) + y_0 \quad (3.8)$$

The result from the linearization of the $\Delta E - E$ distribution is shown on fig3.23.b. It is visible that the linearization is quite good for all atomic charges and projections on both axes can be done in order to study the resolutions (as on fig.3.18.b).

3.4 Physical linearization procedure

A new method was used to linearize the data points from the Z distributions and to gain more A information. It is used for the mass analysis in section 3.2.3 and further in the mass analysis in section 9.4.1. The formalism is based on the Tassa-Got mass fits formula in its simple approximation [Tass02] (see section 2.1.6) and was used for explanation of the experimental data with functional of the energy following Bethe [Beth37, Beth78].

Here this formula is used to linearize the $\Delta E - E$ data, adopted with the appropriate parameters specific for this experimental data set. The basis of this formalism is the following formula:

$$\Delta E = [gE^{\mu+1} + (\lambda Z^{2/(\mu+1)} A^{\mu/(\mu+1)})^{\mu+1}]^{1/(\mu+1)} - gE \quad (3.9)$$

The experimental observables here are the ΔE from the plastic (second ToF) detector and the residual energy E registered by the $CsI(Tl)$+PIN detector. The parameter g is the electronic gain ratio, which in this case is the ratio between the slope (a) coefficients from the energy calibration: $g = a_{\Delta E}/a_E$, which equals to 0.1213. The parameter μ, which is typically between 0 and 1 (see section 2.1.6) is taken to be 0.7, as is usually done in the literature [Butl70, Goul75] when using the Bethe approximation. The parameter λ includes the thickness of the ΔE detector in mg/cm^2, which in this case has to be 206.4 mg/cm^2. However, taken in this way it does not reproduce any sensible value for the data obtained. Therefore, this parameter is taken to be the absolute value of the ratio between the offsets (b) from the energy calibration (which anyhow includes the ΔE detector thickness): $lambda = b_{\Delta E}/b_E$ and equals to 0.2394. One more parameter has to be fixed in advance and this is the Z. In this approximation either the Z of the primary beam or any $Z - n$ (n=0,1,2,3,4,...) can be used. For this procedure all $Z - n$ (n=0,1,2,3,4) functionals are calculated and their values compared. They result in almost the same linearization and similar mass approximation. Hence, for the calculations below

the apriori mentioned Z=$Z_{primary}$ (equals to 18) is used. With the above functional the mass A can be expressed as a function of all these observables and parameters to:

$$A = [\frac{(\Delta E + E)^{\mu+1} - (g \cdot E)^{\mu+1}}{\lambda^{\mu+1} Z^2}]^{1/\mu} \tag{3.10}$$

When the g,μ,λ and $Z = 18$ are substituted, the function A simplifies to:

$$A = [\frac{(\Delta E + 0.1213 \cdot E)^{1.7} - (0.1213 \cdot E)^{1.7}}{28.5088}]^{1.4286} \tag{3.11}$$

and can be calculated event by event from the measured and calibrated energy losses. Further, following the approximation for the particle identification PI a use of the calculated particle mass A can be done for every $Z = Z_i$ and $A \approx 2Z$:

$$PI = Z_i + w(A - 2Z_i)) \tag{3.12}$$

The parameter w is equal to the literature value of 0.2. Note that in a later use in the RISING mass analysis a value of 0.4 was chosen by adjusting to the experimental case. For this calculation Z must be the same as the one used for the calculation of the mass A or in this example Z=Z_i=18. Hence, PI is:

$$PI = 0.2A + 8.4 \tag{3.13}$$

In this way a particle identification spectrum PI as a function of the total energy E_{tot} can be obtained which is already linearized by the physical meaning of the Bethe-Tassan-Got mass approximation. It contains the mass information for all different isotopes produced in this reaction and is successfully used also for the fragmentation reactions in section 9.4.1. Typically, from these values the difference between every two masses can be calculated by the formula:

$$\Delta M = E^p_{tot} - E^p \tag{3.14}$$

where p is the power explained in the section 2.1.5) which varies between 1.69 and 1.75. In these analysis a value of 1.72 is found to be the best representative.

3.5 In-beam $\Delta E - E$ test with Si and $CsI(Tl)$ detectors

To investigate a telescope system consisting of a Si detector and a $CsI(Tl)$ scintillator, an energy resolution in-beam test experiment is performed at the FRS. In this test the $CsI(Tl)$ is readout by PMT, since the $\Delta E - E$ abilities of the $CsI(Tl)$, readout by PIN have already been shown in section section 3.2.3.

The used experimental set-up is similar to the standard for the RISING (fast-beams campaign) set-up (see section 4.2.4). Particular difference in the current case is the existence of two more plastic scintillators to measure ToF behind a glass degrader and a MW for additional position measurement, all placed in the final focus of the FRS (see Appendix 2). Behind all detectors a calorimeter telescope prototype is placed. The selected detectors for the telescope are: a Si position sensitive IPP detector (see section 3.1), placed in front (as a ΔE detector) of the $CsI(Tl)$+PMT (E detector) (see section 3.2.2) in a vacuum chamber.

Experimental conditions

A *primary* 750 A·MeV (SIS [SISG04]) ^{238}U heavy-ion beam is transported trough the FRS [FRSG04] and the tracking detectors (see Appendix 2). These beam particles hit the calorimeter system with energies between 100 A·MeV and 400 A·MeV. Slowing down of the ion's energies is performed by varying the thicknesses of an (Al) shape degrader (placed in the middle focal plane) and an energy (glass) degrader (placed in final focal plane). Besides this, ^{186}Pb *fragments* from **fragmentation** reaction of 750 A·MeV ^{238}U on primary Be/Nb target (1023 mg/cm^2) are also transported with energies between 130 A·MeV and 150 A·MeV and detected by the calorimeter system. For comparison ^{130}Sn *products* from **fission** reaction of 732 A·MeV ^{238}U beam on primary Pb target (1006 mg/cm^2) are detected with an energy of 100 A·MeV by the $\Delta E - E$ detectors.

All detectors are calibrated following the standard FRS procedure. Thus, the parameters needed to represent the exact beam position (x,y), the particle charge (Z), the time of flight (ToF) and mass over charge ratio (A/q) are determined (see Appendix 2).

The position resolution response

To find out how the Si diode behaves in a heavy-ion measurement as detector registering position and energy loss in a combination with another E detector it was studied for position and energy resolution with ^{238}U heavy ions with energy at the detector system of 400 A·MeV. The position resolution of the Si is determined in the data analysis, comparing it to the position resolution of a Multi Wire detector (MW) that is in the order of 1 mm. Under coincidence condition of good events in the closest MW ($\leq$ 50 cm in front of the Si) and in the CsI detector ($\approx$ 2 cm behind the Si) the position spectra of the Si detector in x and y are constructed. The MW x-raw projection *i.e.* shown in the small insert in fig.3.24.a., shows an offset of -17.3 mm which has fist to be corrected to 0 in order to construct MW x-corrected spectrum. A correlation plot of the raw Si x position and the corrected MW x position is plotted as shown on fig.3.24.b. It is visible that direct comparison is not possible because the distribution is not centered and is tilted on a certain angle. The last are determined by fitting the two dimensional spot with a

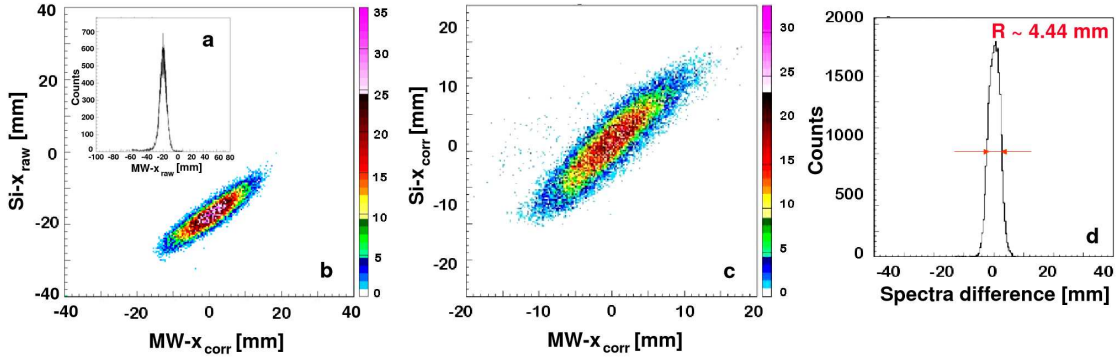

Figure 3.24: **a** - Raw MW x spectrum, **b** - correlation between the raw Si data and the corrected MW data, **c** - normalized correlation between the Si and MW x positions and **d** - spectrum difference between the Si and MW x positions.

linear function $y = a.x + b$, where the Si data represents the y axis and the MW data - the x axis. The coefficients a and b are determined to be 0.71631 and 1.44929, respectively. Using them a new linear reconstruction of the Si data could be performed and correlated

with the MW data (already corrected by the offset) (see 3.24.c). Thus, the distribution is corrected for an offset and tilted on 45 degrees. To compare the resolution is sufficient to compare the FWHM of both distributions. A spectrum which is the difference of the Si and MW spectra is created. Its width corresponds to the difference in the resolution of both detectors, as drawn on the fig.3.24.d. A simple Gaussian fit provides the resolution of 4.44 mm ($\sigma \approx 1.89$ mm), which is the position resolution of the Si with heavy ions.

The $\Delta E - E$ response

With the help of the FRS detectors a separation of charges Z versus A/q ratio can be performed (see section 4.1), as well as a mass separation of the focused ions in the final focal plane versus their A/q ratio. These two identification plots for primary ^{238}U beam particles are shown on fig.3.25.a. In case of fragments the identification requires precise calibration with primary beam in order to locate properly the desired isotope on same type of plots, depicted on fig.3.25.b. For the following procedure is not important to know which is the selected ion, the essential is to separate the different masses (see section 4.1). Therefore, on the figures they are shown as mass A, mass $A-1$, mass $A-2$, mass $A+1$, instead of ^{186}Pb (mass A) and the surrounding fragments of the same Z (82). These ions arrive at the tested detector system with an energy of about 130 A·MeV. Without

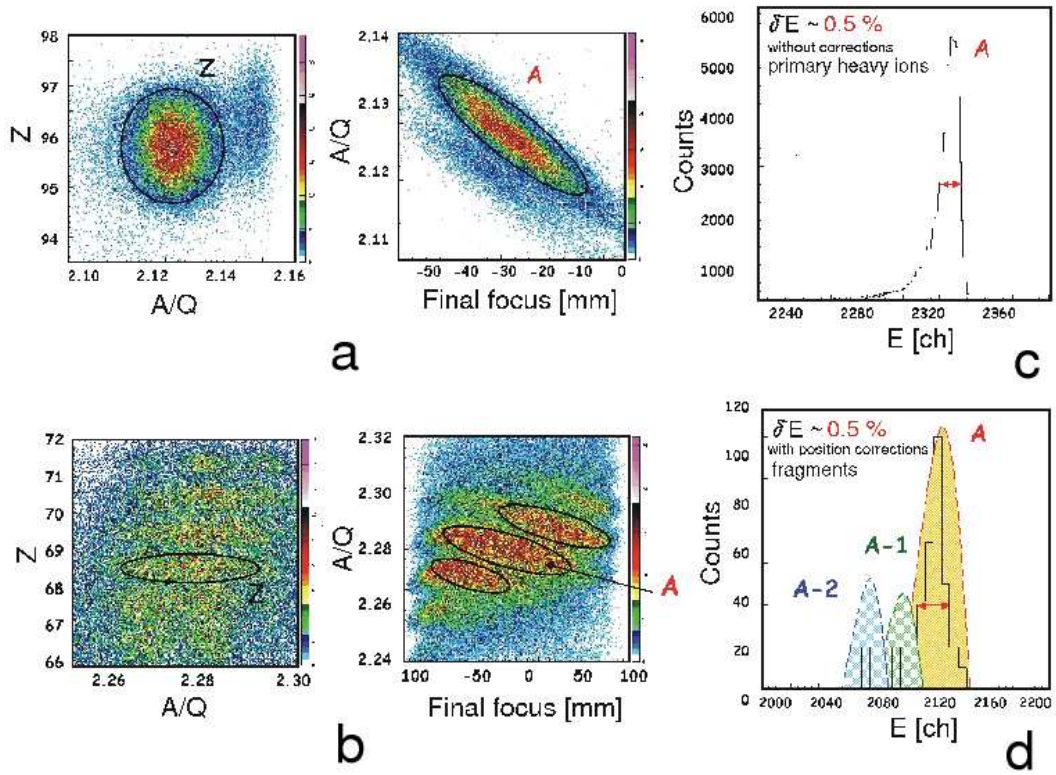

Figure 3.25: Charge (left) and mass (right) separation from the FRS in case of: **a** - primary ^{238}U beam, **b** - fragment ^{186}Pb beam. $CsI(Tl)$+PMT energy resolution in case of: **c** - primary beam and without position corrections and **d** - fragments and with position corrections.

Z and A selection from the FRS detectors the $\Delta E - E$ response is shown on the top-left graph of fig.3.26.a. By applying the different A gates within the same Z from the FRS (fig.3.25.b.), the spectra decreased in statistics (the rest graphs on fig.3.26.a) and a slight Z separation could be distinguished for mass $A-1$ (bottom-right graph), eventually

produced in the glass degrader. This means that due to the small size of our test detectors, the charge selectivity could not be determined. Therefore, to gain this resolution bigger array, covering large opening angle is needed.

The mass resolution

The corresponding projections on the E axis for the (Z,A) selections (from the FRS) (3.25.a) are presented on fig.3.26.b, where a certain mass selectivity is present. This is observed in the peak shifts of the obtained energies, which correspond to the incoming masses. They are plotted in different colors and scaled to the hight of the main mass contribution A (depicted in black). The shift *i.e.* for the both neighboring masses $A-1$ and $A+1$ is $\leq 1\%$. Besides this, this E-detector revealed an excellent energy resolution

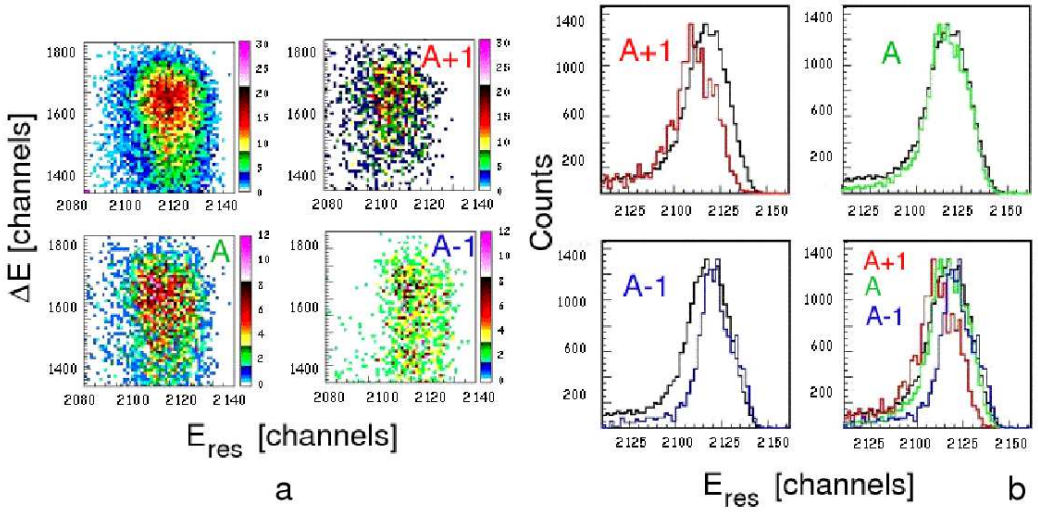

Figure 3.26: **a** - $\Delta E - E$ response on ^{186}Pb fragments, **b** - $CsI(Tl)$+PMT peak shifts corresponding to different masses, selected by the FRS.

of 0.5% (FWHM) for primary beam particles of ^{238}U with energy of 150 A·MeV, prior to any corrections (see fig.3.25.c). This value is also in correspondence with the previous in-beam test of this detector with ^{197}Au and energy of 306 A·MeV, where the intrinsic resolution determination required position corrections. For ^{186}Pb fragments with energy of 130 A·MeV the resolution got worse with energy resolution of 1.2% (FWHM). Performing position cuts on the position distribution at the E detector and selecting a certain Z and A combination from the FRS (as shown on fig.3.25.b) the resolution in the fragment case improved to the primary beam value of 0.5% (FWHM)(see fig.3.25.d).

In case of the ^{130}Sn fission fragments measured with energy of 100 A·MeV, the obtained energy resolution without corrections is between 1.1% (FWHM) and 1.5% (FWHM), depending on the conditions of the measurement. By applying the positions cuts together with the FRS selections (from fig.3.25.b) the resolution improve to almost the same values as in the ^{186}Pb run of 0.46% and 0.52%, correspondingly [Loze03].

This result successfully demonstrates the ability of the $CsI(Tl)$ to identify the neighboring masses of A, namely $A-1$ and $A-2$ and at the same time work in a combination with other detector in a $\Delta E - E$ system.

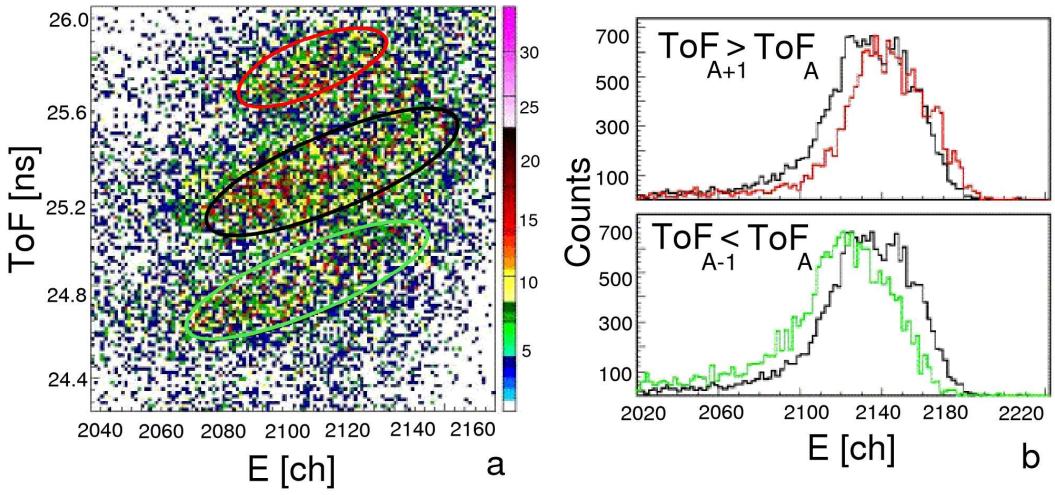

Figure 3.27: **a** - $ToF - E$ response on ^{185,186,187}Pb fragments and **b** - $CsI(Tl)$+PMT peak shifts corresponding to these masses.

The ToF-E dependence

With the availability of the FRS set-up the ToF dependence could be studied (see section 4.1). Following the upper example with ^{186}Pb fragments the ToF between the middle and the final focal plane is measured with the help of fast plastic detectors. After a calibration the ToF, expressed in ns, is plotted versus the energy deposited in the $CsI(Tl)$ detector (see fig.3.27.a), where the mass dependence of the stop detector is additionally observed. By choosing an atomic charge from the FRS and applying ToF gates as sketched on the figure with three different colors, the projections on the E axis from fig.3.27.b. are obtained. The mass $A-1$ and $A+1$ histograms are scaled to the hight of the main mass A (in black). These distributions have an energy resolution of about 1.1% (FWHM) and peak shifts due to the different ToF selections of about 1% (FWHM). This means that the energy in the $CsI(Tl)$ detector, combined with a ToF measurement could also successful method for investigations of different masses.

Outcome from the $Si - CsI(Tl)$ detector tests

During the in-beams tests of Si and $CsI(Tl)$ prototypes their performance as a $\Delta E - E$ system is studied. The Si detectors provide good position resolution, which except for scattering angle measurement, can be used for the corrections of the $CsI(Tl)$ detector. To gain the charge resolution a bigger array of such detectors is required. The mass ability of the $CsI(Tl)$ detector readout by PMT and by PIN diode is successfully tested in the experimental examples. But due to the high current instability of the PMT, the PIN diode readout is selected for the construction of a new system. All tests that have been described in this chapter, prove that a Si and $CsI(Tl)$ $\Delta E - E$ array is feasible.

Chapter 4

The RISING experiments at the FRS

This chapter stands instead of experimental conditions for designing and employing a new detector system CAlorimeter TElescope (CATE), which will be given in the next chapter. This system is a part of the ("fast beams") Rare ISotopes INvestigation at GSI (RISING) spectrometer, which makes use of the former EUROBALL Ge-Cluster detectors, the MINIBALL Ge detectors, BaF_2-HECTOR detectors, and the FRagment Separator (FRS) at GSI. It is aimed at high-resolution in-beam γ-ray studies with radioactive secondary beams, which undergo Coulomb excitation or/and fragmentation with secondary targets.

Brief introduction to these experimental conditions, detector arrays and techniques will be discussed in the first part. The second part is dedicated to the FRS and its experimental set-up, identification methods, detectors and calibration, used for the RISING experiments, and in the CATE analysis. Finally, the acquisition system of RISING and FRS will be introduced.

4.1 The FRagment Separator

The FRagment Separator (FRS) is a high resolution zero degree spectrometer which could separate in-flight mono-isotopic, exotic secondary beams of all elements up to $Z = 92$ by effective combination of ion-optical devices [Muen92]. It is constructed for the isotope selection of projectile fragments by their momentum-loss, called also momentum-loss achromat [Geis87]. The FRS facility which is schematically shown in fig.4.1, consists of four dipole sections, disposed symmetrically to a dispersive intermediate focal plane, and set of quadrupoles and hexapoles before and after the dipoles to fulfill first and second order focusing conditions and to correct optical aberrations [Mage94]. From the dipole radius (ρ) and the magnetic field (B), the magnetic rigidity of the beam ($B\rho$) is defined [Geis91, Geis92]. The act of separating an individual isotope is a combination of two different selection criteria. These selections can be presented as line-cuts in the nuclear chart. The cuts correspond to nuclei, which are deflected to the same positions in the intermediate focal plane (S2) and at the exit of the separator (S4), respectively [FRSG04]. Fig.4.1 shows the experimental set-up with separation and identification examples at every stage of the FRS. The separation of fragments is based on the measurement of their magnetic rigidity ($B\rho$) (between 4-18 Tm [Geis87]) in front and behind an energy degrader mounted in the middle (S2) focal plane. Thus the selection could be described

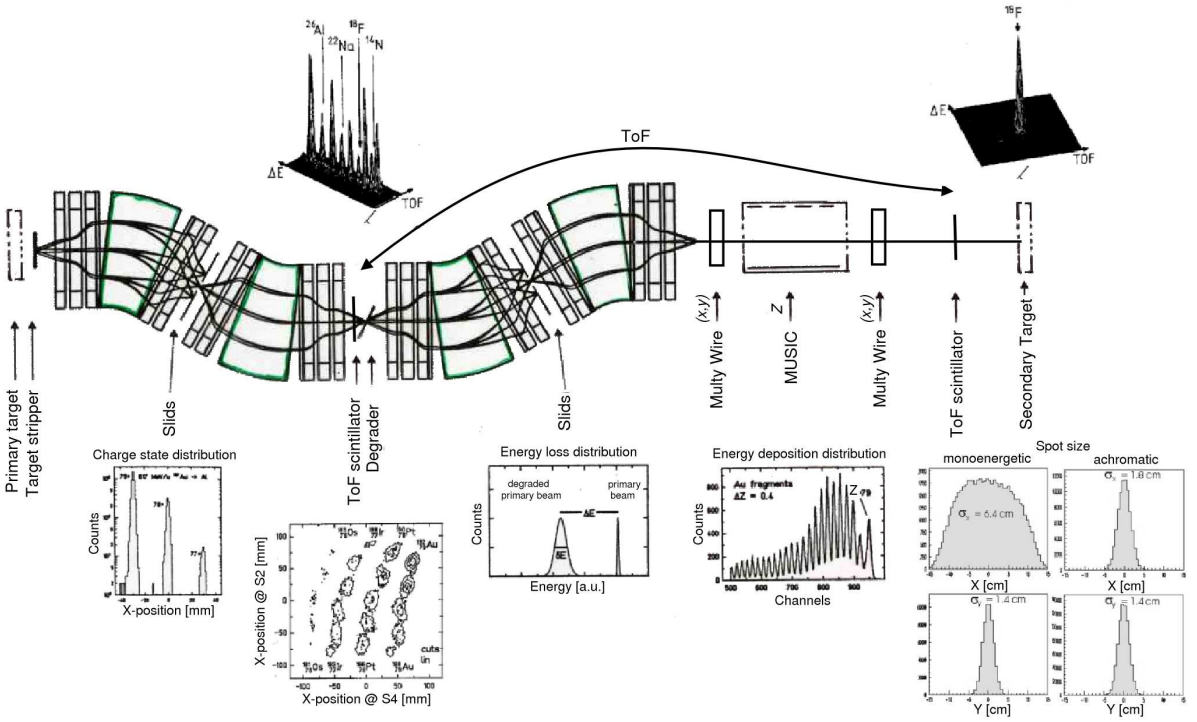

Figure 4.1: The ion-optical system FRS with separation and identification examples [FRSG04].

as follows : In a *first stage*, the ions produced by fragmentation (or fisson of ^{238}U) at the entrance production target of the FRS [Geis95] are deflected and separated according to their A/Z ratio or with nearly the same Bρ values by the first two dipoles (see eq.4.1).

$$\frac{A}{Z} = \frac{p}{q} = \beta\gamma\frac{mc}{\rho} = \frac{B\rho e}{\beta\gamma}\frac{1}{cu} \tag{4.1}$$

Where with the relativistic parameters the velocity $\beta = v/c$, the Lorentz factor $\gamma = \sqrt{(1/1-\beta^2)}$, the speed of light c, the elementary charge e and the atomic mass unit u are labeled. Here it is assumed that the fragments are fully stripped. This could be ensured if $q = Z$ in the first stage of the FRS, what is typical at high particle energies [Geis95]. Even if the velocity distribution of each isotope is narrow, this separation can not select a single isotope, but a variety of nuclei with $A/Z \approx$ constant still reaches the intermediate degrader (see the plots on fig.4.1). Since the momentum loss in this wedge degrader, depends on the parameters (A,Z,velocity) of the fragments, they are slowed down and the separation of a single isotope becomes possible [Geis87].

In a *second stage*, the ions continue to pass trough the other two dipoles, which again deflect and separate them following their charge and A/Z ratio (see the plots on fig.4.1). Dependent on the magnetic rigidity of the ions in the first stage, the profile of the degrader can be chosen in a way that the momentum (energy) dispersion of a selected fragment is compensated by the second dipole section, what means that the system is achromatic.

4.1.1 The isotope identification

The identification set-up associated with the FRS (see fig.4.1) is in charge of measuring the fragments in position (x, y), energy loss (ΔE) and Time of Flight (ToF). This standard set-up is used for many of the detector tests (sections 3.2.2 and 3.2.2), as well as for

RISING (section 4.2.4).
Different kinds of detectors and additional components are used for the identification purpose:
• Degrader for slowing down the ion's energy is used at the middle focus as a wedge degrader and at the final focus (in the experimental tests from section 3.2.2) as a glass degrader.
• Multi Wire (MW) proportional chambers for (x, y) position determination are used for the beam focusing at every focal plane [Stel91]. Typically, only two (or three) of them are used permanently at the final focus for the precise beam tracking.
• Ionization chamber (MUSIC) for energy loss information is used in at the final focus for particle charge (Z) determination [Pfue94].
• A combination of two thin position sensitive plastic scintillators gives the ToF between the two focal planes (called S2-S4) [Voss95]. These detectors give also position and energy loss which can correct these measures in the surrounding detectors. Usually, they are very fast and *i.e.* the plastic detector at the final focus determines the FRS triggering signal.
• Copper blocks (called slids) are used for limiting the space distribution of the ions at every focal plane.
These parameters are, in principle, sufficient to determine completely the mass A and charge Z of each ion reaching the final focal plane. Description, operation and the calibration of all these beam diagnostics elements are given in the Appendix 1 and Appendix 2.

4.2 RISING

RISING is a combination of the FRS at GSI and 15 of the ex-Euroball Cluster detectors for high resolution and high efficient γ-ray spectroscopy of relativistic heavy ion beams. It is a powerful tool for studying reactions of stable and radioactive beams with secondary targets, surrounded in forward angles by the Cluster detectors. For the first RISING campaign (called "Fast Beams"), BaF_2-HECTOR or MINIBALL detectors are added to the combination at backward angles [Woll04].

Objects of interest for the RISING experiments are the shell structure of unstable doubly magic nuclei and nuclei in their vicinity, the isospin symmetry along the $N = Z$ line and mixed symmetry states, the deformed shapes and shape coexistence, and the collective modes of nuclear excitation and $E1$ strength distribution [Woll04].

4.2.1 The experimental conditions

The SIS/FRS facility [Geis92] at GSI provides secondary beams of unstable rare isotopes produced via **fragmentation** reactions (with *i.e.* ^{132}Xe, ^{84}Kr, ^{58}Ni) or **fission** (with ^{238}U) of stable heavy ions at primary reaction target (^{9}Be) (with thickness of 1-4 g/cm^2). Typically, the primary beam energy ranges from 400 A·MeV to 1000 A·MeV for minimal atomic charge state distribution and optimal transmission. The beam intensities from the SIS synchrotron (see section 4.1) vary from $10^{2-3}/s$ up to $10^9/s$ for medium heavy beams (i.e. ^{129}Xe) and $10^8/s$ for ^{238}U). Separated, transported and fully identified by the FRS (see section 4.1), these unique radioactive beams have sufficient intensity, depending on the luminosity and the production cross-section, to perform in-beam γ-ray spectroscopy measurements. For fragmentation reactions the production cross-sections and momentum distributions of the reaction products are rather well known [Enqv99, Benl99] and can be calculated with the EPAX parameterization [SuBl00, EPAX04], while experimental data

are listed for nuclear and electromagnetic fission yields [Woll04].

Typically, these secondary beam nuclei are slowed down to about 100 A·MeV in the FRS and the subsequent tracking detectors before the secondary target is reached (see section 4.1). Therefore, atomic and nuclear processes are relevant at this beam energy. In relativistic heavy-ion reactions, RISING *i.e.* exploit the possibilities of using rather thick secondary targets which compensate for the low beam intensity. The slowing-down of the fragments in the target layer has an important contribution to the kinematics and results in an *energy distribution*. The phase-space is further enlarged by multiple scattering in the target introducing *angular straggling*. Fig.4.2.a depicts the angular straggling (calculated by ATIMA [Zieg80, ATIM04]) in a Au target for Ni, Sn and Pb projectiles at 100 A·MeV as a function of the target thickness. The energy dependence on the straggling is shown for several beams on 4.2.b. Because of this dependence it results in a target effect at CATE (see section 7.2.3). While the energy-loss straggling at relativistic energies is small

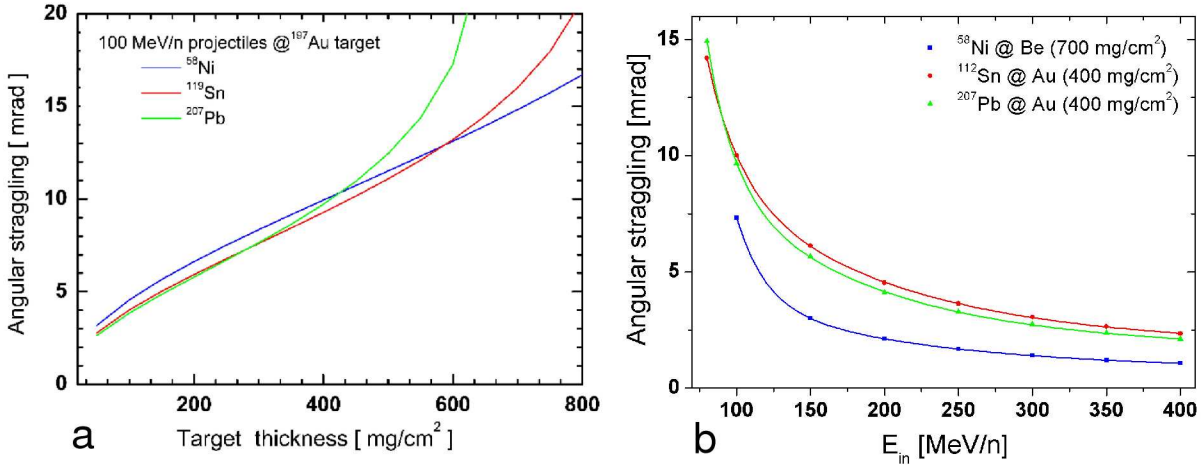

Figure 4.2: **a** - Angular straggling in ^{197}Au secondary target as a function of its thickness for Ni, Sn and Pb projectiles at 100 A·MeV. Note that typical angular straggling of 8 mrad in the Coulex experiments of RISING corresponds to a spot of 26 mm at CATE distance.
b - Angular straggling in secondary target for various beams dependent on their energy.

($< 1\%$), even for relatively thick targets (800 mg/cm^2), the angular straggling shows a strong dependence on the target thickness, which limits an impact parameter measurement for peripheral collisions [Woll04]. Note that, in those experimental cases of RISING, this angular straggling limits the position determination with the CATE system (see section 6.1).

High resolution γ-ray spectroscopy at relativistic beam energies is very difficult. Other limitations are imposed by the large Doppler broadening effects (because of the high velocities) and background, caused by atomic processes (such as radiative electron capture of the target electrons into the projectile, primary and secondary Bremsstrahlung, because of the big atomic numbers of projectile and target). Therefore, the design of the Ge-detector array *i.e.* and the heavy ion tracking detectors in RISING are optimized (apriori these limitations) for the highest possible efficiency and resolution.

The energy range of the RISING secondary beams is between 100 and 400 A·MeV. These beams are used for **relativistic Coulomb excitation** (Coulex) of radioactive projectiles and the spectroscopy of nuclei excited in secondary nuclear reactions such as nucleon removal and **fragmentation**.

4.2.2 Relativistic Coulex

Coulomb excitation at intermediate energies is a powerful spectroscopic method to study low-spin collective states of exotic nuclei. It takes the advantages of large beam velocities and allows the use of thicker secondary targets. Unwanted nuclear contributions to the excitation process are excluded by selecting the reactions with an extremely forward scattering angle, corresponding to a large impact parameter. Thus, a selective device is needed after the reaction target (see section 5.1). Typically, the isotope of interest already selected by the FRS, undergoes this one step excitation at the secondary target and it is important to note here that the incoming particle is equal to the outgoing.

Coulex RISING beams with energies around 100 A·MeV, which will be used in the next chapter are: ^{132}Xe, ^{112}Sn, ^{108}Sn, ^{84}Kr, ^{54,56,58}Cr and ^{68}Ni at 400 A·MeV (for GDR studies). They impinge on secondary target of ^{197}Au with thickness of 1-2 g/cm^2.

4.2.3 Fragmentation

Contrary to Coulex, fragmentation and nucleon removal reactions at the secondary target are a universal method to produce exotic nuclei in rather high spin states. Besides being an excellent way to investigate radioactive fragments in many excitation steps, fragmentation reactions provide a selective trigger, particularly suppressing the huge background of purely atomic interaction events. If in the fragmentation process the cross-section to produce the isotope of interest is large compared to the competing cross-sections of other channels and the primary beam could be used directly. However, in most cases the fraction of the wanted isotope among all isotopes produced is too small to be selectable. Therefore, in RISING, an intermediate fragment is produced and selected by the FRS, which is directed to the secondary target to yield in a secondary fragmentation step the isotope of interest. Typically, the intermediate fragment is chosen with respect to its available intensity and subsequent production cross-section, relative to the abundance in the produced isotope cocktail. The same type of cocktail appears in the secondary target and the incoming particle is anymore equal only to the outgoing but to all abandoned isotopes, products of this reaction, which are almost equally populated.

Secondary fragmentation RISING beams with energies about 120 A·MeV, which will be used in the next chapter are: ^{55}Ni and ^{55}Co. They undergo this process with ^{9}Be secondary target of 400 mg/cm^2 thickness.

4.2.4 The experimental setup

The RISING experimental set-up is schematically shown of fig.4.3.a. It is described as follows: Stable primary beams delivered by the synchrotron (SIS) impinge on a thick production target at the entrance of the FRS (fig.4.3.a.), where via fragmentation or fission of ^{238}U, a cocktail of different isotopes is produced. They are separated with the help of a system with dipole magnets (fig.4.3.a.) and an aluminum degrader at the intermediate focal plane, using the Bρ-ΔE-Bρ method [Geis92]. Afterwards, the ions are identified by a system of tracking detectors. The position measurement in (x,y) is performed by two Multi Wire detectors (MW1 and MW2). The atomic charge (Z) is determined from the energy loss in a Ionization Chamber (MUSIC). The Time of Flight (ToF) between the middle and the final focal plane is measured with two position sensitive plastic detectors (SCI1 and SCI2). ToF and the magnetic rigidity ($B\rho$) of the dipole magnets using the formula inside fig.4.3.a give the mass over charge ratio (A/Q) of the ions. Once the ions are identified

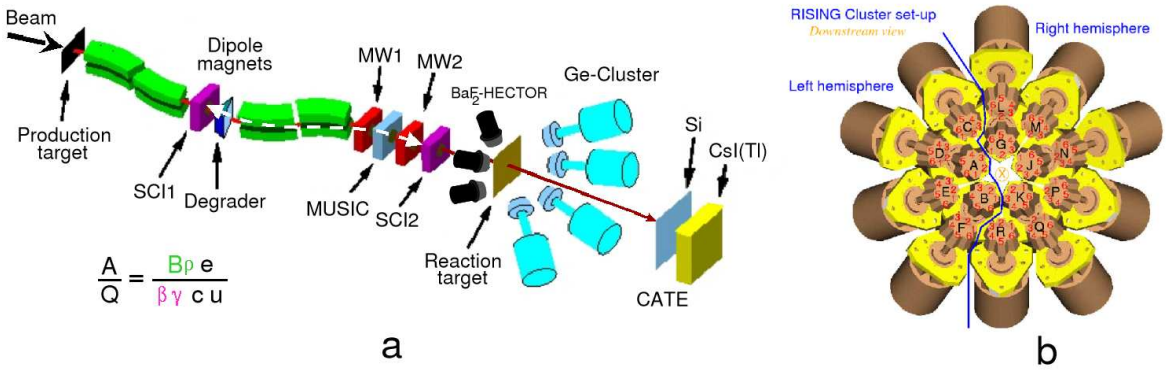

Figure 4.3: **a** - Schematic layout of the RISING setup. **b** - Ge-Cluster detectors.

they impinge on a secondary target undergoing Coulex or fragmentation reactions. The γ-rays associated with nuclei produced at this reaction target are measured with the Ge-Cluster array (see fig.4.3.b.), placed in forward angles and with the BaF_2-HECTOR (or MINIBALL) array, placed in backward angles (see fig.4.3.a.). A subsequent identification of these nuclei in mass (A), charge (Z) and position (x, y) is given by the Calorimeter Telescope (CATE) (see chapter 5.1).

4.3 Data acquisition for RISING and FRS

In RISING three originally stand-alone detector systems are combined together with their individual data acquisition systems (DAQ). These are the Ge-cluster detectors (for γ-detection), the HECTOR (or MINIBALL) array (for γ-detection) and the FRS detectors together with CATE (for particle detection). They are assembled in a common DAQ with a new event synchronization method which utilizes a time-stamp technique, developed in the framework of the GSI standard DAQ Multi-Branch System (MBS) [MBSG04].
Each sub-system (branch) is equipped with a newly developed VME time stamp module TITRIS [HoKu02], which produce a (single buffered 48 bit) time stamp with 20 ns granularity per bit on each external signal. One arbitrary TITRIS module is master and all others are slaves, connected with chain synchronization bus for regular time synchronization of their pulses. The different branches run as independent and fully operational DAQ systems with individual trigger sources and produce their local dead time for the readout, which also is combined to a more global dead time for the set-up.
The germanium cluster detectors signals are processed and digitized by the VXI Ge-Cluster cards [Laza92]. The DAQ system for FRS/CATE and HECTOR are structured in VME crates with identical MBS systems. A VME crate contains a RIO3 readout processor, trigger module, time stamp module, digitisers of QDC, ADC, TDC, scaler and pattern unit. It passes the data to a Lynx-OS PC, which acts as data receiver. On each accepted trigger, the digitizers are readout and the event data is sent via a TCP socket to an event-builder [Woll04]. The time stamp module is stamped by the Master Trigger Out signal of the trigger module, which is raised for each accepted trigger. The collecting and sorting of the data from all sub-systems is made by the RISING master event-builder running on an additional MBS system, which connects the different branches, sorts them and formats all events in output buffers for data store and online monitoring.

An new analysis based on ROOT [ROOT04] and Go4 [Go4G04] pick out from the time

sorted event stream those which have to be combined to a real 'physics' event [Greb03]. During RISING, to overcome the high γ-background the basic trigger signal is derived from the scintillator signal in the FRS beamline (SCI2), indicating a particle in front of the reaction target (see fig.4.3.a). This trigger is used for FRS and CATE calibrations. Two kind of physics triggers are implemented with the help of the SCI2 signal. SCI2 and at least one γ in any cluster detector in coincidence form a physics trigger, which is fed simultaneously to the cluster detector - and the FRS/CATE DAQ system. The second physics trigger takes SCI2 in coincidence with at least a single gamma in the HECTOR detectors. This trigger initiates the readout of FRS/CATE and HECTOR. For some experiments a third coincidence is introduced between FRS-SCI2 and CATE-CsI (separately) and VXI.
During the in-beam tests (from sections 3.2.2 and 3.2.2), the FRS stand-alone system is used. In these cases, the data sender (RIO3) controls alone the VME (and CAMAC) crate readout and sends the events to the data receiver. When formated they become available for the analysis clients as LeA [LEAG01], GOOSY [GOOS01], PAW [PAWC04] or Go4 [Go4G04] (*i.e.* via a remote event server) and for their tape or disk storage [FRSD04].

Chapter 5

The CATE system

A new $\Delta E - E$ CAlorimeter TElescope (CATE) is developed for the identification of the ions streaming out the RISING secondary target. As mentioned in the previous chapters the telescope consists of Si (ΔE) and $CsI(Tl)$ (E) detectors for charge (Z), position (x, y) and mass (A) information, respectively. How the detector system is constructed is explained in this chapter, together with its employment in the RISING set-up and experiments.

5.1 The CATE detectors

The CATE detector array comprises nine $Si - CsI(Tl)$, $\Delta E - E$ telescopes. It is placed 1.4 m downstream from the secondary target in RISING. The reason for that is to have sufficient angular coverage and the same time avoid possible reactions with the detectors themselves (that might be registered in the Ge Clusters and contribute *i.e.* as a γ-ray background). Looking from the target position the array covers an opening angle in $\theta \in [-3.2, 3.2]^\circ$, in $\varphi \in [-180, 180]^\circ$ and has geometrical and measured efficiency with respect to the incoming particles of 92%.

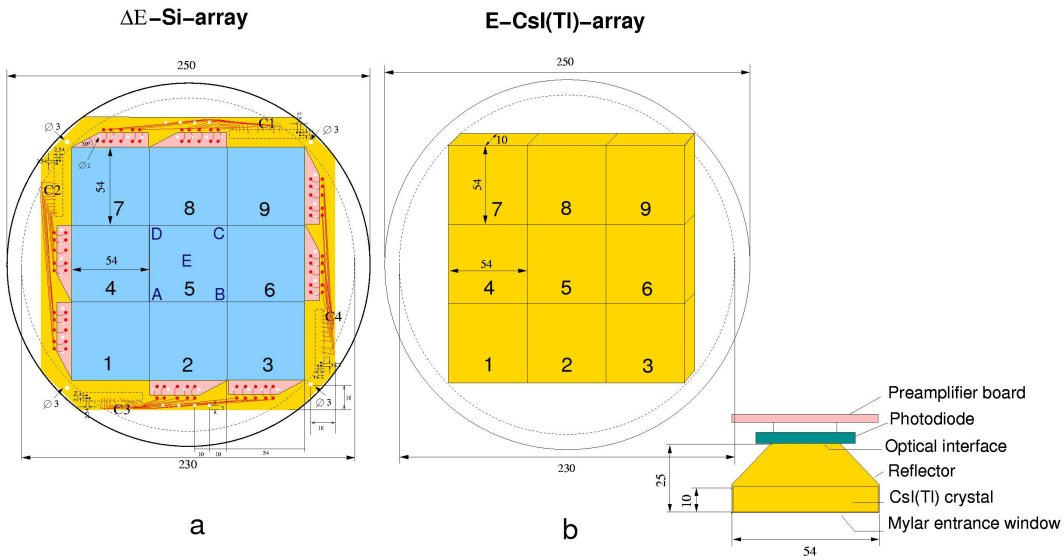

Figure 5.1: The CATE detector is consisting of **a** - Si array and **b** - $CsI(Tl)$ array.

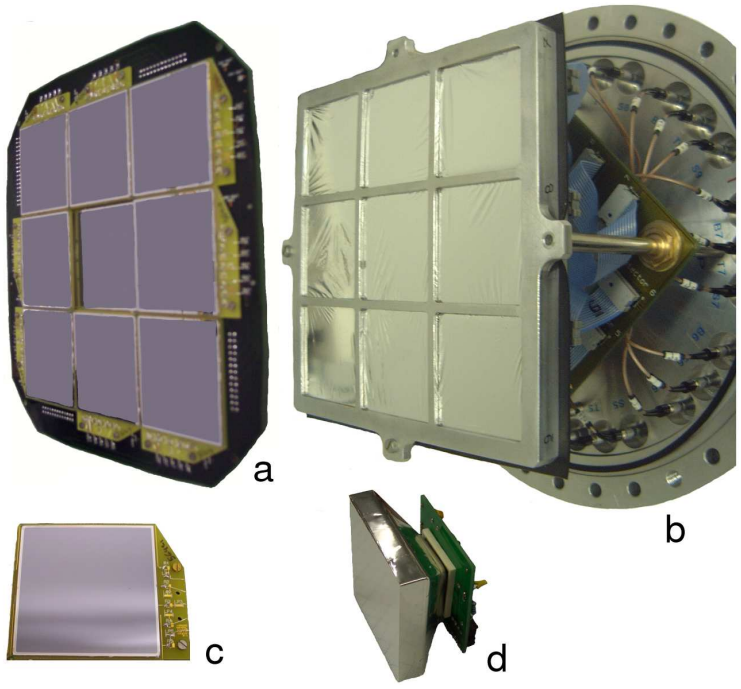

Figure 5.2: A photograph of the CATE **a** - Si array and **b** - $CsI(Tl)$ array. A single **c** - Si detector and **d** - $CsI(Tl)$ detector.

5.1.1 The Si array

Two Si arrays consisting of nine IPP [Euri01] and PIPS[1] [Canb04] Si types (see section 3.1) are used in combination with the $CsI(Tl)$ array in three by three configuration (see fig.5.1.a). As can be seen from the photograph on fig.5.2.a,c every Si detector is placed in a plastic frame with size of (54 x 54) mm^2. This helps the attachment of the fragile detectors together in a motherboard (fig.5.2.a). Thus it acts as a dead (4 mm) zone between each two of them and consequently decreases the geometrical efficiency of the array with 8% (therefore 92%). The connections and installations are the same for both Si arrays, therefore they will not be distinguished in the explanations. In a later section about the position determination (see section 6.1), the difference in the response will be described.

5.1.2 The $CsI(Tl)$ array

The $CsI(Tl)$ array contains also nine $CsI(Tl)$ detectors in three by three configuration (see fig.5.1.b). Each $CsI(Tl)$ [Scio04] scintillator has a truncated pyramid shape with base's size of (54 x 54) mm^2 and height of 10-25 mm, what is the crystal thickness. At the smaller base, for readout, a photodiode with size (18 x 18) mm^2 is attached to yield the residual energy of the fragments after passing the Si detectors. As can be seen on the right bottom of fig.5.1.b, afterwards, a small motherboard is attached to hold the low gain preamplifier [Puli02] and the integral connectors between the preamplifier and the motherboard. All of the detectors (see fig.5.2.b,d) are covered by 2 mm thick Mylar, except the rear read-out side, to protect the crystal, assure good light collection and reduce eventual scatterings. The detectors are mounted in very close geometry (almost

[1]PIPS is a Trademark of Canberra

without space inbetween) and separated in front by an Al holder frame, which covers spacing of 4 mm between each two of them as in the *Si* case and hence reproduces the same geometrical efficiency. It is calculated (using ATIMA ion ranges [ATIM04]) that, in 10 mm of the detector thickness all heavy ions with Z$\geq$ 7 and A $\geq$ 14 with energy of 100 A·MeV are fully stopped.

5.2 Connections and installations

The CATE detectors, installed in arrays are mounted together in a chamber (called CATE chamber) as described below:

5.2.1 The *Si* array

All eight side *Si* detectors (numbered on fig.5.1 as: 1-9), placed in their separate frames are attached to a motherboard on the same plane. The central (numbered as 5) detector is attached to a separate frame, installed parallel and $\approx$ 4 mm behind the other detectors. In total this array provides 45 detector signals which are taken out from the motherboard via four integral connectors. The location and the numeration of these signals are sketched on fig.5.3. The front view representing this sketch, is shown at fig.5.4.a. This side of the

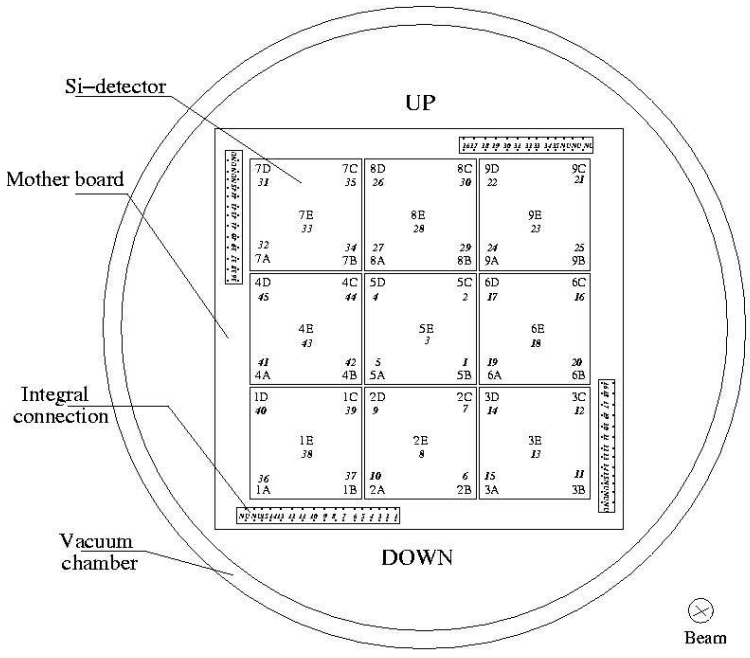

Figure 5.3: CATE-*Si* motherboard connections - front view.

chamber is attached to the beam line. The connections inside the CATE chamber are pictured on fig.5.4.b. Afterwards, they lead to lemo connectors around the whole chamber, which are used outside to feed (with 15 cm long lemo cables) the detector preamplifiers. The last surround the chamber as shown at the CATE installation onto the RISING beam line fig.5.7. Each of these 45 low gain preamplifiers, type CSTA 2 [Bone01] (see section 3.1.1), is providing time and energy signals to the front-end electronics. The low voltage is applied to each of them via additional preamplifier connection. The HV is applied to

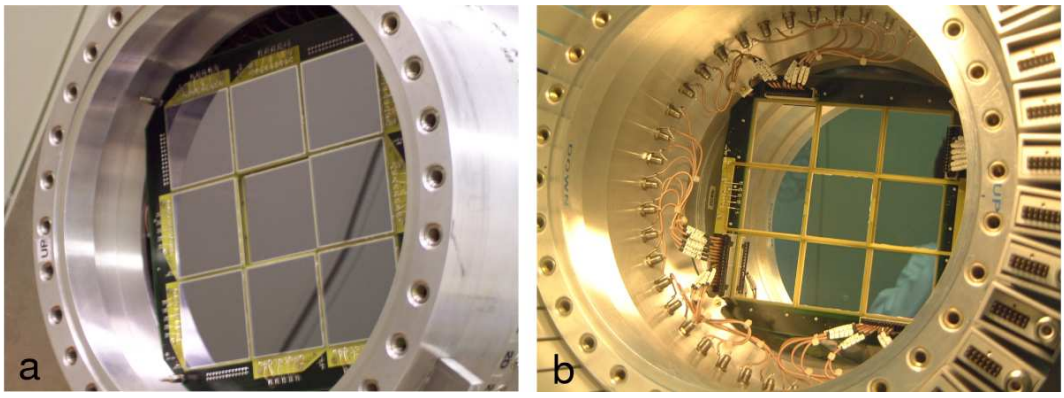

Figure 5.4: Installation of the CATE-Si detectors in the CATE chamber **a** - front and **b** - rear view.

every channel, corresponding to a back contact from a detector (nine in total). All rest preamplifiers (36 in total) are terminated with 50 Ω resistors.

5.2.2 The $CsI(Tl)$ array

The $CsI(Tl)$ holder frame is supported by Al sticks to the back flange of the CATE chamber. In between a PCB board is placed, which acts as an intermediate connector of the detector signals coming from the nine motherboards via integrally connected Teflon cables (see fig.5.5.a and fig.5.6.a). In total 27 signal cables (energy, time and test input

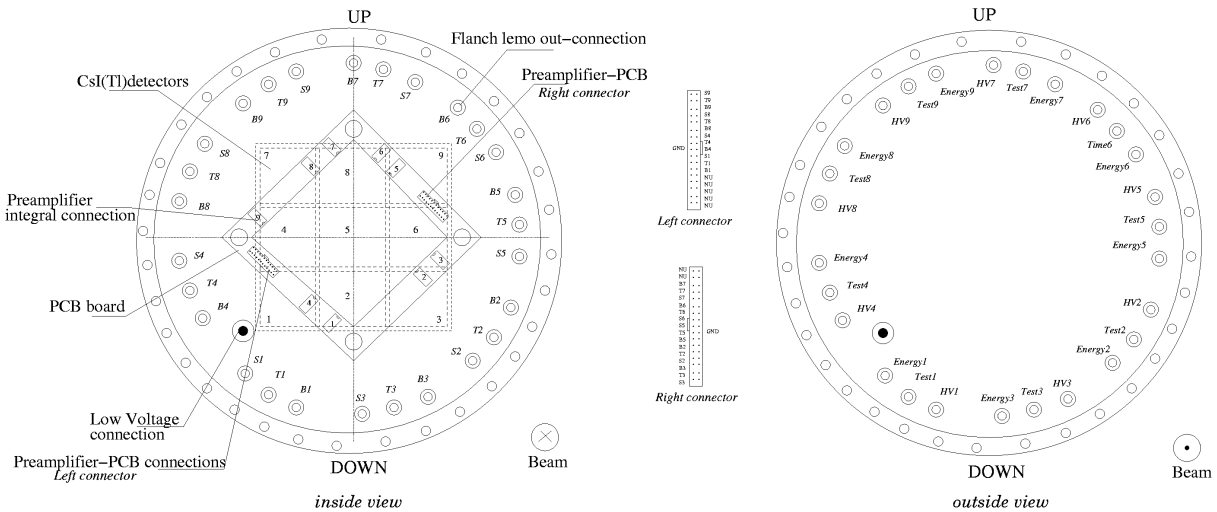

Figure 5.5: CATE-$CsI(Tl)$ back flange connections **a** - inside and **b** - outside view.

for the preamplifier from each detector), nine high voltage and one low voltage cables (distributed to all preamplifiers internally) are connected to the back flange of the chamber as shown on fig.5.5.b and fig.5.6.b. Two additional (left and right on fig.5.5.b) integral connectors are used to transport the signals up to the PCB. There they are distributed via (10 mm long) lemo cables to the flanch. Outside the chamber lemo cables are used to further transport the signals to the electronics. The HV inputs for all nine detectors are fed outside the chamber to a distributor box (see fig.5.7.a) and one common HV is delivered to all $CsI(Tl)$ detectors simultaneously.

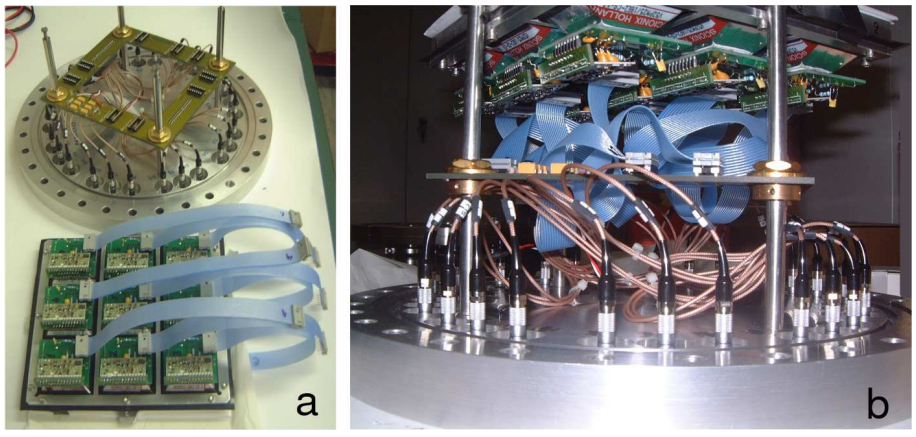

Figure 5.6: CATE-$CsI(Tl)$ connections **a** - PCB board and detectors, **b** - back flange of the CATE chamber.

The installation of the CATE chamber onto the RISING beam line is photographed in fig.5.7.a. Although far from the secondary target, the CATE detectors are source of γ background (because of reactions with their materials), detected by the RISING Ge-detectors and by the HECTOR BaF_2-detectors. Therefore, additionally the CATE chamber is shielded in its front part by two Pb blocks, attached to the beam line as shown on fig.5.7.b. The CATE chamber is usually under vacuum of about 10^{-5} torr,

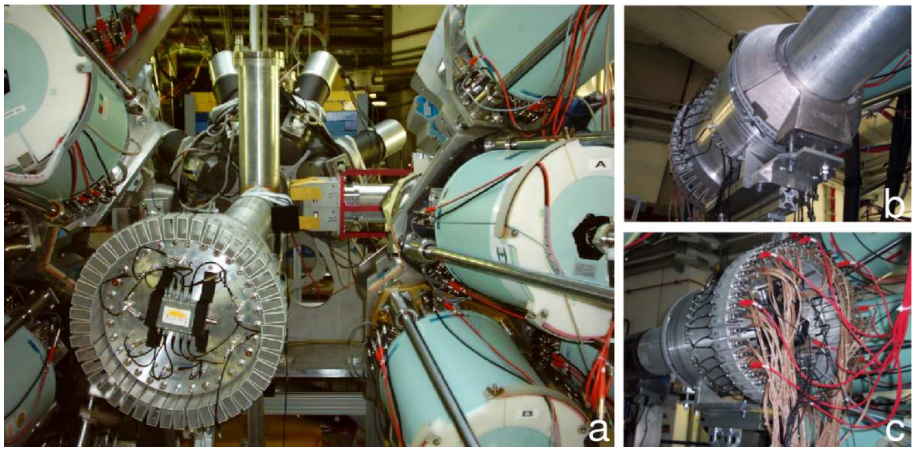

Figure 5.7: CATE in the RISING set-up **a** - upstream view, **b** - downstream view of the CATE Pb shield, **c** - CATE chamber cabling.

thus allowing vacuum operational conditions for all detectors placed inside. The vacuum is supplied by a vacuum pump at the FRS-RISING beam line and is common for all detectors at the experimental set-up. Internally in the CATE chamber, the spacings between the Si and $CsI(Tl)$ arrays are shown on fig.5.8. Because of the high vacuum the distance between the Si and the $CsI(Tl)$ arrays does not play a big role, in comparison to air or dry N_2 spacing. Nevertheless, it is important to know the angular coverage and the exact position of this detectors in order to apply certain experimental conditions, as will be shown in the analysis later.

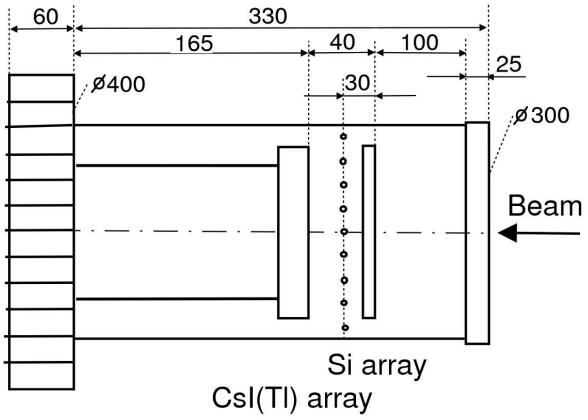

Figure 5.8: Position of the CATE arrays inside the CATE chamber.

5.3 Electronics

After cabling the CATE detectors, the signal and bias connections are transported to (NIM) electronic racs (using standard BNC, lemo and SHV cables with $\approx$ 20 m length)). The preamplifier supplies ($\pm$ 12 V) for the Si's and the common $CsI(Tl)$ preamplifier supply are placed relatively close to the CATE chamber (via $\approx$ 10 m long cables).

All CATE detectors are biased in four HV modules (of type four fold Quad Bias Supply 710 Ortec [Orte04]), which help the monitoring of the HV and the respective leakage current for every channel. The Si detectors (1-9) are biased separately (at +40 V in the beginning of the experiments) and control of their leakage current (of about mean value for all of 0.22 μA in the beginning of the experiments) depending on the particle rate is done every 30 to 60 minutes during an experiment (see section 7.2.3). The $CsI(Tl)$ are biased together in one channel at +30 V and corresponding leakage current (of about 0.34 μA for all) monitoring is also performed.

The electronics scheme of the CATE detectors during the RISING experiments is shown on fig.5.9. After the preamplifiers (see above) the detector signals are processed as follows: The Si detectors provide 36 position energy signals, 9 energy loss signals and 9 time signals (or 6 signals form each preamplifier with 50 Ω impedance and DC coupling). All 45 energy signals are amplified in main amplifiers (MA) (of type 4 fold Quad Amplifier E&Σ 230 [Euri01]) with typically 20 to 50 coarse gain (CG), variable fine gain (FG) and variable P/Z adjustment to $\approx$ 3 V. The position signals are positive and no inversion is required, while the energy loss signals are negative and inversion at the MA inputs are set. The shaping time for all channels is 2 μs. Note that, in some experimental cases the particle energy is much smaller (*i.e.* 70-80 A·MeV) than in others (*i.e.* 120-150 A·MeV) and the deposition in the Si detectors increase (5 to 8 or more A·MeV). In these cases attenuators depending on the pulse heights of 50 Ω, 5-20 dB or attenuator boxes are used either at the MA inputs or at their outputs after the amplification. These signals are transported (with $\approx$ 10 m long lemo cables) to NIM/ECL converters and then fed into a 8 V VME ADC (type CAEN V785c 32-channel [CAEN02]) with 1 MΩ impedance positive input and DC coupling . Typically, the ADC gate is prepared from the accepted trigger of the FRS, as shown of the fig.5.9 (note that the CATE detectors are read out in the FRS branch - see section 4.3). In very rare cases in the preparation of this accepted trigger, usually processed from the accepted and free trigger - signal from the scintillator at the

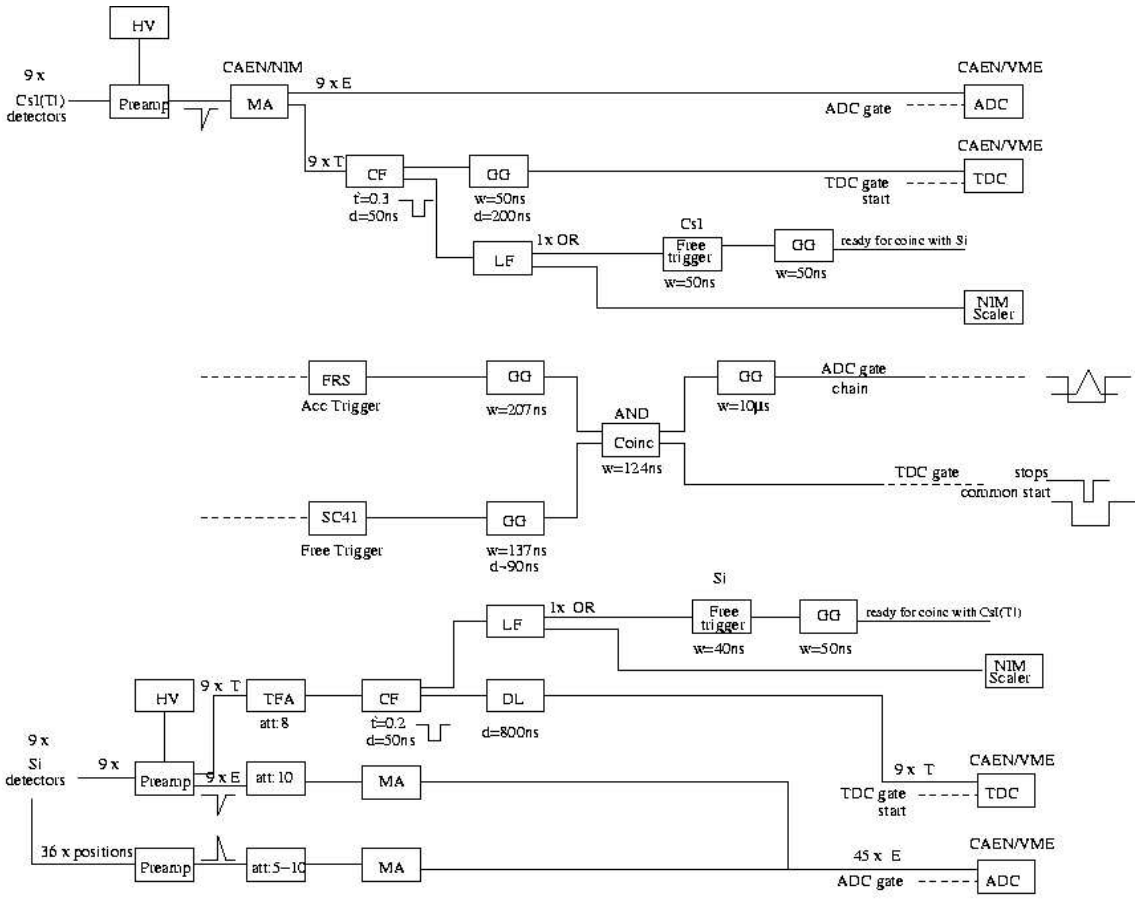

Figure 5.9: Electronics scheme of the CATE detectors during RISING.

final focus, (logical) OR of all CATE detectors is taken as an additional coincidence with the scintillator. The common width of the ADC gate is 10 μs (rarely 12 μs).

The time signals from the 9 Si's input timing filter amplifiers (TFA) (type 1 fold TFA S07-05012 from TU-Darmstadt [TUDA02]). Every amplifier inverts the positive time signals from the preamplifier and amplifies them to typically 400-600 mV, or more depending on the saturation level which often appears for that TFA. Attenuation of the signal is set using switches at the module panel (used from 8-20 times). The TFA provides differentiation and integration of the signal, which are usually used as 1 μs and none, respectively; its output has 50 Ω impedance and DC coupling. Those 9 negative time signals are then prepared to be fed further into constant fraction discriminators (CFD) (type 4 fold CF 4000 of GSI-Darmstadt [ElMo02]). The fraction and delay of these modules is internally set in advance to 0.2 and 50 ns, respectively and external cable delay corresponding to 2 ns is done. Two fast NIM logical outputs from each CFD are used after adjustment of the walk, the width (with typically 50 ns) and the threshold (being just above the noise in the range 15-25 mV). One of these logical signals is fed into a distributor as logic fan (LF) (type 8 fold LF 8000 of GSI-Darmstadt [ElMo02]), whose several outputs are used to input a gate generator (GG) (type 8 fold GG 8000 of GSI-Darmstadt [ElMo02]) with adjustable width and delay (in ranges of 1 or 10 μs). These signals are used for preparing a free trigger of one Si or (OR) of all Si signals or coincidence (AND) with the $CsI(Tl)$ signals etc. and importantly during an experiment for monitoring of the OR or AND Si rate with scaler. The second CFD output is logically

delayed (using LD 8000 [ElMo02] and sometimes also with GG) with 50 to 300-400 ns (depending on the requirement) transported (with approximately the same cable length as the energy signals) and converted NIM/ECL. Afterwards, these 9 signals are used as stops of a 8 V VME TDC (type CAEN V878a 32-channel [CAEN02]) with 1 MΩ impedance and DC coupling, where they are read out. Depending on the range of the TDC (used are usually 280 or 320 ns). The stops which come after the start given by the accepted (and free) FRS trigger, are delayed at least 70 ns. When more is needed, this is adjusted with the LD and/or the GG before. The TDC gate is as well given by the FRS accepted trigger and has typical width of 70-200 ns.

The $CsI(Tl)$ preamplifiers provide only 9 energy signals with 1 MΩ impedance and AC coupling. They are directly fed into a MA (type 16 fold CAEN N568B [CAEN02]). It allows the adjustment to typically 3-5 V using CG of (3-4), variable FG (40-60) and P/Z (always at the maximum setting of 255, with unavoidable undershot of 50-300 mV). The shaping time used for all $CsI(Tl)$ energy signals is 3 μs. Since the output of the preamplifiers is negative the MA works in inverting regime and simultaneously provides fast time outputs from every input. The energy outputs are with 1 MΩ impedance and DC coupling and exactly in the same way as for the Si signals they are connected to an ADC with the same gate of 10 μs and read out. The time signals are also transported to CFD, whose internal fraction and delay are 0.3 and 50 ns, respectively. The external delay is again 2 ns. After adjustment with same widths (50 ns) and noise cutoffs (of about 15-20 mV) the signals are used via LF and GG for free trigger and monitoring scaler. After a DL of about 200 ns (when needed and up to 500 ns) the time logical signals reproduce the TDC stops and as explained before be accepted for readout.

5.3.1 Preliminary tests

The CATE detector electronics is tested before each experiment. The pulse characteristics are simulated with a pulser generator, which input the test inputs of the preamplifiers.

For the Si preamplifiers a charge adapter is used as an input connector. All 45 Si preamplifiers are usually tested with pulser for DC offset and gain and calibrated to the same level via the provided screw control. Afterwards the CG (via switches) and the FG (via screw control) of all MA are adjusted in the same way to have equal output pulses. The time branch is electronically calibrated using these pulses as well, what includes TFA adjustments, CFD noises, GG widths and delays *etc.* to the same output levels.

The $CsI(Tl)$ preamplifiers do not support fine control and their electronics calibration reduces to the MA adjustment using pulser. The MA is checked in advance that no crosstalk between the different channels exists.

The CG and FG and DC offset of the MA channels are adjusted (via a digital controller) to the same pulse heights and with he same shaping times. The time outputs are usually not requiring any changes, therefore further only the CFD and GG are adjusted to the have equal characteristics as explained before.

5.3.2 Pulse shapes

The electronic preamplifier pulses from the CATE Si and $CsI(Tl)$ detectors are depicted on fig.5.10 using a digital oscilloscope DPO Tektronix (model: TDS 7104 - 1GHz, 10Gs/s) without a frequency filter. In this example the response of one of the central CATE detectors (numbered as 5) on ^{58}Cr particles with energy of about 140 A·MeV at the CATE detectors shows the following pulse characteristics: The rise time of the Si position

channels (fig.5.10.a) is about 600 ns. Their pulse clearly distinguishes by hight and shape the position of the impinging particles (and their counting rate at this position). The fall (decay) time for all of them (fig.5.10.b) is about 100 μs. In comparison to an α-source measurement done with this detector the rise and fall times of these positions signals are measured to be 200 ns and 5-10 μs, respectively. The comparison of the back energy contact accounts to the values of 1-2 μs rise (fig.5.10.c) and 100 μ s fall times (fig.5.9.d) from heavy ions and 360-400 ns rise and 5-10 μs fall times with source. The difference

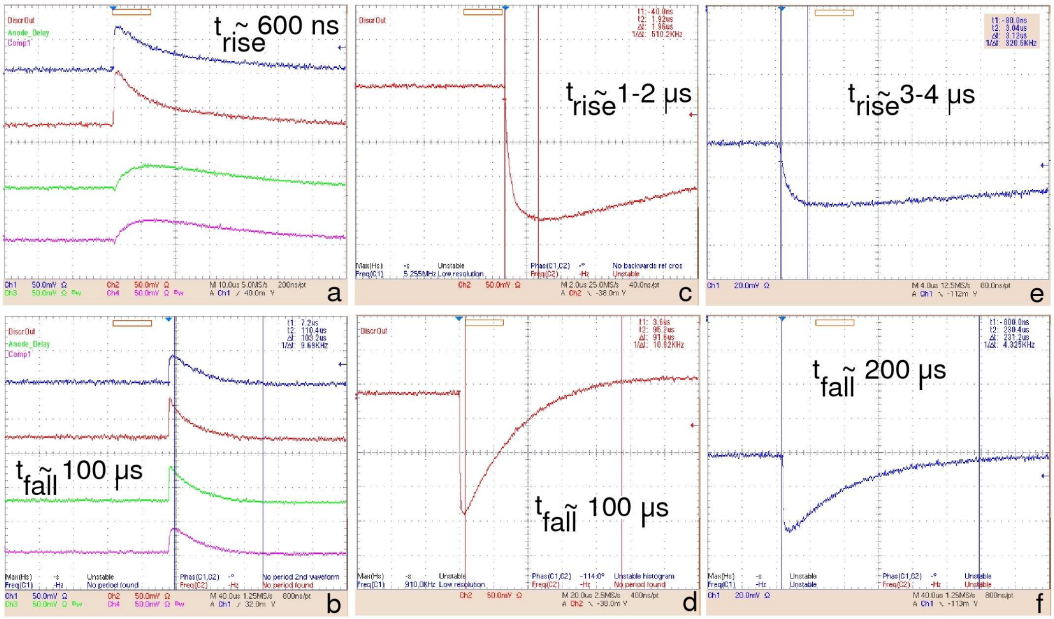

Figure 5.10: Electronic preamplifier pulses from the CATE detectors on ^{58}Cr particles with 140 A·MeV. *Si* position channels: **a** - rise times, **b** - fall times; *Si* energy loss: **c** - rise time, **d** - fall time; $CsI(Tl)$ energy: **e** - rise time, **f** - fall time.

in the preamplifier pulses comes from the different experimental conditions and from the energy deposition in the *Si* detector. In this case the deposited energy is in the order of 290 MeV (or about 58 times more than with the source) and the *Si* acts as a transmission detector. These measurements are done with a *Si*-PIPS detector but since the *Si*-IPP type show almost the same response characteristics, they are not distinguished here.

The preamplifier pulse of the (central) $CsI(Tl)$ detector (numbered also as 5) responds to the energetic heavy particles with 3-4 μs rise (fig.5.10.e) and 200 μs fall times (fig.5.10.f). The obtained pulse characteristics come due to the build up of optically active centers and their subsequent decay and from the electronic time constant of the preamplifier. This is independent of the particle energy and generally independent of the nature of the heavy particle. As a comparison the measurement of the pulse characteristics with ^{132}Xe ions (with energy depositions given in the table below) shows *Si*-ΔE rise time of 2 μs and fall time of 80-100 μs, *Si*-positions rise times of 1 μs and fall times of 100 μs and $CsI(Tl)$-E rise time of 4 μs and fall time of 300 μs.
Although pulse shape analysis are difficult, comparison of the pulse response from the CATE detectors on different incoming heavy ions and energy can be made, especially of their pulse heights (which reproduce exactly the measured energy deposition).

A comparison of the pulse heights from the central detector signals for different incoming particle types is given in table 5.3.2. The pulse characteristics of the other detectors

are similar that is why they are not described separately. As can be seen from the table, the response of the Si detectors is not linear to the incoming particles and energy, the same is valid for the $CsI(Tl)$ energy signals what makes the extrapolation and the prediction to other particle types only approximate. Here one has to note, that the difference in the gain factors comes from quenching effects in the interaction. Assuming linear behaviour, usually, the pulse heights are estimated in advance using one or more measurements of these characteristics. The corresponding exact energy in the CATE detectors is calculated using ATIMA [ATIM04] knowing the precise thicknesses of the matter in the experimental set-up (see second and third column in table 5.3.2). Attenuators and amplifier settings can then be set in advance and slightly readjusted in-beam.

Particle type	ΔE in Si [MeV/n] [MeV]	E in CsI(Tl) [MeV/n] [MeV]	Pulse height Si-ΔE [mV]	Pulse height Si-positions [mV]	Pulse height CsI(Tl)-E [mV]
^{55}Ni	4.3 255	130 7150	180	140	80
^{58}Cr	5 290	135 7830	200	60-120	50-100
^{108}Sn	24.8 2680	135 14580	5000	2000	200-300
^{132}Xe	7.8 1030	108 14260	1300	500	200-400

Table 5.3.2. Pulse heights of the CATE central detectors on different beam particles and energy.

Chapter 6

The Position measurement

6.1 Position measurements

The position measurement of the primary particles or of those outcoming after the reaction in the secondary target are measured with the CATE-Si array. The particle tracking before and after the target is done as shown on fig.6.1. The scattering angle of the

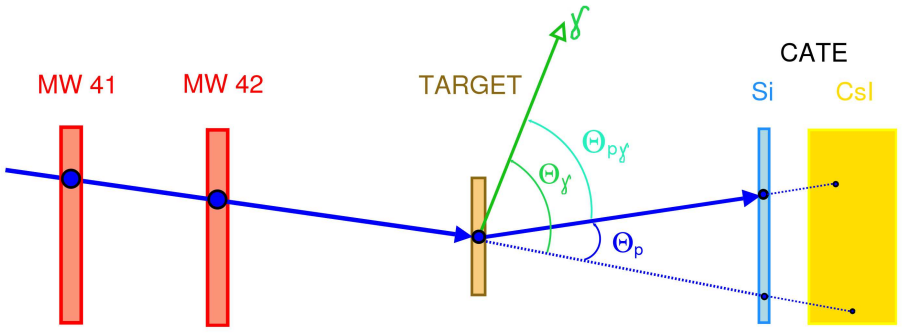

Figure 6.1: Particle tracking before and after the secondary target.

particles (θ_p) can be determined as precise as the reaction kinematics is and as better the position is measured in the CATE detectors. For the Coulex γ-ray studies in RISING *i.e.* in order to select the particles which undergo the low spin excitation process an extremely forward scattering angles are needed, they are corresponding to large impact parameters. To exclude the unwanted in this case nuclear contributions the Si position sensitive array is designed to cover the maximum angular range (called grazing angle [Woll04]) in all possible projectile-target combinations of RISING. This corresponds, to at least $\pm 3^0$ ($\pm 52 mrad$) coverage for impact parameter measurements. Practically, in some of these cases (as shown on fig.4.2) the angular straggling in the thick targets is so large that the position precision requirement from the CATE-Si detectors is as big as each of the separate detectors in the array. But in other cases *i.e.* during a fragmentation at the secondary target every better position selection improves the quality of the particle-γ correlation and hence the Ge γ-ray spectra from the high spin de-excitations.

In its employment, this array was first consisting of 9 Si IPP detectors and later of 9 Si PIPS detectors, which showed definite differences. Since the response of the position does not depend on the particle type or energy but on their special distribution, following the kinematics only several examples will be given here.

6.1.1 Performance of CATE with Si IPP detectors

The response on ^{58}Ni particles with energy of about 120 A·MeV of the CATE Si array is shown on the fig.6.2. Already here is visible that the position reconstruction does not

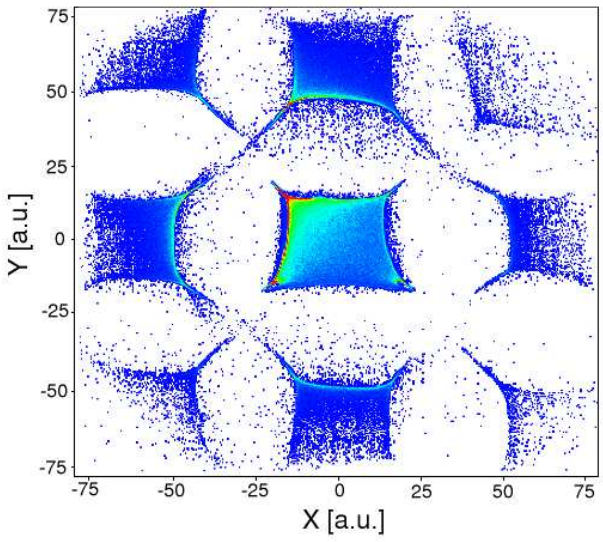

Figure 6.2: Raw position from the CATE-Si IPP array on ^{58}Ni particles with 120 A·MeV.

follow the real geometrical shape of the detectors, neither the spacing between them are as in reality (see fig.5.2.a). The existing nonlinearity deteriorates the position measurement in simultaneously x and y directions.

The effect that causes this picture is known as a **pin cushion effect** (because looks as cushion). It was studied in the past by Gear and Doke [Doke87] and explained as nonlinear distortion of the position shape from Si (2D-PSD) detectors. Investigations have been done by *i.e.* [Yagi89, Brun92, Cowi97] to simulate and calculate the origin of this cushion. They confirm that the shape of the obtained position from such detectors strongly depends on the resistivity of the resistive sheet, the guard ring resistance surrounding this layer (that is normally a low resistance ring whose presence causes perimeter charge flow working against the cushion), the electrode termination resistors, without which no charge flows to these electrodes, the filter components of the preamplifier and the shaping of the amplifier. In our case *i.e.* the resistive sheet is quite small and a guard ring does not exist at all but the termination resistors are sufficient to assure charge flow, however they might compress the energy signal amplitudes that are non-zero but small and lower them below the detection threshold set by the electronics circuit. Consequently some of them might not be detected. To avoid the ballistic deficit (incomplete pulse amplitudes) in the preamplifier pulse, large shaping times are set at the amplifier. Following all these descriptions our Si IPP detectors are quite good candidates for a pin cushion, that seem to be strong. The distortion radius (named with a) has been quantitatively classified to be the ratio between the sheet resistance R, the length of the low resistive strip (the guard ring) L and the resistance per unit length R_L: $R/L.R_L = a/L$. The exact position of the charge particle, following the geometrical algorithm (eq. 3.1) given in section 3.1, can only be determined if the above relation is valid. Any changes will cause a distortion and the lower the ratio $R/L.R_L$ is, the higher the distortion becomes [Cowi97]. In our case however none of these prescriptions could be followed because of the absence of guard ring, because of absence of electronics details and separate current flow measurements.

Therefore another **correction of this effect** is needed in order to obtain the precise position from the CATE-Si detectors excluding the detector electronics.

6.1.2 Corrections of the position measurement

Because of the angular straggling in the set-up materials it is investigated, that beam connected correction of the geometrical shape introduces large errors at the position of the CATE-Si detectors. Therefore more suitable is a software correction, using only the detected position. Such new correction is developed for the Si detectors, and described in the following:

As can be seen from the raw data (fig.6.2), the size of every detector is squeezed. Since the impinging particle creates the charge carrier, it follows the created local electric field in the whole resistive layer and ends at the corner. The registered signal amplitude depends on this position. When the interaction position is in the center of the layer the carrier is distributed to all contacts equally and create almost the same signal amplitudes.

When the interaction occur very close or directly at one corner, most of the signal is collected there. The other three contacts detect very small part of it or do not detect it at all. This might than result in a signal, compatible with the noise level, which is usually ignored.

In the separate pin spectra from the four contacts the noise level is represented as the low channels exponentially decreasing part. Such spectra of the central detector (5) are shown on fig.6.3. Then a valley is formed by the noise and the rising signal amplitude.

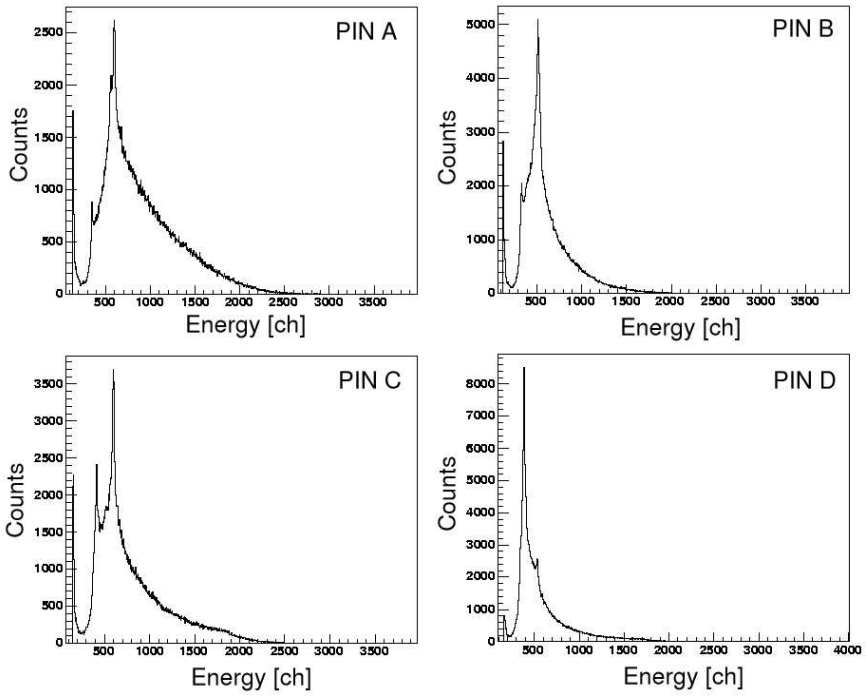

Figure 6.3: Raw position signals from the central Si detector **a** - pin A, **b** - pin B, **c** - pin C and **d** - pin D.

The useful information about the position starts at that point because it corresponds to low amplitude events detected from the interaction with the diagonal opposite corner. If we try to simulate this spectral response *i.e.* of one pin with circle, whose center is at

this corner, will see that the maximum radius (R_{max}) it can achieve is equal to the size of the detector L ($L_x = L = L_y$, $R \in (0, R_{max}) = (0, L)$) (see fig.6.4.a). This means, that the peak in a pin spectrum is corresponding to this radius. When going to higher channels in the spectrum, bigger amplitudes are created in this corner, or the interaction points are closer. The highest channels observed in this spectrum will than correspond to events that hit either the corner or are very close to it. Here one has to note, that the position is always reconstructed when a multiplicity four events are present, or all four contacts register charge simultaneously. To achieve better correspondence to the radius

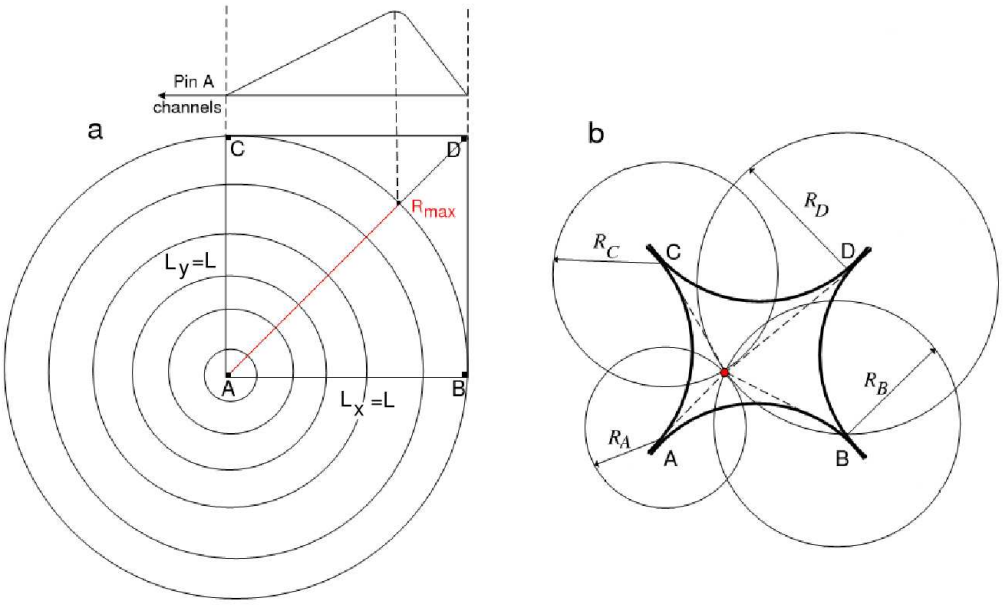

Figure 6.4: *Si* detector: **a** - charge collection in a pin approximated with circles, **b** - approximation of the interaction position with circles.

approximation and decrease the noise contribution, a normalization to the back contact (E) is performed for every pin spectrum (labeled A,B,C and D) as:

$$PinI(normalized) = \frac{PinI(raw)}{E(raw)} \cdot 10^3, \quad I = A, B, C, D \tag{6.1}$$

and shown on fig.6.5.a,b,c,d, respectively. The factor 10^3 comes only for expansion to fit 4096 channels (which the raw spectra had before). The normalization does not play a role in the position reconstruction, because its existence for every pin is being canceled in the calculations for x and y (see the geometrical algorithm for calculation of x and y (eq. 3.1 given in section 3.1). In principle, the back contact represents the sum of the front pins. It is checked that those two spectra are identical. After the normalization to the back contact, every separate pin has to be symmetrized to the other tree. The name symmetrized here, comes from the shape of the obtained (x,y) position spectrum, which is symmetrical when the four pin spectra are treated with four linear functions:

$$PinI(symmetrized) = PinI(normalized) \cdot slope_I + offset_I, \quad I = A, B, C, D \tag{6.2}$$

The noise levels, where the peaks start rising (at lower channel positions with not more than 10 counts), represent the offset values and they are subtracted from the spectra in

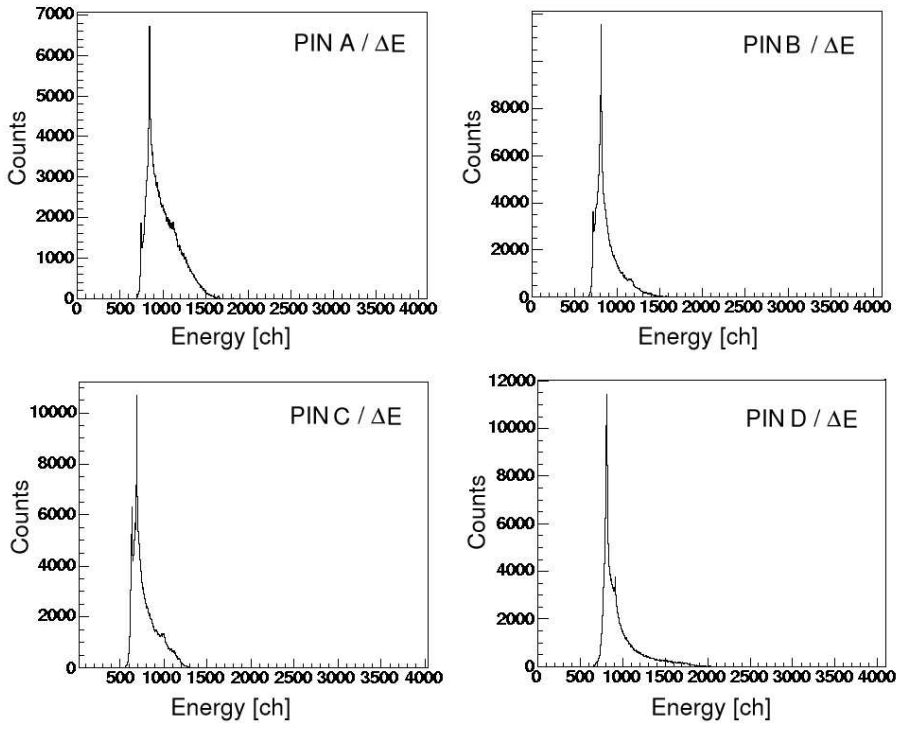

Figure 6.5: Normalized Si-pin spectra from the central CATE detector **a** - pin A/E, **b** - pin B/E, **c** -pin C/E and **d** - pin D/E.

the same way as a pedestal is subtracted. The obtained new spectra, start rising directly at the spectral beginning, but are peaking and ending at different channel positions. One of the pin spectra can be taken as a reference and its peak position in channels fixed. Usually, we choose the pin spectrum, which has the highest peak channel position. The ratios between its peak value and the rest three peak values are calculated and represent the slope coefficients in eq.6.2. If the peak with highest channel is taken as a reference, its slope coefficient is 1 and the other three slope coefficients are < 1. Another possibility to arrange the four spectra, being as identical as possible, is their adjustment to a free reference value, which *i.e.* expands all of them in the whole channels range. After the symmetrization of the pins, the position (x,y) spectrum (fig.6.6.a) is obtained, where x and y are calculated using the geometrical eq.3.1.

To normalize to the real size of the detector, the following new coefficients are used in the calculation:

$$\begin{aligned} x_{normalized} &= blow_x \cdot (x + offset_x), \\ y_{normalized} &= blow_y \cdot (y + offset_y), \end{aligned} \tag{6.3}$$

where the $blow_{x,y}$ factors correct for the measured position squeezing and the $offset_{x,y}$ factors correct for the measured position offset. They are obtained from the projections on the x (fig.6.6.b) and y (fig.6.6.c) axes. The x- and y-ranges represent the measured size in x and y, and are determined as shown on the plots. To find the "*blow*" factors, the ratios between the real size of 50 mm (in x and y) and the measured x,y-ranges are calculated. Since they introduce an expansion, they are always > 1. The mean values of the x,y-projections show also some small offsets from the "zero" (of -3.9 for x and 1.1 for y, note that this detector is in the center of the beam). Since using any offset might

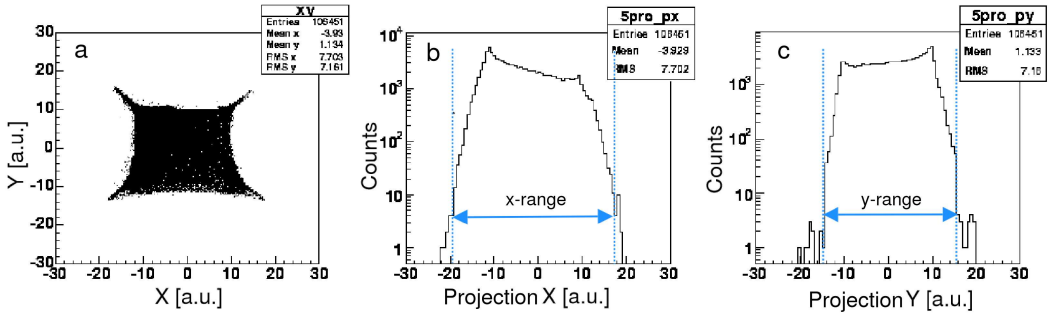

Figure 6.6: **a** - Normalized and symmetrized *Si* position; projections on **b** - X and **c** - Y.

destroy the precision of the scattering angle measurement, the x,y-*offsets* are typically set to "zero".

Further, as mentioned, it is assumed that all particles impinging on an equidistant position from a certain corner produce the same pulse height at this corner. This is valid for all other corners as well, and the position can be approximated with circles, whose four centers are the four corners. In this way the position (x,y), becomes a function of the distance to each of the corners (see see fig.6.4.b) $f(R) = 1/(R + const)$, namely:

$$x = c_1 \cdot c_2 \cdot \frac{\frac{1}{R_A+c_1} + \frac{1}{R_D+c_1}}{\frac{1}{R_A+c_1} + \frac{1}{R_B+c_1} + \frac{1}{R_C+c_1} + \frac{1}{R_D+c_1}},$$
$$y = c_1 \cdot c_2 \cdot \frac{\frac{1}{R_B+c_1} + \frac{1}{R_C+c_1}}{\frac{1}{R_A+c_1} + \frac{1}{R_B+c_1} + \frac{1}{R_C+c_1} + \frac{1}{R_D+c_1}}, \qquad (6.4)$$

where $1/R_A$, $1/R_B$, $1/R_C$ and $1/R_D$ are the distances to corners and *A, B, C, D*, respectively. The two constants c_1 and c_2 utilized in eq.6.4, are equal to 30 and 4.9, respectively. They are used for normalization purpose in the calculation of the theoretical pin cushion. This theoretical cushion is simulated with the above formula. For the radiuses R_A, R_B, R_C and R_D are calculated values between their minimum and maximum, corresponding to a two dimensional position with known coordinates X and Y:

$$\begin{cases} R_A = \sqrt{X^2+Y^2}, & \text{for} \quad X \in [-25,25],\ Y \in [-25,25]; \\ R_B = \sqrt{X^2+Y^2}, & \text{for} \quad X \in [25,-25],\ Y \in [-25,25]; \\ R_C = \sqrt{X^2+Y^2}, & \text{for} \quad X \in [25,-25],\ Y \in [25,-25]; \\ R_D = \sqrt{X^2+Y^2}, & \text{for} \quad X \in [-25,25],\ Y \in [25,-25]. \end{cases}$$

First, the theoretical cushion (fig.6.7.a) is simulated for (11 x 11) two dimensional position maps (pixels) with size of (5 x 5) mm^2 (in x and y), covering the size of (50 x 50) mm^2. The correction to the real square is calculated for every map in x and y, as a difference between the simulated and the geometrical shape. These correction factors are plotted *i.e.* inside their corresponding maps on fig.6.7.b for x and on fig.6.7.c for y. Here the differences to the real position are given only as an example, but in reality it turned out that this granularity is not sufficient, and (50 x 50) position maps are created as shown on fig.6.8.a. The correction coefficients (called δx and δy) to the square shape (see fig.6.8.b) are calculated, with respect to the difference from the calculated pin cushion effect. Note that once calculated and stored in arrays, they are used always for the this type of position correction. They do not change in the different experiments, or at different beam and particle conditions.

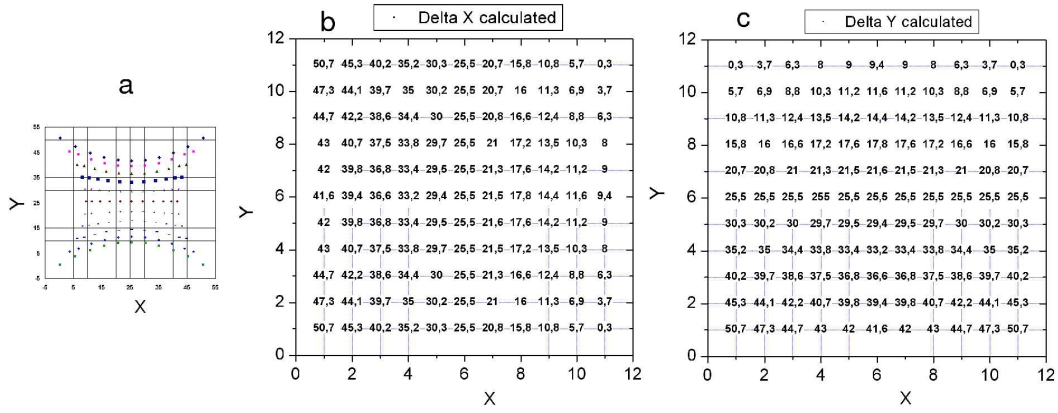

Figure 6.7: **a** - Simulated pin cushion for (11 x 11) position maps, correction factors **b** - for x and for **c** - y direction.

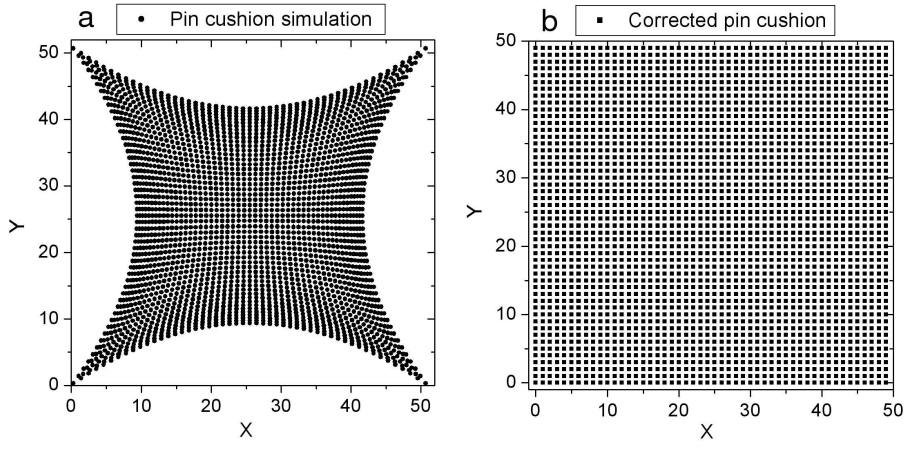

Figure 6.8: **a** - Simulated pin cushion for (50 x 50) position maps and **b** - calculated pin cushion correction.

To apply this correction to the measured data, first the shape of the obtained position has to be symmetrized and normalized to the real one as shown above (so that is looks as the simulated).
With a help of a grid that comprises (50 x 50) position polygons with size of (±0.5 x ±0.5) mm^2, covering the total size of the detector ((50 x 50) mm^2), the corrections δx,δy are applied to the (x,y) position. This is done in the user routines on event by event basis, so, that the data points within a polygon (i, j) are selected and summed with the correction δx,δy, separately for x and for y. Afterwards, all corrected polygons are summed up, to form the ($x_{corrected}$,$y_{corrected}$) spectrum:

$$x_{corrected} = \sum_{i=1}^{50} x_i + \delta x_i,\ i = i + 1$$
$$y_{corrected} = \sum_{j=1}^{50} y_j + \delta y_j,\ j = j + 1 \qquad (6.5)$$

The correction for this central detector is demonstrated in comparison with the measured distribution on fig.6.9.

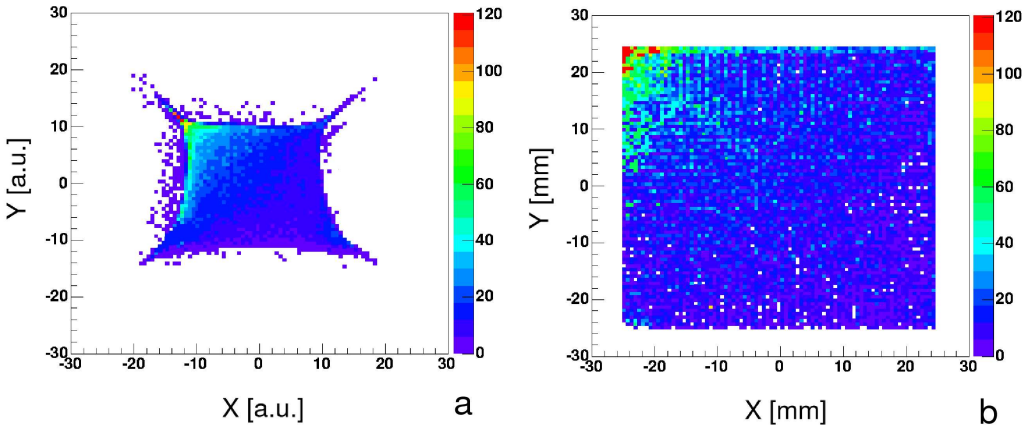

Figure 6.9: **a** - Measured and **b**-corrected position with the central Si detector.

To perform the correction procedure for all detectors, which usually are not fully irradiated, a calibration run is done. For this purpose data with defocussed primary beam (in this case ^{58}Ni) are accumulated, until each detector is almost equally irradiated, and the single pin spectra from all nine detectors have sufficient counts. With the explained correction, for the total Si-array, from the raw measured spectrum (fig.6.10.a) the resulted corrected spectrum (fig.6.10.b) is achieved. The obtained square geometrical shape, helps

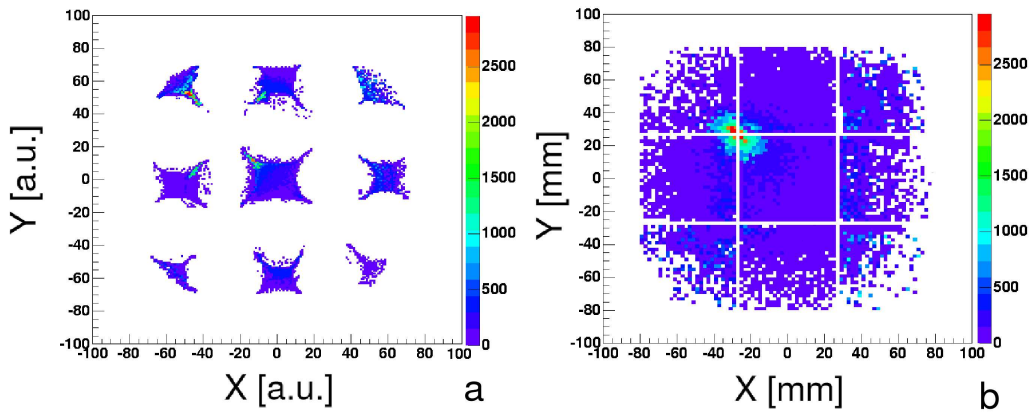

Figure 6.10: **a** - Measured position with the Si array, **b** - corrected position of the Si array.

for better reconstruction of the scattering angle of the particles outgoing from the secondary target and only few event losses, because of the noise cut-offs are registered. However, unavoidable, some (although very small) errors contribute to the reconstructed position, because of the linearization procedure.

6.1.3 Performance of CATE with Si PIPS detectors

The other type detectors used in the CATE-Si array are the Si PIPS detectors. As presented in section 3.1.2, their position resolution to α-particles is better than with the Si IPP detectors. Additionally, the resistivity of their resistive layer is bigger and thus more suitable for a measurement without deformation of the position shape. These

detectors are employed for the position detection of *i.e.* ^{86}Kr and ^{54,56,58}Cr particles. An example of their registration of ^{58}Cr particles with energy of about 100 A·MeV is given on fig.6.11.a. Using the Multi Wire detectors in the experimental setup and no secondary

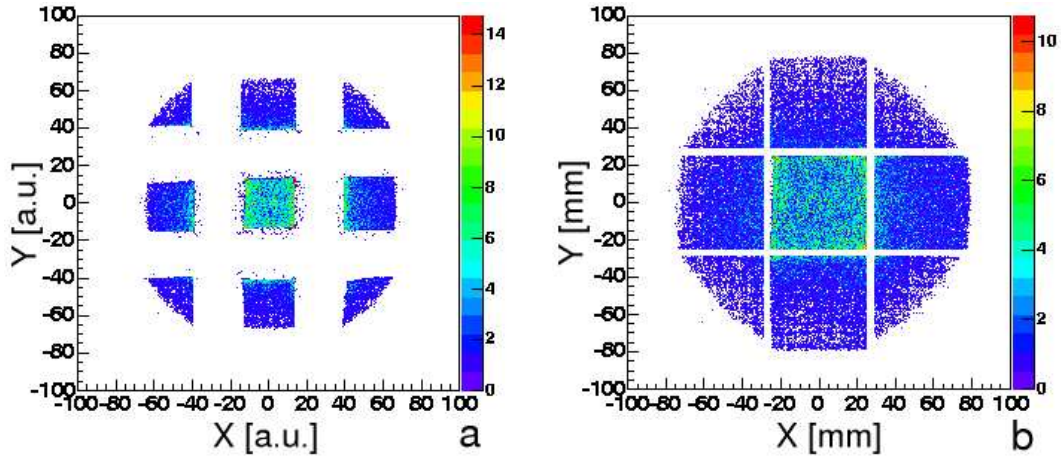

Figure 6.11: **a** - Raw and **b** - corrected position from the CATE-Si PIPS detector array.

target (see fig. 6.1), it is found that the number of particles which irradiate the detector array, is almost equal to the number of the particles registered. The surviving particles are between 88 to 90%, which is close to the geometrical efficiency of the array of 92%.

These detectors do not require linearization as the IPP detectors. In case the amplification is not the same for all four position channels from a detector, a slight tuning can be done for symmetrizing them (using eq.6.2).

Since their size is squeezed as for the IPP detectors, only correction of the type "blow" coefficients is used (see eq.6.3). The coefficients are found, as explained, by projections on x and y for every detector. The ranges that correspond to the measured size are expanded via the "*blow*" factors to the real size of (50 x 50) mm^2. As can be seen on fig.6.11.b several sporadic events exist between every two detectors. They can be avoided (since coming from chance coincidences) by requiring a software gate of the corrected (x, y) single position spectrum of ($\pm$25,$\pm$25). Note that the spectrum of the total array is created from the nine single position spectra, using their geometry in the Si array. The corrected position spectrum is plotted on fig.6.11.b with almost no event losses.

The position reconstruction of the Si-PIPS detectors is, in principle, more precise than of the Si-IPP detectors and the scattering angle of the impinging particles can be calculated with better accuracy. In general, the accuracy from both types of Si detectors in the secondary beam measurement, is of about 1-2 cm, because of the angular straggling in the secondary target (see fig.4.2). Nevertheless, it is sufficient for the correct reconstruction of the particle scattering angle. This measurement helps than for the particle-γ angular correlations with the γ-rays, registered by the Ge detectors. Since this angle is important for the event by event Doppler correction, it is checked that using that tracking with the CATE-Si, the energy resolution of the γ-spectra improve sufficiently. Another important application of the proper position measurement in the Si detectors, is the (intrinsic) position correction on the energy loss in the Si and the following downstream $CsI(Tl)$ detectors (see next chapter).

Chapter 7

The Energy measurement

In this chapter will be described the other important measurement - the energy measurement with the CATE detector. The energy loss (ΔE) detected by the Si detectors is a measure of the particle atomic number (**Z**). It is approximated with particle charge, because in the used relativistic energy regime, the ions are fully stripped. The residual energy (E_{res}) is detected by the $CsI(Tl)$ scintillators, where the ions are fully stopped. Combining the information from both energy losses the information about the particle mass (**A**) is obtained. The information, all together, is completely sufficient to identify the different ions by means of (**Z,A**).

The CATE system is utilized with a variety of ion beams, starting from ^{40}Ar up to ^{132}Xe ranging in energies from 90 up to 400 A·MeV and particle rates from $1{\cdot}10^2$ up to $5{\cdot}10^4$ Hz (pps).

In the following explanations the primary and the secondary beam measurements are distinguished because the energy measurement of the CATE detectors is strongly influenced upon the beam characteristics and conditions.
The percentage energy values used in the text are always in convention of FWHM.

7.1 Performance of CATE with primary beams

Many different primary beams as ^{40}Ar, ^{58}Ni, ^{84,86}Kr, ^{124}Xe and ^{132}Xe (Z∈[18,54], A∈[40,132]) with relativistic velocities (β) from 0.41 up to 0.75 v/c have been detected by the CATE system.

7.1.1 Beam conditions

The main sources of energy straggling and widened momentum distribution are the primary target, the wedge degrader and the secondary target because of their big thicknesses used in RISING. In the primary beam studies these materials are not used. In these cases in the experimental set-up are present only the FRS identification detectors (the ToF scintillators, the position sensitive MW counters and the charge determining MUSIC chamber). In order to estimate the effect of the secondary target, in several measurements it is inserted onto the primary beam path in front of the CATE detectors. These beams can be easily focused at the final focus and defocussed for irradiating the total size of the beam-line detectors. They have very good energy definition and small velocity spread. Therefore, their advantage is typically taken for the calibration of the FRS (see Appendix 2) and additionally for the calibration of the CATE detectors. For that purpose, usually

their particle rate is low from about 100 to about 2000 pps in order to reject the rate influence of the FRS and (as will see later) the CATE detectors.

A simulation performed with MOCADI [MOCA04] illustrates *i.e.* the primary beam size at the CATE detectors (fig.7.1.a of (x,y) (±20,±20) mm^2 (FWHM) for ^{58}Ni primary particles at 120 A·MeV. The experimental data of the extrapolated position with the two MW in the set-up is depicted on fig.7.1.b with spot size of (x,y) (±25,±25) mm^2 (FWHM). The good agreement shows that these two cases can be compared, in sense

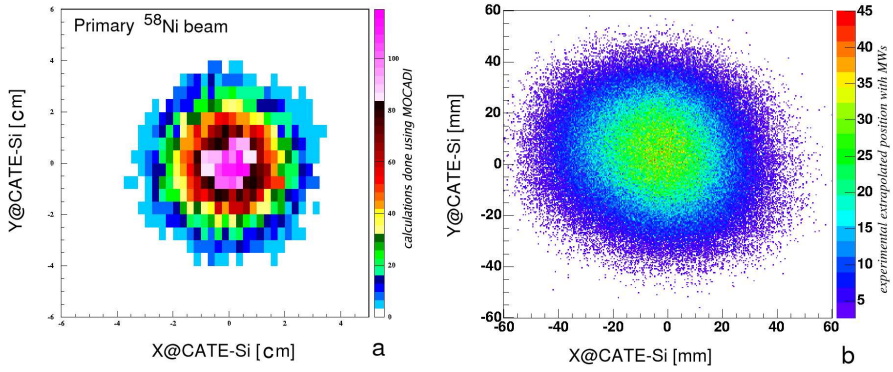

Figure 7.1: Primary ^{58}Ni beam spot at CATE: **a** - simulation with MOCADI [MOCA04], **b** - experimental data using extrapolation with two Multi Wires.

of the responding beam definitions and resolution in the CATE detectors. The good beam definition results in a narrow Time Of Flight (ToF) distribution measured with the FRS scintillators and consequently to a narrow energy definition in front of the CATE detectors. This beam quality, allows investigations of the effects that contribute to the energy measurement as: its intrinsic position dependence, ToF-velocity dependence, beam rate dependence and secondary target effect. How effectively, these effects influence are measured with CATE for various beams and energies, and is it possible to find the intrinsic energy resolutions of CATE in-beam is described in the next sections.

7.1.2 Energy resolution and effects for ^{86}Kr particles

With primary ^{86}Kr particles, which have SIS energy of 300 A·MeV and low rate of 1 kHz, investigations on the energy resolution of the CATE detectors is performed to find its intrinsic values. The good beam definition in this case accounts to a precise ToF measurement which is demonstrated on fig.7.2.a. To calculate the kinetic energy (E_{kin}), corresponding to this definition, the ToF is converted into velocity (β) using calibration measurements. Then using β, the E_{kin} is calculated (see Appendix 2). Thus the mean value of the kinetic energy at the final focus, where the CATE detectors are, is 283.1 A·MeV with resolution of only 0.34% (FWHM) (see fig.7.2.b). This energy definition, allows very precise energy measurement from the CATE array. Its $\Delta E - E$ response is measured *i.e.* with the central telescope and depicted on fig.7.2.c. The detected few scattering events, around the main distribution, are caused by losses in the materials of the experimental set-up before CATE. Since the beam is centered in a small spot, about 92% of the detected by the Multi Wires events, are detected in the CATE detectors (as much as the geometrical efficiency is) and 85% of them are, in fact, registered by the central (5) detectors. This beam position is detected by central CATE-Si detector, as

can be seen on fig. 7.2.d. In this example the position correction on the used Si detectors is not included.

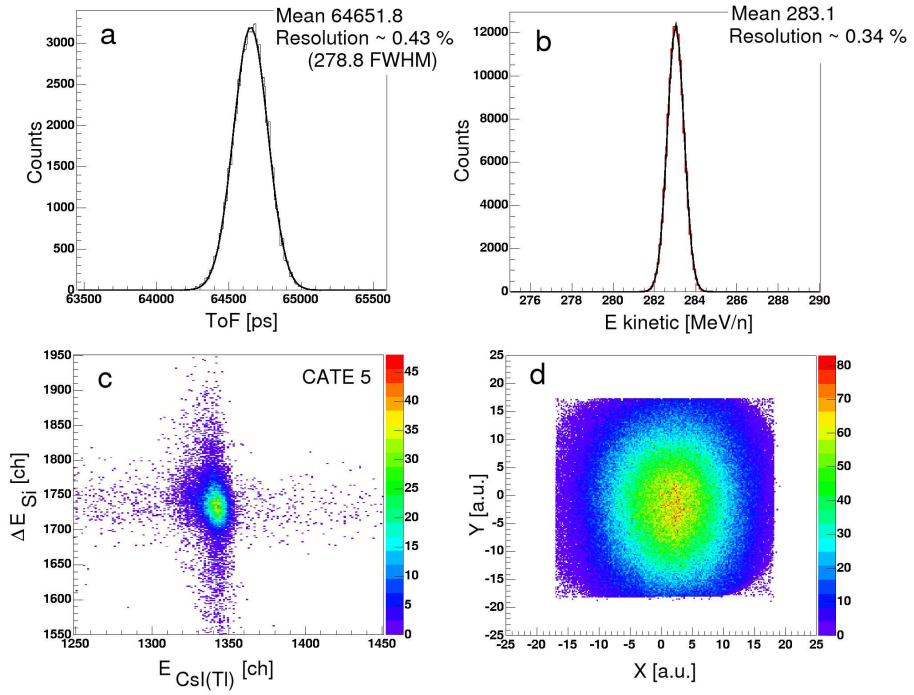

Figure 7.2: Response on ^{86}Kr primary beam: **a** - Time Of Flight, **b** - calculated kinetic energy, **c** - $\Delta E - E$ and **d** - position (x,y) from the central CATE telescope.

For these ^{86}Kr particles, the energy resolution of a CATE telescope, can be determined from raw the $\Delta E - E$ spectrum (shown on fig. 7.2.c), by projecting on the X ($CsI(Tl)$) and Y (Si) axes. The obtained energy resolution values (from the central CATE detectors) are of 2.72% for the Si (fig.7.3.a), and of 0.89% for the $CsI(Tl)$ (fig.7.3.b). Already at this point the good beam definition and the small scatterings in the beam-line materials show their impact on the resolution. However, as has been mentioned before, that are not the only effects that influence the resolution.

The position influence on the energy resolution

After applying a position cut on the corrected Si position spectrum at the central region with size of (x,y) corresponding to ($\pm$2.5,$\pm$2.5) mm^2, the energy resolution improves. It accounts to 2.25% for the Si data (fig.7.3.c) and to 0.72% for the $CsI(Tl)$ data (fig.7.3.d). From the numbers on the top and bottom graphs, is clear, that the mean values of the raw and the spectra under position condition are different. By applying position pixels (conditions) at the whole Si position distribution with the same size, it turned out, that a centroid shift is present for every position-cutted spectrum. This means, that position dependence of the ΔE and E is so pronounced that a pixelization of the detector surface of approximately ($\pm$2.5x$\pm$2.5) mm^2 is needed for maximal resolution. Further decrease of the pixel size does not help, because of the statistical uncertainty of the determined energies. In the center of the detectors a larger pixel size of ($\pm$5x$\pm$5) mm^2 might be chosen, because the corresponding energy centroids do not shift much. The correction for this position effect, will be explained in details for the example with ^{58}Ni primary beams below. Here is important to mention that the shifts in the centroids under such

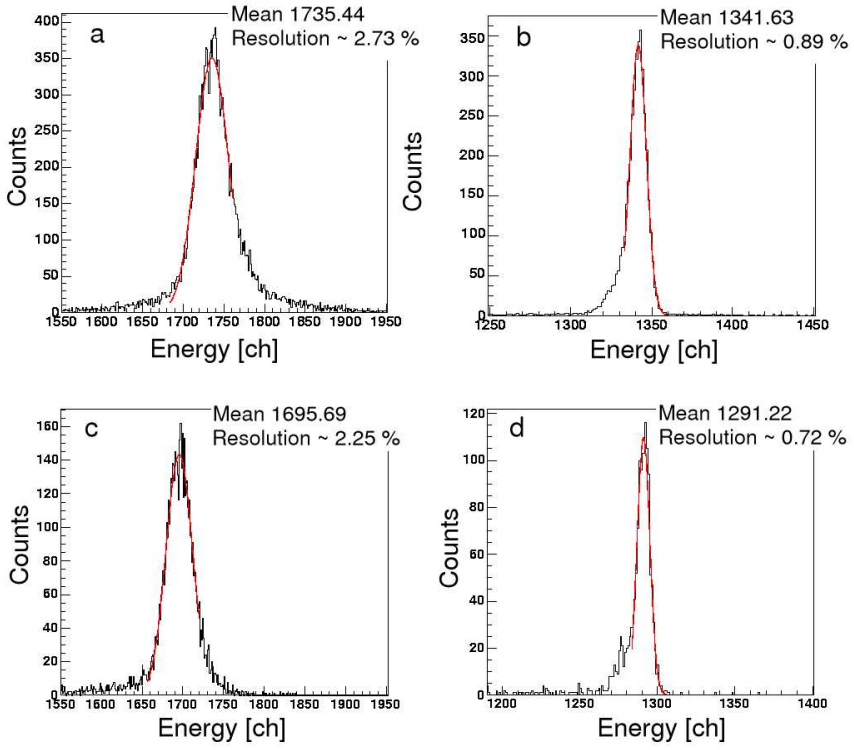

Figure 7.3: CATE spectra on primary ^{86}Kr beam with 300 A·MeV: **a** - Si raw, **b** - $CsI(Tl)$ raw, **c** - Si with position correction, **d** - $CsI(Tl)$ with position correction.

position conditions are between 0.6-1.4% for the Si single spectra and between 0.2-2.4% for the $CsI(Tl)$ single spectra. The uncertainty which contributes to these values is approximately 0.2-0.3% and comes due to the mean values determination.

The velocity distribution influence on the energy resolution

Except the position effect, although the beam definition is very precise, some small effect on the energy resolution exist due to the width of the kinetic energy distribution.

Because of the momentum acceptance of the FRS, of about 1% [FRSG04], the ToF distribution need to be determined with highest accuracy. Since this is corresponding to a velocity distribution, realistically a cut of 0.3% is chosen due to the time resolution of the S2 and S4 scintillators.

By selecting a position condition at the CATE detectors, performing a ToF cut of 0.3% and taking low intensity data set, no dependences are found on the energies of the CATE detectors. In this way is it found that the intrinsic energy resolution of the Si detectors is 2.0% and of the $CsI(Tl)$ detectors $-$ 0.7%.

In order to reproduce the real measured widths, by simulating the response of the CATE detectors in more complicated cases when primary and secondary targets are used, these intrinsic values are inserted into a simulation as the LISE code [LISE04]. Their advantage it taken for the calculation of several experimental cases with primary and secondary beams, as will be described in chapter 8.

7.1.3 Energy resolution and effects for ^{58}Ni particles

Primary ^{58}Ni beam with lower SIS energy of 215 A·MeV and no thick matter included in the beam path (as targets and degraders) helped to study the response of the CATE detectors (where the beam energy is around 162 A·MeV). These data are used to find out what influences the energy resolution, how it can be corrected methodically and is it possible to determine the intrinsic values obtained with ^{86}Kr particles.

Further the detailed analysis of these effects and methods for their correction are given for the central CATE detectors (5), which are a good example for all the rest detectors in the arrays.

The detector's nature connected effect - position influence on the energy resolution

If and how the energy response of the Si and $CsI(Tl)$ is deteriorated because of **position dependence** is investigated when particles, selected by their impinging position, irradiate the detectors. After the linearization procedure (described in 6.1.2) on the position of the Si, several polygons (maps) are performed, to cut some parts of this distribution. Such examples, are depicted in different colors on fig.7.4.a. The corresponding single energy spectra (in channels) from the Si are shown on fig.7.4.b and for the $CsI(Tl)$ on fig.7.4.c in logarithmic scales. Obviously, the spectra produced under the position maps have different mean channel values and different widths, depicted with the same colors as the position cuts on the Si - two dimensional distribution. As turned out in the previous

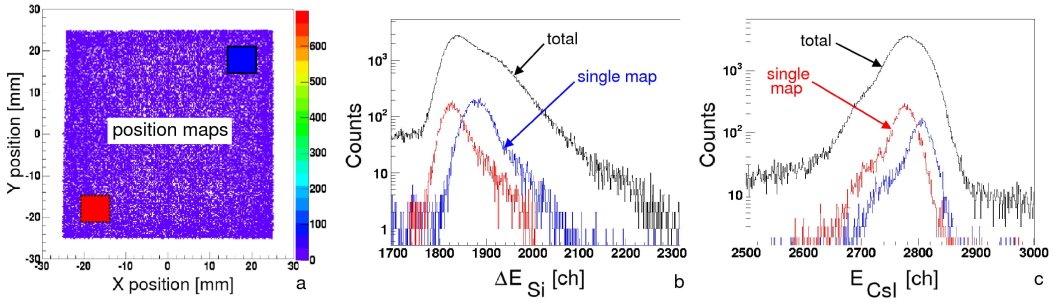

Figure 7.4: Primary ^{58}Ni particles with 130 A·MeV: **a** - Position maps on the Si central detector, **b** - Si raw (black) and map (color code of the map) spectra, **c** - CsI(Tl) raw (black) and map (color code of the map) spectra.

investigations, this effect seems to be severe. All single distributions contribute to the width of the total spectrum from the Si (or the $CsI(Tl)$), depicted as an envelope curve (in black). It is produced when the segmentation of the whole detector is taken into account. To avoid the peak shifts of the single spectra, which deteriorate the energy resolution of a CATE detector a correction is needed. It has to be done prior to any other corrections because it accounts for an effect connected to nature of the detectors themselves. To add in addition a quantitative impression about the effect, the next figure (7.5) is demonstrated. From the projections at the CATE-Si and -$CsI(Tl)$ *i.e.* is visible, that the raw (without any position map) spectra have an energy resolution between 2.8 and 3.4% for the Si and between 1.9 and 2.4% for the $CsI(Tl)$ (fig.7.5.a,b). The earlier investigations of this effect are used here, for the selection of the optimal position map's size. Also in this example the dependance is visibly pronounced when the size accounts to ±2.5 or to ±3 mm in each direction. After applying position maps, covering the total

Si detector, with sizes of (3 x 3) mm^2, the single projections for one such map (close to the central position) on the Si and the $CsI(Tl)$ are demonstrated (see fig.7.5.c,d). These single spectra have resolution between 2.0 and 2.4% for the Si and between 1.2 and 1.4% for the $CsI(Tl)$. The improvement appears, because the position effect is avoided by selecting a small region.

To **correct** the total spectra, all these single one dimensional spectra are stored, and fitted one by one, using a user routine based on ROOT [ROOT04] and Go4 [Go4G04] libraries and functions. The fitting is done for both type of distributions (Si and $CsI(Tl)$), with multiple Gauss fits, with adjustable widths, after a background subtraction from a line fit. This part makes the position correction a slow process, which takes certain com-

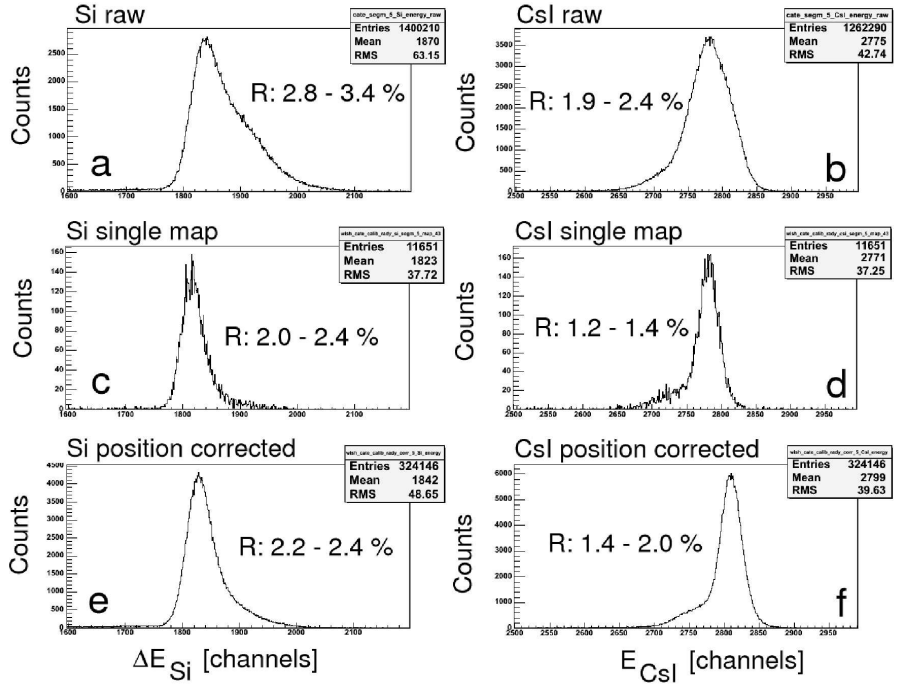

Figure 7.5: Energy resolution of the central CATE detectors with primary ^{58}Ni particles: **a** - Si total raw spectrum, **a** - $CsI(Tl)$ total raw spectrum; **c** - Si single spectrum under position cut, **d** - $CsI(Tl)$ single spectrum under position cut; **e** - Si total corrected for the position dependence spectrum, **f** - $CsI(Tl)$ total corrected for the position dependence spectrum.

puting time of several hours for the fit 81 Si and 81 $CsI(Tl)$ spectra, and nine times more to prepare the same mean values for the total CATE array of nine Si and nine $CsI(Tl)$ detectors. After fitting, the mean values are stored in arrays for the Si and $CsI(Tl)$. The alignment is done with respect to one central map, which is different for every separate detector, but is close or directly is at its center. To align every spectrum from each separate detector (from both arrays), the differences from the central map (mean value) to every other map (mean value) are calculated. The differences (called "delta shifts"), are actually the offset values from the center. They are stored in arrays of elements and typically numbered as the corresponding maps. To correct the total spectra of a pair (the example here is for the central one) of Si and $CsI(Tl)$ detectors, the two arrays with correction factors are read in the user analysis. Event by event they correct (by adding) the centroid values for the single spectra produced under a single map condition. Afterwards, all Si spectra are summed up in a total spectrum, which is already position corrected. Correspondingly, the same procedure is done for all single $CsI(Tl)$ spectra, in order to

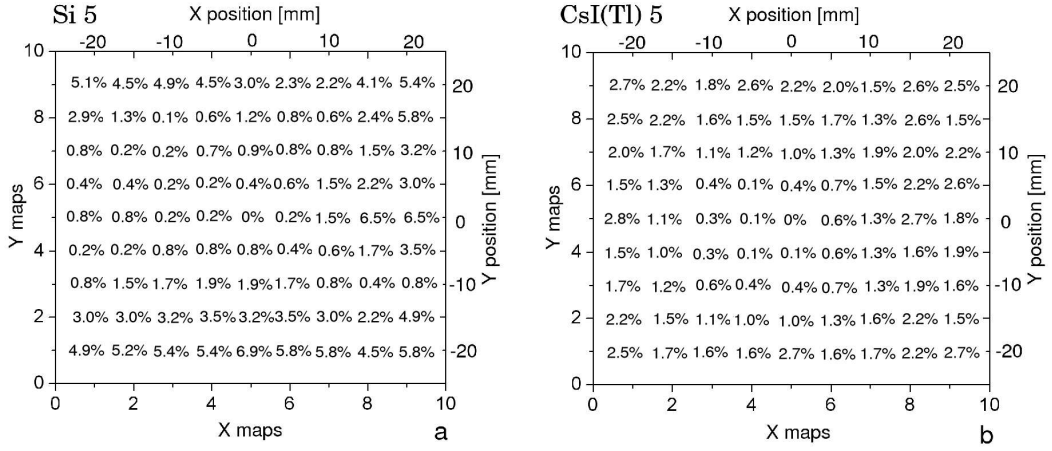

Figure 7.6: Position maps for primary ^{58}Ni particles on the Si central detector. The numbers inside correspond to the shifts from the central map in channels for a **a** - Si detector, **b** - $CsI(Tl)$ detector.

create the total corrected spectrum. As an illustration, the corrected spectra, from the central Si and $CsI(Tl)$ are shown on fig.7.5.e,f. Because of the statistic errors they are slightly wider, than the single projections. However, the improvement is excellent and corresponds to an energy resolution of 2.0 to 2.4% for the Si and 1.4 to 2.0% for the $CsI(Tl)$.
The "delta shifts" from the center (in channels) are converted in a percentage difference from the center. As an illustration, they are displayed, corresponding to the map location in fig.7.6.a,b for the Si and $CsI(Tl)$ detectors, respectively. It is visible that their values do not follow any simple functional, and have to be determined and corrected always separately. Besides this, they differ for secondary beam particles what makes their prediction very difficult.

The beam connected effect - velocity influence on the energy resolution

The identification of the FRS detectors for the primary ^{58}Ni particles is depicted on fig.7.7.a. It is visible that small scatterings from other isotopes and charge states (because of the low energy) are produced by the interaction with the the plastic scintillator at the middle focus or/and the MW before the ionization chamber (where the particle charge Z is detected). They are avoided, with the help of a cut on the identification spectrum, as shown on the figure. The ToF spectrum (on fig.7.7.b) represents the **beam definition** and has width in ps, which corresponds to 0.8% (FWHM). Note that, even without matter it is almost twice worse than the definition with the ^{86}Kr particles due to the lowered energy. Thus it corresponds to an energy distribution at the final focus with the same width. The last is calculated by including the energy loss in the matter of the final focus detectors. As will be shown below, for the secondary ^{58}Cr particles, whose corresponding energy, at the CATE detectors, is almost twice wider of about 1.4% (FWHM). The particle velocities β calculated from the measured ToF and β calculated from the Bρ have corresponding widths of 0.15% and 0.11%, respectively (see Appendix 2).

To inspect the effect of these beam conditions on the CATE detectors, the correlations of the Si energy and ToF (fig.7.7.c) and the $CsI(Tl)$ energy and ToF (fig.7.7.d) are plotted. As can be seen, the ToF (or β) **influences the energies** via certain angular tilting. The

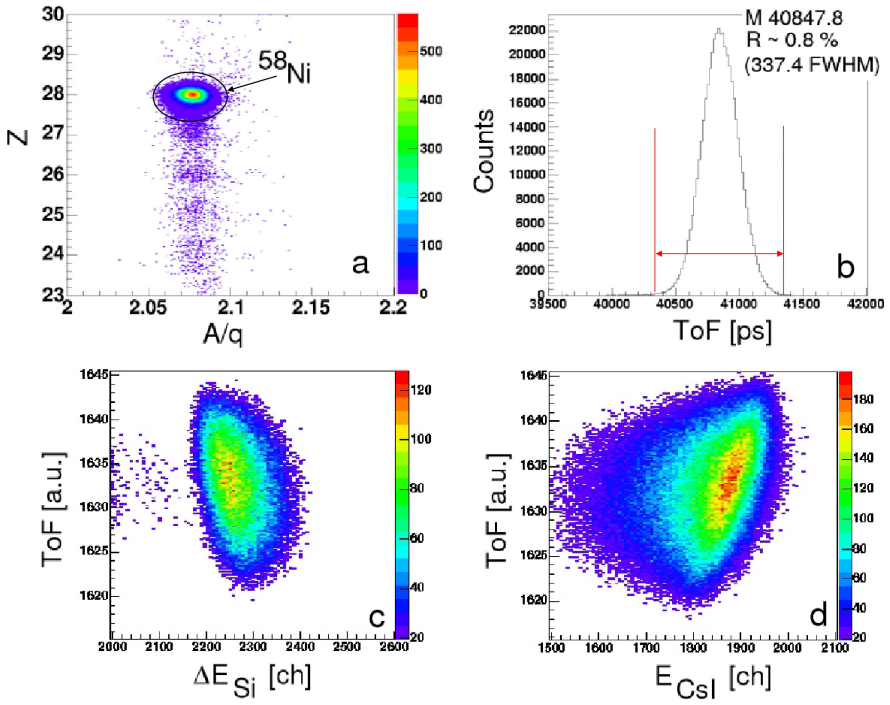

Figure 7.7: Primary ^{58}Ni particles with 130 A·MeV: **a** - $A/Q - Z$ identification from the FRS, **b** - ToF spectrum, **c** - ToF dependance on the Si-ΔE, **d** - ToF dependance on the $CsI(Tl)$-E.

dependance is less pronounced for the Si detector and much stronger for the scintillator, because of the bigger amount of deposited energy. On account of the energy definition width of the incoming beam, some particles arrive at the tail of this distribution, apart from the centroid.

In order to get the precise energy resolution from the CATE detectors this dependence has to be corrected. The method will be explained and compared with secondary ^{55}Ni particles in section 7.2.3. At this stage, in order to avoid its influence on the energy, a ToF cut, corresponding 0.3% of its width is performed. Together with the position correction it accounts to energy resolution from the CATE detectors to 2.2% for the Si and 1.2% for the $CsI(Tl)$. For beam definition cut of 0.1% these values account to the obtained intrinsic resolution values with ^{86}Kr particles of 2.0% for the Si and 0.7% for the $CsI(Tl)$.

7.2 Performance of CATE with secondary beams

Many different secondary beams as ^{54,56,58}Cr, ^{55}Ni, ^{55}Co, ^{68}Ni and ^{108,112}Sn (Z∈[24,50], A∈[54,112]) with relativistic velocities (β) from 0.41 up to 0.75 v/c have been detected by the CATE telescope.

7.2.1 Beam conditions

The beam conditions using these secondary beams are in principle similar, and can be generalized as follows: relativistic primary SIS energies between 400-750 A·MeV with high particle rate up to 5x10^8 pps are used for the fragmentation production of nuclei from thick ^{9}Be primary targets (2.5-4.0 g/cm^2) in front of the FRS. Combination of thick Al

degraders at the first and the middle focus (1.0-6.3 g/cm^2) are used for slowing down the ion velocities and for the achromatic separation of the desired ones (see section 4.1). Widen in momentum, because of the energy straggling and the momentum acceptance of the FRS, in ToF or energy, between 0.8 and 1.4% (and in some extreme cases up to 2.4%), the ions enter the final focus with the FRS identification detectors with energies between 120-420 A·MeV and with particle rate up to 5x10^4 pps. Fully identified by means of Z and A (see section 4.1) the ions impinge on the secondary target, placed at the final focus. The secondary targets used, are either ^{197}Au of 1 or 2 g/cm^2 or ^{9}Be of 0.4 or 0.7 g/cm^2. Depending on the experimental purpose the ions undergo Coulomb excitation (Coulex) and/or fragmentation, including knockout of only few nucleons, with energies between 100 and 400 A·MeV. These secondary reactions widen the particle momentum even more, and reach energy width between 2% up to 4-5%, especially in the fragmentation reactions.

7.2.2 The reaction mechanism

The reason for the particle momentum widening is the fragmentation reaction mechanism. This effect is described in the past by Goldhaber [Gold74] as momentum broadening because of the abrasion of nucleons, which can reach several A·MeV. This type of parameterization by the mass number of the fragment explains the fragment momentum distributions measured in relativistic heavy-ion collisions. They are typically observed to be Gaussian shaped where the center of the distribution corresponds to the projectile velocity. Later investigations and parametrizations appeared from Morissey [Mori89] and de Joung [Jong97], which further expanded the components of the particle momentum and velocity. Tarasov [Tara04] added experimental parameters from low energy data and created the "Universal parametrization". It reproduces an energy distribution, which does not follow a regular shape but has an asymmetric tail to lower energy. In this parametrization, several features are better described like anomalously lower values of the reduced Fermi momentum at lower energies, or differences in widths, associated with nuclides of the same mass, together with the reduction of the velocity between fragment and projectile at low energies, found together with the exponential tail in the fragment momentum distributions in reactions at low energies [Tara04]. Furthermore, the shape depend of the mass number and the beam conditions, something that is observed in the CATE analysis as well (see section 9.4.2). Important note here is that the contribution from this effect can not be corrected in the experiment.

7.2.3 Effects and corrections

During the RISING experiments, already in the primary beam studies, as shown in the previous section, it turned out that the energy measurement is influenced by several effects connected to: (i) the intrinsic detector dependence on the impinging particle position,(ii) the beam velocity and (iii) particle rate. To get the precise beam velocity, additionally its position dependence at the middle and final focuses needs to be corrected. To obtain the rate dependence, the spill structure influence need also to be studied. Additionally, because of the set-up matter and the thick secondary targets the energy straggling is also taken into account. All these effects, are strongly pronounced in case of the secondary beams, therefore corrections are performed in order to improve the energy resolution to its intrinsic values.

- The position correction

The detector-connected position effect has been described above for the ^{58}Ni particles (see section 7.1.3). This effect is pronounced also with secondary particles. Because of the statistical uncertainty in the measurement, the values differ from those for primary particles. Therefore, they have to be determined and corrected in every separate measurement.

The position maps are determined in the same way as in the primary beam case. Comparing the influence on the energy resolution of CATE, shows that improvements of the relative energy resolution values appear, from 4.5-6.0% to 2.5-3.5% for the Si and from 6.1-8.4% to 3.5-5.6% for the $CsI(Tl)$.

- The beam velocity position correction

A dependence that has to be corrected also for secondary particles, is the angular dependence of the particle position, described in Appendix 2. Because of the different trajectories that the particle might follow (see fig.11.9 from Appendix 2) they exit at the final ficus at different positions. Thus they change their energy and accordingly affect the beam definition width. Hereafter an example for the corrections performed at the middle and the final focus are given. The correlation between the calculated velocity β from the experimental ToF and the position at the middle focus, measured by the first ToF scintillator is shown on fig.7.8.a. For the correction of the angle the algorithm described in section 3.3 (see fig.3.23) is used. As can be seen from the fig.7.8 the rotational angle is small (equals to 0.005707 degrees), but nevertheless, brings improvements of the measured velocity as presented on fig.7.8.b. After the correction at the middle focus,

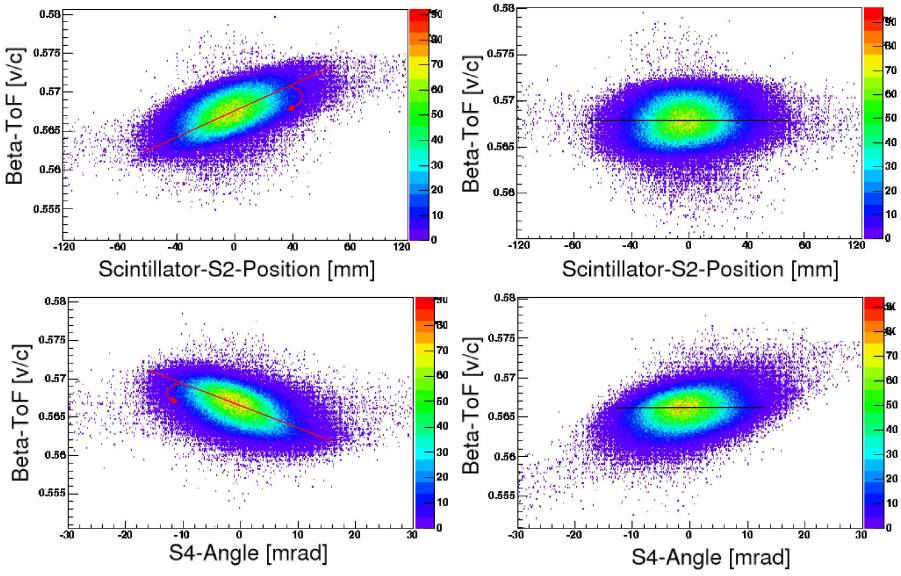

Figure 7.8: Correction of the particle position for ^{55}Ni fragments: **a** - raw dependence at the middle focus, **b** - corrected dependence at the middle focus; **c** - raw dependence at the final focus, **d** - corrected dependence at the final focus;

the newly corrected velocity is used for another correlation at the final focus with the particle S4 angle (see fig.7.8.c). This angle is extracted from the FRS tracking detectors (for position determination), as explained in Appendix 2. The correction is performed on the velocity by rotation on angle (here accounts to 0.00788 degrees). The rotational directions in both correlations, are depicted on the figure with arrows. The corrected velocity-ToF distribution improves after these corrections from 1.2% to 0.9%.

- The ToF correction

After the above correction, the velocity is correlated with the energies of the CATE detectors. As mentioned for primary beams, the velocity-ToF dependence, is the most severe beam dependent effect on the energy resolution. This dependence, as already shown fig.7.7.c,d, is strongly pronounced for the secondary beams in means of angle. The angles for the different fragment charges vary with $\leq 0.1\%$ and for simplicity in the correction a common angle is used for all. This is the angle for the main distribution and it is determined to be 10.052 degrees for the Si and 13.499 degrees for the $CsI(Tl)$. The tilting angle in the correlation with the $CsI(Tl)$ energy, is *i.e.* shown on fig.7.9.a. The projection on the x-axis, which in this case is the energy of the $CsI(Tl)$ is drawn on fig.7.9.b. When the rotational correction is performed (fig.7.9.c), the energy resolution improves from 4.8% to 2.6% (fig.7.9.d). This improved value is than the resolution, with which the detector responds to the different masses.

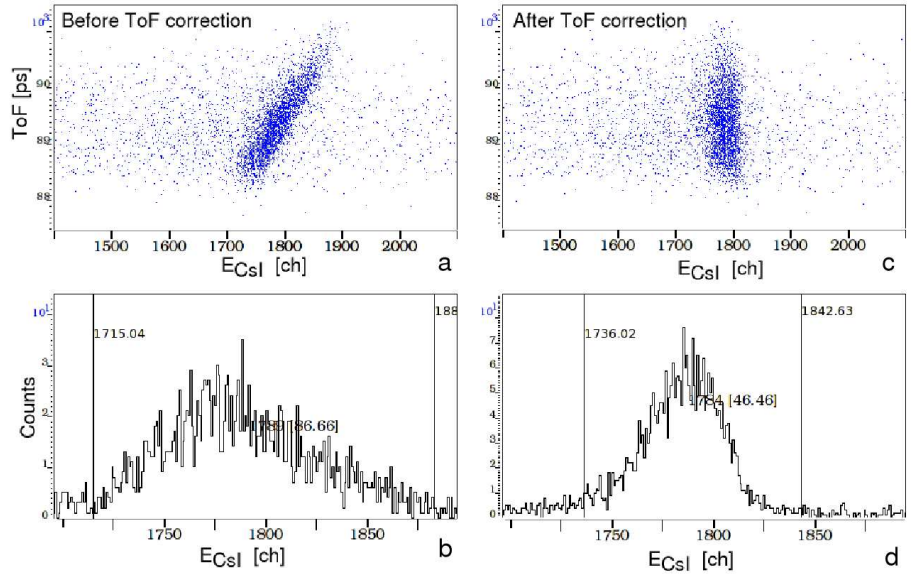

Figure 7.9: **a** - β-ToF correlation with the $CsI(Tl)$ energy, **b** - projection on the $CsI(Tl)$ energy, **c** - correction of the β-ToF dependence, **d** - projection on the corrected $CsI(Tl)$ energy.

- The rate dependence

If the used data set, has high particle rate it influences also the energy of the CATE detectors. The detectors that are strongly influenced are the Si semiconductors. The rate dependence is pronounced as a gain shift of the mean energy peak towards lower energies (see fig.7.10.a), when the particle rate exceeds 10^4 pps. This appears because of the increase of the leakage current and consequently the decrease of the effective high voltage, applied on the resistive layer with constant resistance (see section 3.1.6). When many particles interact and create charge carrier, their collection becomes incomplete, because the detector can not react to all of them. Since in result, the signal pulse decreases its gain, the semiconductors are slightly over-biased. This can avoid the influence of the variating effective high voltage to effect the detector amplitude. However, this is not always sufficient and correction is needed. The $CsI(Tl)$'s are more stable on the particle rate, because of the gain stability of the readout (photo) diode (fig.7.10.b). Rarely, when affected by the high rate, the readout of the detector (semiconductor type) can also cause

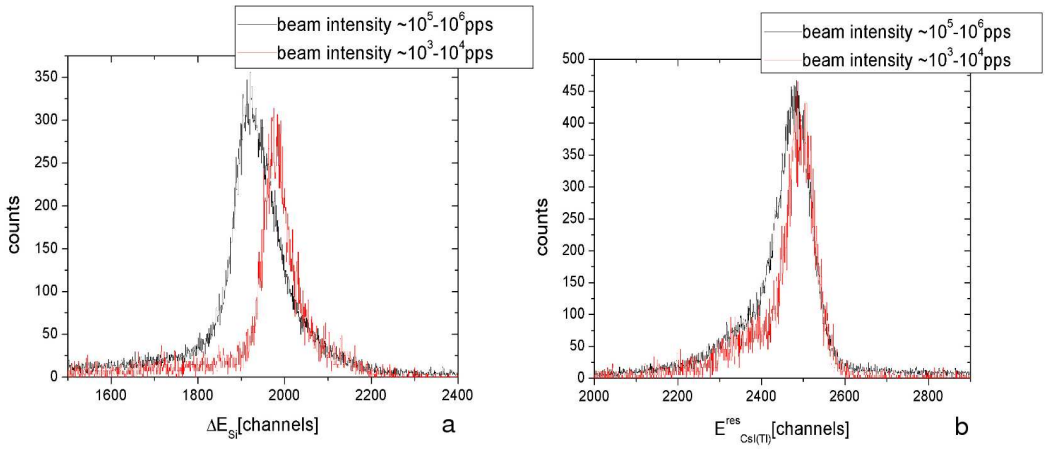

Figure 7.10: Particle rate dependence on **a** - Si detector, **b** - $CsI(Tl)$ detector with ^{108}Sn beam.

gain variations, and be observed as an amplitude shift. The mean values of these gain shifts have to be corrected depending on the time of irradiation. In long data sets form ($i.e.$. several days of irradiation), where the rate might increase and decrease, a table of the mean values with the corresponding time can be created within the software. This should be used than in the offline sorting, as a time dependent gain correction.

In case the particle rate is not very high, the rate effect can be determined after multiplications by factors from the absolute energy calibration and afterwards the linearization of the $\Delta E - E$ signals.

In the following example (for ^{55}Ni fragments), a particle identification function (PI) is calculated from the energy loss in the Si (central) detector. The sum of the energies from the Si and the $CsI(Tl)$ after the energy calibration represents the total energy (E_{tot}). The variation (in MeV), depending on the irradiation time, is shown in fig.7.11, for a data set of 42 hours. The stored (about 18 Gb of) data are divided into 20 sets, each with time length of 2.1 hours. As can be seen, there is a variation around the first measured point (the dotted line). Therefore, shift factors are introduced to return the next data points to the first one, depending on the time.

- The spill structure

The other connected with the high particle rate effect, is the spill structure. During an experiment it might become "spiky", because of the big amount of particles, coming at the same time. This causes pile-ups not only to the FRS and Ge detectors, but also at CATE. Typically, this structure is revised by the logical signals from the ToF scintillators in time periods of 20 ns, 200 ns (or 100 ns) and 1.3 μs (or 3 μs) due the RISING runs. They are readout in the software and can be rejected in the analysis.

The pile-up of particles is registered at the CATE detectors already on electronics level, as pulse pile-up (see fig.**??**), and is observed in the histograms as a long correlated tail of Si and $CsI(Tl)$ to higher channels. In principle these pulses are rejected and consequently the detector signals cleaned within the software. An example of the pile-up tail is given on fig.7.12.a. The good events which are used in the analysis are determined after the its rejection on fig.7.12.b.

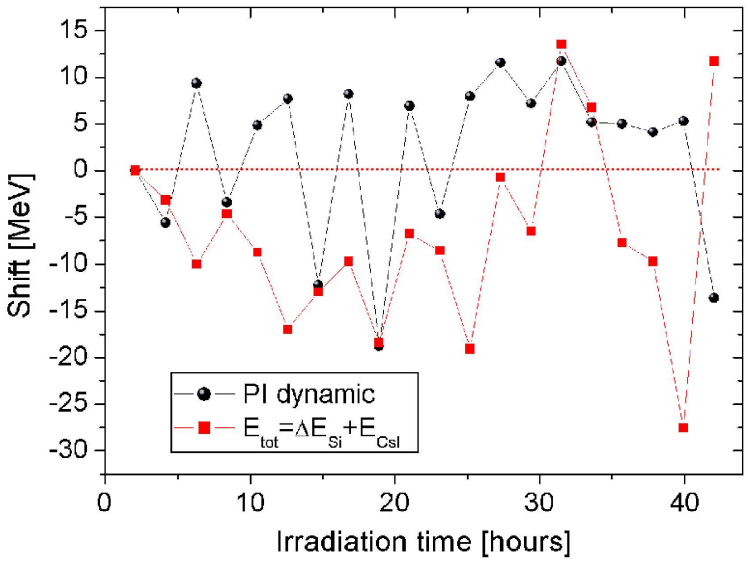

Figure 7.11: The gain shift of the CATE energies cause shifts in the determination of the particle identification and the total energy.

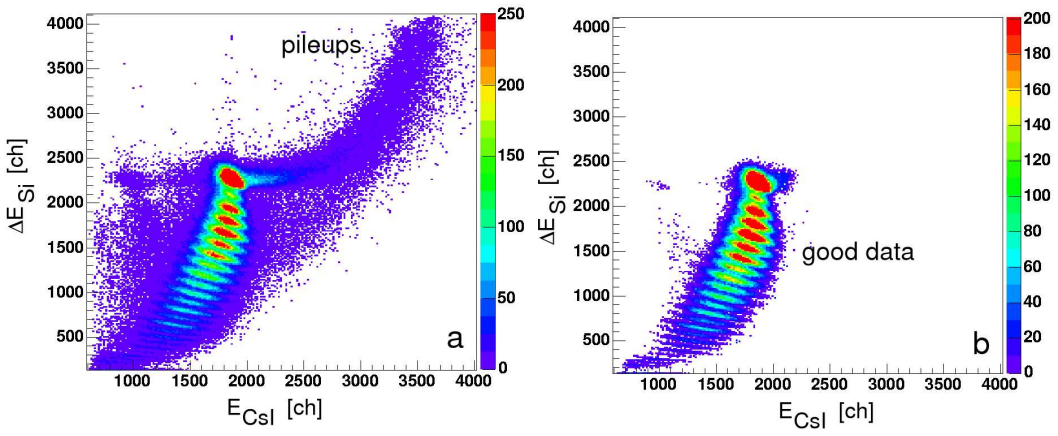

Figure 7.12: ^{55}Ni fragments: **a** - pileup of CATE, **b** - rejected pileup.

- The consequence of the irradiation / dose

A consequence of the irradiation by particles and its effect, is the dose of the detectors. It is examined for CATE after each run with heavy ions. The dose is more important for the *Si* semiconductors, which as shown in section 3.1.5 have a lifetime, depending on the dose. Often the high amount of particles destroy a part of the crystal lattice and cause the creation of local pockets. These formations register much slowly the impinging particle or do not register it at all, acting as a dead zone. Consciously, this effect is limited to certain amount of irradiation by these heavy particles and can be reached faster in case of high rate and pileups in the spill structure. In the previous chapters, was already mentioned that the *Si* detectors have been exchanged, due to their instability of pulse caused by the high irradiation and consequently increased leakage current. However, in none of these cases the detectors reached their lifetime. The particle rate at the CATE detectors and their leakage current is monitored during the RISING runs. The rates are monitored at the central *Si* and central *CsI(Tl)*, and the OR of all *Si* and

all $CsI(Tl)$ (as described in section 5.3). The mean ratio between the total amount of particles irradiating all Si detectors, with respect to the central detector, is determined to be about 0.87. The same is valid for the central $CsI(Tl)$, but since all of them are biased together only the total leakage current of the readout diode can be examined. From the time of irradiation (in seconds) and the rate of the particles (per second) the dose can be determined. On the example shown in fig.7.13.a the Si (IPP type detector) dose is estimated from the experimental notes with the ratio coefficient mentioned. Many

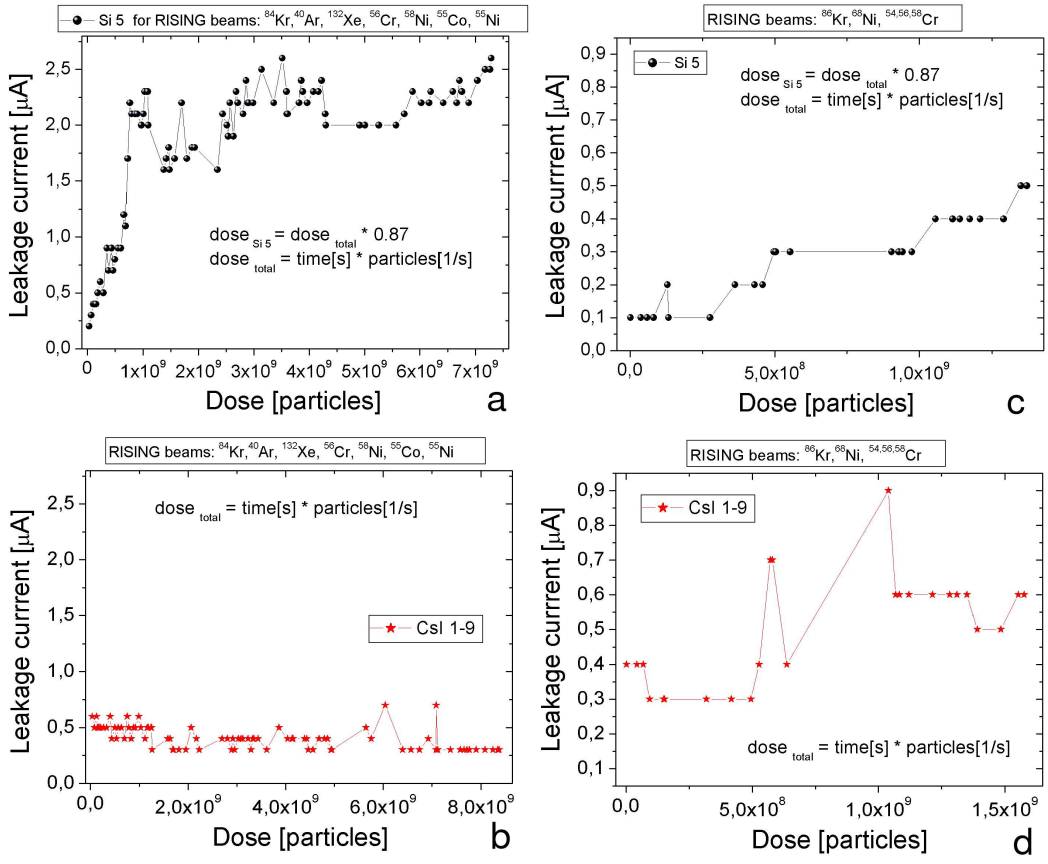

Figure 7.13: **a** - Si-IPP leakage current increase depending on its dose; **b** - comparison with the leakage current and total dose of all $CsI(Tl)$ detectors; **b** - Si-PIPS leakage current increase depending on its dose; **d** - comparison with the leakage current and total dose of all $CsI(Tl)$ detectors.

different beams with various energies and beam rates caused the behavior that is depicted. In comparison the leakage current for the total $CsI(Tl)$ stays stable during the these long runs of irradiation. In both cases, the local minima come from the decreasing of the particle rate, or beam stop, which helps the restore of the detectors. After the exchange with the Si PIPS type, the irradiation, caused by different beams, revealed a similar dose estimation as depicted on fig.7.13.c. Its comparison with all $CsI(Tl)$ in the same scale is shown in fig.7.13.d. Obviously, the behavior of these Si detectors is more stable than in the IPP case, although the estimated doses are comparable. The main reason for that is the improved spill structure of the beam, that is monitored and rejected during the runs.

- The secondary target effect

The secondary beam definition is much worse, than that of a primary beam, and in the final focus it is further widened by the straggling in the identification detectors and in

the secondary target. This widening is different for the two different reaction types at the secondary target. In case of the Coulex reactions, it appears because of the thick targets and in the fragmentation reactions because of the nucleon removals, which change their angular directions inside the target. A schematic representation of the beam widths widening is presented on fig.7.14.a. The energy response of *i.e.* the CATE-$CsI(Tl)$ to a

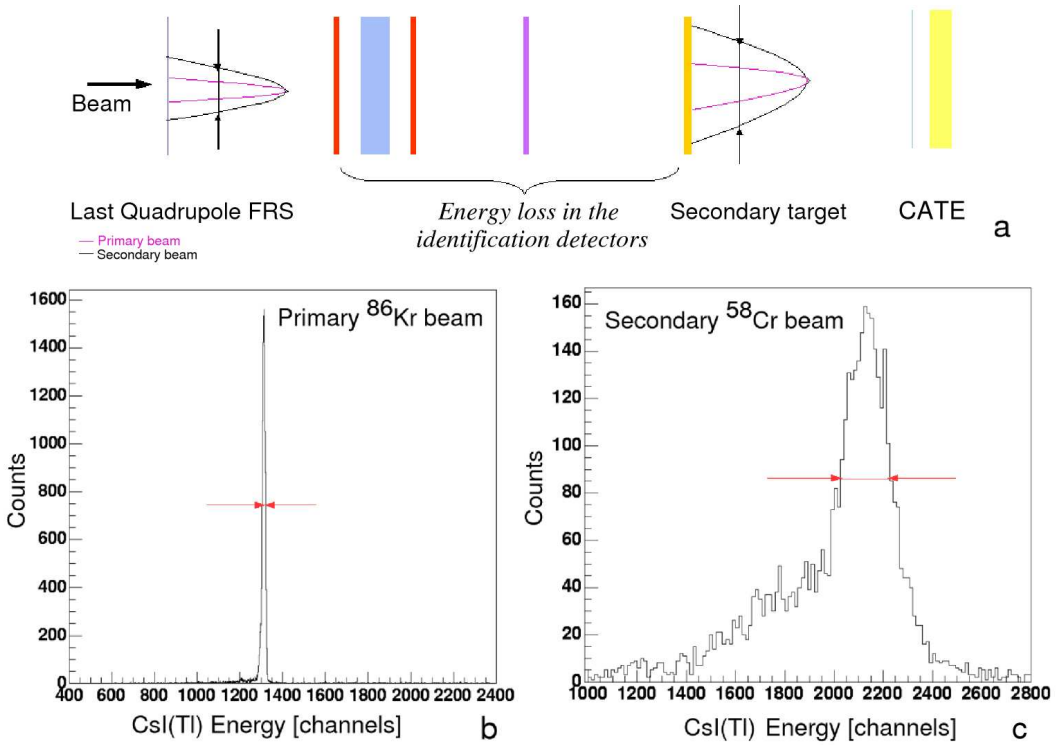

Figure 7.14: **a** - Schematic representation of the beam distribution width for primary (violet) and secondary (black) particles at the final focus S4. **b** - Energy distribution of primary ^{86}Kr particles, detected by $CsI(Tl)$ and **c** - energy distribution of secondary ^{58}Cr particles, detected by $CsI(Tl)$.

primary beam (fig.7.14.b) is much wider not only because of the beam definition but also because of the reactions of the secondary particles as shown on fig.7.14.c. In principle the target effect can be corrected when the exact energy loss of the particles is calculated and corrected (event by event) for an angular dependence with the CATE Si and $CsI(Tl)$ detectors.

The target effect is severe for a thick target as 1 g/cm^2 of ^{197}Au and hereafter an example for the Coulex of the ^{58}Cr ions is described. For the estimation of the effect the energies at the CATE detectors are calculated (event by event) in the following way.
A polynomial function is constructed for the energy at the final focus ($E_{@S4}$) and the energy at the CATE detectors ($E_{@CATE}$). The energy at the final focus is calculated from both velocities in the measurement: the velocity β taken from the magnet $B\rho$ ($\beta_{B\rho}$) and the velocity β taken from the ToF measurement (β_{ToF}): $\beta=\sqrt{\beta_{B\rho}\cdot\beta_{ToF}}$, using $E_{@S4}$=931.5$\cdot((1/\sqrt{1-\beta^2})-1))\cdot A$, where A is the mass of the incoming particles (in this case 58) (that gives the energy in MeV). Several calculations are performed with ATIMA for various energies $E_{@S4}$, whose range surround the energy during the measurement (have *i.e.* corresponding velocities $\beta\in$[0.48,0.70]). By including the matter from the detectors at the final focus, the secondary target and the Si detector, three different functions

are constructed: dE_1 including the energy loss in all tracking detectors at S4 (MW, ToF-scintillator and MUSIC), dE_2 including the energy loss in the secondary target and dE_3 including the energy loss in the Si detector like $dE \approx (Parameter(Z), Z^2, \beta^2)$. To construct them the Bethe [Beth33, Beth36, Beth37] parametrization is used:

$$-\frac{dE}{dx} = \frac{4\pi e^4 Z_p^2}{A_t v_p^2} \cdot N_t Z_t (ln(\frac{2A_t v_p^2}{I_t}) - ln(1-\beta_p^2) - \beta_p^2)$$

where Z_t, A_t, N_t and I_t are the target connected charge, mass, number density and ionization potential, respectively, v_p, Z_p and β_p are the particle connected velocity, charge and relative velocity (β=v/c), respectively, and the rest are constants. The energy losses ($dE_{1,2,3}$) as a function of the relative particle velocity β can than be written as:

$$dE_{1,2,3} \approx P_1 \cdot \frac{Z_p^2}{\beta^2} \cdot ln(C_1 \cdot \beta^2) - C_2 \cdot ln(1-\beta^2) - C_3 \cdot \beta^2$$

where Z_p (or just Z) is the particle charge (here equals to 24), P_1 is the parameter that will vary for the different functions in respect to the energy loss, representing the mass (A) dependence, and the constants $C_{1,2,3}$ will be fixed for every function. Constructing the first function dE_1 = $E_{@S4}$ - $E_{@TA-S4}$, the constants $C_{1,2,3}$ are fixed to: 7.05e15; 1; 1, respectively (see fig.7.15.a). The parameter P_1 for this function is determined than for the smallest χ^2 (equals to 152.6) to be 0.02397 (± 6.0e-5). The second function representing the energy loss in the target dE_2 = $E_{@TA-S4}$ - $E_{@CATE-Si}$ undergo variations until the best constants $C_{1,2,3}$ are chosen to be: 3.28349; 0.9155; 1, respectively (see fig.7.15.b). The parameter P_1 for this function is is determined than for the smallest χ^2 (equals to 909.6) to be -1.36375 (± 7.26e-3). Note that, up to this point the energy loss can be used for the correlation with the Si detectors. The third function representing the energy loss in Si dE_3 = $E_{@CATE-Si}$ - $E_{@CATE-CsI}$, also vary until the best constants $C_{1,2,3}$ are found to be: 9.49394; -2.43383; 6.59076, respectively (see fig.7.15.c). The parameter P_1 for this function is is determined than for the smallest χ^2 (equals to 52.7) to be -1.77304 (± 16.34e-3). In principle the parameter P_1 is Z dependent and has to be examined in advance before implementing it in the dE functions for various Z (around the measured one). The dependence of the parameter P_1 for dE_2 and P_1 for dE_3 as functions of the particle β are depicted on fig.7.15.d,e, respectively. These functions are fitted with second order polynoms, which can than be used in the calculation functions for the dE_2, dE_3 if the precision is required. The implementation in the user code for the event by event calculation is than done via the the following chain: As mentioned, $E_{@S4}$ is calculated from β. This β is used as β_1 in the calculation of the first energy loss dE_1, using the above functions with its P_1 and constants:

$$E_{@S4}(\beta_1) - dE_1(\beta_1) = E_{@TA-S4}(\beta_2),$$

therefrom β_2 is calculated using:

$$\beta_2 = 1 - 931.5/(E_{@TA-S4} + 931.5)^2.$$

This β_2 is used than for the second function dE_2, with its P_1 and constants:

$$E_{@TA-S4}(\beta_2) - dE_2(\beta_2) = E_{@CATE-Si}(\beta_3),$$

where-from β_3 is calculated using:

$$\beta_3 = 1 - 931.5/(E_{@CATE-Si} + 931.5)^2.$$

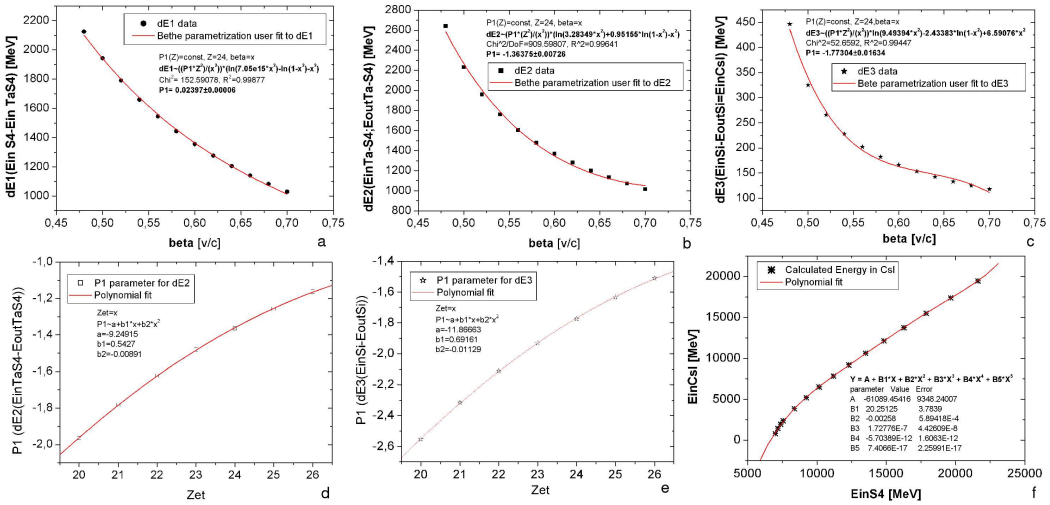

Figure 7.15: Bethe parametrization of the energy loss in the final focus with three different functions: **a** - dE_1, **b** - dE_2, **c** - dE_3. Parameter P_1 dependence on the particle charge Z for **d** - dE_2 and **e** - dE_3. **f** - Total energy loss calculation in the final focus with one function.

This β_3 is used than for the third function dE_3, with its P_1 and constants:

$$E_{CATE-Si}(\beta_3) - dE_3(\beta_3) = E_{@CATE-CsI}(\beta_4),$$

$E_{@CATE-CsI}$ is the energy at the $CsI(Tl)$ with corresponding velocity β_4. It can now be correlated with the measured energy. The same is valid for dE_3, which is the energy loss in the Si and can be correlated with its measured energy. The correlations look in the same way as the β-ToF correlations with the CATE energies. Fitting these two dimensional distribution gives than the corresponding angles, of the required rotational correction, which acts as the ToF correction but is more proper. The described Bethe parametrization of the CATE data from a RISING experiment is quite time consuming and is different for all different ions, that are to be used. Therefore, for simplicity, the energy loss in the whole S4 media can be calculated, using only one function, although being not in the above form. Again the energy loss is calculated for various velocities in the measured range at *i.e.* a CATE-$CsI(Tl)$ detector and is plotted versus the input energy at the final focus (see fig.7.15.f). The function is fitted with a fifth order polynom:

$$E_{@CATE-CsI} = A + B_1 \cdot E_{@S4} + B_2 \cdot E^2_{@S4} + B_3 \cdot E^3_{@S4} + B_4 \cdot E^4_{@S4} + B_5 \cdot E^5_{@S4}.$$

where A=-61089.45416, B_1=20.25125, B_2=-0.00258, B_3=1.72776e-7, B_4=-5.70389e-12 and B_5=7.4066e-17. For the Si correspondingly, the energy is calculated only until the its location in the experimental set-up. The polynomial approximation of the energy loss is not worst than the Bethe algorithm and is used for simplicity, however the Bethe approximation is more precise.

7.3 The CATE timing

The time signals of the CATE detectors, as already mentioned (in section 5.3), do not bring much information about the identification, what CATE is used for. However, they are useful for the "cleaning" of the energy spectra, when gating around their main distributions, especially in case of pile-up events.

Here has to be noted, that for every experimental data set, the amplification of the timing filter amplifiers are adjusted separately and the noise of the constant fraction discriminators (CFD) is adjusted in respect to the energy. The delay in respect to the TDC, is being also changed in the range, described in section 5.3, but often jitter of the CATE time signals caused deterioration of the respective spectra. These time spectra are converted from channels to ns from the range of the readout TDC. The time delay which is introduced to every separate channel, corresponds to the mean channel (or ns) position in the time spectrum. Typical time spectra from the CATE detectors are presented on

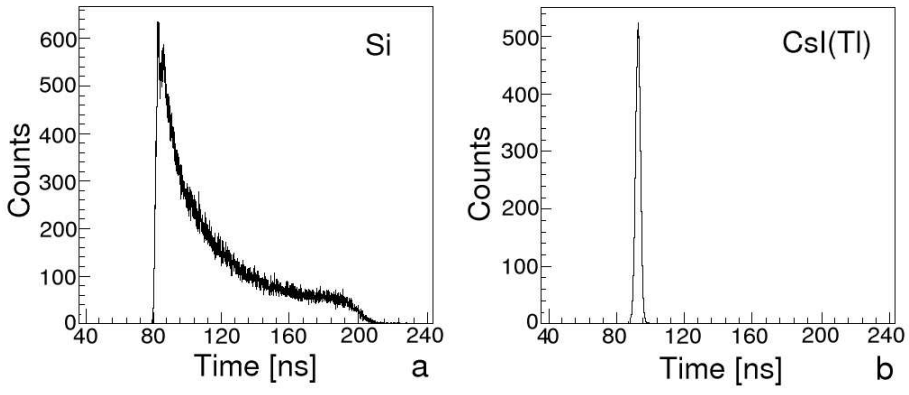

Figure 7.16: CATE **a** - Si, **b** - $CsI(Tl)$ time spectra from the central detector for ^{58}Ni particles.

fig.7.16.a for the central Si detector and on fig.7.16.b for the central $CsI(Tl)$ detector. As can be seen, the Si time covers a wide range, which is connected to the various ions with various energies. It is studied and found that, the Si time signal is position dependent and covers spectral time range, depending on the position of the illumination.

The time spectrum of a $CsI(Tl)$ detector has a Gaussian shape. The resolution for this example is about 10 ns. Depending on the incoming ion energy, the time resolution of the scintillator revealed values between 3 ns and 20 ns, for energies of 400 A·MeV and 100 A·MeV, respectively. In the case of 3 ns, this signal is used to suppress the unwanted contributions from some of the light particles produced in fragmentation with the secondary target and introduced electronically to the trigger of the RISING acquisition system.

Since the time resolution of both CATE detectors does not allow timing applications it is used in the analysis only to avoid the noise contributions to the CATE energies.

Chapter 8

The Simulations for primary and secondary beams

Several sets of simulations and calculations are performed to understand the response of the CATE detectors when reproduce exactly the beam conditions.

As shown in sections 7.1.2 and 7.1.3, the intrinsic energy resolutions of CATE - Si and $CsI(Tl)$ are found with precise primary ^{86}Kr particles that have SIS energy of 300 A·MeV and energy of about 282 A·MeV at the final focus and with ^{58}Ni particles that have SIS energy of 215 A·MeV and energy at the final focus of 190 A·MeV. These values of 2.0 - 2.2% for the Si and 0.72-0.86% for the $CsI(Tl)$ are object of the investigations below.

To simulate the exact conditions of the incoming to CATE particles, their energy depositions in the experimental set-up and inside the CATE detectors, and most importantly to find out what kind of energy uncertainty of the beam corresponds the measured resolution, the Monte Carlo code LISE++ [LISE04] is used. The code LISE allows simulation of an ion optical spectrometer (such as the FRS), including energy losses, reactions with target materials, energy distributions and particle rates. It is similar to the GSI Monte Carlo code MOCADI [MOCA04] (also used in this work), which can similarly and very precise simulate the whole experiment at the FRS set-up. Both codes make use of experimental parameters from in-beam studies, in order to better represent the real conditions. Hereafter the code LISE is used, because of its recent optimisations concerning mass spectroscopy [Tara04].

8.1 Primary ^{86}Kr particles

In order to achieve the experimental resolution, theoretical values of 2.68% for the Si and 0.84% for the $CsI(Tl)$ from the simulation, the energy uncertainty of the beam as an input to the simulation has to be set to as small as possible (0.0001%) and the intrinsic energy resolutions of the two detectors in the input set to 0.12% and 0.35% for the Si and $CsI(Tl)$, respectively. To find these values, a scan is realized for the smallest possible energy uncertainty of the beam, until the various input resolutions equalized to the experimental values. These values are graphed in an input - output functions and it turned out that in case of the $CsI(Tl)$ they have a linear behavior, while for the Si they have second order polynomial behavior. This means that the input - output values follow exactly the behavior of the energy loss in the detectors in terms of particle charge and mass and are representing the ideal intrinsic energy resolution. The output values are then deteriorated because of the beam optics and the materials media.

However, the assumed energy uncertainty of the beam is not so small in reality. From the experimental data it is measured by the ToF to about 0.4%, which converted into velocity definition equals to 0.2%. Certainly, this resolution is obtained from detectors which also have their resolution (in this case time resolution) and also cause errors in the ToF-β calculation. When the energy uncertainty of the beam width in the simulation is set to 0.3% or 0.1% as in the analysis (see section 7.1.2) and the intrinsic resolution of the CATE detectors as above, the measurement is exactly reproduced with outcoming resolution values of 2.9% and 2.2% for the Si and 0.9% and 0.8% for the $CsI(Tl)$. This primary beam example is shown on fig.8.1.a, where the two dimensional spot and its projections on the ΔE (Si) and the E ($CsI(Tl)$) axes are performed. One has to note

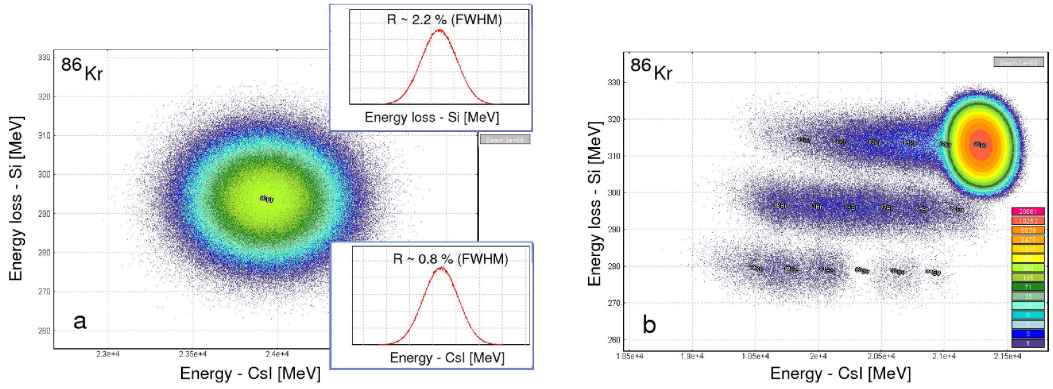

Figure 8.1: Lise simulations with ^{86}Kr particles for **a** - "no matter" (see text) setting and **b** - with additional secondary ^{197}Au target.

here that, only the FRS identification detectors are existing on the beam path (called "no matter" setting) at the final focal plane (S4).

8.2 Primary ^{58}Ni particles

To reproduce the experimental resolution for the ^{58}Ni primary particles, setting without matter is used, as for the ^{86}Kr particles. The minimum input resolutions of 0.001% (for both Si and $CsI(Tl)$) and energy uncertainty of the beam of 0.001% manifest the widening only from the interaction media of the FRS identification detectors. This minimum input show output of 1.72% for the Si and 0.25% for the $CsI(Tl)$, or ΔE in the Si of 3.9 A·MeV and 158.2 A·MeV in the $CsI(Tl)$. In the experiment the beam is not a point like and the detectors are not ideal as assumed here, therefore more realistic input is used. Thus, for an input energy resolutions of 0.001% for the Si and 0.27% for the $CsI(Tl)$ with energy uncertainty of the beam of 0.001% are produced the output resolutions of 2.5% for the Si and 0.69% for the $CsI(Tl)$. The experimental values, in comparison, showed for an input beam of 0.1% resolution of the Si of 2.0-2.2% and of the $CsI(Tl)$ resolution of 0.82-0.89%.

8.3 Secondary ^{55}Ni particles

This input resolution setting is further used for the ^{55}Ni fragments produced at the primary ^{9}Be target (with thickness of 2.5 g/cm^2) which enter the final focus with energy of 196.1 A·MeV (according to the LISE calculation). They are used to fragment with

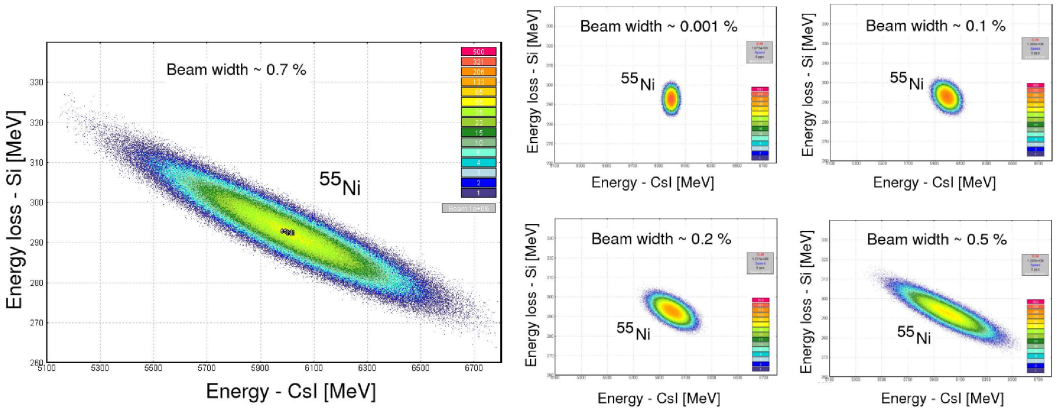

Figure 8.2: Development of the ^{55}Ni spot for different uncertainty of the beam widths (0.0001-0.7)%.

the secondary ^{9}Be target with thickness of 0.7 g/cm^2. For several energy uncertainties of the beam, the input energy resolution of the CATE detectors revealed not only different output resolutions, bigger than the experimentally observed, but also a different behavior of the $\Delta E - E$ identification plot. The LISE simulation of the beam spot development of ^{55}Ni fragments for the different definition widths is demonstrated on fig.8.2 and the outcoming resolution presented on table 8.3. The simulations for each setting are performed at the same conditions for the same 1.2x10^6 Monte Carlo events in the distributions. They are plotted in the same scale for comparison.

energy uncertainty of the beam [%]	input Si [%]	input $CsI(Tl)$ [%]	output Si [%]	output $CsI(Tl)$ [%]
0.0001	0.001	0.27	1.97	0.82
0.1	0.001	0.27	2.1	1.4
0.2	0.001	0.27	2.5	2.4
0.5	0.001	0.27	4.3	5.8
0.7	0.001	0.27	5.7	8.1

Table 8.3. Energy resolution of the CATE detectors expected from a LISE simulation for ^{55}Ni fragments for different uncertainty of the beam widths.

The setting that represents the experimental resolution with the fragment beam has an energy uncertainty of the beam of 0.3% and outcoming resolutions of 3.2% for the Si and 3.9% for the $CsI(Tl)$. The corresponding shape of the correlation distribution is extended in the way, shown on the picture for the 0.5% energy uncertainty of the beam. That is relevant to *i.e.* the simulation of fragmentation of ^{55}Ni on the target which shows mean values difference in the energy at the $CsI(Tl)$ of 4.3% between the ^{54}Ni and ^{53}Ni fragments. Excluding the Ni isotopes in the simulation with energy uncertainty of the beam of 0.1% and the same input energy resolutions (of 0.001% for the Si and 0.27% for the $CsI(Tl)$), the set-up media and the secondary target indicate the fragmentation channels, scaled by their abundance shown on fig.8.3.

The produced fragmentation channels for *i.e.* Z=25 (ΔE between 215.7 and 221.7 MeV) differ in the E$_{res}$ projection (between 5831 and 6446 MeV) for one mass unit ΔA=1 from 3.2-3.5%, what is slightly better present in the experimental data. In order to identify the experimental masses, as will be shown in section 9.4.2, the centroids shift of the different

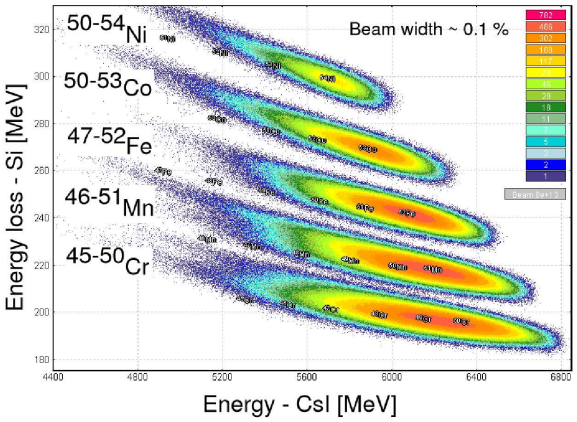

Figure 8.3: Lise simulations for fragmentation of ^{55}Ni particles on ^{9}Be (0.7 g/cm^2).

mass distributions is found. Such displacement is observed in the plots demonstrated on fig.8.4, where all distributions are plotted on the same scale and the single distributions are depicted with mass difference of ΔA=2 (instead of ΔA=1) for the comparison. Note that the mass shift is present without designating the algorithm of the fragment production in LISE [LISE04].

8.4 Secondary ^{58}Cr particles

In further experimental investigations, using *i.e.* ^{86}Kr primary particles, secondary ^{58}Cr isotopes are produced via fragmentation in the primary target. Transported to the same set-up, with an energy of about 160 A·MeV, they react with a secondary target of ^{197}Au (thickness of 1 g/cm^2) via Coulomb excitation and fragmentation. Using the input energy resolutions of the CATE detectors, obtained from the comparison with the primary beam, the output resolutions for the secondary particles are compared.

To exclude several effects on the energy resolution of the CATE detectors (see sections 7.1 and 7.2.3) the following conditions are performed: (1) the proper fragment selection of low intensity data set is cut-off from the Z(A/q) identification (for ^{58}Cr), (2) the energy uncertainty of the beam from the measured ToF of 1.2% is cut-off to 0.13%, (3) the position dependence of CATE is avoided with position cutt-off of small center map with size of ($\pm$5,$\pm$5) mm^2, (4) additionally cleaning conditions on the CATE time spectra that avoid *i.e.* self triggering (as start and stop) and (5) $\Delta E - E$ conditions at the energy correlation spectra, that take into account only the Z=24 isotopes. In the comparison with the simulations an energy uncertainty of the beam scan is performed until the experimental values are reproduced (see the simulated and experimental resolutions for several energy uncertainty of the beams on the table 8.4).

As can be seen from the table, the experimental energy uncertainty of the beam of 1.2% corresponds to theoretical value of 0.68%, when comparing the CATE detectors resolution. For energy uncertainty of the beam of 0.17% *i.e.* the simulated energy resolutions reveal to be 1.9 to 2.1% for the Si and 2.0 to 3.9% for the $CsI(Tl)$. This is already a hint that our experimental data are better than the simulation.

Generally, the above comparisons of the experimental data with the simulations show good agreement. The differences in the obtained values come due to the parametrization

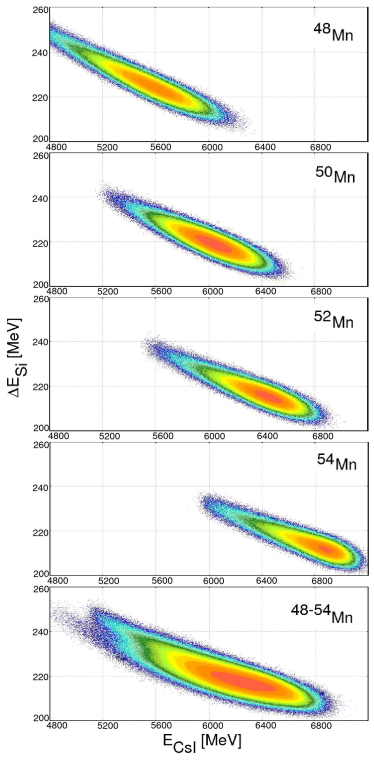

Figure 8.4: Lise simulation for the energy shift of the reaction products (with ΔA=2) from the reaction ^{9}Be(^{55}Ni,xn,3p), x∈[48,54]. These displacements are used for the mass identification in the experimental data.

of the simulation models [LISE04], which are optimized for low energy. As will be shown in section 9.4.2, our new experimental data allow the expansion of this range to relativistic energies.

simulated beam [%]	Si [%]	$CsI(Tl)$ [%]	experimental beam [%]	Si [%]	$CsI(Tl)$ [%]
0.1	2.1	1.4	0.126	1.9-2.1	2.0-3.9
0.2	2.4	2.3	0.21	3.2-3.4	1.4-3.6
0.5	4.1	5.3	0.42	3.8	5.1
0.7	5.3	7.3	0.68	4.5	6.2
1.2	8.8	12.6	1.26	5.2	7.2

Table 8.4. Comparison of a LISE simulation with the experimental data for the energy resolutions of ^{58}Cr particles.

Chapter 9

Analysis and comparison with simulations

In order to study the proper energy response of the CATE detectors, all above mentioned corrections (as described in sections 7.1 and 7.2.3) have to be performed. To obtain the charge resolution Z and the particle mass A, the energy loss ΔE form the Si and the residual energy E_{res} of the $CsI(Tl)$ are absolute energy calibrated and linearized. How the identification is performed is described in this chapter, together with comparison of the simulated response of CATE.

9.1 Charge (Z) determination

From the energy loss ΔE in the Si detectors of CATE the registered particle atomic number Z can be deduced as $\sqrt{\Delta E}$. Because of the incoming from the FRS bare heavy ions, which have relativistic energies, the probability for electron pickup is extremely low [Geis92]. Therefore, the deduced atomic number is assumed being equivalent to the particle charge q (see the FRS A/q identification in Appendix 2).

In the variety of in-beam studies, the CATE detector response reveals an unique Z identification. In a secondary reaction ^{9}Be(^{55}Ni,xn,yp) at 100 A·MeV, the detector measured that the dominating process is the **fragmentation**, as depicted on fig.9.1.a In a reaction ^{197}Au(^{112}Sn,xn,yp) at 120 A·MeV, CATE measured that the reaction is

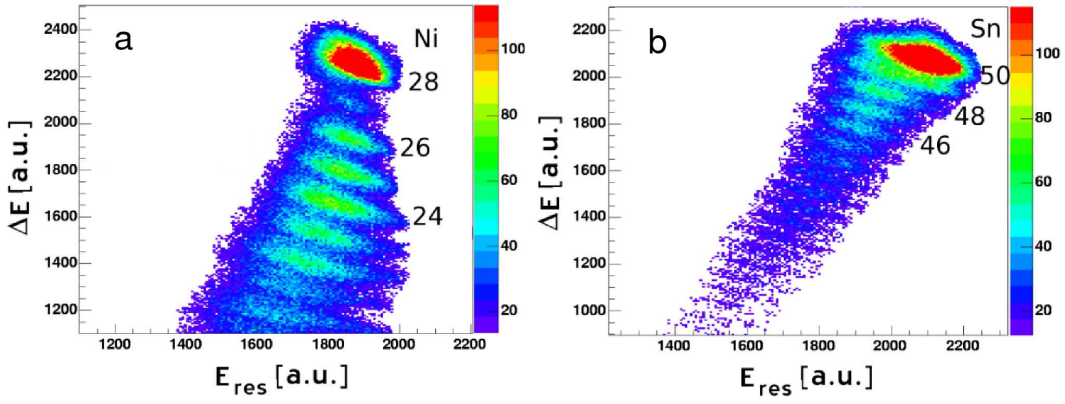

Figure 9.1: The Z resolution **a** - for the products from the reaction ^{9}Be(^{55}Ni,xn,yp), **b** - for the products from the reaction ^{197}Au(^{112}Sn,xn,yp).

dominated by **Coulex**, as demonstrated on fig.9.1.b.
CATE separates all other reactions performed on the secondary targets in charge but only those two extreme cases for the determination of the charge resolution are described hereafter.

In both cases the two dimensional distributions are first linearized (parallel to the E_{res} axes) by the rotation used and described in section 3.3 (see fig.3.22 and fig.3.23). As explained there, the most important parameter for this procedure is the angle of rotation, which here equals to -27.53° for the fragmentation example and to -17.3864° for the Coulex example. It is determined by two dimensional linear fitting procedure from the Go4 package [Go4G04]. The center of the rotation is determined from the mean coordinates of the primary like spot in the distributions. From there are determined the other two parameters, used to move to the coordinate system where the rotation is performed and to return to its original channel position afterwards. The linearization has to be examined as projections on the already rotated ΔE and E_{res} axes for both distributions. Here, only the ΔE projection is important for the Z determination. Therefore, it is performed under a condition on the E_{res}, which avoids the noise contribution at low channels and the pile-up events at higher channels. The Z projections are then fit with appropriate

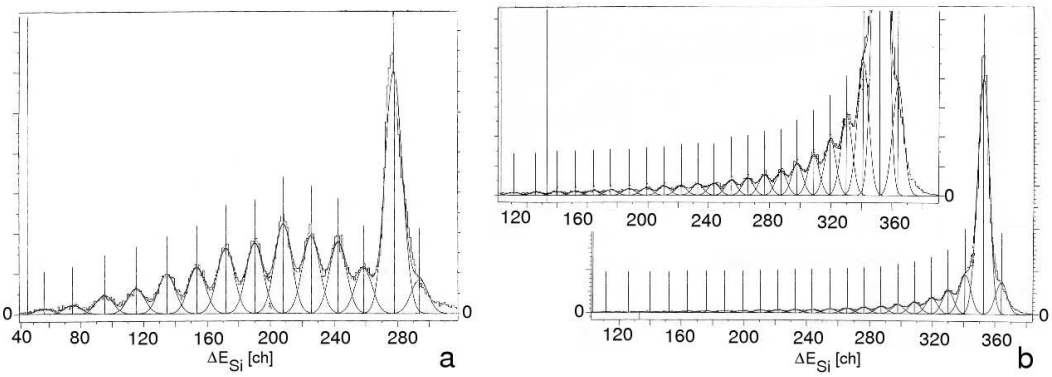

Figure 9.2: Fitting the energy loss distribution **a** - for the products from the reaction ^{9}Be(^{55}Ni,xn,yp), **b** - for the products from the reaction ^{197}A(^{112}Sn,xn,yp).

multiple Gaussian functions with background cutoff and with constant widths. For this purpose the IKP developed program TV is used [IKPT00]. The fits for the fragmentation and for the Coulex cases are depicted on the top of the experimental data, as can be seen on fig.9.2.a and on fig.9.2.b, respectively. Knowing the incoming particles charge, two functions are constructed for both cases, whose x-axes are the experimental square roots of the energy losses in channels ($\sqrt{\Delta E}$). They are fit with linear functions as shown in fig.9.3.a for the fragmentation and in fig.9.3.b for the Coulex cases. The widths from the Gaussian fits are depicted in both figures as error bars. From the linear regression $y = a + b.x$ the two slope parameters b_{55Ni} and b_{112Sn} (with errors δ_b of 5.1% and 2.6%, respectively), are used for the determination of the charge resolution $\Delta Z/Z$ as *i.e.* for the ^{112}Sn:

$$\frac{FWHM_i \cdot b_{112Sn}}{Z_i} = \left(\frac{\Delta Z}{Z}\right)_i, \quad i = 1,..,21 \; for \; Z = 50,...,Z = 29;$$

$$\overline{\frac{\Delta Z}{Z}} = \frac{1}{n}\sum_{i=1}^{n}\left(\frac{\Delta Z}{Z}\right)_i$$

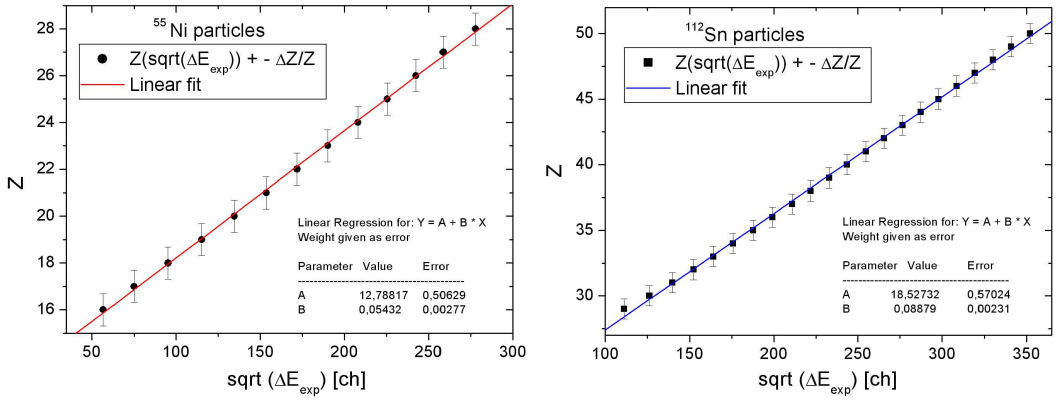

Figure 9.3: The Z determination for the products from the reactions **a** - ^{9}Be(^{55}Ni,xn,yp) and **b** - ^{197}Au(^{112}Sn,xn,yp).

9.1.1 Charge (Z) resolution

In this way the extracted mean Z resolution from the outcoming particle cocktail after the secondary target is ΔZ of 0.687 Z (FWHM) for the fragmentation ^{55}Ni particles (see fig.9.4.a) and ΔZ of 0.774 Z (FWHM) for the Coulex ^{112}Sn particles (see fig.9.4.b).

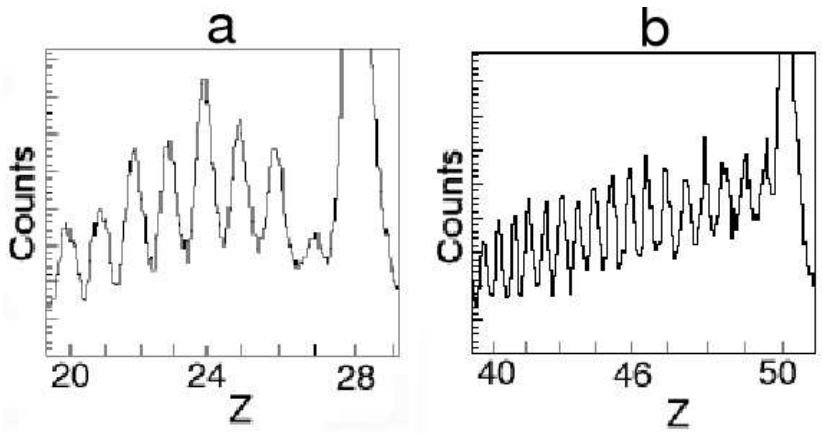

Figure 9.4: The Z resolution for the products from the reaction **a** - ^{9}Be(^{55}Ni,xn,yp) and **b** - ^{197}Au(^{112}Sn,xn,yp).

The precision of the Z measurement, is revised by a calculation of the total errors in both Z determinations:

$$\delta\left(\frac{\Delta Z}{Z}\right)_{55Ni,112Sn} = \sqrt{(\delta_{Mean})^2 + (\delta_{FWHM})^2 + (\delta_b)^2 + (\delta_{rotation})^2 + ...}$$

Where, the major part in the uncertainty is due to the rotational angle determination (which is 7.8% and 8.9% for the fragmentation and for the Coulex cases). The contributions from the other uncertainties is small and the total uncertainty is calculated to be of 11.6% and 12.2% for the respective cases.

The analysis for other experiments with reactions, except those that undergo Coulex, but also fragmentation in the secondary target show that the charge resolution of the CATE Si detectors is almost always at the same order, or of about 0.7 Z (FWHM).

9.2 Mass (A) determination

The residual energy (E_{res}), deposited in the $CsI(Tl)$ detectors of CATE, gives an information about the particle mass A, when is combined with the energy loss in the Si detectors (ΔE) and under the assumption that all particles with the same mass A have the same velocity β_A:

$$\Delta E + E_{res} = E_{tot} = A \cdot \beta_A^2, \qquad \beta_A = const \neq \beta_{A-1} \neq \beta_{A+1}$$

$$\Rightarrow \Delta E + E_{res} \approx A$$

The mass resolution can be estimated from the energy resolutions of both CATE detectors of 2% for the Si and 0.8% for the $CsI(Tl)$ in the primary *i.e.* ^{58}Ni beam case:

$$\frac{\delta \Delta E}{E} \approx 2\ \% \approx 43.6\ MeV, \qquad \frac{\delta E_{res}}{E_{res}} \approx 0.8\ \% \approx 3787.7\ MeV$$

In this way using error propagation:

$$\frac{\Delta A}{A} = \sqrt{\frac{\delta \Delta E}{E}^2 + \frac{\delta E_{res}}{E_{res}}^2}, \quad \Rightarrow \frac{\Delta A}{A} \approx 1\%$$

If this mass resolution is present in the RISING experiments will be examined below *i.e.* for the central (5) CATE detectors.

9.3 Mass determination for Coulex reactions

The energy spread detected in CATE depends (i) on the straggling effects in the isotope production, the straggling in the FRS tracking detectors, the straggling in the secondary target and the intrinsic resolution of the CATE detectors themselves; and (ii) on the isotope cocktail produced by neutron knock-out/fragmentation in the secondary target. In relativistic Coulomb excitation reactions, CATE is used to detect the same outgoing particles which impinge on the secondary target. Therefore, the incoming ions of interest are selected with the FRS identification detectors and no absolute energy calibration needs to be performed for the CATE detectors.
One way to determine the mass resolution is from the particle singles or from particle-γ events with very small scattering angles corresponding to atomic interactions because only the above mentioned "type (i)" effects are relevant (see section 9.3.2). Another way to determine the mass resolution for the Coulex channels is to compare the energy centroids at the E_{res} detectors of CATE for masses apriori selected in front of the secondary targets. For this purpose a geometrical linearization by rotation of the distribution around the main spot is performed. After a Z selection from the linearized $\Delta E - E_{res}$ distribution the deposited residual energy, E_{res}, is projected.

As already shown in chapter 7, a primary beam has beam definition, much better than a secondary beam. Neglecting the target effect, which is present in both cases, it is expected that the mass resolution using primary beams is much better and can be studied separately.

9.3.1 Mass resolution with primary Coulex beams

Primary ^{84}Kr particles, at low particle rate of 2 kHz, with SIS energy of 435 A·MeV and without matter on their fly-path, except the FRS identification detectors, arrive at the secondary target position with energy of about 408 A·MeV, according to a LISE simulation of the experimental energy losses in the set-up [LISE04].

A thin secondary target of 96.6 mg/cm^2 of ^{197}Au is inserted on an Al target holder frame (with thickness of 27 mg/cm^2). The beam velocity is defined with precision of only 0.1%, which allows precise study of the incoming to and the outgoing from the target particles. On fig.9.5.a the experimental $\Delta E - E$ response, detected by the central CATE detectors is drawn. The fragmentation and knockout channels appear in the correlation plot towards lower energies, while the Coulex channels are concentrated in the main beam spot. The tiny correlated structure observed parallel (and with higher residual energies) to the fragmentation channels with the target, originates from interactions with the target frame. In expanded region around the main Kr particles (undergoing Coulex) is located on the plot of fig.9.5.b. This spectrum is obtained without any beam corrections, except a position selection at the CATE-Si, in order to avoid the position dependence of the detectors. The pronounced mass structure is enclosed in black ellipses.

E_{res} contains the mass information and the contribution of the ΔE due to the small amount of energy loss is typically neglected. The corresponding E_{res} projection is plotted in fig.9.5.c. The spectral structure is marked with dotted curves and labeled in correspondence with the cross sections to produce the knockout masses of ^{83,82}Kr from the incoming ^{84}Kr.

Before comparing this experimental result with calculations, on the particle path a thicker target of 386.4 mg/cm^2 is inserted. The CATE detector response in this case is depicted in fig.9.5.d and zoomed around the Coulex part, as shown on fig.9.5.e. The main (spot) distributions are thicker than with the thinner target, and are also marked with black polygons. The projections on the E_{res} axis are done in the same way and presented on fig.9.5.f. As can be seen, in both target cases the resolution of the CATE detectors is sufficient to distinguish the different channels after the secondary target. The projections are marked and the difference in energy peaks (in channels) manifests the mass resolution of about 1.7-2.7% for the thinner target and about 1.9-3.2% for the thicker target.

A simulation, corresponding to the experimental conditions, is performed with LISE [LISE04] with an input intrinsic resolution values of 0.001% for the Si and 0.3% for $CsI(Tl)$ (see chapter 8). They give output values of 2.5% for Si and 0.71% $CsI(Tl)$, when used without targets. For the simulation 4x10^6 particle events are used, with beam definition of 0.1% to calculate the behavior of the fragmentation channels ^{83,82,81}Kr, assuming all possible reaction mechanisms (see section 7.2.2). As shown on fig.9.6.a, the simulation for the thin target reproduces different shapes of the $\Delta E - E$ distribution which are similar to those detected in the experiment. From the projection on the E-axis (in MeV) the difference in two neighboring masses accounts to about 400 MeV which is at the order of 1.7%. The same, can be expected from the simulation with the thicker target (see fig.9.6.b), with the same input beam definition and intrinsic resolutions. Thus the mass difference, expected from the simulation accounts to about 2.5%, calculated from the residual energy projection (E-axis). Since no absolute energy calibration is performed to the experimental data, the results can not be compared quantitatively, but rather qualitatively. Nevertheless, the experimental results are encouraging and despite of the experimental errors and the absence of corrections to the energy, are at the same order as the simulation.

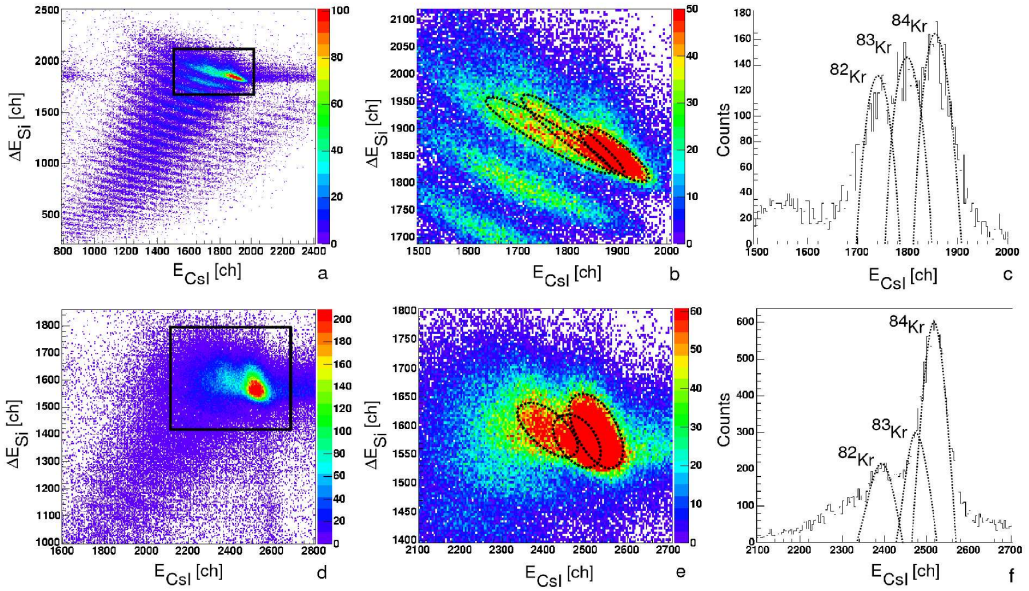

Figure 9.5: Experimental data from the central CATE detectors: **a** - $\Delta E - E$ response on primary ^{84}Kr ions with thin ^{197}Au target, **b** - expanded region around the main Kr isotopes, **c** - CsI(Tl)-E projection where the different isotopes are marked with dotted curves; **d** - $\Delta E - E$ response on primary ^{84}Kr ions with thick ^{197}Au target, **e** - expanded region around the main Kr isotopes, **f** - CsI(Tl)-E projection where the different isotopes are marked with dotted curves.

9.3.2 Identification with secondary Coulex beams

The Coulex reactions which have been available for study, are ^{197}Au(^{54}Cr,0n,0p) with energy about 174 A·MeV at the secondary ^{197}Au (1 g/cm^2 thick); ^{197}Au(^{56}Cr,0n,0p) with energy about 162 A·MeV at the same secondary target; ^{197}Au(^{58}Cr,0n,0p) with energy of about 135 A·MeV at the same secondary target and ^{197}Au(^{68}Ni,0n,0p) with energy about 420 A·MeV at the secondary ^{197}Au (2 g/cm^2 thick). All of the above nuclei are produced in fragmentation reaction of ^{86}Kr primary beam on primary ^{9}Be target of 2.5 g/cm^2 thickness and SIS energies of 477 A·MeV for the Cr's and 750 A·MeV for the Ni's. Thick Al degraders at the first focus (S1) and middle focus (S2) with total thickness of about 4.3 g/cm^2 are used for the separation and for the slowing down of the Cr's and of about 5 g/cm^2 for the ^{68}Ni.

The ^{54,56,58}Cr cases will be demostrated by examples with ^{54}Cr and ^{58}Cr. Additionally, the experimental observations with CATE for the higher energetic ^{68}Ni will be given. According to calculations with ATIMA for the losses in the experimental set-up, the energies at the CATE detectors, for the ^{54}Cr ions are about 111 A·MeV at the Si and 106 A·MeV at the $CsI(Tl)$; for the ^{58}Cr ions - about 137 A·MeV at the Si and 133 A·MeV at the $CsI(Tl)$; and for the ^{68}Ni - about 388 A·MeV at the Si and 385 A·MeV at the $CsI(Tl)$.

Before the secondary target, together with the ^{54}Cr ions, separated and identified by the FRS, come other two isotopes, taken in the investigations, namely ^{55}Mn and ^{53}V. These isotopes are uniquely identified by their charge Z in CATE.

In comparison, to the lower in energy Cr isotopes, where fragmentation and knockout reactions appeared additionally at the secondary target, no fragmentation is registered in the for the Ni ions. This is because of the range of the ^{68}Ni ions, which is equal to

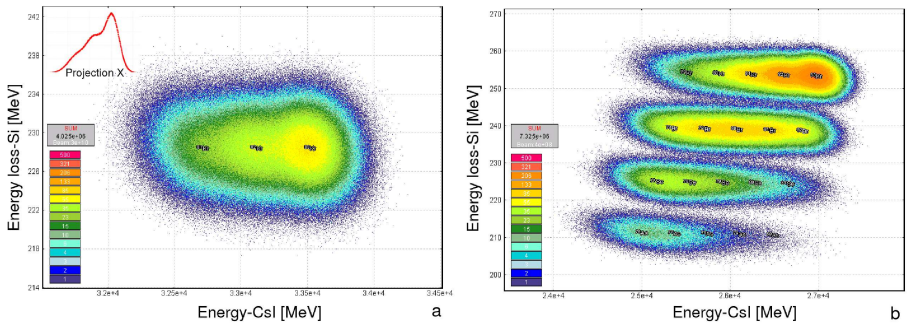

Figure 9.6: LISE simulation of the experimental case with ^{84}Kr particles for **a** - thin and **b** - thick secondary targets.

the detector thickness. Therefore, any longer particle range caused by nucleon removal or change of the particle trajectory punch trough the scintillator.

9.3.3 The beam definition and the target effect

As already mentioned, the beam definition widening and the target effect are severe for secondary beams. Therefore, several investigations have been performed in order to estimate the widening of the particle momentum by the FRS and by the energy loss in the final focus and the thick targets.

Because of the small energy loss in Si compared to the $CsI(Tl)$, these effects are more important for the second detector of CATE, whose energy resolution mainly determines the mass of the incoming ions. The energy definition of the beam particles is observed typically, in the calibrated ToF spectrum. Its effect on the CATE energies could be than studied under the different FRS identification (A/q and Z) conditions. The total ToF

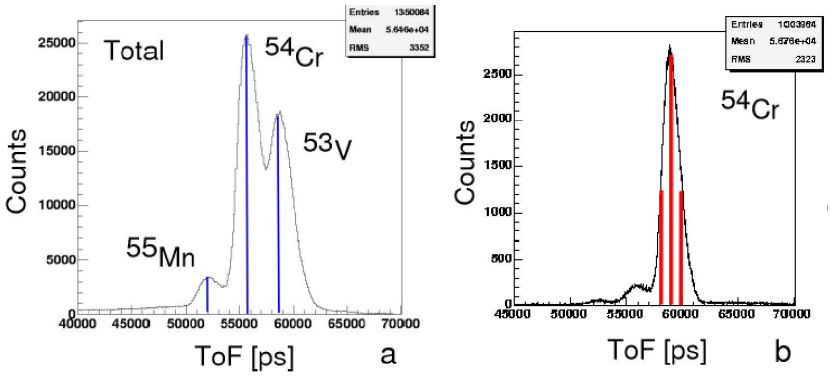

Figure 9.7: **a** - Total ToF spectrum for the ^{53}V, ^{54}Cr and ^{55}Mn isotopes, **b** - ToF spectrum for the ^{54}Cr isotopes, selected by the FRS.

spectrum for all selected (^{55}Mn, ^{54}Cr and ^{53}V) isotopes is depicted in fig.9.7.a. They correspond to the different peaks as marked with blue lines. A typical ToF distribution for one of these isotopes *i.e.* ^{54}Cr, is depicted separately (after selection by the FRS) in fig.9.7.b. The measured resolution for these distributions is between 2.6% and 3.1%, which corresponds to velocity uncertainty (β_{ToF}, calculated from the ToF) between 0.87% and 0.92%. In comparison to the ^{86}Kr primary beam (with energy of 300 A·MeV), the corresponding values are 0.52% and only 0.17% for the ToF and velocity, respectively.

To limit the corresponding energy definition in the secondary beam case, cuts are performed as marked by vertical red markers on the plot of fig.9.7.b. As can be seen, they are located around the mean peak and around the half width heights on the shoulders of an experimental ToF spectrum, in a way that each of these three gates corresponds to a 0.3% selection from the ToF distribution. This means, that only 0.3% of the energy is taken into account, as required by the investigations from chapter 8. From the ToF, under these conditions, the experimental velocity β is calculated, using the ToF calibration and afterwards the kinetic energy (see Appendix 2). Employing ATIMA [ATIM04] this energy is used as an input of calculations. They are reproducing the corresponding energy at the CATE-$CsI(Tl)$ detector (see section 7.2.3), assuming all the losses in the experimental setup and the secondary target. Additionally, calculations, corresponding to measurements without secondary target are performed. All calculated energies, are compared then with the measured energies at the $CsI(Tl)$. In order to produce the corresponding measured spectra, several conditions are applied as follows:

- FRS trigger and FRS events are matched only in the acquisition
- Pile-up rejection by rejecting events from histograms counting the pileuped events in the S4-scintillator and CATE
- A/q-Z gate on the isotope of interest
- Tof-β cuts of 0.3% at three places on a ToF distribution, corresponding to the isotope of interest
- Position correction or position cut in the center of the CATE-Si detector with size (x,y) of ($\pm$2.5,$\pm$2.5) mm^2
- Z polygon for the ion of interest on the $\Delta E - E$ identification spectrum of CATE

Rarely, when need a charge state clean up is performed by gating on a distribution created from the charge deposition in the music at S4 and the energy loss in the degrader at S2. The last is calculated from the Bρ of the magnets, the velocity of the ions and their A/q ratio.
The comparison of the calculated and measured energy at the $CsI(Tl)$, using thick ^{197}Au target of 1 g/cm^2, is depicted in fig.9.8.a for ^{53}V, ^{54}Cr and ^{55}Mn isotopes. The experimental widths (FWHM) of the $CsI(Tl)$ spectra are plotted as error bars. As can be seen, the calculated and measured energies have linear behavior. Every three points (from the ToF gates of one selected isotope) belong to a straight line. However, the line is shifted when going to other isotopes. This means, that the different incoming channels contribute to parallel distributions and overlap to one common, widen distribution, as observed in the $CsI(Tl)$. The last, have indeed, sufficient intrinsic resolution to distinguish them with corresponding widths for the different isotopes between 2.9 and 4.3%. Additionally, on fig.9.8.b is drawn a comparison between "target" and "no target" response of the calculated and measured energies at the $CsI(Tl)$ for the ^{57}V, ^{58}Cr and ^{59}Mn. The widths of the incoming energies are smaller than the symbols, while the widths of the measured energies are visible as error bars of the measured data points. The "no target" data *i.e.* belong to a straight line (y=a+b·x), whose coefficients are determined from a fit to be 2378.418 $\pm$ 174.619 and 1.649 $\pm$ 0.057 for a and b, respectively. As expected, the "target" widens the energy responses several times compared to "no target" measurement. Moreover, the energies overlap. This causes an increase of their widths from 1.1 - 1.7% for the "no target" measurement to 4.3 - 5.9% for the "target" measurement.

The explained investigation shows quantatively how the target effect deteriorates the energy resolution of the CATE scintillators. It consequently diminishes the precise energy measurement of the corresponding masses.

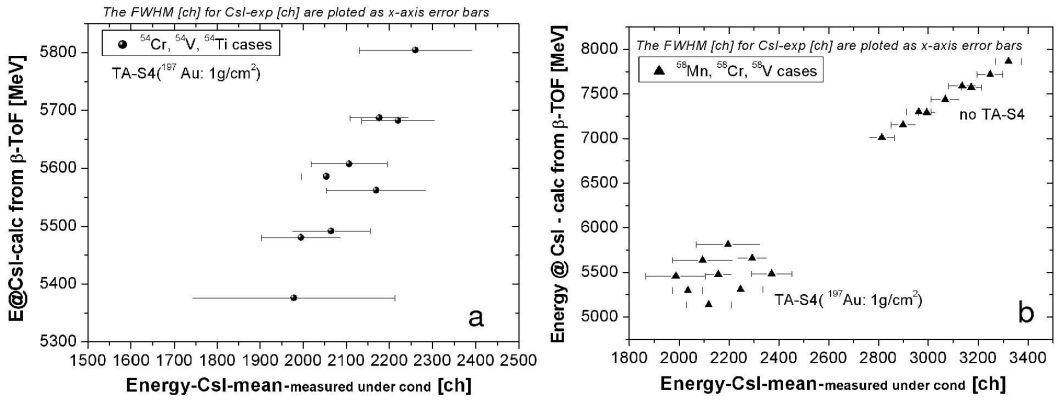

Figure 9.8: Comparison of calculations and experimental data **a** - for the ^{53}V, ^{54}Cr and ^{55}Mn isotopes, **b** - for the ^{57}V, ^{58}Cr and ^{59}Mn isotopes.

Simulation of the beam distribution for ^{58}Cr ions

A MOCADI [MOCA04] simulation is performed in order to calculate the beam widths at the final focus and at the CATE-$CsI(Tl)$ detector. For this purpose the experimental setup, the energy loss in the S4 detectors and target are implemented, together with the possibility to calculate these ions as a primary beam and as secondary fragments. The rather thick media of the first focus (S1) and the middle (S2) wedge degraders (in total of more than 4 g/cm^2 Al), results in a wide momentum of the outcoming ions already at the middle focus of the FRS. During the experiment, this distribution is cut in position with the help of slits at first or at the middle focus (of $(x, y) \approx (\pm 4.0, \pm 4.0)$ cm and additionally, at the final focus with slids (of $(x, y) \approx (\pm 3.5, \pm 7.5)$ cm.

As already shown above, during an experiment, the beam distribution of only a few percents in the beginning of the S4 results of several percents width at the $CsI(Tl)$. Therefore, the simulation of the incoming energies and their distribution widths for ^{58}Cr ions as secondary fragments is performed as sketched on fig.9.9.a. According to the simulation, the mean value of the energies at the final focus for these ions is 162.26 A·MeV, with distribution widths of 3.65 A·MeV (or 2.23%). Imaginary slits are implemented after the last quadrupole of the FRS, cutting this distribution $(x, y) \approx (\pm 0.115, \pm 1)$ cm. Thus, representing a momentum cut of the distribution with widths of 0.321 A·MeV, or only 0.20% of the distribution. The simulations with open slids at the final focus show, that 0.321 A·MeV cut at S4 corresponds to 2.6 A·MeV spread at the $CsI(Tl)$, where the mean energy is 97.74 A·MeV, or to 2.7% widening. The energy and its spread are calculated at the $CsI(Tl)$, and plotted versus the incoming energy and spread at the beginning of the S4, as demonstrated on fig.9.9.b. The spreads on both energy axes are plotted as error bars. It can be seen, that the widths increase only with few percents, because of the S4 slids, cutting the distributions in reality. According to the simulation, a distribution width of 1.62 A·MeV (or 0.98%), results in a width of 2.21 A·MeV (or 2.17%). This spread is severe. It is measured also in the experiment to be at the same order of 2-4%, when a ToF cut with width of 0.3-0.8% is present.

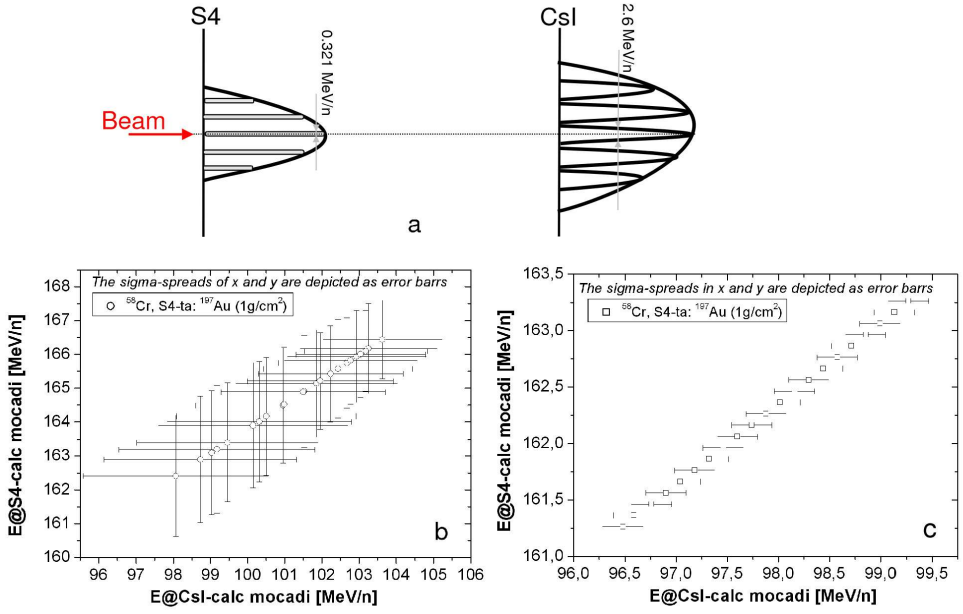

Figure 9.9: **a** - Schematical representation of the beam widths and cuts at S4 and at the $CsI(Tl)$ detector, **b** - MOCADI simulation for ^{58}Cr ions, considered as fragment beam and their energy widths at the $CsI(Tl)$, **c** - MOCADI simulation for ^{58}Cr ions, considered as primary beam and their energy widths at the $CsI(Tl)$.

To compare with the primary beam spread, the same simulation (with secondary target) is performed, where the ^{58}Cr ions are assumed as primary beam particles. In this case the position cuts are bigger than with fragments ($(x, y) \approx (\pm 0.15, \pm 2)$ cm), in order to have sufficient statistics. The primary beam energies and widths at S4 versus the corresponding energies and spreads at the $CsI(Tl)$ are represented on fig.9.9.c. Correspondingly, the widths are plotted as error bars, which, for the input energies, are smaller than the symbols. In example, 0.19 A·MeV width (or 0.12%), results in a width of 1.95 A·MeV (or 1.9%). The simulation without secondary target for the beam definition at S4 of 0.17% results in 0.9% width at the $CsI(Tl)$ detectors. Thus, the comparison between primary and secondary beams, clearly shows the influence of the beam quality and the secondary target on the $CsI(Tl)$ detectors and helps to understand the experimental observations. The experimentally measured spreads with and without secondary target for ^{86}Kr primary beam, show result, indeed, with values even slightly better than the simulation. Beam definition at S4 of 0.17% for secondary target measurement revealed resolution of the $CsI(Tl)$ of 1.2-1.4% and without target of 0.7-0.9%.

All these investigations show the influence of the beam definition and the target on the energy measurement of the Coulex particles using CATE. The calculated and observed energy distributions prove that few percents in the velocity distribution widths account to several percents at the CATE energy. At the same time, the relative mean peak energies measured by gating on the different isotopes are consistent with their calculated energies. These estimations are conducive for the correlation of the calculated energy with the measured for performing a polynomial corrections as explained in the section 7.2.3.

9.3.4 The mass resolution

With the above conditions and after the position, ToF and target corrections the $\Delta E - E$ distribution of CATE is linearized, using the geometrical algorithm from section 3.3. Since no energy calibration is performed the algorithm from section 3.4 is not applicable.

The system ^{53}V, ^{54}Cr and ^{55}Mn after the reaction with ^{197}Au target at an energy of about 170 A·MeV has similar $\Delta E - E_{res}$ identification with CATE to the one depicted in fig. 9.5(a). After a Z selection from the linearized $\Delta E - E_{res}$ distribution the deposited residual energy, E_{res}, is projected in order to obtain the mass information.

As mentioned before, due to the high probability for knockout and fragmentation, these events typically appear when selecting a particle tigger from the FRS in coincidence with a γ-trigger from the "OR" of all Ge detectors. To extract the Coulomb excitation events for such trigger combination a condition can be set on the Coulex peak, registered by the Ge detectors. The Coulomb excitation events for one of the isotopes of interest can be represented only with particle trigger in order to suppress the background from the secondary nuclear reactions. Additionally, the scattering angle can be limited to very small or forward angles in order to select the peripheral collisions with the secondary target nuclei. For this purpose is set a condition on the position spectrum of the central CATE-Si detector.

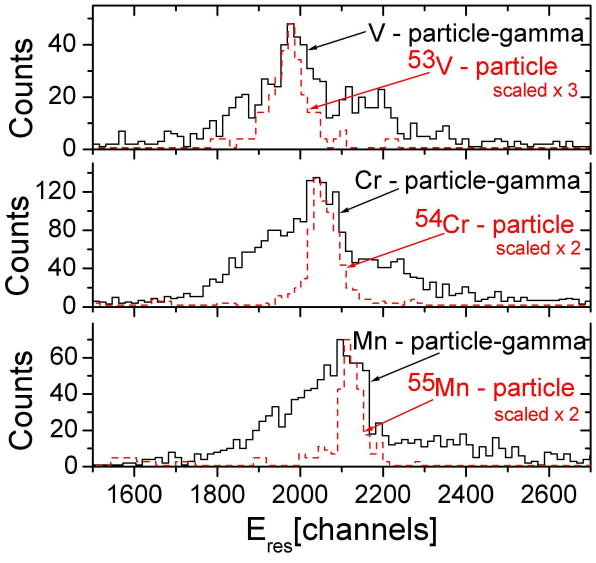

Figure 9.10: Mass spectrum for the ^{53}V (top), ^{54}Cr (middle) and ^{55}Mn (bottom) isotopes with solid line for particle-gamma condition and with dashed line for particle singles.

The mass spectra with particle-γ coincidence condition for the three isotopes ^{53}V (top), ^{54}Cr (middle) and ^{55}Mn (bottom) are plotted in fig. 9.10 with black solid line. The nuclear reaction channels form in this case a wide distribution. Selecting a particle trigger condition pronounces the secondary beam-like residues, as depicted in fig. 9.10 with red dashed line. The mass resolution of CATE corresponds then to the width of these Coulomb excitation channels which is determined to be between 2 and 3% (FWHM).

The mass resolution for the Coulex channels can also be obtained from the difference of the mean values (in channels) in the E_{res} projection. For the above example the calculated values are consistent with the widths of the single distributions.

In a different experimental set at higher energies of 400 MeV/u, ^{67}Ni, ^{68}Ni and ^{69}Ni

isotopes also interact mainly in a Coulomb excitation with the secondary ^{197}Au target. After a selection by Z their E_{res} projections are plotted together in fig.9.11 with particle-gamma trigger condition. The main Coulex channel, ^{68}Ni, is scaled 0.1 times on the figure. Since for this data set a particle trigger condition was not available, the mass resolution is

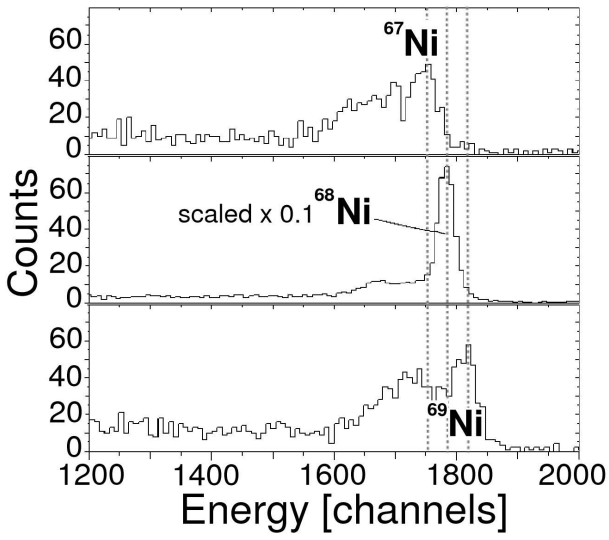

Figure 9.11: Mass spectrum for the ^{67}Ni (top), ^{68}Ni (middle) and ^{69}Ni (bottom) isotopes with particle-gamma trigger.

obtained from difference in the mean values (in channels). It reveals values of about 1-2% (FWHM). The tails in the projected spectra originate from the secondary reactions of the particles inside the E_{res} detector. Because of the higher energy the beam definition in this example is better. Although the selected masses are neighboring they are distinguished by their mean energy in the $CsI(Tl)$ detector.

The mass measurements with the Coulex beams reveal that the different channels are sufficiently distinguished by CATE. This information is used for the analysis of γ-rays detected by the Ge detectors. Such analysis showed γ-peaks, allowing to determine the $BE(2)$ values of the corresponding low spin excitation transitions for *i.e.* the ^{54,56,58}Cr isotopes [Buer05].

9.4 Mass determination for fragmentation reactions

A typical data set from a secondary fragmentation is the reaction of ^{55}Ni particles, with an energy of about 100 A·MeV, with secondary Be (S4) target with thickness of 0.7 g/cm^2. Many investigations have been performed using this data in order to correct the CATE energies for all possible effects, described in sections 7.1 and 7.2.3, and optimize the determination of the mass resolution. Hereafter, the analysis with central CATE detectors are described, where the used conditions are as follows:

- A/q and Z selection from the FRS identification on the ^{55}Ni fragments
- FRS triggered and matched events in the acquisition and when needed with the Ge events because of γ-rays correlation later
- Position correction or position cut on the corrected Si position spectrum in the center of the detector of ($\pm$5,$\pm$5) mm

- ToF-β correction of the CATE Si and $CsI(Tl)$ energies
- ToF-β cut of 0.3% on the experimental ToF distribution
- Time gates on the Si and $CsI(Tl)$ time spectra taking only the corresponding peaks into account in order to clean up the energy spectra of the Si and the $CsI(Tl)$
- $\Delta E - E$ cut for the investigation of a certain Z

In the investigations several other selections are also performed as:

- Degrader vs S2 position selection to avoid charge states
- Selection on the incoming ^{55}Ni position by the MW tracking
- pile-up rejector from the ToF scintillator at the final focus
- Correction by angle of the distributions created from the calculated energy at CATE (using the target effect) vs the measured energy in CATE

The second set of conditions is not of a big importance and is typically used to additionally clean the spectra from the CATE detectors. After applying the above mentioned selections and corrections the energies of the CATE-Si (ΔE) and CATE-$CsI(Tl)$ (E_{res}) are absolute calibrated (see section 11.2).

9.4.1 Linearization of the $\Delta E - E$ distribution

Further, these energies are treated with the linearization algorithm described in section 2.1.6 (eq.2.12-2.20). However, some changes are needed due to the specific data set. They are determined from the calibration coefficients and from Z of the incoming ions. The parameter g is calculated to be 0.0392, the parameter μ set to 0.7, the parameter λ equals to 0.0063 and the charge Z is 28 in this case. The corresponding calculation of the mass A after the substitution becomes than:

$$A = [\frac{(\Delta E + 0.0392 \cdot E_{res})^{1.7} - (0.0392 \cdot E_{res})^{1.7}}{1.8265 \cdot 10{-}4 \cdot Z^2}]^{1.4286} \tag{9.1}$$

In the calculation of the particle identification, PI, the particle charge is included, which means that it is different for the different charges. Two functions are constructed: one (PI_{fixed}), which does not consider variation in the PI from the charge and therefore the charge is fixed to the primary like Z=28:

$$PI_{fixed} = (w \cdot A + 16.8)/k \tag{9.2}$$

where the w coefficient is taken as before to 0.2 and k is a scaling coefficient equal to $2.5{\cdot}10^3$. The corresponding calculation of the mass difference ΔM is:

$$\Delta M = E_{tot}^p - E_{res}^p \tag{9.3}$$

The power p is varied between 1.67 to 1.75 until the optimal one for the data set is found to be 1.71 (see fig.9.12). The second function ($PI_{dynamic}$) is constructed including the Z dependence of ΔM. In this case the ΔM is calculated from the calibrated energies with power p=1.72 (eq.9.3) and then plotted for the different charges Z, which are observed in

the experimental data between 19 and 28. The data points are then fitted with a second order polynomial:

$$Z(\Delta M) = A + B_1 \cdot \Delta M + B_2 \cdot \Delta M^2,$$

with coefficients: A=2.6360, B_1=1.2457·10^{-4}, B_2=-1.1211·10^{-10}. The calculation of the $PI_{dynamic}$ includes this function as:

$$PI_{dynamic} = (Z(\Delta M) + w \cdot A - 2 \cdot Z(\Delta M))/k \tag{9.4}$$

here the coefficient w is varied between 0.2, 0.3 and 0.4 and the optimal value is found to be 0.4. The last, needs change also in the scaling coefficient k which is chosen to be 6·10^3 in this case and 5·10^3 for w=0.3 case. The identification of the different particles in terms of Z and A is then given by the correlation of the particle identification PI_{fixed} or $PI_{dynamic}$ vs the total energy E_{tot}. Such examples are given on fig.9.12.b for the $PI_{dynamic}$ with coefficient w=0.2, fig.9.12.c with coefficient w=0.3 and fig.9.12.d for w=0.4 for a small data set without gain shift in the CATE energies. This set is one of the 20 data sets discussed for fig.7.11 in section 7.2.3. It is visible, that the linearization is excellent and

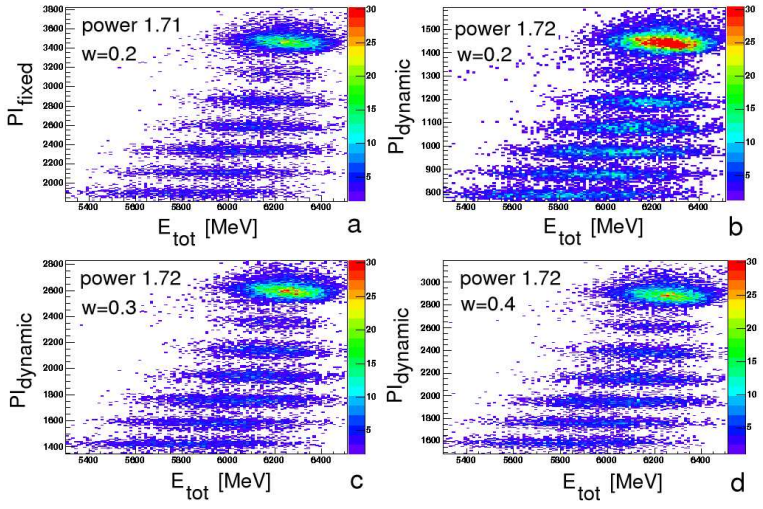

Figure 9.12: Particle identification from PI and E_{tot}: **a** - PI_{fixed} with w=0.2, **b** - $PI_{dynamic}$ with w=0.2, **c** - $PI_{dynamic}$ with w=0.3 and **d** - $PI_{dynamic}$ with w=0.4.

there are hints of the different masses inside the Z distributions. Additionally, a check is performed by including the polynomial function of the Z and ΔM in the calculation of the mass A in eq.9.1, where Z=28 is substituted with the $Z(\Delta M)$ function. Since this type of additional parameterization does not change the quality of the identification, it is excluded in the parameterization. As already mentioned, the quality of the $PI_{dynamic}$ with w=0.4 seems to be the best, what is confirmed in the analysis of the other data sets. Therefore, it is chosen for the further investigations.

The mass analysis are then performed by projecting a certain Z selected by the PI to the total energy axis. Such projections are made for a narrow selection from the $PI_{dynamic}$, as depicted on fig.9.13(top), and are plotted on the bottom of the figure for Z=28 to Z=21. The structure which can be seen in the projections represents the different masses. A slight shift in the projected structures exists, when the narrow gates are performed higher or lower in PI then the showed once. This means that the masses are overlapping and the main intensity is distributed tilted on an angle inside a Z spot.

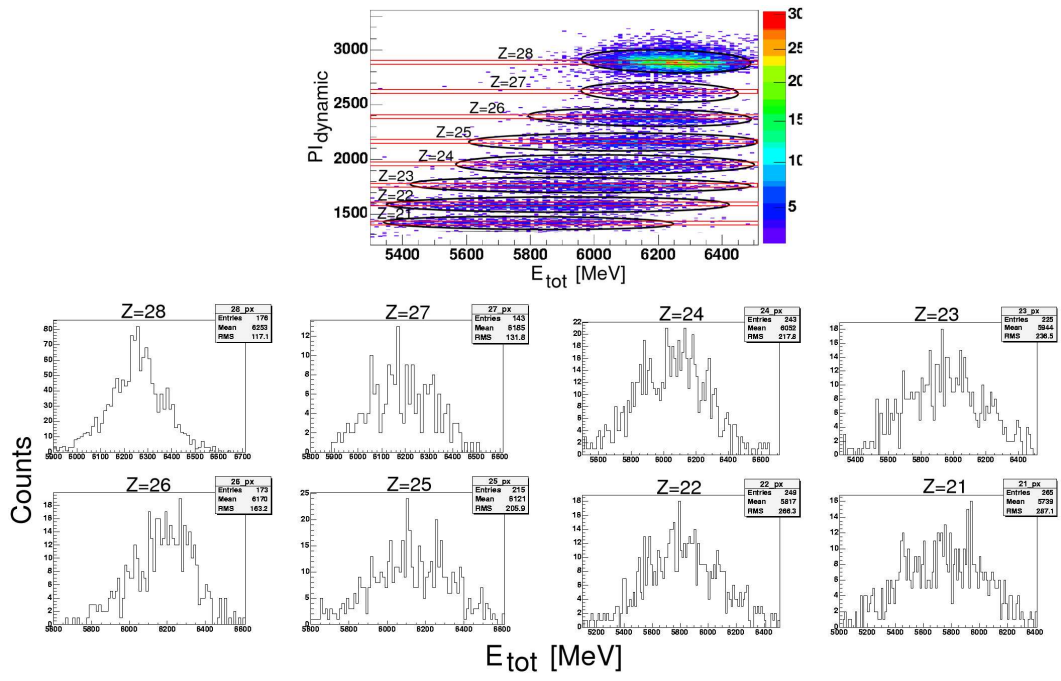

Figure 9.13: Cuts (top) for the different Z at the particle identification spectrum and projections (bottom) for the different isotopes on the total energy axis.

9.4.2 Comparison with simulation and mass resolution

To find out to which masses *i.e.* a Z projection corresponds a comparison with a simulation is performed using the LISE code [LISE04]. As mentioned in section 8.3, the real experimental resolution is reproduced by LISE together with the experimental conditions and the abundances for producing different nuclei in the reaction of fragmentation with ^{55}Ni particles. In a step back, a comparison of the $\Delta E - E$ distributions from the simulation and the experiment for this reaction shows an excellent Z resolution which is expected (see fig.9.14.a). As can be seen on fig.9.14.b the same charge resolution is present in the experimental data. To note here is the fact, that the abundance to produce the different

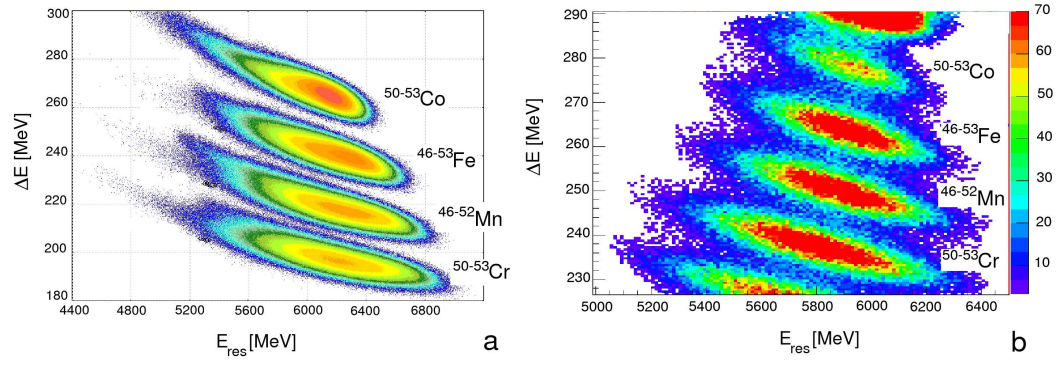

Figure 9.14: Comparison of **a** - a simulation and **b** - the experimental data for the reaction ^{9}Be(^{55}Ni,xn,yp).

isotopes decrease with increasing the amount of the knockout nucleons. However, in the experimental spectrum the Co isotopes are less intense than those with lower Z. This

is caused by the triggering condition which is present, namely the particle-γ coincidence. Since the Co nuclei, produced have less γ rays, they come with less abundance than *i.e.* the Fe, Mn or the Cr isotopes in the presented correlation. The other important discussion, which has to be done here is, that neither in the simulated data, nor in the experimental spectra a mass separation is present, such that two neighboring masses ($\Delta A/A \leq 1$) for this (A≈55) region can be distinguished. As mentioned already in section 7.2.2, the effect which influences severe the mass resolution in this case is the reaction mechanism and it can not be corrected as the other effects. This Goldhaber effect [Gold74] causes the widening of the particle momentum of 3.4 A·MeV, when calculated for the current case. The recent parameterization of the effect by Tarasov [Tara04], using low energy data, does not follow a Gaussian shape, but is slightly asymmetric. It reproduces asymmetric tails of the mass distributions to low energy which might better explain the experimental behavior. For a single Z, *i.e.* Z=25, all produced isotopes are overlapping and creating one common $\Delta E - E$ distribution, according to the simulation (see fig.8.2 in section 8.3).

When a separate calculation for each single isotope is performed, a clear shift in the centroid of the E_{res} and of the total (ΔE+E_{res}) energy distribution is observed (see fig.8.4). Simulated total energy distributions for each Mn isotope are presented on fig.9.15

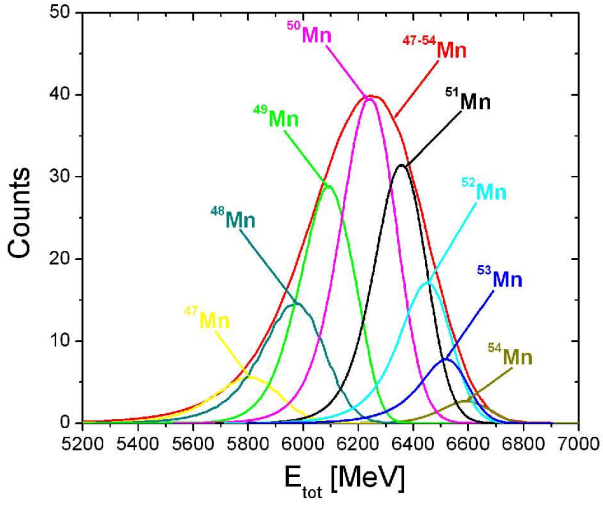

Figure 9.15: A simulated single mass distribution spectrum for the Mn isotopes, produced in the reaction ^{9}Be(^{55}Ni,xn,3p). The total mass distribution for all $^{47-54}$Mn is plotted as a top curve in red.

and the total mass distribution for Z=25 is plotted as an envelope curve. The corresponding experimental data can be compared with the peak positions and widths with the simulation in order to identify the different masses. The mass resolution from the simulation found from the difference between every two mass distributions is about 2.6-3.5%.

An experimental example of the mass spectrum for the Cr isotopes is presented on fig.9.16. It is constructed after an absolute energy calibration and linearization of the data. The E_{tot} spectrum for $Z = 24$ isotopes is fitted with a multiple Gaussian fit and deconvoluted to single distributions (with reduced $\chi^2 \leq 15$; $\chi^2 = \chi^2/n$, where n is the number of degrees of freedom). With respect to the centroids and widths of the simulated single mass distribution the different products from the reaction with the ^{9}Be target are identified. Two of the distributions, which will be used in the next section, for ^{49}Cr and ^{50}Cr are marked with solid and dash-dotted lines, respectively. The experimental mass resolution determined from the difference between every two masses is between 2.2 and

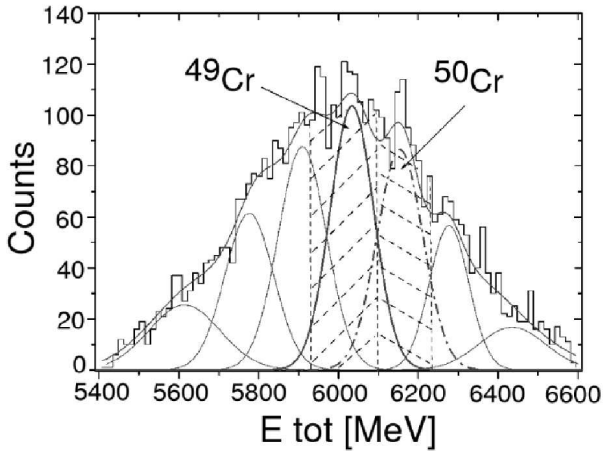

Figure 9.16: Measured total energy spectrum (E_{tot}) and the identified mass distributions for the ^{49}Cr (solid line) and ^{50}Cr (dash-dotted line) isotopes produced in the reaction ^{55}Ni(^{9}Be,xn,4p).

3.1%. The mean value of 2.5% is present for the rest channels from the fragmentation reaction and as can be seen on fig.9.13 is of the same order.

9.4.3 Channel selection by CATE

To inspect the mass correlation with the Ge detectors, which have already a good energy resolution for registering γ rays, the CATE corrections and linearization are implemented in a user code which creates Ntuples [CERN95] of these data. Another user code takes afterwards the Ntuples and constructs (event by event) histograms in the desired correlations.

The 20 data sets, mentioned in the section 7.2.3 have to be gain-matched in the sense of the time shifts (see there fig.7.11), to avoid the jitter in the mean values of the PI and E_{tot}. The channel selection by CATE is applied afterwards in order to select the nucleus, whose γ-rays are detected by the RISING-Ge detectors. A particle-γ correlation is constructed when the particle is tracked before the secondary target with the help of the MW detectors and after the secondary target with the help of the CATE-Si detectors (see fig.6.1). The particle-γ angle, $\theta_{p\gamma}$, is calculated from the measured after the secondary target particle angle, θ_p, by CATE and the γ-ray angle, θ_γ, determined from the hit in a single Ge cluster capsule, which has already in advance known geometry with respect to the target. This angle is important for the Doppler correction (E_{dopp}), calculated from:

$$E_{dopp} = \frac{1 - \beta_{corr} \cdot cos(\theta_{p\gamma})}{\sqrt{1 - \beta_{corr}^2}}$$

and applied to the measured, calibrated energy of all Ge-Clusters [CLU] and Ge-Capsules [CAP] ($E_{calibrated}[CLU][CAP]$):

$$E^{Doppler}_{corrected}[CLU][CAP] = E_{calibrated}[CLU][CAP] \cdot E_{dopp}.$$

β_{corr} in these calculations is the corrected velocity calculated from the ToF measurement (β_{ToF}). It is corrected by a theoretical velocity (β_{theory}), calculated from a simulation like LISE, MOCADI or ATIMA. The calculation should be performed for the nucleus of

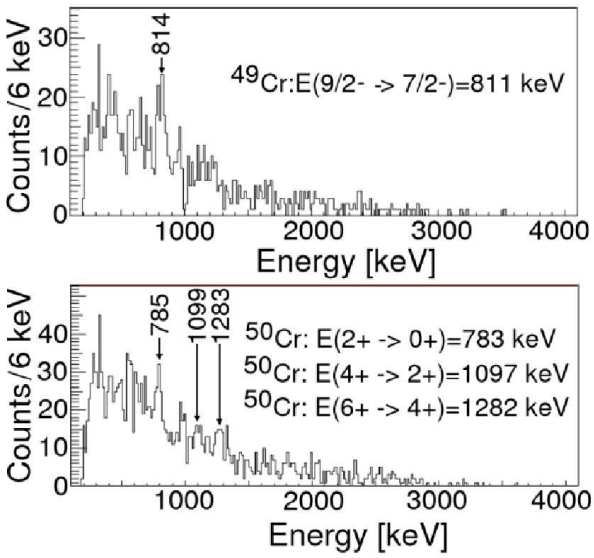

Figure 9.17: Measured γ-spectra for the ^{49}Cr (top) and ^{50}Cr (bottom) isotopes. The γ-transitions are identified by use of nuclear data center ENSDF [ENSD04].

interest, and the velocity normalized to the velocity of the primary like beam $\beta_{primary}$ (in this case ^{55}Ni) particles:

$$\beta_{corr} = \frac{\beta_{theory}}{\beta_{primary}} \cdot \beta_{ToF}, \quad \beta_{ToF} = \frac{c_1}{c_0 - ToF[ps]} \tag{9.5}$$

where $c_{0,1}$ are the calibration factors from the β-ToF calibration (see Appendix 2), which are calculated in correspondence with the losses in the final focus, including CATE. The $c_{0,1}$ coefficients equal to 264355.35 and 124983.03, respectively. The velocity $\beta_{primary}$ for the ^{55}Ni equals to 0.568 and the theoretical velocity β_{theory} calculated with LISE and ATIMA gives a value of 0.46536.

The total actions to the Ge-detectors energy are:

- Particle-γ trigger in the acquisition, where FRS and Ge branches are matched together
- Ge energy calibration, time alignment, addback
- Time gate on the Ge's around the peak of the main contribution (in order to clean the energy spectra from unwanted contributions, that appear for reactions not connected to the secondary target)
- Multiplicity 1 and 2 selection (since these reactions have high multiplicity origin in comparison to the Coulex reactions)
- A CATE telescope selection (the central CATE telescope has the highest amount of detected particles)
- Tracking of the incoming particles (with MW's) and outgoing particles by CATE-Si (fig.6.1) to determine the angle θ_{p_γ}

- Doppler correction with velocity corrected using the measured ToF, the velocity of the primary beam and theoretical velocity
- Z gate (on Cr isotopes) by CATE from the identification $\mathrm{PI}_{dynamic}(\mathrm{E}_{tot})$ correlation
- A gates (on ^{49}Cr and ^{50}Cr isotopes) by CATE on the E_{tot} projection for the Cr isotopes, according to the theoretical position of the masses.

All these conditions cleaned the background at low energy but also decreased the statistics of the total Ge energy spectrum. However, no gamma peak corresponding to a Cr isotope is observed. The reason is the velocity, used for the Doppler correction.

The calculated velocity (β_{theory}) could not assume where the interaction takes place in the target, where and when exactly this nucleus is produced and if it does not travel already inside the target media with this velocity. The last would correspondingly decrease it. Therefore, the theoretical velocity in the above calculations is replaced by other velocity, calculated from the total energy of the isotope deposited at CATE, being an experimental velocity $\beta_{expCATE}$. Since the Cr isotopes (*i.e.* ^{49}Cr and ^{50}Cr) have been identified from the abundance of the main isotope, the mean values on the experimental E_{tot} spectrum have energies $\mathrm{E}_{tot}^{^{49}Cr}$, $\mathrm{E}_{tot}^{^{50}Cr}$. Thus, a simple calculation from energy to velocity is sufficient:

$$\beta_{expCATE}^{^{49}Cr,^{50}Cr} = \sqrt{1 - \left(\frac{1}{\frac{E_{tot}^{^{49}Cr,^{50}Cr}}{931.5} + 1} \right)^2}$$

The β values for the ^{49}Cr and ^{50}Cr isotopes are different than theoretically calculated and equal to 0.45592 and 0.45606, respectively. When they are used for the calculation of the β_{corr} in eq.9.5 instead of the β_{theory}, the Doppler correction for the Ge detectors becomes more precise. Ge spectra, achieved under the same conditions which are itemized above, present the γ-lines, shown in fig.9.17 (top) for the ^{49}Cr and on fig.9.17 (bottom) for the ^{50}Cr.

The observed γ-rays correspond to the known transitions in these nuclei. These lines can not be seen when applying only Z selection from CATE, which proves the importance of the both Z and A identification after the RISING secondary target. The unidentified lines in the spectra originate from higher excited states and from (n,γ) reactions in the Ge detectors.

The described example proves how important is the use of the CATE detectors for the identification after the secondary target. Although quite complicated for use because of the corrections on the energies, the linearization and the calculations, the fits and the comparisons with a simulation, and the limitation by the reaction mechanism, the CATE detector is the first array that identifies heavy particles in a relativistic energy regime and even more, as already proven, it works much better than expected in the simulations.

Chapter 10

Summary

Different investigations were performed in order to develop a new $\Delta E - E$ calorimeter device, which has to identify the different reaction channels after a secondary target in position, charge Z and mass A. This includes Si semiconductor tests to study of the position and the energy response of the ΔE detector candidate. The achieved position resolution of less than 3 mm in each direction and energy resolution for α-particles of about 1.5% (FWHM), and for ^{86}Kr and ^{58}Ni heavy ions with energy between 120 and 280 A·MeV of about 2% (FWHM), is completely sufficient for the intended use. Investigation of different scintillation materials showed, that the most suitable material for residual energy deposition (E_{res}) or mass spectroscopy measurement is the $CsI(Tl)$. Coupled to PMT (for low particle rates) or to PIN diode (for high particle rates), it manifested that the $CsI(Tl)$+PMT has an intrinsic energy resolution of 0.5% (FWHM) for ^{238}U and ^{197}Au heavy ions and that the $CsI(Tl)$+PIN diode has an intrinsic energy resolution of 0.7% for ^{86}Kr and ^{58}Ni heavy ions.

Selecting the Si and $CsI(Tl)$+PIN detectors, the new $\Delta E - E$ calorimeter telescope CATE is designed with geometrical and measured efficiency of 92% with respect to the RISING secondary target location. It is successfully employed in the RISING experiments at GSI for the particle position, Z and A determination at energies between 90 and 400 A·MeV and particle rates from $1{\cdot}10^2$ up to $5{\cdot}10^4$ p/s. The good (x, y) position resolution of the Si detector array of better than (3 x 3) mm^2 for the Si (PIPS type) detectors and better than (5 x 5) mm^2 for the Si (IPP type) detectors, allows precise measurement of the particle scattering angle after the secondary target. The CATE-Si array distinguishes the different particle charges with an unique resolution $\Delta Z/Z$ of about 0.7 (FWHM) for heavy ions with $Z \in$[24,50] and $A \in$[54,112] with relativistic velocities (β) from 0.41 up to 0.75 v/c and not depending on the reaction type. The CATE (ΔE and E_{res}) energy resolution is influenced by (i) the impact position, (ii) the velocity distribution, (iii) the particle rate and (iv) spill structure. These detector and beam related effects need to be corrected for optimal resolution. Moreover, the mass resolution of the CATE-$CsI(Tl)$ array is affected by the reaction mechanism. For knock-out and fragmentation the momentum spread limits the resolution considerably. In fragmentation reactions of heavy ions with $Z \in$[21,28] and $A \in$[40,58], the mass resolution $\Delta A/A$ is about 2-3% (FWHM). While for Coulex of secondary particles with $Z \in$[24,50] and $A \in$[54,112], the mass resolution can be determined to about 1-3% (FWHM).

Thus, the intrinsic reaction channel identification with the first calorimeter telescope CATE, that works at relativistic energies and with heavy ions is unique. It is employed in many experiments for the selection of the particles, whose γ-rays are detected by the RISING Ge detectors.

Chapter 11

Contributions of the present work and Outlook

11.1 Contributions

The main contributions of this work are as follows:

- Developed, tested, calibrated and used, is a new $\Delta E - E$ ($Si - CsI(Tl)$) calorimeter telescope CATE, for identification and scattering angle determination of the relativistic heavy ion reactions channels, outcoming from the RISING secondary target.

- Created is a new method for the identification, using corrections and linearization of the measurement, which allows the determination of the products from relativistic Coulomb excitation and secondary fragmentation reactions.

- The main parameters of the CATE system are:
  + Position (x, y) sensitivity of $(\Delta x, \Delta y) \approx$(3,3) to (5,5) mm^2,
  + Charge Z resolution of $\Delta Z \approx 0.7{-}0.8$ Z,
  + Mass A resolution $\Delta A/A \approx 1{-}3\%$.
  These parameters are, in principle, sufficient for the performed "fast beams" campaign RISING experiments. Since the energy resolution $\delta E/E$ of the $CsI(Tl)$ detectors is $\approx 0.7{-}1\%$, a ToF measurement after the secondary target, would allow a mass determination $\Delta A/A \approx 0.7{-}1\%$.

11.2 Outlook

The investigations about the Si and $CsI(Tl)$ detectors, as well as the development of a new calorimeter telescope array, have an importance in the detector physics and in its nuclear physics applications. The investigations of the detector effects, can be used for future improvements in their materials, couplings and integrated electronics. While the investigations on the beam effects, are of experimental advantage for the complicated beam studies at the FRS at GSI.

The $\Delta E - E$ method, that has been used, shows a good compatibility with the $B\rho$-ToF method for identification of secondary reaction products. Compared to the second method, it requires less space in the experimental set-up and less complicated devices, electronics etc. It is compact, easy to operate, monitor and exchange partially if required

by an experiment. The data analysis become easy and fast with the developed methods. Therefore, the CATE system is successfully used in many experiments that continue in present time for the identification of middle heavy and heavy particles at energies above 100 A·MeV, and is the important ion triggering channel device for RISING.

Despite the sufficient energy resolution of the CATE detectors, no unique mass resolution beyond A≥40 is possible due to the momentum spread in knock-out and fragmentation reactions. If the device is combined with an additional ToF measurement after the secondary target in order to perform E_{tot} - ToF measurement, the channel selections for heavier masses would be possible, prior to any experimental corrections. This is planned for the next version of CATE.

Appendix 1

A.1. The FRS identification detectors

As pointed out in section 4.1 the identification of the FRS is done by using several beam diagnostics elements. Their description and operation is described below. To have a precise beam tracking and identification with them an absolute calibration is usually performed, as described in the Appendix 2.

A.1.1. The multi wire proportional counters

Multi Wire Proportional Counters (MWPC or only MW) have been developed at GSI [Stel91] for the detection of heavy ions at relativistic energies and beam tracking. Usually two Multi Wires can be used to track the beam along the FRS and to give the beam position at the S2 and S4 focal planes, when setting up the beam line.

A.1.1.1. Description

They have a size of (20 x 20) cm^2 and a thickness of 10 cm. A schematic layout of a two stage MW is shown in fig.11.1.a. In most cases the MW pockets have 100 μm Ti

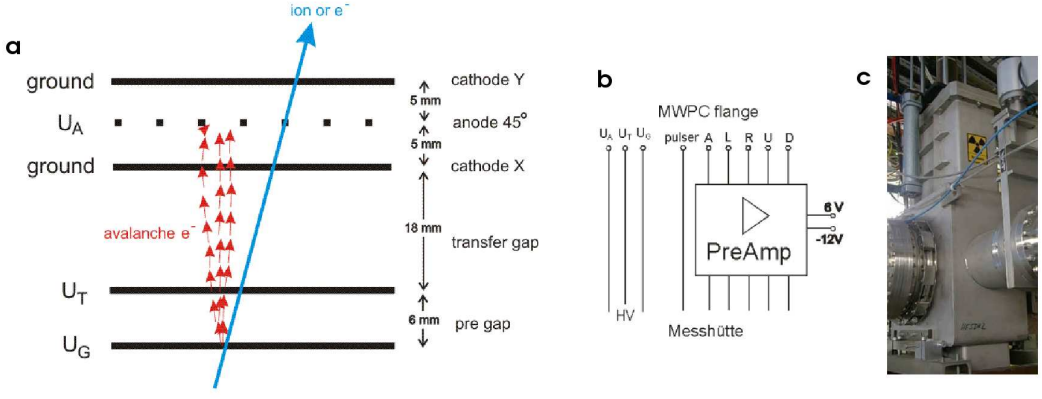

Figure 11.1: **a** - Schematic layout of a MW [Stel91], **b** - the preamplifier connection [Weic04] and **c** - a photograph of a MW chamber on the FRS beam line.

(or Fe) windows on both sides. The MW at the final focus (MW 2) stands on air and in this case the gas volume is separated from the air by 25 μm Kapton foils. The planar anode A consists of 20 μm gold plated tungsten wires with a pitch of 1 mm while the cathodes X and Y are made of 50 μm gold plated tungsten wires with a pitch of 1 mm. The wire directions in X and Y are orthogonal to each other, while the wires of plane A are diagonal to them. Furthermore, a planar electrode structure is added consisting of

two meshes labeled G and T with a spacing of 6 mm. Typical potentials applied to the electrodes are indicated in fig.11.1.b and readout planes X and Y are on ground potential. The detector is filled with a gas mixture of 80% argon, 19% CO_2 at a pressure of 1 atm [Stel91, Weic04].

A.1.1.2. Operation

The electron avalanche caused by the passage of a charged particle through the detector is collected on the anode A and induces positive signals on the adjacent wires in the X and Y cathodes. These signals are used to determine the (x, y) positions of the incident ion by the delay line readout technique [Stel91]. Each wire of the planes X and Y is connected to a tap of a delay line with a delay of 4 ns per tap. The signal propagates through the left and right side of the delay line. At the end of the delay line, the signals are amplified and fed in the STOP of a TDC while the START is derived from the anode. The time difference between the left and the right side of the delay line is a measure of the position with a resolution better than 1 mm, whereas the sum of left and right should be a constant, namely the total length of the delay line (≈1 s). The Multi Wires are stored and operate in chambers. The Preamplifiers are located directly at the flange with internal connectors to the Multi Wires as shown on fig.11.1.b. For testing the pulser entrance is fed directly to the center of the delay lines. The installation chamber in the beam line is photographed on fig.11.1.c.

A.1.1.3. Multi-wire detector signals

Each multi-wire detector delivers five signals: one anode time and four cathode times, measured with a TDC relative to a common start (normally the accepted trigger). Using known properties of the MW delay lines, the times can be related to position of the interaction in the detector [FRSA04]. In order to select 'good' events, a condition (called sum condition) placed on the respective sums of the X and Y cathode times should be fulfilled. To make these sums independent of trigger timing, the anode (A) times are subtracted for MW detector number i:

$$MW^{x}_{sum} = MW^{x}_{right-tdc}(i) - MW^{A}_{tdc}(i) + MW^{x}_{left-tdc}(i) - MW^{A}_{tdc}(i);$$

$$MW^{y}_{sum} = MW^{y}_{up-tdc}(i) - MW^{A}_{tdc}(i) + MW^{y}_{down-tdc}(i) - MW^{A}_{tdc}(i)).$$

A.1.1.4. Position determination

From the cathode time differences, the 'relative' x and y positions can then be determined for those events fulfilling the sum conditions:

$$MW^{x}_{rel}(i) = 1/2 \cdot (MW^{x}_{right-tdc}(i) - MW^{x}_{left-tdc}(i));$$

$$MW^{y}_{rel}(i) = 1/2 \cdot (MW^{y}_{up-tdc}(i) - MW^{y}_{down-tdc}(i)).$$

An appropriate calibration is performed to determine the positions in mm (see Appendix 2 - MW calibration)

A.1.1.5. Particle tracking

At any given focus equipped with two (or more) position-sensitive detectors, the trajectory of each beam particle can be extrapolated (or tracked). For determining the width of the particle position distributions at the intended focal planes and/or at the location of other detectors. The distances involved, *i.e.* between the MW detectors themselves combined with the x and y positions between two Multi Wires are needed for the particle angle determination.

A.1.2. The MUSIC chambers

MUlti Sampling Ionization Chambers (MUSIC) installed at the exit of the separator are used to measure energy loss of the ions. Two different MUSIC detectors the 'old' type with 4 anodes and the 'new' Munich design with 8 anodes are used in the standard FRS tests and in RISING.

A.1.2.1. Description

The 'old' chamber MUSIC, shown in fig.11.2.a, consists of a cathode, a frisch grid and an anode plane divided into four independent volumes of gas with a total efficient length of 40 cm [Pfue94]. It covers an area of (200 x 200) mm^2 and it is operated sustaining

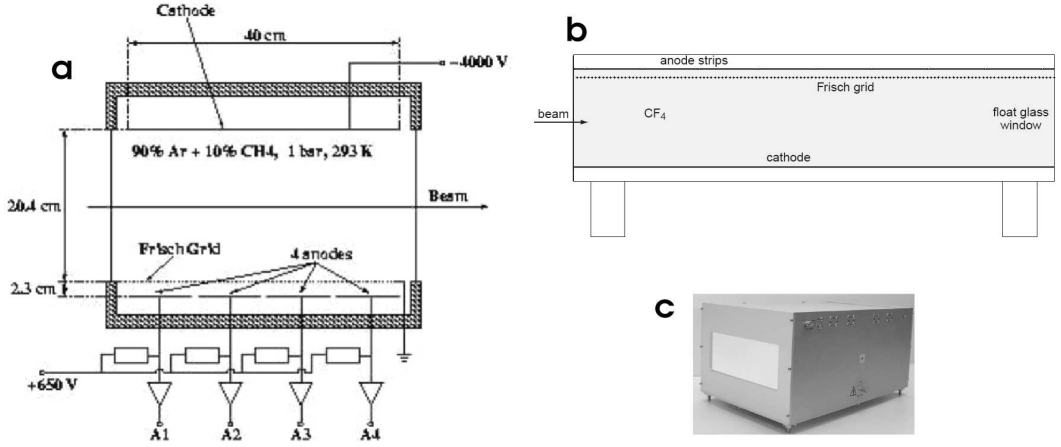

Figure 11.2: Schematic layout of **a** - MUSIC [Pfue94] and **b** - MUSIC80; **c**- a photograph of MUSIC80 [ScSt01].

a constant flow of a mixture of 90% argon and 10% methane at atmospheric pressure. Entrance and exit windows were made of Kapton[1] foil [DuPo04] covered by an aluminum layer. The electric field is horizontal, perpendicular to the direction of the heavy ion beam. The four sections of gas volume deliver four energy loss signals through four anodes, each coupled to a charge sensitive preamplifier [Pfue94]. This MUSIC type stands on a counting particle rate to max 10 kHz [FRSG04].

The 'new' type ionization chamber MUSIC80 is a fast (see fig.11.2.b,c [ScSt01]), multiple sampling ionization chamber with 8 anode strips and a vertical drift length of 80 mm. It is operated with pure CF_4 at room temperature and atmospheric pressure as a counting gas. The homogeneous entrance windows consisting of thin float glass with integrated

[1]Kapton is Trademark of DuPont

field homogenisation enable a compact setup. The field homogenisation consist of 1 μm aluminum strips, deposited on the float glass by photo-lithography and a voltage divider with resistors glued directly onto the glass plate. The anode strips are read out with an optimized charge sensitive preamplifier and shaper combination for particle rates up to 200 kHz [ScSt01].

A.1.2.2. Operation

Since the number of generated electrons in the counting gas is roughly proportional to the square of the charge of the penetrating particle, the output voltage of the shaper is a measure for the atomic number of this particle Z. Using an additional fast start signal (scintillator FRS trigger signal) the drift time of the electron cloud provides information about the vertical position of the passing particle. The stop signal can be derived from the common timing output of the shaper module [ScSt01].

The high voltage input is used to supply the cathode and the Frisch grid (see fig.11.2.b) and a filter circuit for the cathode voltage is included in the chamber. The effective potential over the active drift distance is equal to 81% of the HV input voltage. To cover the complete dynamic range of the charge signal caused by particles with nuclear charges from Z=92 to Z=3 (variation by a factor 10^3) three sets of preamplifiers are supplied. Additionally the shaper sensitivity can be varied by a factor of eight [ScSt01]. The independent MUSIC anodes which deliver energy loss (and time) information.

A.1.2.3. Energy loss

The raw ADC signals, read out from the anodes (A), numbered with i, are corrected for the pedestal values (see section 3.2.3) refer in the following as offsets:

$$MUSIC^{A}_{energy}(i) = MUSIC^{A}_{adc}(i) - MUSIC^{A}_{offset}(i).$$

Afterwards these anode values can be used to form pairwise products which are combined to 'truncated' mean values - this procedure results in better resolution than simple averaging. In the case of 4 anodes:

$$r_1 = MUSIC^{A}_{energy}(1) \cdot MUSIC^{A}_{energy}(2);$$

$$r_2 = MUSIC^{A}_{energy}(3) \cdot MUSIC^{A}_{energy}(4);$$

$$MUSIC_{energy} = \sqrt{\sqrt{r_1} \cdot \sqrt{r_2}}.$$

Correspondingly, in the case of 8 anodes two more equations are added and they also contribute to the calculated energy (ΔE). Typically, using the MUSIC energy loss information the atomic charge of the particles can be determined after an appropriate calibration procedure (see Appendix 2 - (MUSIC - ΔE and Z calibration)). The charge resolving power of $\Delta Z/Z \leq 1/100$ is usually present for the different isotopes [FRSG04].

A.1.3. The FRS degraders

The energy degrader system (see fig.11.3.a.,b.), which is positioned in the dispersive intermediate focal plane (S2) of the FRS, consists mechanically of three different parts [Hane89], which altogether form a wedge of aluminum with adjustable slope and thickness. By adjusting the slope of the wedge, different ion optical conditions can be fulfilled

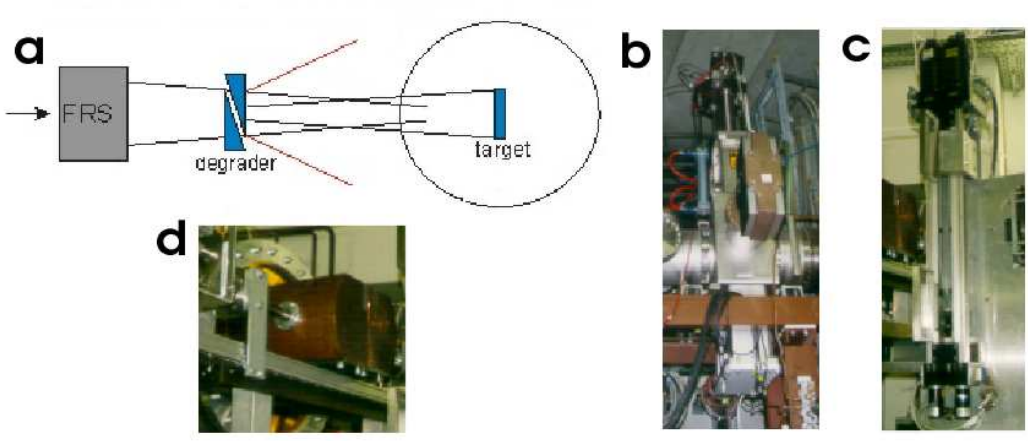

Figure 11.3: **a** - Schematic representation and **b** - photograph of the degrader at S2; photograph of the **c** - degrader at S4, **d** - copper slits at S4.

which result in two operation modes: an achromatic mode and a mono-energetic mode [Weck90]. In the intermediate focal plane, the momentum distribution of the produced ions is dispersed along the wedge. If the slope of the wedge is adjusted in such a way that the momentum of the selected ions decrease by a constant factor due to their energy loss in the wedge, then the resulting momentum distribution of the ions behind the degrader is refocused on a small spot at the exit of the degrader (the *achromatic mode*). If the slope of the wedge is adjusted in such a way that all different momentum distributions of the selected ions in front of the degrader are exactly compensated by their different path lengths through the wedge, then the degrader acts in the *mono-energetic mode*. In this case, all ions are deflected by the second dipole stage in the same way and their spatial distribution at the exit of the separator stays the same as in the intermediate focal plane. During the experimental tests and the RISING experiments (see sections 3.2.2 and 7.2) the first degrader is operated in achromatic mode with thicknesses between 0 and 4000 mg/cm^2.
The second degrader (fig.11.3.c.) is placed at the last focal plane (S4) between two MUSIC chambers, usually is made of glass and it works in the same way as the first one. During the test experiments (see sections 3.2.2 and 3.2.2) the degrader is used only for slowing down the beam energy. Its thicknesses used varied between 0 and 2633 mg/cm^2. Therefore in these cases, secondary reactions occurred also in the glass material.

A.1.4. The FRS slits

Slits, usually made of two or four thick copper blocks, as those shown of fig.11.3.d, are used at every focal plane to cut off the momentum distribution in x and y direction. Since the different masses or/and charge states of the selected ions come at different positions (as shown on one of the examples in fig.**??**) these stopping blocks are helpful for the proper ion selection. The slids are placed in vacuum and are driven by robots. They are calibrated in advance for (x,y) position. At the final focus the silts are typically in air and only in x direction because of the momentum distribution of the ions. It is a consequence due to the acceptance of the FRS, that is at the order of 1-1.5%.

A.1.5. The Scintillators

The FRS standard scintillators are made of thin plastic material with thickness typically of 0.5 to 5 mm. Their fast signal is read out simultaneously by a pair of photo-multiplier tubes and gives energy loss and timing information. They have a typical intrinsic time resolution of 100 ps (FWHM) [Geis92].

A.1.5.1. Energy loss

The scintillator energy loss information (collected using a QDC), does not have very high resolution, but is useful for vetoing secondary reaction products. For scintillators with two PMTs (left and right sides), the energy loss is estimated by taking the square root of the product of the two individual QDC signals, after subtracting the corresponding pedestal offsets.

A.1.5.2. Position information

The position information from the scintillators is also used in the FRS identification, but before that certain corrections are applied as described in Appendix 2 -Scintillators calibration.

A.1.5.3. Time-of-flight (ToF)

The ToF of particles through the FRS is determined by measuring and averaging time differences between the two scintillators, both with simultaneous readout of the right and left sides, placed at middle (S2) and final focal (S4) planes (see fig4.3.a). The first scintillator (SCI 1) gives the *stop* signal (after an electronics delay) for the ToF measurement, whereas the second scintillator (SCI 2) at the final focal plane gives the *start* signal.

In order to partially compensate for differences in path length for particles that deviate from the ideal trajectory, the right-right and left-left time differences are averaged [FRSA04]. The ToF, calibrated (in ps/ch), between S2 and S4 is:

$$SCI^{ToF}_{1-2} = \frac{SCI^{ToF}_{1L-2L} + SCI^{ToF}_{1R-2R}}{2}.$$

The ToF calibration is experiment-specific and is determined in a calibration procedure (see Appendix 2 - ToF calibration). Therefrom the experimental velocity β is determined using the distance about 37 m between the middle and the final focus.

Using the information from all these detectors a calibration of the FRS is performed (see Appendix 2). Combined with the ion optical separation of the FRS it leads to an unique particle identification (see Appendix 2 -Particle identification), used afterwards for different studies as *i.e.* in the RISING campaign.

Appendix 2

A.2. Calibration of the FRS

In this Appendix 2 the calibration of the FRS detectors will be described, together with several experimental results from such an offline procedure with a primary ^{58}Ni beam. Usually, this calibration is unique for every separate experiment at the FRS, including the experimental tests described in sections 3.2.2 and 3.2.2, and every RISING run. It is roughly done online but is preferable to be more precisely revised (or repeated in the offline analysis), in order to precisely set the beam conditions and investigate further the performance *i.e.* of the CATE detectors (see section 5.1).

Typically, several primary beam energies with low particle rate (about 1 kHz) are chosen, which in range surround the energy during a fragment production, to perform calibrations and corrections for every beam diagnostics element. This includes exact position in the set-up, absolute ToF, charge (Z) and mass (A) identification, as mentioned in the Appendix 1. During the calibration and the real run the operational voltages, gas pressure, dynamic and electronic ranges of the detectors (and their readouts), amplifications, delays etc. are kept unchanged.

A.2.1. The multi wire : (x, y) calibration

The beam tracking detectors, the Multi Wires (MW) [Stel91], need precise source and in-beam calibration in order to determine the absolute position calibration parameters. As described in Appendix 1 (MWPC - Position determination), these are the MW^x_{slope} and MW^x_{offset} (same for y), expressed in mm/ns and mm, respectively [FRSA04]. Further only the determination in one direction (x) will be described.
After an electronic calibration of their readout TDC, with used range of 1200 ns for 4096 channels (0.29297 ns/ch) and delay line value of 2 mm/4 ns, the theoretical slope parameter is calculated to be 0.0732. However, in real experiment this parameter is different and can be determined *i.e.* from the active size of the detector (200 mm) divided by the number of channels which correspond to full size irradiation (expressed in mm/ch). The offset parameter can also be determined from such a measurement as a mean value of the constructed position spectrum (in ch). Note that before accumulating these data both slope and offset parameters should be set as 1 and 0, respectively.

A.2.1.1. Source calibration

To determine the real size of both MW 41 and MW 42 used in the RISING set-up (see fig.4.3.a.) a source measurement with ^{90}Sr with an aperture in front is performed [Beck03]. Nine equidistantly spaced (by 5 mm) holes with size of 2 mm diameter are placed in tree by tree geometry on the aperture. Different sets of data are recorded corresponding to different positions of the source in front of an aperture hole. Example

spectra from this measurement are shown on fig.11.4. The accumulated *i.e.* MW 42 (x, y) position is depicted on fig.11.4.a. In advance gate conditions are set to the sum spectra (see Appendix 1 (MWPC - Position determination)) from the four cathodes (one of them is visible on fig.11.4.b.) as shown on fig.11.4.c,d. The obtained positions in x and y under these conditions are depicted on fig.11.4.e,f. In principle from this single

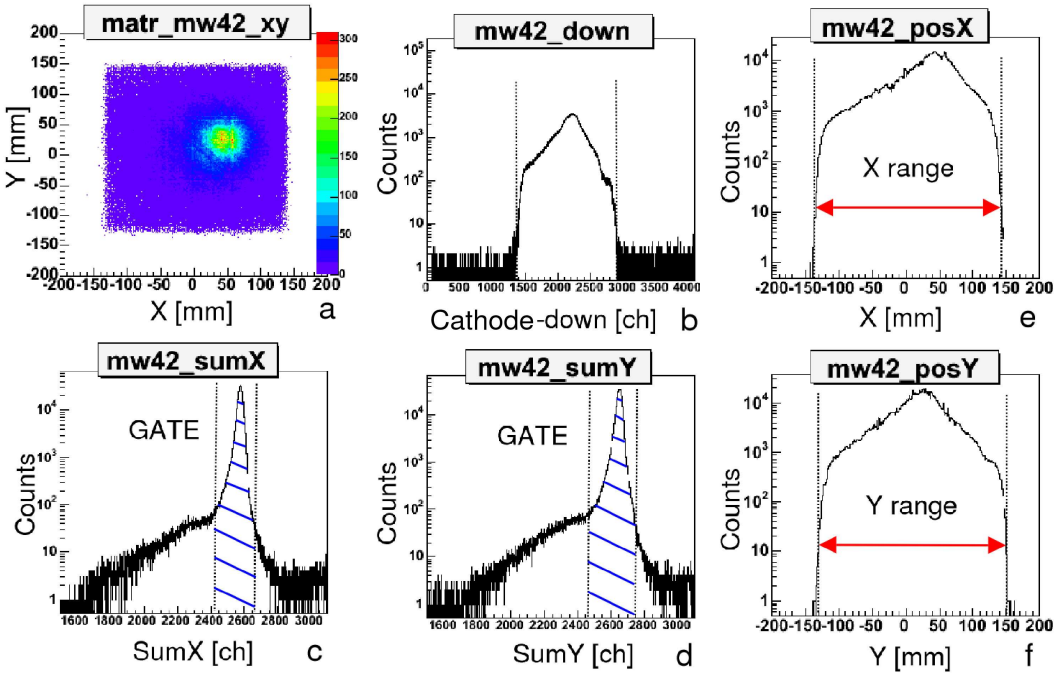

Figure 11.4: MW 42 spectra from a source measurement: **a** - (x, y) position, **b** - a cathode, **c** - sum of anode signals in X, **d** - sum of anode signals in Y, **e** - x position and **f** - y position.

measurement the position resolution of the MW can be obtained knowing the size of the hole. This value is corresponding to the FWHM of the shown x and y spectra (MW 42) and has a value of $\approx$ 50 ch (for both of them). Using the theoretical slope parameter that corresponds to a resolution of $\approx$ 3.5 mm (FWHM). In principle the MW have much better intrinsic resolution (which can be studied with removed entrance windows). In this measurement they caused certain scatterings and deteriorated the absolute position resolution measurement. By accumulating all sets with different source positions the total size of the MW is irradiated. Using the same type of sum signal's gates the slope parameters are deduced from the projections in x and y. From the source measurement of MW 41 the slope parameters for x and y are: 0.07380074 and 0.07326007, respectively and for MW 42: 0.07692307 and 0.06896517, respectively. The errors in the (software) determination are $\approx$ 2% when $\leq$ 10 counts were considered as a background.

A.2.1.1. In-beam calibration

The in-beam measurement aims to find the absolute 'zero' of the detectors and determine the offset parameters directly for the fragment's case. For that purpose the secondary ^{55}Ni particles with $\approx$ 160 A·MeV at the final focus (S4) and particle rate of about 4 kHz are selected. The beam is centered in x and y direction with the help of steerer magnets [FRSO04]. Using slids (see Appendix 1 (Slids)), located between the MW's in the RISING set-up, two sets of measurements are performed at their different positions. When the slids

are closed at ± 35 mm in x direction and ± 2 mm in y direction (estimated error in these positions is ≈ ± 0.2 mm) the MW 41 and MW 42 are irradiated as shown on fig.11.5.a and b, respectively. More precise is the measurement with slids closed at ± 1 mm in x and ± 2 mm in y direction (with the same error). The response of the MWs (41 and 42) is shown on 11.5.c and d, respectively. Setting only the slope parameter, determined as described above, the projections in x and y of the position spectra are reconstructed. The narrow widths of about 8.0 mm and 10.3 mm for MW 41, and 2.8 mm and 5.2 mm for MW 42 allow the precise determination of the mean values for both detectors using a Gaussian fit. These centroids correspond to the offset parameters namely 1.186 and 10.906 in x and y for MW 41 and -3.463 and 13.759 in x and y for MW 42. The estimated errors for the measurement from the mechanical placement and the fitting procedure together does not go beyond 10%. The parameters are revised afterwards with opened slits and are

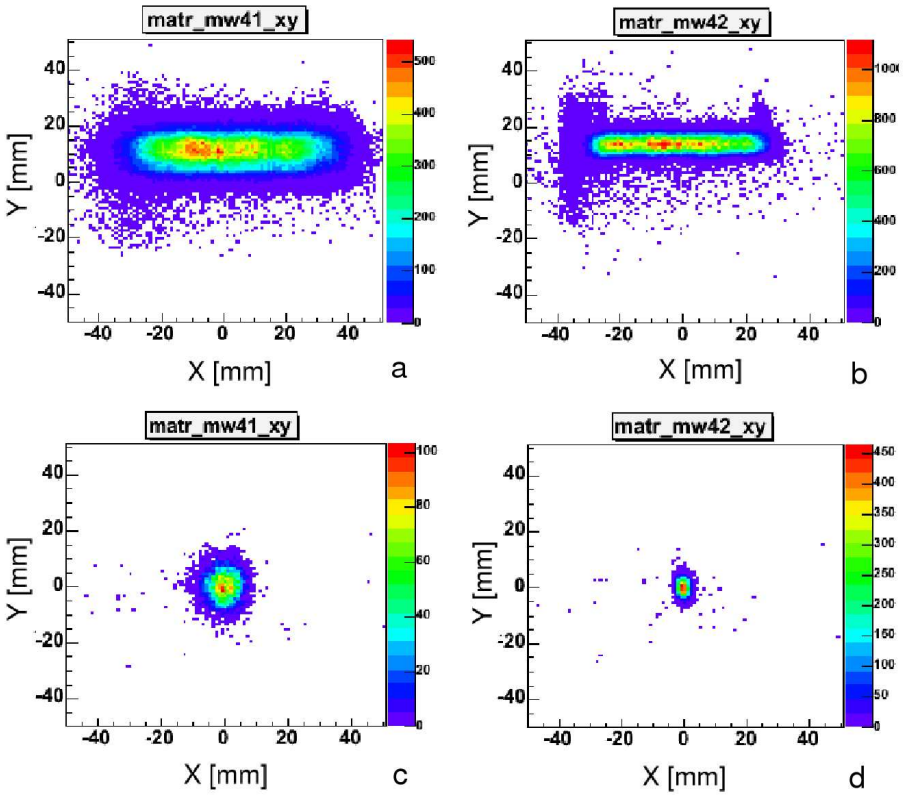

Figure 11.5: In-beam (x,y) position measured with **a** - MW 41 and **b** - MW 42 with S4 slids closed to (x:± 35 mm, y:± 2 mm), **c** - MW 41 and **d** - MW 42 with S4 slids closed to (x:± 1 mm, y:± 2 mm).

used for the fragment runs. Note that small change in these slope and offset parameters introduces different positions, which translated on a big distance as the secondary target and/or CATE become much bigger.

A.2.2. The MUSIC : ΔE, Z calibration

Four different primary beam energies are selected for the calibration of the MUSIC, the plastic scintillators and ToF with low particle rate of about 2 kHz. ^{58}Ni with 600 A·MeV is slowed down first only by the SCI 1 at the middle focus (see fig.4.3.a.) and later with including the ^{9}Be primary target. Further the energy is decreased by adding a thin

thickness and finally adding thicker thickness of the Al wedge degrader, placed in the middle focus of the FRS.

The energy loss in the MUSIC [Pfue94, ScSt01] detector is dependent on the position of the particles and on their velocity. Therefore such corrections are required in order to obtain precise charge determination, which is an important part of the FRS fragment identification.

A.2.2.1. Position correction

The position dependence is detected by simultaneously illuminating the MUSIC detector and a calibrated (position sensitive) MWs with (defocussed) primary beam. The the coefficients of the correction polynomial are determined by fitting the dependence of MUSIC energy on the x-position of the interaction point. The latter is determined using tracking with the MWs, but in certain cases the MUSIC can itself provide x-position information [FRSA04]. On fig.11.6.a such a dependence and its fit are shown. The example is taken from an off-line calibration of experimental in-beam test (see section 3.2.2) with ^{238}U beam of 500 A·MeV. The parameters from the fit: $f(x) = a + b_1 \cdot x + b_2 \cdot$

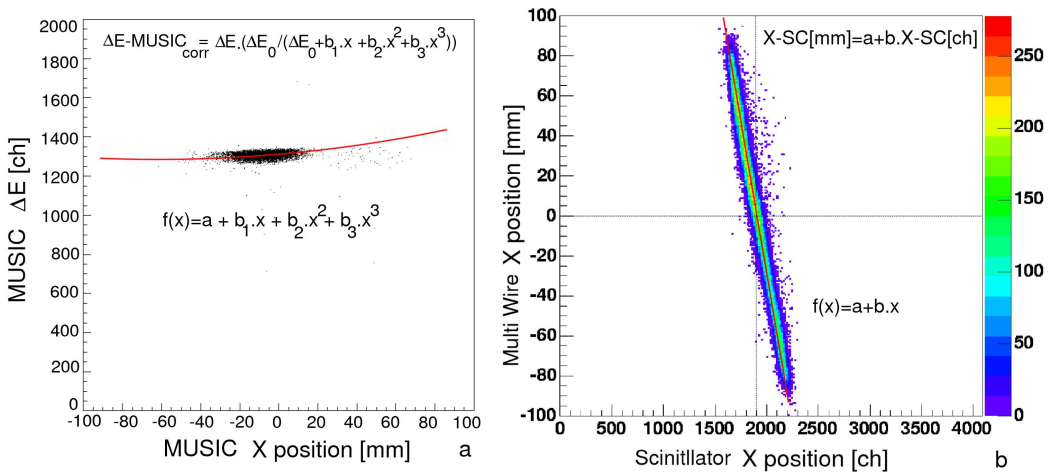

Figure 11.6: **a** - MUSIC position correction, **b** - scintillator (SCI 2) position correction using primary beam.

$x^2 + b_3 \cdot x^3$ in case of the ^{58}Ni particles are *i.e.* as follows: a = 2039.74, b_1 = 0.0313157, b_2 = 8.40651e-04, b_3 = 0. To obtain the corrected energy loss (ΔE_{corr}), the correction function is multiplied by the energy loss (ΔE) from the detector (see Appendix 1 (MUSIC-Energy loss)):

$$\Delta E_{corr} = \Delta E \cdot \frac{\Delta E_0}{\Delta E_0 + b_1 \cdot x + b_2 \cdot x^2 + b_3 \cdot x^3}$$

An example of a single anode spectrum and the total MUSIC energy loss spectrum are shown on fig.11.8.a and b, respectively.

A.2.2.2. Velocity correction

The energy loss (ΔE) can be expressed as a function of the particle velocity β and the nuclear charge Z as follows :

$$\Delta E = \frac{Z^2}{f(\beta)}$$

The function $f(\beta)$ is deduced from the settings using the primary beam with different energies and usually is a polynomial of third order (see fig.11.7.a). The velocity β is theoretically calculated with ATIMA [ATIM04]. The correction coefficients for the ^{58}Ni particles *i.e.* are as follows: a = 15151.46932, b_1 = -46097.96452, b_2 = 52035.59245, b_3 = -20549.4203.

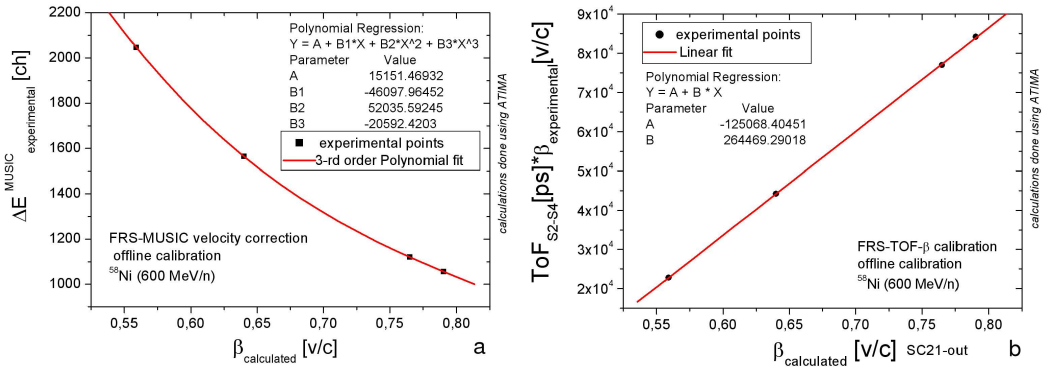

Figure 11.7: **a** - MUSIC velocity correction and **b** - ToF-β calibration using primary beam.

Sometimes, in order to accurately calculate Z over a wide range of elements, it is necessary to renormalize this value. This can be done by applying a linear or quadratic correction as:

$$Z_{normalized} = Z_{raw}^2 \cdot Z_{quad} + Z_{raw} \cdot Z_{slope} + Z_{offset}$$

from data containing information for several primary particles.

A.2.3. The Scintillators : ToF, β calibration

The scintillators placed at middle and the final focal planes (see fig.4.3.a.) give the ToF of the particles (see Appendix 1 (The Scintillators-ToF)).

A.2.3.1. ToF-β calibration

The ToF itself is experiment-specific and is calibrated using the primary ^{58}Ni beam with several different energies. After a calibration from channels to ps via a clock calibrating the TAC signal of each scintillator, from the ToF left and ToF right raw signals (given as an example on fig.11.8.c and d) the averaged ToF spectrum in ps is achieved, shown on fig.11.8.e. However, the real ToF is a superposition of this absolute ToF (calibrated in ps) and an experimental specific offset. The offset is determined in the FRS primary beam calibration procedure with different energies, corresponding to experimental relativistic velocity parameters β_{exp}, which can also be calculated theoretically. A function is constructed from the measured ToF (in ps), β_{exp} and the calculated β_{calc} from the type:

$$ToF_{exp} \cdot \beta_{exp}(\beta_{calc}) = c_0 + c_1 \cdot \beta_{calc}.$$

The parameters from the linear fit (see fig.11.7.b.) are c_0 and c_1 and have special physical meaning. The absolute value of $c_0 \cdot c$ (c is the velocity of light) is equal to the average flight path, while c_1 represents the ToF offset mentioned above. The values of this parameters in the ^{58}Ni beam case are: -125068.40451 and 264469.28018 for the offset and slope,

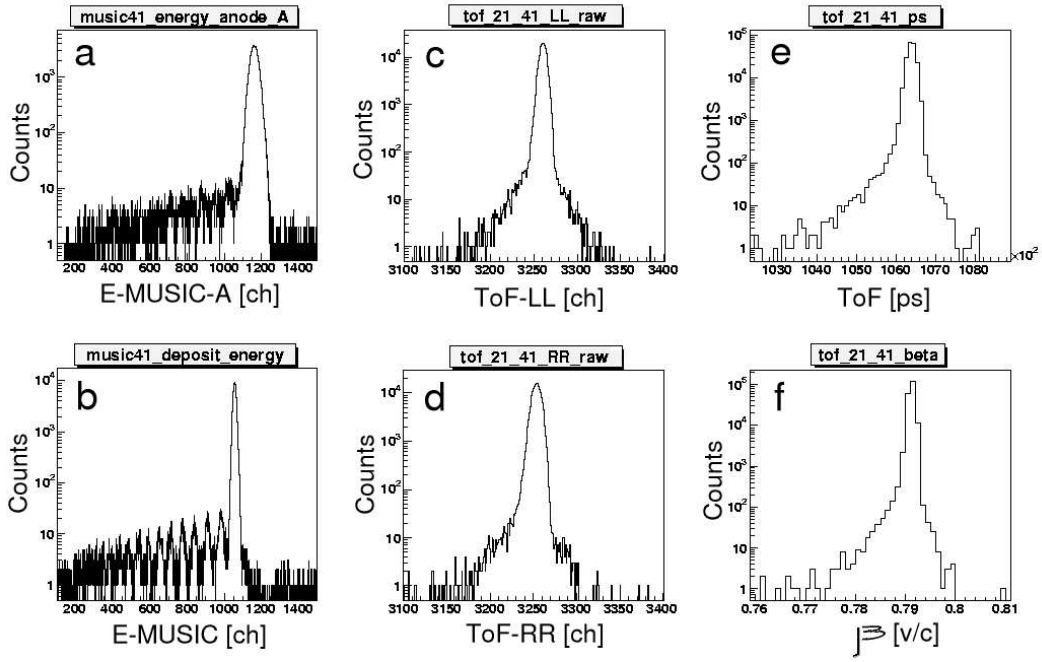

Figure 11.8: Example spectra from: **a** - MUSIC anode, **b** - MUSIC ΔE, **c** - raw ToF-left, **d** - raw ToF-right, **e** - calibrated ToF and **f** - experimental β.

respectively. Note that here the calculated energies and velocities are at the SCI 1. These parameters are used later for the calculation of A/q.

The velocity β_{ToF} (depicted on fig.11.8.f) of the particles is deduced as:

$$\beta_{ToF} = \frac{c_1}{\mid c_0 \mid -ToF[ps]}$$

and correspondingly the relativistic parameter γ and the kinetic energy per mass unit E_{kin}, associated with this velocity are:

$$\gamma = \frac{1}{\sqrt{1-\beta^2}}, \quad E_{kin} = (\gamma - 1) \cdot 931.5$$

To match more the realistic conditions in the RISING studies of CATE, similar calibration of the fragment velocity β_{ToF} is done via including more matter in the calculations. For measurements without secondary target, the detector materials up to the SCI 2 scintillator are included and for the measurements with secondary target, its 'imaginary' contribution is added as well. These cases changed very slightly the linear behavior shown on fig.11.7.b. and new calibration parameters are determined. For the case without target the offset and the slope are: -95624.86782 and 228410.62715 and for the case with 'imaginary' target they are: -62303.68193 and 186434.57781, respectively.

A.2.3.2. Position correction

For the better reconstruction of the particle trajectory it is necessary to measure its position with the scintillators at the middle and the final focus. In case the trajectory is slightly different than the one directed from the magnets as shown on fig.11.9, the track with the scintillators (SCI 1 and SCI 2) becomes important. Therefore they are also used

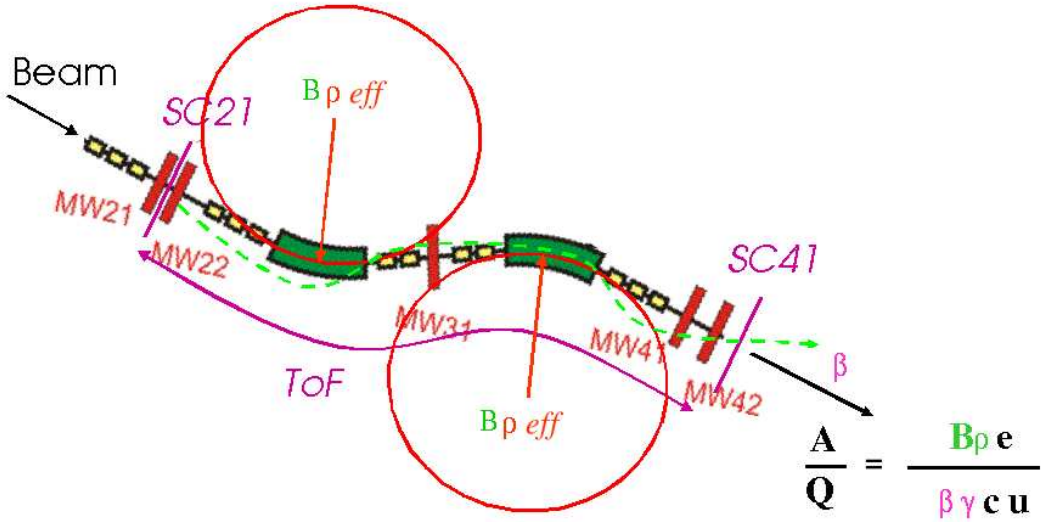

Figure 11.9: Sketch of changed particle trajectory which can be registered only if the position in the middle and the final focus are measured by the scintillators.

as position-sensitive detectors. The position is determined by the time difference of the TAC signals between left and right sides of each detector. The calibration is obtained by defocusing the primary beam of ^{58}Ni in order to cover completely the scintillators in horizontal position x. The linear calibration of the positions in the scintillators SCI 1 and SCI 2 is obtained by using their extrapolated position with the help of the MWs at the middle and the final focus correspondingly. An example of such correction for the SCI 2 is shown on fig.11.6.b.

A.2.4. A/q particle identification

The position information from the scintillators is then used to achieve the proper geometrical corrections to the magnetic rigidity ($B\rho_{2corr}$) of each fragment in the second FRS stage (see section 4.3.1):

$$B\rho_{2corr} = B\rho_2 \cdot (1 - \frac{x_4 - V_2 \cdot x_2}{1000 \cdot D_2}),$$

where Bρ_2 is the magnetic rigidity of the fragment at the ion-optical axis, given by the magnetic fields of the dipole magnets (B) and their radii (ρ), x_2 and x_4 are the positions of the fragment at the intermediate and final focal planes, given by the two scintillators. $V_2 = 1.12$ and $D_2 = 7.239$ are respectively the magnification and the dispersion of the FRS second stage ([FRSA04, GICO04]).
Using the above formula a different calculation of the velocity β of the fragment *i.e.* with known A and q can be expressed as:

$$beta_{B\rho} = \sqrt{\frac{1}{1 + (3.108 \cdot (A/q))^2 / B\rho^2_{2corr}}}.$$

This determination of the velocity is, not only in principle but in practice, much better defined than the velocity which is calculated from the ToF in case the dependence of the

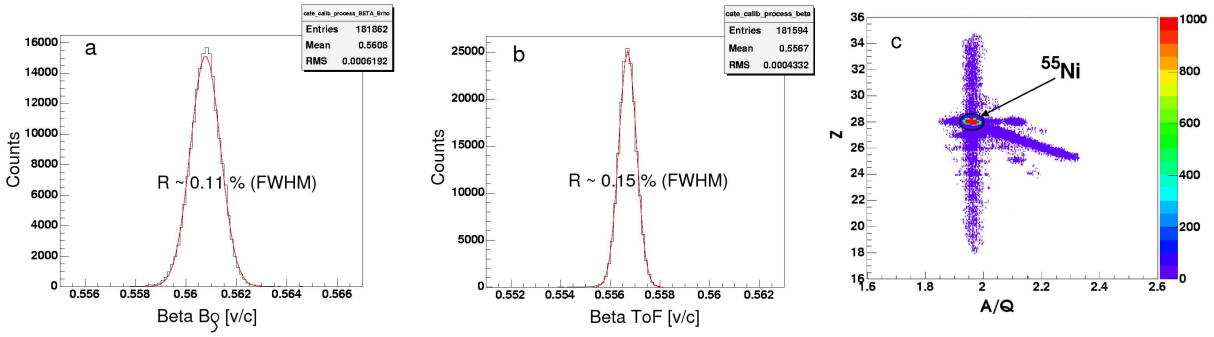

Figure 11.10: Comparison between the velocity β calculated from **a** - Bρ with **b** - measured ToF for ^{58}Ni primary particles with SIS energy of 215 A·MeV. **c** - The identification of ^{55}Ni fragments in Z and A/q from the calibrated FRS.

angle at the middle and final focus are corrected properly. The comparison *i.e.* for the primary ^{58}Ni beam is given on fig.11.10.a and b. The velocity from Bρ here have precision of only 0.11% (FWHM) and the velocity from the ToF precision of 0.15% (FWHM). This difference is not so severe with the primary beams, but with fragment beams it can reach 20-30% from their values. Therefore is important to measure this velocity and compare it with the measured via the ToF. In case the difference between them becomes even bigger, a correction of the ToF velocity could be performed with respect to the calculated from the magnets. As proper is the definition of the velocity as better is the definition of the particle beam, and this results in a better resolution of the CATE detectors, where *i.e.* the effect on the particle velocity requires corrections of measured energy (see section 7.2.3).

Combining the ToF and Bρ_2 information, the mass-to-charge ratio A/q corrected for position is finally deduced :

$$\frac{A}{q} = \frac{e}{cu}\frac{B\rho_{2corr}}{\beta\gamma} = \frac{e}{cu}\frac{(B\rho)_2}{\beta\gamma}(1 - \frac{x_4 - V_2 x_2}{D_2}).$$

The constants e, c and u are the electron charge (1.602 x 10^{-19} C), the speed of light (299.792 Mm/s) and the mass unit (931.494), respectively.

After the above described calibrations and corrections to the atomic charge Z, the ToF and x-positions at the middle and final focus the identification of the FRS is revised. The result from that, expressed in an Z as a function of A/q plot for the ^{55}Ni fragments produced at the ^{9}Be primary reaction target, is shown on fig.11.10.c.

Appendix 3

A. 3. Absolute energy calibration of CATE

The calibration of the FRS with ^{58}Ni particles with SIS energy of 600 A·MeV is described in the Appendix 2. Some of these settings, are also used for the primary beam studies of the CATE detectors. Additionally, four other settings with lower SIS energy of 215 A·MeV are prepared for the absolute calibration of the calorimeter telescope detectors. The particles, are chosen to have low intensity at CATE of ≈ 1 kHz (rate of 3000 particles per spill (pps), distributed in a spill length of 4 s and period of 8 s). For the **calibration** points, no matter in the FRS except the identification detectors is used. The settings (labeled as points p.1 to p.4) and the corresponding energies are given in table 11.2.

	Primary beam Primary energy [MeV/n]	Primary target Thickness [g/cm^2]	Bρ (D3-D4) [Tm]	β E @ S4 [MeV/n]	Secondary target Thickness [g/cm^2]	E @ CATE [MeV/n] [MeV]	ΔE in Si [MeV/n] [MeV]	E @ CsI(Tl) [MeV/n] [MeV]
p.1	^{58}Ni 215.00	- -	4.3606	0.561 193.66	- -	162.26 9411.08	3.97 230.03	158.29 9180.82
p.2	^{58}Ni 215.00	- -	4.3606	0.561 193.66	^{9}Be 0.70	118.25 6858.50	4.92 285.36	113.33 6573.14
p.3	^{58}Ni 215.00	H_4C_2 0.51	3.8444	0.512 152.78	- -	120.63 6996.54	4.85 281.30	115.78 6515.24
p.4	^{58}Ni 215.00	H_4C_2 0.51	3.8444	0.512 152.78	^{9}Be 0.70	60.92 3533.36	8.04 466.32	52.88 3067.04

Table 11.2. Calibration settings for the CATE detectors with primary ^{58}Ni particles.

The energies at the CATE detectors and the energy depositions inside them are calculated ([ATIM04, LISE04]) from the energy, defined by the last stage FRS magnets (see section 4.1) and the energy loss in the experimental set-up. As can be seen from the table, the setting with the best defined energy, because of the less matter included, is the first calibration point (p1). The analysis of the energy resolution for this calibration point, were explained in section 7.1.3. Although the energy straggling is small (about 8 MeV) the settings with secondary target did not respond linearly on the CATE detectors. Therefore after analysis (under well defined position of (5 x 5) mm^2 and ToF-β of 0.3% conditions), the absolute energy calibration is performed using the calculated energies (in MeV), and those registered by the Si and the $CsI(Tl)$ detectors (in channels). The calibration coefficients are determined from straight line fits (y=$a_{Si,CsI}$.x+$b_{Si,CsI}$). For the central detectors, the calibration coefficients are: $a_{Si5} = 0.09644$ and $b_{Si5} = 51.8369$ for the Si and $a_{CsI5} = 2.4600$ and $b_{CsI5} = 2237.9073$ for the $CsI(Tl)$, with total error from the channel peak finder and the polynomial fit of about 0.98% for both detectors. These calibration coefficients are needed for the secondary fragmentation and mass analysis in section 9.4.1.

Bibliography

[AccG04] www-aix.gsi.de/accelerator/index.html

[Advp04] www.advancedphotonix.com

[Aiel95] S. Aiello *et al*, *Nucl. Phys.* **A** 583 (1995) 461

[Aiel97] S. Aiello *et al*, *Nucl. Instr. Meth.* **A** 400 (1997) 469

[Aiel00] S. Aiello *et al*, *IEEE Trans. of Nucl. Sci.* **Vol.47** No.2 (2000) 114

[Alar86] J. Alaria *et al*, *Nucl. Instr. Meth.* **A** 242 (1986) 352

[Alar87] J. Alaria *et al*, *Nucl. Instr. Meth.* **A** 242 (1986) 352

[Arfe97] F. Arfelli *et al*, *IEEE Trans. Nucl. Sci.* **Vol.44** (1997) 874

[Arfe96] F. Arfelli *et al*, *Nucl. Instr. and Meth.* **A** 377 (1996) 508

[Artu69] A. Artukh, *Nucl. Phys.* **A** 137 (1969) 348

[Artu70] A. Artukh, *Phys. Lett.* **B** 32 (1970) 43

[Asch55] F. Aschenbrenner, *Phys. Rev.* 98 (1955) 657

[ATIM04] www-aix.gsi.de/~weick/atima/

[Avde94] V. Avdeichikov *et al*, *Nucl. Instr. Meth.* **A** 349 (1994) 216

[Badw67] G. Badwhar *et al*, *Nucl. Instr. Meth.* 57 (1967) 116

[Barn96] R. Barnett *et al*, *Phys. Lett.* **D** 54 (1996) 1

[Becc76] F. Beccetti *et al*, *Nucl. Instr. Meth.* 138 (1976) 93

[Beck03] F. Becker, MW source measurement FRS, Private communication (2003)

[Benl99] J. Benlliure *et al*, *Nucl. Phys.* **A** 660 (1999) 87

[Benr89] F. Benrachi *et al*, *Nucl. Instr. Meth.* **A** 281 (1989) 137

[BePu93] G. Bertuccio and A. Pullia, *Rev. Sci. Instrum.* 64 (1993) 3294

[Beth30] H. Bethe, *Ann. Phys.* 5 (1930) 325

[Beth33] H. Bethe, *Handbuch der Physik* **Vol.42/1** Spinger Verlag, Belin (1933)

[Beth36] H. Bethe and R. Bacher, *Rev. Mod. Phys.* 8 (1936) 82

[Beth37] H. Bethe, *Rev. Mod. Phys.* 9 (1937) 69

[Beth78] K. Bethge, *Exp. Meth. Heavy Ion Phys.* Spinger Verlag, Belin (1978)

[Bicr04] Bicron Co., www.bicron.com

[Bigg61] J. Biggerstaff *et al*, *Nucl. Instr. Meth.* 10 (1961) 327

[Birk51] J. Birks and F. Blank, *Proc. Phys. Soc.* **A** 64 (1951) 511

[Birk62] J. Birks, *Proc. Symp. Nucl. Instr.* Harwell 1961, London-Heyword (1962)

[Birk64] J. Birks, The theory and practise in scintillation counting, Pergamon press, New York (1964)

[Bisw00] D. Biswas and R. Choudhury, Nuclear Physics Division, Bhabha Atomic Research Centre
www.barc.ernet.in/webpages/letter/newsletter_year_2000/paper5.htm

[Blan60] J. Blankenship, *IEEE Trans. Nucl. Sci.* **NS7** 2, 3 (1960) 190, 195

[Bloc33] F. Bloch, *Ann. Phys.* 16 (1933) 285

[Blum93] W. Blum and L. Rolandi, Particle Detection with Drift Chambers, Springer Verlag, Berlin (1993)

[Bock98] R. Bock, `rkb.home.cern.ch/rkb/PH14pp/node19.html`

[Bohr13] N. Bohr, *Phil. Mag.* 25 (1913) 10

[Bohr15] N. Bohr, *Phil. Mag.* 30 (1915) 581

[Bohr48] N. Bohr, *Mat. Fys. Medd.* 18 (1948) No.8

[BohM69] A. Bohr and B. Mottelson, *Nuclear Structure* **Vol. I** Benjamin press, New York (1969)

[Bone01] U. Bones, Institute of Nuclear Physics, TU-Darmstadt, Private communication via H-J Wollersheim (2001)

[Bord89] B. Borderie *et al*, *GANIL reports* **89-10A** Apr. (1989)

[Brau74] F. Braun, *Ann Phys. Chem.* 153 (1874) 556

[Brya62] D. Brayant *et al*, *IRE Trans. Nucl. Sci.* **NS-9**, No.3 (1962) 376

[Bree93] M. Breese *et al*, *J. Appl. Phys.* 73 (1993) 2640

[Breh75] S. Brehin *et al*, *Nucl. Instr. Meth.* 123 (1975) 225

[Brun92] M. Bruno *et al*, *Nucl. Instr. Meth.* A311 (1992) 189

[Buer05] A. Bürger *et al*, *Physics Letters* **B** (2005) accepted

[Butl70] G. Butler *et al*, *Nucl. Instr. Meth.* 89 (1970) 189

[CAEN02] Technical Information Manual, 16ch. Sp. Amp. CAEN , Model N568B
`www.caen.it/nuclear/printable.php?mod=N568B`
CAEN ADC V785 and TDC V878
`www-wnt.gsi.de/frs/technical/electronics/`

[Canb04] PIPS Specification and performance sheet, PIPS detector instruction sheet, Canberra Industries, Canberra Smiconductor (2004), `www.canberra.com`, `www.canberraeurisys.com`,

[CERN95] CERN Program Library entry Y250, HBOOK Statistic Analysis and Histogramming, CERN, Geneva (1995), `paw.web.cern.ch/paw/objects.html`

[CERN99] CERN Program Long Writeup Q121, PAW Physics Analysis Workstation, An User's guide Tutorial, CERN, Geneva (1999), `paw.web.cern.ch/paw/`

[ChuP69] W. Chu and D. Powers, *Phys. Lett.* **A** 10 (1972) 23

[Cowi97] R. Cowin *et al*, *Nucl. Instr. Meth.* **A** 399 (1997) 365

[Curr48] S. Curran and W. Baker, *Rev. Sci. Instr.* 19 (1948) 116

[Dauv99] D. Dauvergne, C. Scheidenberger *et al*, *Phys. Rev.* **A** 59 (1999) 2813

[DLTT04] `www.dlttape.com/Home.htm`

[Dobr01] D. Dobrev, Private communication, GSI (2001)

[Doke87] T. Doke *et al*, *Nucl. Instr. Meth.* **A** 261 (1987) 605, and the ref. therein

[Door03] P. Doornenbal, Diploma Thesis, University of Frankfurt (2003)

[DuPo04] `www.dupont.com`

[Drai89] D. Drain *et al*, *Nucl. Instr. Meth.* **A** 281 (1989) 528

[Dufo86] J.P. Dufour *et al*, *Nucl. Instrum. Meth.* **A** 248 (1986) 267

[Eber96] J. Eberth *et al*, *Nucl. Instrum. Meth.* **A** 369 (1996) 135

[Eise72] F. Eisen *et al*, *Radiat. Eff.* 13 (1972) 93

[EleT01] `www.electron-tubes.co.uk/menu.html`
`www.photonic.saint-gobian.com`

[ElMo02] Electronic Modules Pool GSI-Darmstadt,
`www-aix.gsi.de/~gfe_o/module/`

[EmAu02] H. Emling, T. Auman, K. Jones, Private communication (2002)

[Engs52] R. Engstrom *et al*, *Nucleonics* 10, No.4 (1952) 58

[Enqv99] T. Enqvist *et al*, *Nucl. Phys.* **A** 658 (1999) 47

[ENSD04] `ENSDF data surver, ie.lbl.gov/ensdf/`

[EPAX04] `www-wnt.gsi.de/hellstr/asp/gsi/epaxv21m.asp`
`www-aix.gsi.de/~sue/epax/epax_v2.html`

[Euri01] Eurisys Measures Co. 2001
User's Manual for Si IPP-IPP 2D detectors, Eurisys Measures (2001)

[Fabj80] C. Fabjan and H. Fischer, *Rev. Prog. Phys.* 43 (1980) 1003

[Fano63] U. Fano *et al*, *Ann. Rev. Nucl. Sci.* 13 (1963) 1

[Fast04] `www.fastcomtec.com`

[Feld82] L. Feldman, J. Mayer and S. Picraux, Materials Analysis by Ion Channeling, Academic Press, New York, (1982)

[Ferm40] E. Fermi *et al*, *Phys. Rev.* 57 (1940) 485

[Fowl89] M. Fiwler *et al*, *Nucl. Instr. Meth.* **A** 281 (1989) 517

[Fomi94] A. Fomichev *et at.*, *Nucl.Instr. Meth.* **A** 344 (1994) 378

[Fret96] E. Fretwurst *et al*, *Nucl. Instr. Meth.* **A** 372 (1996) 368

[FRSA04] `www-wnt.gsi.de/frs/technical/daq/frs-algorithms.asp`

[FRSD04] `www-wnt.gsi.de/frs/technical/daq/frs-datastructure.asp`
`www-wnt.gsi.de/frs/technical/daq/frs-standalone.asp`

[FRSE04] `www-wnt.gsi.de/frs/technical/electronics/overview.asp`

[FRSG04] `www-wnt.gsi.de/frs/index.asp`

[FRSS04] `www-linux.gsi.de/~weick/frs/frs-steps.html`

[FRSO04] `www-linux.gsi.de/~weick/frs/frs-ion-optics.html`

[Geig13] H. Geiger and E. Marsten, *Phil. Mag.* **VI** 25 (1913) 604

[Geis87] H. Geissel *et al*, Projectile-Fragment Separator, A proposal for the SIS-ESR Experimental Programme, GSI, Darmstadt (1987)

[Geis91] H. Geissel *et al*, *GSI reports* 91/46 preprint (1991)

[Geis92] H. Geissel *et al*, *Nucl. Instr. Meth.* **B** 70 (1992) 286

[Geis95] H. Geissel *et al*, *Annu. Rev. Nucl. Part. Sci.* (1995) 163

[Geis02] H. Geissel *et al*, *Nucl. Instr. Meth.* **B** 195 (2002) 3

[GICO04] `www-aix.gsi.de/~weick/gico/gico.html`

[Go4G04] `www-w2k.gsi.de/go4/`

[Gold74] A. Goldhaber *et al Phys. Lett* **B** 53 (1974) 306

[GoBa62] C. Goodman and J. Ball, Proc. Symp. Nucl. Instr., Harwell (1961), London-Heyword (1962) 163

[GOOS01] `www-gsi-vms.gsi.de/anal/home.html`

[Gord28] W. Gordon *et al*, *Z. Phys.* 48 (1928) 180

[Goul64] F. Goulding *et al*, *Nucl. Instr. Meth.* 34 (1964) 1

[Goul66] F. Goulding and D. Landis, *IEEE Trans. Nucl. Sci.* **NS-13** (1966) 514

[Goul75] F. Goulding and B. Harvey, *Ann. Rev. Nucl. Sciu.* 25 (1975) 167

[GoLa82] F. Goulding FS and D. Landis, *IEEE Trans. Nuc. Sci.* **NS-29** (1982) 1125

[Gram97] F. Gramegna *et al*, *Nucl. Phys.* **A** 389 (1997) 474

[Gras85] H. Grassman *et al*, *Nucl. Instr. Meth.* 228 (1985) 323

[Greb03] J.Grębosz, Spy user analysis, Private communication (2003-2004)

[Groo84] D. Groom, *Nucl. Instr. Meth.* **A** 219 (1984) 141

[Guin89] D. Guinet *et al*, *Nucl. Instr. Meth.* **A** 278 (1989) 614

[Gwin63] R. Gwin and R. Murray, *Phys Rev.* 131 (1963) 598

[HanD02] D. Han *et al*, *Nucl. Instr. Meth.* **B** 195 (2002) 339

[Hane89] E. Hanelt *et al*, *GSI Sci. Rep.* (1989) 90

[Halb57] M. Halbert, *Phys. Rev* 107, No.3 (1957) 647

[Hall96] G. Hallewell, *Nucl. Instrum. Meth.* **A** 383 (1996) 44

[Hama04] `www.hamammatsu.com`

[Harv72] B. Harvey and F. Goulding, *Nucl. Instr. Meth.* 104 (1972) 21

[Heij89] E. Heijne and P. Jarron, Silicon Detector Development in Europe, SSSHP-1990, 739, World Scientific (1989)

[Hild97] K. Hildenbrand, Experimental Techniques in Nuclear physics, Scintillation Detectors, Walter de Gruyter, Berlin-New York (1997)

[HoKu02] J. Hoffmann and N. Kurz, *GSI Sci. Rep.* (2002) 224

[Hofs48] R. Hofstadter *et al*, *Phys. Rev.* 74 (1948) 100 and 75 (1949) 796

[Hofs64] R. Hofstadter, Electron scattering and nuclear and nucleon structure, Benjamin press, New York (1963)

[Holl89] S. Holland, *Nucl. Instr. and Meth.* **A** 275 (1989) 537

[Horn92] D. Horn *et al*, *Nucl. Instr. Meth.* **A** 320 (1992) 273

[Hubb62] E. Hubbard, *IRE. Trans. Nucl. Sci.* **NS-9**, No.3 (1962) 357

[IBMS00] IBM SRIM 2000.39 and IBM SRIM 2003.1, `www.srim.org`

[IKPT00] J. Theuerkanf, A. Fizler *et al* 2000, IKP TV program, University of Cologne, `www.ikp.uni-koeln.de/~fitz/viewspectra/Tv_user-manual/`

[IMPG91] `spdf.gsfc.nasa.gov/imp8_GME/GME_instrument.html`

[Inok71] M. Inokuti *et al*, *Rev. Mod. Phys.* 43 (1971) 297

[IonG04] `bel.gsi.de/mk/init/initset.html`

[Iori93] I. Iori *et al*, *Nucl. Instr. Meth.* **A** 325 (1993) 458

[Ishi92] M. Ishii and M. Kobayashi, *Prog. Cryst. Grouth and Charact. of Mat.* 23 (1992) 245

[Iwas97] N.Iwasa *et al*, *Nucl. Instr. Meth.* **B** 126 (1997) 284

[Jabl35] A. Jablonski, *Z. Phys.* 94 (1935) 38

[Jacm69] J. Jacmart *et al*, *Rev. Phys. Appl.* (1969) 99

[Jinc96] W. Jinchuan *et al*, *Nucl. Phys.* **A** 368 (1996) 473

[Jong97] M. de Jong *et al*, *Nucl. Phys.* **A** 613 (1997) 435

[Kalu88] A. Kaluza *et al*, *IEEE Trans. Nucl. Sci.* 45 (1998) 724

[Karo02] The Karol code, K-H. Schmidt, `www-wnt.gsi.de/kschmidt/karol.htm`

[Kara23] E. Karamihailova, A devotion to their science: Pioneer Women of radioactivity, eds. Rayner-Canham, McGill-Queen's University press (1997); N. Sretenova, E. Karamihailova biography (1998) www.phys.uni-sofia.bg/~upb/Karam.html; H. Protohristov, prof. E. Karamihailova in the world's physics, Universe, science and technics, eds. Letera prima 6 (2005) 7

[Keho92] K. Kehoe *et al*, *Nucl. Instr. Meth.* **A** 311 (1992) 258

[Kell56] G. Kelley *et al*, *IRE Trans. Nucl. Sci.* **NS-3** No.4 (1956) 57

[Kemm80] J. Kemmer, *Nucl. Instrum. Meth.* 169 (1980) 499

[Kilg90] U. Kilgus *et al*, *Nucl. Instr. Meth.* **A** 297 (1990) 425

[King95] P. King *et al*, Phys. Rev. B 51 (1995) 2732

[Kitt00] C. Kittel, Introduction to Solid State Physics, 6th ed., John Wiley & Son, New York (1984)

[Knol00] G. Knoll, Radiation detection and measurement, 2-nd ed., Wiley press, New York (2000)

[Kreb41] A. Krebs, *Ann. Pysic.* 39 (1941) 330

[Kreu87] P. Kreutz *et al*, *Nucl. Instr. Meth.* **A** 260 (1987) 120

[Kroe97] R. Kröger *et al*, *IEEE Trans. Nucl. Sci.* **Vol.44.** No.3 (1997) 881

[KuoL61] L. Kuo *et al*, *Nucl. Instr. Meth.* 10 (1961) 53

[LAND02] www-land.gsi.de/a_new_land/experiments/experiments.html

[Lava83] M. Laval *et al*, *Nucl. Instr. Meth.* **A** 206 (1983) 169

[Laza92] I. Lazarus *et al*, *IEEE Trans. Nucl. Sci.* 39 (1992) 1352,
I. Lazarus and P. Coleman-Smith, *IEEE Trans. Nucl. Sci.* 42 (1995) 891

[LEAG01] www-gsi-vms.gsi.de/anal/home.html

[LeoW94] W. Leo, Techniques for Nuclear and Particle Physics Experiments, 2-nd ed., Spinger Verlag, Berlin-Heidelberg (1994)

[Lind63] J. Lindhard, M. Scharff and H. Schitt, Dan. Vid. Selsk., Mat. Fys. Medd. 33 (1963) No.14

[Lind96] J. Lindhard and A. Sorensen, *Phys. Rev.* **A** 53 (1996) 2443

[Lint87] V. van Lint *et al*, *Nucl. Instr. Meth.* **A** 253 (1987) 453

[LISE04] O. Tarasov and D. Bazin, *Nucl. Instr. Meth.* **B** 204 (2003) 174
groups.nscl.msu.edu/lise and dnr080.jinr.ru/lise

[LMDF90] P.N. Dean *et al*, List Mode Data File, Data file standard forflow cytometry, Cytometry 11, 323 (1990)

[Loze00] R. Lozeva, CsI(Na) and BGO shield test, *GSI Sum. St. Pro. reports* (2000)

[Loze01] R. Lozeva, Diploma thesis (MSC degree), Univerisity of Sofia (2001)

[Loze03] R. Lozeva *et al*, *Nucl. Instr. Meth.* **B** 204 (2003) 678
www-linux.gsi.de/~lozeva/cate/cateweb.htm

[Loze05] R. Lozeva *et al Acta Phys. Pol.* B **36** No.4 (2005) 1245

[Lutz99] G. Lutz, Semiconductor Radiation Detectors, Device Physics, Spinger Verlag, Berlin-Heidelberg-New York (1999)

[Mage94] A. Magel *et al*, *Nucl. Instr. Meth* **B** 94 (1994) 548

[Marc58] G. Marcazzan *et al*, *Nuovo Cimento* 10 (1958) 155

[Mart78] B. Martin, Detectors for heavy ions, Lecture Notes in Physics, Spinger Verlag, Belin (1978)

[Mori89] D. Morissey *et al*, *Phys. Rev.* **C** 39 No.2 (1989) 460

[MBSG04] H. Essel, J. Hoffmann, N. Kurz *et al*, *IEEE Trans. Nucl. Sci.* **Vol.43** No.1, (1996) 132
H.G. Essel and N. Kurz *IEEE Trans. Nucl. Sci.* **Vol.47** No.2 (2000) 337
`www-w2k.gsi.de/daq/`

[Micr04] `www.micron.com`

[MOCA04] `www.gsi.de/~scheid/mocadi.html`

[MoMi48] G. Morton and J. Mitchell, *RCA Review* 9 (1948) 632; *Nucleonics* 4 No.1 (1949) 16

[Mosz93] M. Moszysnki *et al*, *Nucl. Instr. Meth.* **A** 336 (1993) 587

[Mott29] N. Mott *et al*, *Proc. Roy. Soc. London* **A** 124 (1929) 425

[Mott31] N. Mott, *Proc. Camb. Phil. Soc.* 34 (1931) 568

[Mott32] N. Mott *et al*, *Proc. Roy. Soc. London* **A** 135 (1932) 429

[MoSu58] W. Mott and R. Sutton, Encyclopedia of Physics, Springer Verlag, Berlin, 45, 86 (1958)

[Muen92] G. Münzenberg *et al*, *Nucl. Instr. Meth.* **B** 70 (1992) 265

[Mura89] T. Murakami *et al*, *Nucl. Instr. Meth.* **A** 275 (1989) 112

[Nage03] S.V.S. Nageswara Rao *et al*, *Nucl. Instr. Meth.* **B** 111 (2003) 1

[Nein02] N. Le Neindre *et al*, *Nucl. Instr. Meth.* **A** 490 (2002) 251

[Norb95] E. Norbeck, *Nucl. Instr. Meth.* **A** 360 (1995) 642

[Nort70] C. Nortcliffe and F. Schilling, Range and stopping power for heavy ions, Nuclear Data tables A7 (1970) 233

[Orte04] `www.ortec-online.com`,
`www.ortec-online.com/electronics/supplies/`

[Paga96] A. Pagano *et al*, *Proc. of Int. Workshop on 4PI detectors* ed. by M. Petrovici, World Scientific (1996) 129

[Paga01] A. Pagano *et al*, *Nucl. Phys.* **A** 681 (2001) 331c

[Parl02] M. Parlog *et al*, *Nucl. Instr. Meth.* **A** 482 (2002) 674 and 693

[PAWC04] `www-wnt.gsi.de/frs/technical/Software/PAWonline/PAW_online.html`
`wwwasd.web.cern.ch/wwwasd/paw/`

[PeBr55] G. Pearson and W. Brattain, History of semiconductor research, *Proc. IRE* **Vol.43** (1955) 1794

[Pelt82] D. Pelte and D. Schwalm, In-beam Gamma-ray Spectroscopy with Heavy Ions, North-Holland, Amsterdam (1982)

[Plat49] J. Platt, *J. Chem. Phys.* 17 (1949) 484

[Pfue91] M. Pfützner *et al*, *GSI Sci. Rep.* **91-1** (1991) 288

[Pfue94] M. Pfützner *et al*, *Nucl Instr. Meth.*, **B** 86 (1994) 213

[Posk68] A. Poskaner *et al*, *Phys. Lett.* **B** 27 (1968) 414

[Poul88] J. Pouliot *et al*, *Nucl. Instr. Meth.* **A** 270 (1988) 69

[Pour95] J. Pourthas *et al*, *Nucl. Instr. Meth.* **A** 357 (1995) 418

[PrRu61] J. Prescott and A. Ruppal, *Canad. J. Phys.* 39 (1961) 221

[Puli02] A. Pulia, Milano, Private comunication via I. Kojouharov, GSI (2002-2003)
A. Pullia, R.Bassini, C.Boiano, S.Brambilla , *IEEE Trans. Nucl. Sci.* **Vol.48** No.3 (2001) 530

[Quin59] A. Quinton, *Phys. Rev 115* No.4 (1959) 886

[Rade82] V. Radeka, *Ann. Rev. Nucl. Part. Sci.* 38 (1988) 217

[ROOT04] `root.cern.ch/`

[Saml86] L. Salmeri *et al*, *Nucl. Instr. Meth.* **A** 251 (1986) 410

[Sara88] D. Saranties *et al*, *Nucl. Instr. Meth.* **A** 264 (1988) 319

[Saul91] F. Sauli, Principles of Operation of Multiwire Proportional and Drift Chambers, in: Experimental Techniques in Nuclear and Particle Physics, ed. by T.Ferbel, World Scientific (1991)

[ScBa51] N. Schaeti and W. Baumgartner, *Helv. Phys. Acta* 24 (1951) 614

[Sche98] C. Scheidenberger and H. Geissel, *Nucl. Instr. Meth.* **B** 135 (1998) 25

[Schw72] D. Schwalm *et al*, *Nucl. Phys.* **A** 192 (1972) 449

[Scho31] W. Schottky, *Naturwisenschaften* 26 (1931) 843

[ScSt01] R. Schneider and A. Stolz, Technical Manual Ionisation Chamber MUSIC80 (2001) `www-wnt.gsi.de/frs/technical/FRSsetup/detectors/music80/`

[Scio04] `www.scionix.nl, www.scionixusa.com`

[ScNo04] `www.scionixusa.com/nomen.html`

[Sele02] L. Selen *et al*, *Nucl. Instr. Meth.* **B** 194 (2002) 479

[Shap91] D. Shapira *et al*, *Nucl. Instr. Meth.* **A** 301 (1991) 76

[Shim79] T. Shimoda *et al*, *Nucl. Instr. Meth.* 165 (1970) 261

[Sigm98] P. Sigmund, *Nucl. Instr. Meth.* **B** 135 (1998) 1

[Sile04] Silena International SpA, `www.geocities.com/silena_spa/4418V.htm`

[Simo00] M. Simon *et al*, *Nucl. Instr. Meth.* **A** 452 (2000) 205

[Simp92] J. Simpson *et al*, *Astron. Astrophys. Suppl. Set* 92 (1992) 365

[SISG04] `www-aix.gsi.de/accelerator/sis.p14.html`

[Sore97] A. Sorensen *et al*, *Phys. Rev.* **A** 55 (1997) 2896

[Souz90] R.T De Souza *et al*, *Nucl. Instr. Meth.* **A** 295 (1990) 109

[Spie99] H. Spieler, Introduction to Radiation Detectors and Electronics, Lecture Notes - Physics 198 - UC Berkeley, (1999)

[Stel89] H. Stelzer, Detectors for heavy ions, GSI print (1989)

[Stel91] H. Stelzer, *Nucl. Instr. Meth.* **A** 310 (1991) 103

[Suda02] T. Suda *et al*, *RIKEN Accel. Prog. Rep.* 35 (2002) 42

[SuBl00] K. Sümmerer and B. Blank, *Phys. Rev.* **C** 034607 (2000)

[Suem90] K. Sümmerer *et al*, *Phys. Rev.* **C** 42 (1990) 2546

[SzeS81] S. Sze, The Physics of Semiconductor Devices, 2-nd ed., Wiley Interscience (1981)

[Taba99] G. Tabacaru *et al*, *Nucl. Instr. Meth.* **A** 428 (1999) 379 and ref. therein

[Tama02] M. Tamaki *et al*, *CNS Ann. Rep.* 2 (2002) 76
`www.cns.s.u-tokyo.ac.jp/ann02/pdfs/2-16tamaki.pdf`

[Tass02] L. Tassan-Got, *Nucl. Instr. Meth.* **B** 194 (2002) 503

[Tara04] O. Tarasov *et al* 2004 *Nucl. Instr. Meth.* **A** 734 536

[Thom68] T. Thomas *et al*, *Phys. Lett.* **B** 27 (1968) 504

[Timm50] K. Timmerhaus *et al*, *Nucleonics 6* No.6 (1950) 37

[Tiss00] B. Tissue, `www.chem.vt.edu/chemed/optics/detector/pmt.html`

[TUDA02] TU-Darmstadt, Electronics Department; M. Mutterer, J. Kopach and H. J. Wollersheim, Private communication

[Valt90] E. Valtonen, *Nucl. Instr. Meth.* **A** 286(1990) 169

[Voll74] O. Vollmer *et al*, *Nucl. Instr. Meth.* 121 (1974) 373

[Voss95] B. Voss *at al.*, *Nucl Instr. Meth.* **A** 364 (1995) 150

[Wagn01] A. Wagner *et at.*, *Nucl.Instr. Meth.* **A** 456 (2001) 290

[Wale71] A. Walenta *et al*, *Nucl. Instr. Meth.* 92 (1971) 373

[Wang02] X. Wang *et al*, *Nucl.Instr. Meth.* **B** 196 (2002) 100

[Weck90] J. Weckenmann et al, *GSI Sci. Rep.* (1990) 91

[Weic04] `www-linux.gsi.de/ weick/frs/mwpc.html`

[Weiz35] C. von Weizsäcker, *Z. Physik* 96 (1935) 431

[Wilc80] W. Wilcke *et al*, *At. Data Nucl. Data Tables* 25 (1980) 391

[Wilc81] W. Wilcke *et al*, *Nucl. Instr. Meth.* 188 (1981) 293

[WiFr76] B. Wilcken and T. Fritz, *Nucl. Instr. Meth.* 138 (1976) 331

[Winy71] R. Winyard, *Nucl. Instr. Meth.* 95 (1971) 141

[Wolf55] B. Wolfe *et al*, *Rev. Sci. Instr.* 26 (1955) 504

[Woll04] H.-J. Wollersheim *et al*, *Nucl. Instr. Meth.* **A** 537 (2005) 637
`www-aix.gsi.de/~wolle/EB_at_GSI/rising.html`

[XieZ00] Z. Xie, X. Wang *et al*, *Appl. Acc. Res. and Ind.* AIP Conf.Proc. ed. by J. Duggan and I. Morgan 576 (2000) 987

[Yagi89] T. Yagimachi *et al*, *Nucl. Instr. Meth.* **A** 275 (1989) 307

[Zeid74] B. Zeidmann and W. Henning, *Nucl. Instr. Meth.* 118 (1974) 361

[Zieg80] J.Ziegler, Stopping cross sections for energetic ions in all elements, Stopping and ranges of ions in matter handbook, V5 (1980)

[Zieg85] J. Ziegler, J. Biersack, U. Littmark, The Stopping and Range of Ions in Solids, Pergamon Press, New York (1985)

[Zmer59] A. Zmerli, *J. Chem. Phys.* 56 (1959) 387

Acknowledgements

At first I would gratefully like to thank to two persons, who guided me on the physics stairway:

To my supervisor Dr. Dimiter Balabanski for giving me the opportunity to work, for his guidance, for his support and confidence about me during many years.

To my supervisor Dr. Jürgen Gerl for guiding my work, for his support, believe and understanding, for our fruitful work together in experiments, analysis, discussions and for the great time in GSI.

My special thanks are to Dipl.Ing. Ivan Kojouharov for his guidance in the detector world, for his invaluable help in the preparations, tests and experiments with the CATE detectors, and for his friendship.

I'm very thankful to Dr. Samit Mandal for his help in physics, electronics, tests and experiments, PAW and Spy analysis and generous discussions about my work, and for his friendship.

I'd like to express my acknowledgements to Dr. Magda Górska for her guidance and help in the variety of CATE experiments and for the fruitful discussions about my analysis and results.

To Dr. Frank Becker I'd like to thank for his enormous help in the simulations with MOCADI and LISE, with the ROOT trees, for the FRS adjustments for the CATE calibrations, and for the generous discussions about my work and for his friendship.

To Dr. Jurek Grębosz I'm very thankful for his continues help in programming and computing during my analysis with Spy and for his friendly, young spirit office atmosphere.

I'd like to express my acknowledgements to Dr. Hans-Juergen Wollersheim for his guidance in the first Si tests, for his clever advises, for his strictness and for his help during my conference preparations. I thank to Dipl. Phys. Adriana Banu for her help during the CATE adjustments and experiments, to Dipl. Phys. Pieter Doornenbal for his friendly work together in the Si tests and during the CATE experiments, to Dr. Piotr Bednarzcuk for the discussions about the corrections of the Si detectors, to Dipl. Ing. Hennig Schaffner for preparing always the acquisition for the CATE tests and experiments, to Dr. Nami Saito for the discussions about the ToF detectors, to Dr. Take Saitoh for the electronics during the CAVE C CsI tests and its Go4 programs, and the discussions about the RISING triggers, to Dipl. Ing. Wawjec Prokopowicz for the preparations of the holders and set-up during the CATE tests and experiments, to Miroslav Kavatshuk for his help with the gcc compilers and Go4, to Oksana Kavatshuk and Torsten Beck for being nice colleagues. I'd like to thank also to Dr. Joern Adamszewski for his help with Go4 and programming to Dr. Hans Essel for the fruitful discussions about Go4 and to Dr. Sergey Linev for his help with ROOT and the Go4 fitting procedures. My thanks are addressed as well to the FRS team in GSI for setting up the separator for the CATE experiments and to the accelerator group for providing us the beam. I'd like also to thank to those people, who had the patience to wait the investigations and the complicated analysis of the CATE system. I hope that you have now a recipe to follow in your studies.

A special place for me, during my stay in GSI, take my friends: Dr. Andrey Blazhev, who helped me often with computing, Dr. Orlin Jordanov who explained me the reaction mechanisms and Dr. Vladimir Arsov. I'd like to acknowledge many other people which helped me during my work and life and which are not listed here.

For the stronghold, love and understanding I thank to my family and my friends - I'm really lucky having you!